

FOR REFERENCE ONLY

45 007773 4



ProQuest Number: 10183165

All rights reserved

INFORMATION TO ALL USERS

The quality of this reproduction is dependent upon the quality of the copy submitted.

In the unlikely event that the author did not send a complete manuscript and there are missing pages, these will be noted. Also, if material had to be removed, a note will indicate the deletion.



ProQuest 10183165

Published by ProQuest LLC (2017). Copyright of the Dissertation is held by the Author.

All rights reserved.

This work is protected against unauthorized copying under Title 17, United States Code
Microform Edition © ProQuest LLC.

ProQuest LLC.
789 East Eisenhower Parkway
P.O. Box 1346
Ann Arbor, MI 48106 – 1346

**Novel Zeolite-Templated Metal Nitride and Oxide
Quantum Structures for use in Optoelectronic
Applications**

Gary Baker

**A thesis submitted in partial fulfilment of the
requirements of Nottingham Trent University for the
Degree of Ph.D**

September 2010

This work is the intellectual property of the author. You may copy up to 5% of this work for private study, or personal, non-commercial research. Any re-use of the information contained within this document should be fully referenced, quoting the author, title, university, degree level and pagination. Queries or requests for any other use, or if a more substantial copy is required, should be directed in the owner(s) of the Intellectual Property Rights.

Acknowledgements

To Dr. Gary Hix, my Director of Studies, I owe my thanks and apologies for both guiding and tolerating me for four years. I believe I did my best to be a good student, yet I also know I pushed it sometimes. Dr. Hix found a very happy medium between work and play and I thank him for the guidance he provided to keep me on track and lead me astray equally. My second supervisor, Dr. Fouzia Ouali, I also thank for her advice and support given the difficulties when marrying chemistry and physics. Other members of staff at Nottingham Trent University that deserve thanks for their help and support include Mark Sladen, Marilyn Johnson, Dr. Dave Belton, Dr. Robert Rantsen and Tom Miller. Staff at external institutions, namely Dr. David Morgan and Dr. Wuzong Zhou, that are part of the EPSRC Open Access scheme are also due thanks for their kindness in allowing me to use their equipment and for their continued support after my visits.

I would also like to thank many of the people who have passed through Nottingham Trent University over the years and have been there with me when I fancied an eating challenge or needed someone to talk to over a beer and a game of pool after a hard day in the lab or after receiving bad news. These include Andy, Neil, Muriel, Sara, Dan, Vicky, Laura, Tracey, Alberth, Adam and even Roy!

A special thank you must go to my wife, Marie, who conveniently wanted to get married during my last year as a PhD student! Honestly, the wedding was the best day of my life and a welcome distraction from the troubles life brings. Marie stuck with me through 6 years of education so I suppose I have some making up to do!

I also thank the EPSRC for funding this work.

Abstract

The aim of this work was to develop methods to produce zeolite-templated metal nitrides and oxides and to investigate the effect of zeolite inclusion on the optoelectronic properties of the guest materials and the role of the zeolite in any changes.

The bulk of the work concentrated on the oxides and nitrides of Zn and Ga, due to the relatively low cost of producing ZnO and Zn₃N₂ and the commercial significance of GaN as a fairly new wide band gap semiconductor. To this end, a series of experiments were conducted to investigate the effect of zeolite inclusion on these materials in which two precursor impregnation methods were investigated with 3 very different zeolite types. In addition, a mixed nitride series (In_xGa_{1-x}N), lanthanide nitrides and a selection of other nitride materials were also studied in order to evaluate the feasibility of applying the techniques to a wider range of materials.

It was found that in using many semiconducting materials as guest phases distinct changes in band gap energies can be observed upon zeolite inclusion and that the degree and nature of the changes are dependent on the impregnation method and the host zeolite. By employing a novel, molten-salt based method of zeolite impregnation a dense guest phase can be achieved, producing significantly different electronic properties to the disperse phases attainable by traditional solution-based methods. This showcases the tuneable capabilities of zeolites as crystal engineering templates, but also highlights the incredible complexity of zeolite science.

Table of Contents

1.	Introduction	11
1.1.	Zeolites	11
1.1.1.	<i>Background</i>	11
1.1.2.	<i>History</i>	12
1.1.3.	<i>Structure</i>	14
1.1.4.	<i>Synthesis</i>	19
1.1.5.	<i>Frameworks used in this Project</i>	20
	<i>Chemistry</i>	23
1.1.6.	<i>Zeolites in Electronics</i>	32
1.2.	Metal Nitrides and Oxides	34
1.2.1.	<i>Nitrides</i>	34
1.2.2.	<i>Oxides</i>	36
1.3.	Semiconductors	37
1.4.	Quantum Confinement	40
2.	Aims	44
2.1.	Zeolite Encapsulation of Metal Nitride Clusters	44
2.2.	Structural Characterisation	46
2.3.	Optoelectronic Investigation	47
3.	Experimental Techniques	48
3.1.	Ion Exchange	48
3.2.	Precursor Impregnation	49

3.2.1.	<i>Aqueous Solution Impregnation</i>	49
3.2.2.	<i>Molten Salt Impregnation</i>	50
3.3.	Nitridation and Oxidation	51
4.	Analytical Techniques	52
4.1.	X-ray Diffraction	52
4.1.1.	<i>Introduction</i>	52
4.1.2.	<i>X-ray Generation</i>	53
4.1.3.	<i>Crystal Symmetry</i>	56
4.1.4.	<i>Diffraction of X-rays by Crystals</i>	59
4.1.5.	<i>Single Crystal X-ray Diffraction</i>	61
4.1.6.	<i>Powder X-ray Diffraction</i>	62
4.1.7.	<i>Rietveld Refinement</i>	63
4.2.	X-ray Photoelectron Spectroscopy	68
4.2.1.	<i>Introduction</i>	68
4.2.2.	<i>Data Analysis</i>	72
4.3.	Electron Microscopy	74
4.3.1.	<i>Transmission Electron Microscopy</i>	75
4.3.2.	<i>Scanning Electron Microscopy</i>	76
4.3.3.	<i>Energy Dispersive X-ray Spectroscopy</i>	77
4.4.	UV-Visible Spectroscopy	78
4.4.1.	<i>Introduction</i>	78
4.4.2.	<i>Band Structure Determination</i>	80
4.5.	Photoluminescence	83

5.	Gallium Nitride	85
5.1.	Results	87
5.1.1.	<i>ZSM-5</i>	87
5.1.2.	<i>Faujasite</i>	105
5.1.3.	<i>Ferrierite</i>	115
5.2.	Discussion and Conclusions	126
6.	Gallium Oxide.....	128
6.1.	Results	130
6.1.1.	<i>ZSM-5</i>	130
6.1.2.	<i>Faujasite</i>	141
6.1.3.	<i>Ferrierite</i>	150
6.2.	Discussion and Conclusions	160
7.	Zinc Nitride	161
7.1.	Results	163
7.1.1.	<i>ZSM-5</i>	163
7.1.2.	<i>Faujasite</i>	171
7.1.3.	<i>Ferrierite</i>	179
7.2.	Discussion and Conclusions	188
8.	Zinc Oxide.....	189
8.1.	Results	192
8.1.1.	<i>ZSM-5</i>	192
8.1.2.	<i>Faujasite</i>	203

8.1.3. <i>Ferrierite</i>	213
8.2. Discussion and Conclusions	222
9. Indium Gallium Nitride.....	224
9.1. Introduction	224
9.2. Results	225
9.2.1. <i>ZSM-5</i>	225
9.2.2. <i>Faujasite</i>	231
9.3. Discussion and Conclusions	236
10. Lanthanides.....	238
10.1. Introduction	238
10.2. Results	240
10.2.1. <i>Europium Nitride</i>	240
10.2.2. <i>Ytterbium Nitride</i>	248
10.2.3. <i>Terbium Nitride</i>	254
10.3. Discussion and Conclusions	259
11. Other Nitrides in ZSM-5.....	261
11.1. Cerium Nitride	262
11.2. Chromium Nitride	265
11.3. Copper Nitride	268
11.4. Tin Nitride	271
11.5. Discussion and Conclusions	274
12. Conclusions and Further Work	275

12.1. Summary and Conclusions	275
12.2. Further Work	279
13. References.....	281

Abbreviations

(HR)TEM	(High Resolution) Transmission Electron Microscopy
SEM	Scanning Electron Microscopy
EDX	Energy Dispersive X-rays
FWHM	Full Width at Half Maximum
XPS	X-ray Photoelectron Spectroscopy
(P)XRD	(Powder) X-ray Diffraction
PL	Photo Luminescence
SBU	Secondary Building Unit
IZA-SC	International Zeolite Association – Structure Commission
SDA	Structure Directing Agent
T	Tetrahedral Atom in a Zeolite Framework
TCHZ	Thompson-Cox-Hastings pseudo-Voigt Peak Type
UV-Vis	Ultra Violet – Visible
a.u.	Arbitrary Units
CB	Conduction Band
VB	Valence Band
QB	Quantum Box
QD	Quantum Dot
QW	Quantum Well
QWi	Quantum Wire

1. Introduction

1.1. Zeolites

1.1.1. Background

Zeolites are a class of crystalline, microporous compounds covering both naturally occurring and synthetic materials with rigid, three dimensional, open framework structures consisting of corner-sharing oxide tetrahedra of mainly, but not limited to, silicon and aluminium. The open frameworks give rise to regular arrays of channels and cavities that initially contain water molecules and charge-balancing cations (see Chapter 1.1.3) but can also accommodate some small molecules. Zeolites have very small and defined pore dimensions, particularly in comparison to other porous materials. For example, activated carbon has pore dimensions in the range 20 – 1000 Å and typical silica gel has pores in the range 10 – 100 Å, whereas zeolite A, for example, has pore windows of 5 Å in diameter. ^[1]

1.1.2. History

The term 'Zeolite' was coined by the Swedish mineralogist Baron Axel Friedrik Cronstedt after discovering the mineral stilbite in volcanic rocks in 1756. Cronstedt noticed a degree of water loss upon heating the mineral with a blowpipe flame, also known as 'intumescence'. Thus the name 'zeolite', which comes from the Greek for 'Boiling Stone', was conceived. [2]

For approximately 200 years, until 1845, the only industry using zeolites was the jewellery industry, when H.S. Thompson demonstrated that some soils 'decomposed' and retained ammonium salts [3], then J.T. Way showed that hydrated silicates in the soil were the reason for this phenomenon [4]. It wasn't until 1858 that Eichorn demonstrated the reversible ion exchange properties of chabazite and natrolite. [5] The molecular sieving properties of chabazite were shown in 1925 by Weigl and Steinhoff. [6]

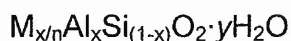
Richard Maling Barrer is acclaimed as the pioneer of initial research into zeolites. He worked on zeolites from 1938 right up until his death in 1996. His achievements include characterisation of ion exchange, dehydration and gas-sorption of natural zeolites, procedures for synthetic zeolite formation and entirely new phases through hydrothermal methods. Zeolites soon became widely used as catalysts in the 1960s, taking advantage of their molecular sieving properties to apply them to processes requiring selective catalysis. [1]

The initial commercial success of zeolites is credited to their molecular sieving properties: the ability to preferentially absorb small molecules over larger

molecules. This led to the widespread use of the molecular sieves 3A, 4A and 5A, first made by Linde Corp in the 1940s, which are zeolite A exchanged with different charge-balancing cations to alter the pore window dimensions, providing varying molecular sieving properties.

1.1.3. Structure

The typical formula of a zeolite is:



Where x generally ≥ 2 as AlO_4 can only be joined to SiO_4 according to Löwenstein's Rule^[7] and n is the cation valence.

Zeolites can be categorised as zeolites and 'zeotypes', according to their chemical composition. The frameworks are formed by corner-sharing tetrahedral oxides of so called 'T-atoms', i.e. $(SiO_4)^{4-}$ and $(AlO_4)^{5-}$, where the 'T-atoms' are Si and Al. Zeolites are generally thought of as aluminosilicates and zeotypes as materials with the same framework topology as a known zeolite, but with atoms other than silicon or aluminium, such as Ga, Fe or P, occupying the T-atom sites. Zeotypes have been found naturally (for example: Viseite and Keohite – P containing Analcime structures) and also made synthetically and post-synthesis via the substitution of T-atoms (i.e. B and Ga in ZSM-5 where Al is substituted). The replacement of T-atoms is usually confirmed by MAS-NMR.^[8, 9]

Where a zeolite contains a number of non-silicon atoms in the framework, there is a charge imbalance (i.e. compare the charges of the tetrahedra $(SiO_4)^{4-}$ and $(AlO_4)^{5-}$). This charge imbalance is compensated for by the presence of cations located within the pores. In naturally occurring zeolites these cations tend to be group I and II metals, such as sodium, potassium and calcium. The number of cations present in the structure is directly related to the aluminium (or other non-silicon species) content. These cations are highly mobile and are easily exchanged by other cations, leading to the use of zeolites as ion-exchangers, in which the initial cation is replaced by cations, which are undesirable in the system,

i.e. calcium can be removed from hard water or radioactive elements may be removed from infected areas. Cations can also be introduced to alter the structural, adsorptive or catalytic properties of the zeolite. Commonly, the natural/synthetic charge-balancing cations are replaced with transition metals, rare earth metals, NH_4^+ and H^+ . A zeolite will typically show preference for one ion over another, which can be due to (1) zeolite geometry (2) cation size (solvated or otherwise) (3) cation charge (4) zeolite synthesis method (5) charge distribution through the zeolite.

As well as the pores containing charge-balancing cations, the pores also generally contain water molecules, known as 'Zeolitic Water'. Zeolitic water can be removed continuously and reversibly, in most cases having little or no effect on the structure of the zeolite itself. The water content of a zeolite can depend on the size and shape of the pores, but also on the number and nature of any charge-balancing cations. It has been shown that cations within hydrated zeolites will tend to be as hydrated as possible, given spatial limitations, as long as they are not too far away from the framework and the negative charge distribution. ^[1] This action of reversibly adsorbing and desorbing water has led to the use of zeolites as desiccants, particularly as molecular sieves, which can be found in most laboratories.

There are currently nearly 200 known zeolite framework types, offering a vast range of pore geometries and sizes ^[10], a selection of which is presented in Figure 1.

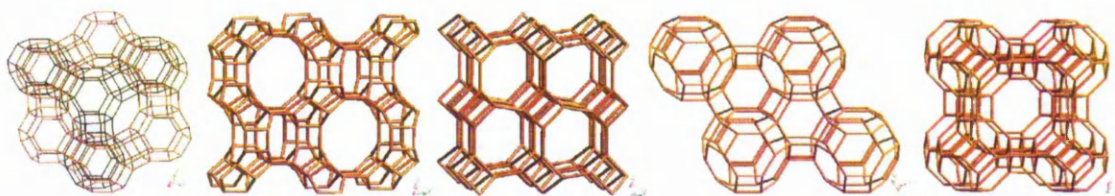


Figure 1: Left to right: Faujasite (FAU), Mordenite (MOR), Phillipsite (PHI), TMA-E (EAB) and Linde Type A (LTA). ^[10] Each line represents a T-O-T bond.

As Figure 1 shows, the vast range of geometries available provide structures with one-dimensional channels, 2-dimensional interlinking channels and 3-dimensional cages, allowing zeolite technology to be applied to a variety of applications to accommodate small molecules.

In order to classify the different zeolites, unit cells could be used, but that would be difficult. Instead, 'secondary building units' (SBUs) are used, which are less complex recurring sub-units. The simplest way is by using 8 SBUs, in Figure 2, which take account of the Si, Al and O atoms, but not cations or water molecules, the positions of which have not been defined for every zeolite and is not trivial.

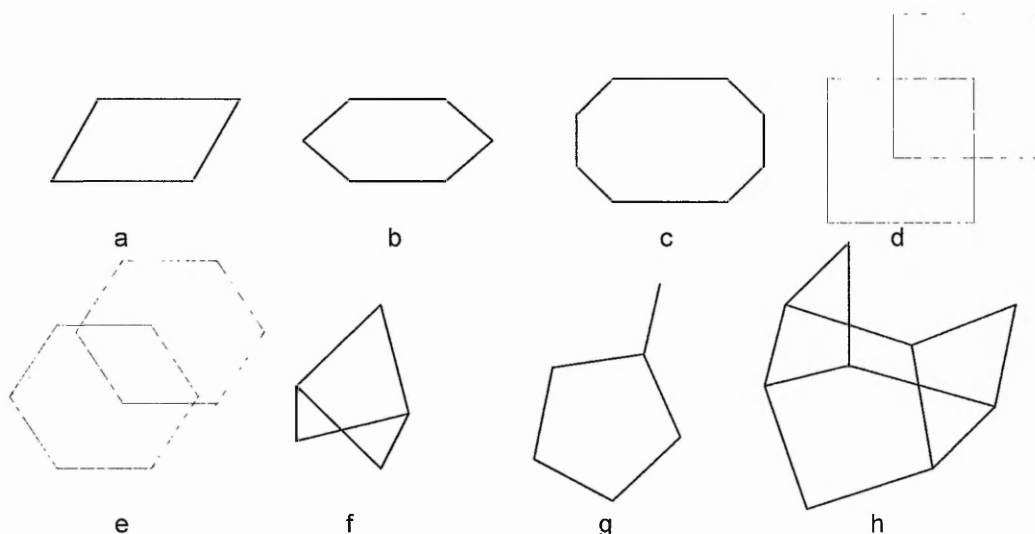


Figure 2: The 8 SBUs used to classify zeolites: a) single four ring (S4R), b) single 6 ring (S6R), c) single eight ring (S8R), d) double four ring (D4R), e) double six ring (D6R), f) complex 4-1, g) complex 5-1 and h) complex 4-4-1.

In Figure 2 each line represents a T–O–T bond, where the O lies near the centre of the line and each point represents a T-atom. This is represented by TO_4 tetrahedra in Figure 3, where the bold lines indicate the SBU.

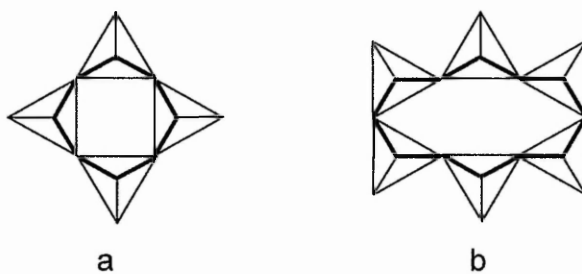


Figure 3: The arrangement of tetrahedra in a) 4R and b) S6R SBU.

The SBUs can join to give larger rings of 8, 10 or 12 oxygen atoms, or 'Oxygen Windows', which are structurally very important with regards to the admission of small molecules.

1.1.4. Synthesis

Many of the naturally occurring zeolites can be synthesised in the laboratory by hydrothermal methods. There is also a vast range of zeolites not found naturally that can be synthesised, such as zeolite A, which is structurally closely related to natural sodalite. The method by which most zeolites are made in the laboratory was originally reported by Schafhautele in 1845 in the synthesis of quartz by heating a 'gel' silica with water in an autoclave.^[11] Later, in 1862, Deville reported the first synthesis of a zeolite (Levynite) by hydrothermal methods. The first reports of zeolite synthesis, however, had no X-ray Diffraction (XRD) data to support the claims. The first reliable claims of zeolite synthesis came courtesy of RM Barrer et al in 1940, with the synthesis of zeolites identical to those found naturally.^[1] The first synthesis widely accepted as the first to be completely characterised was from Milton, Breck et al at Union Carbide as they synthesised zeolite A in 1956.^[12]

In general, synthetic zeolite crystallisation is carried out in an inhomogeneous gel from a silica and alumina source with water at a high pH from hydroxide anions and usually metal or ammonium cations. The framework composition is controlled exclusively by the $\text{SiO}_2:\text{Al}_2\text{O}_3$ ratio and the geometry can be controlled by using Structure Directing Agents (SDAs). A few other factors can also be influential, such as salt impurities, trace aluminium in silica sources, mode and nature of stirring, order of reactant addition and the reaction vessel (i.e. glass can exhibit a memory effect). After heating to $\sim 100^\circ\text{C}$ for several hours with or without agitation the synthesis mixture is then filtered, washed and dried.

1.1.5. Frameworks used in this Project

Information from the IZA-Structure Commission. ^[10]

Faujasite (FAU)

Also known as: Zeolite X (High Alumina), Zeolite Y (High Silica)

Space Group: Fd-3m (origin choice 2)

Cell Parameters: $a = b = c = 24.345 \text{ \AA}$ $\alpha = \beta = \gamma = 90^\circ$

Volume = 14428.77 \AA^3

$R_{\text{DLS}} = 0.0009$

Framework Density: $13.3 \text{ T}/1000 \text{ \AA}^3$

Ring Sizes (# T-atoms): 12 6 4'

Channel System: 3-dimensional

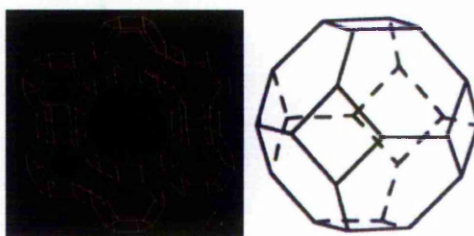


Figure 4: FAU Structure viewed along {111} and a beta cage.

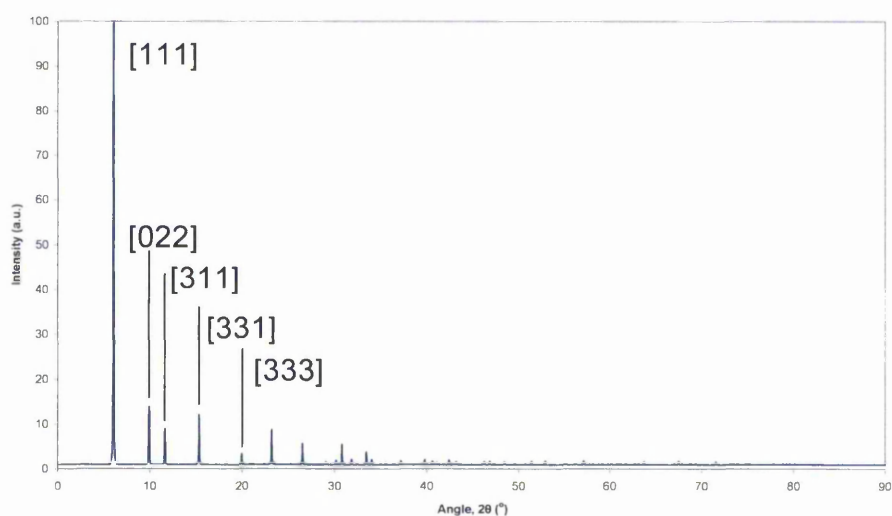


Figure 5: Typical P-XRD Plot for Dehydrated Na-X (Si/Al = 1.2).

ZSM-5 (MFI)

Space Group: Pnma

Cell Parameters: $a = 20.090 \text{ \AA}$ $b = 19.738 \text{ \AA}$ $c = 13.142 \text{ \AA}$

$\alpha = 90^\circ$ $\beta = 90^\circ$ $\gamma = 90^\circ$

Volume = 5211.28 \AA^3

$R_{\text{DLS}} = 0.0020$

Framework Density: $18.4 \text{ T}/1000 \text{ \AA}^3$

Ring Sizes (# T-atoms): 10 6 5 4

Channel System: 3-dimensional

$\{100\}$ 10-ring $5.1 \times 5.5 \text{ \AA}$ $\{010\}$ 10-ring $5.3 \times 5.6 \text{ \AA}$

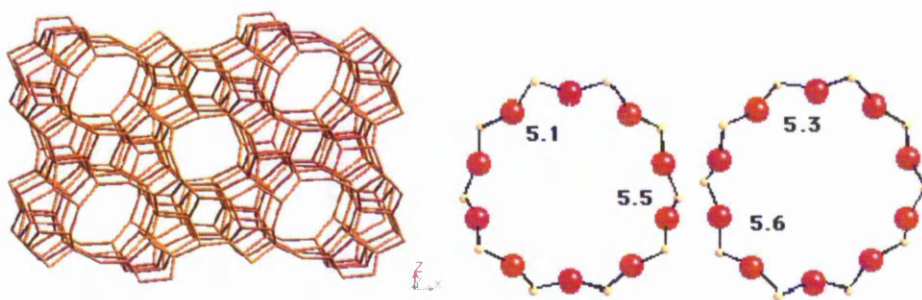


Figure 6: MFI Structure viewed along $\{010\}$ and the main 2 channels (measurements in \AA).

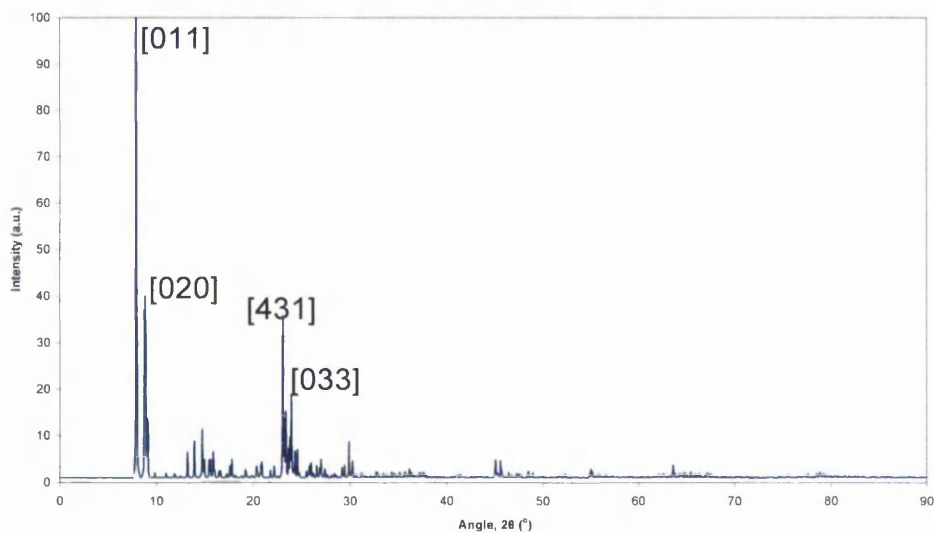


Figure 7: Typical P-XRD Plot for Calcined ZSM-5 (Si/Al = 299).

Ferrierite (FER)

Space Group: Immm

Cell Parameters: $a = 19.018 \text{ \AA}$ $b = 14.303 \text{ \AA}$ $c = 7.541 \text{ \AA}$

$\alpha = 90^\circ$ $\beta = 90^\circ$ $\gamma = 90^\circ$

Volume = 2051.26 \AA^3

$R_{\text{DLS}} = 0.0036$

Framework Density: $17.6 \text{ T}/1000 \text{ \AA}^3$

Ring Sizes (# T-atoms): 10 8 6 5

Channel System: 2-dimensional

$\{001\}$ 10-ring $4.2 \times 5.4 \text{ \AA}$ $\{010\}$ 8-ring $3.5 \times 4.8 \text{ \AA}$

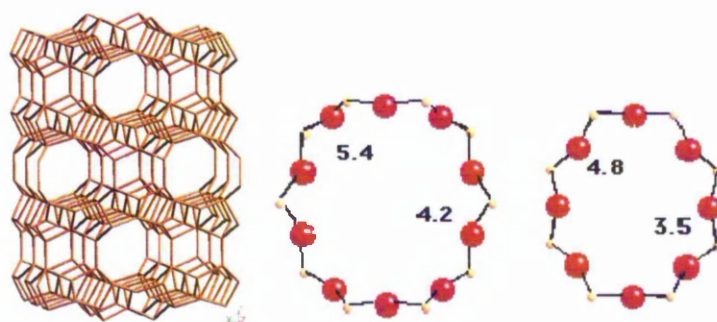


Figure 8: FER Structure viewed along $\{001\}$ and the 2 main channels (measurements in \AA).

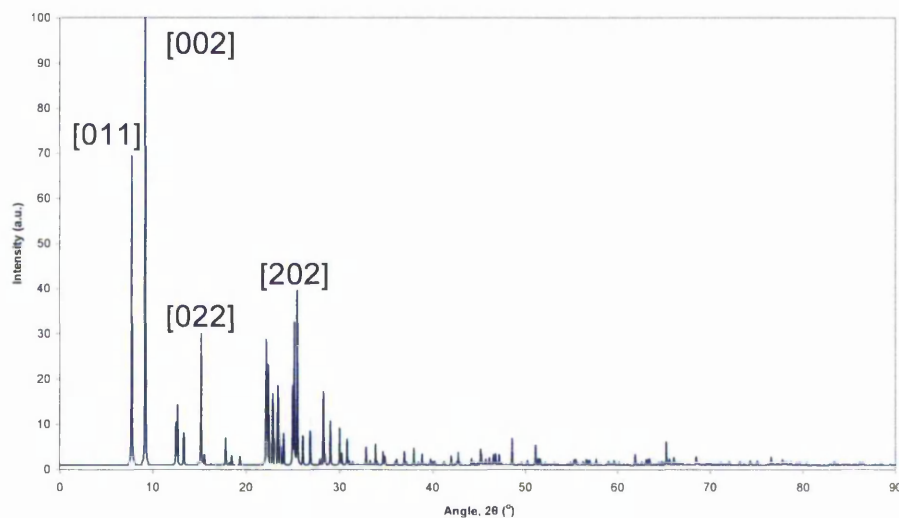


Figure 9: Typical P-XRD Plot for Calcined FER (Si/Al = 25).

Chemistry

Most applications making use of zeolites take advantage of the wide range of pore sizes and geometries and the charge-balancing cations available. Uses such as catalysis and water absorption make use of the porous nature of the frameworks to absorb molecules and the use of zeolites as water-softeners exploits the ability to exchange the charge-balancing cations with calcium and magnesium ions from hard water supplies. ^[1]

Dehydration and Thermal Stability

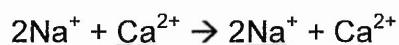
One of the most interesting properties of zeolites, the gain and loss of zeolitic, water, can sometimes alter the structure of a zeolite. In most cases it will be a simple case of altered cell dimensions, but in some cases can cause recrystallisation of different phases or complete structure collapse.

For those zeolites that can withstand dehydration, they are generally stable at temperatures in the region of 700°C in air, although there are some exceptions. Above these temperatures the zeolite structure will break down, giving an amorphous solid or a crystalline species that may or may not be zeolitic. For example, zeolite A will convert to the non-zeolitic species β -cristobalite at 800°C while at 1000°C zeolite Y will become a glass. There are some zeolites, such as Paulingite and Phillipsite, which are only stable up to 250°C, whereas mordenite and offretite have been known to retain their structure at 900°C. ^[1]

The stability of a zeolite under extreme conditions, whether it is temperature, pH or pressure is a complex matter, but generally depends on the nature and population of the cations present and the aluminium content.

Ion Exchange

Arguably the most widely applied property of zeolites is their ability to undergo ion exchange processes by replacing the charge-balancing cations present within the pores with cations in a solution. For example; the replacement of potassium ions by sodium ions, or monovalent sodium ions by divalent calcium ions:



This phenomenon was first observed around 1875, inciting interest in using zeolites as water softeners, in particular in washing powders. They have also been used to remove radioactive ions from waste materials. ^[13] Other applications include the modification of zeolites for use as catalysts and molecular sieves. The ability of a zeolite to ion-exchange relies on a number of factors, namely; the nature of the cation species, the anhydrous and hydrated size of the cation, the charge on the cation, temperature, cation concentration in solution, the anionic species associated with the cation in solution, the solvent system and the structural characteristics of the zeolite. Ion exchange is not necessarily a facile process, indeed, some dense zeolite structures, such as analcime and natrolite don't tend to undergo any appreciable ion-exchange at all. Although most zeolites don't undergo any appreciable dimensional changes with ion exchange, the process can alter other properties, such as the stability, adsorptive behaviour and selectivity and catalytic activity. ^[1]

Ion exchange is usually carried out in aqueous solution although organic exchange media have been investigated. This is, however, a complicated process as to

obtain reliable data the zeolite must be completely dehydrated and there can be issues regarding the adsorptive capabilities of the zeolite towards the organic solvent molecule, for example, if the solvent molecule is too large ion exchange may not occur. It is widely accepted that any ion exchange processes that occur in non-aqueous solvents are slower than those in water and the rate of exchange decreases with decreasing dielectric constant. [1]

In order for ion exchange to occur, the zeolite must be able to readily accept the solvent molecules. Zeolites with a high Al content, and therefore a high loading of cations, will accept polar solvent molecules more readily than more siliceous zeolites. A cation within a zeolite pore structure will generally be coordinated to the oxygen atoms of the framework by one side, leaving the other side of the cation uncoordinated. If there is another cation in close proximity there will be repulsion of charge between the two uncoordinated halves of the cations. In accepting polar solvent molecules, i.e. water, the repulsion of charge between the cations may be stabilised.

Ion exchange processes are generally carried out in acidic solution, but this can dramatically alter the zeolite framework structure. It is often assumed that zeolites have a low resistance to acid, indeed this is the case for some, such as zeolites A and X that dissolve in a low concentration of hydrochloric acid. The reason for zeolite instability in acid is the process of dealumination, or the leaching of Al from the framework. Zeolites with high Si:Al ratios may still leach Al, but generally their structure will be retained. Some good examples of this are clinoptilolite, mordenite and ferrierite, which are stable in 8M nitric acid for 6 months. Even after complete

dealumination, zeolites such as clinoptilolite, mordenite and ZSM-5 can retain their structure. [1]

Some examples where zeolites have been used for their ion exchange properties include commercial detergents, where they are used as an environment friendlier alternative to polyphosphates to remove Ca^{2+} and Mg^{2+} from hard water to prevent precipitation by surfactants, the treatment of animals affected by the Chernobyl disaster to remove or reduce the uptake of ^{137}Cs and $^{90}\text{Sr}/^{90}\text{Y}$ and the treatment of waste water, soil and manure to control pH, moisture content and odour.

Reaction with Ammonia

As this work involves performing the synthesis of nitrides, which requires the use of gaseous ammonia at elevated temperatures, within the pore systems of several zeolites, it is prudent to mention how zeolites may react under these conditions.

Upon introduction to gaseous ammonia at 500°C at ambient pressure the surface hydroxyl groups of a hydrogen zeolite form will be replaced by H₂N- groups whilst retaining the crystal structure of the parent zeolite (See Figure 10). In the case of zeolite Y the quantity of ammonia uptake is equivalent to 50% conversion of H⁺ to NH₄⁺. [14]

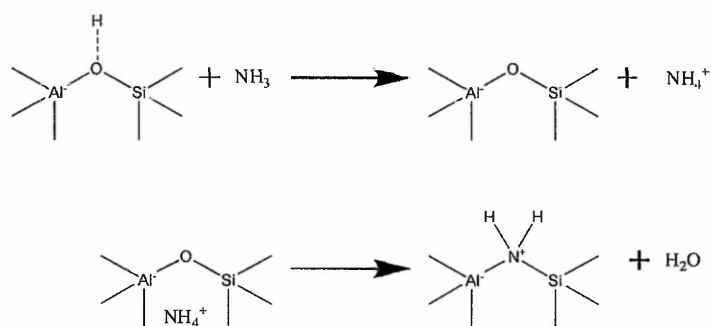


Figure 10: Mechanism of amido zeolite formation.

This is an example of how the “O” groups of a zeolite may be modified, ultimately altering the structural, adsorptive and reactive properties of the parent zeolite. As this does not affect the structure of the zeolite it was not deemed a relevant concern in this project, in which the function of the zeolite is purely as a template.

Catalysis

Zeolites were first used as catalysts in 1959 when Union Carbide used zeolite Y as an isomerisation catalyst. ^[12] In 1962, based on the work by Planck and Rosinski, zeolite X was used as a cracking catalyst. ^[1] This quickly became the main reason for zeolite research. Today, the main application of zeolite science is in the area of catalysis.

The key property that presents zeolites as useful catalysts is their high surface area, especially within the pore structures; which can be as much as twenty times that of the external surface. This internal-external surface area difference, along with the defined 'window' sizes lead to zeolites being used very effectively as shape-selective catalysts.

As well as using ion exchange as a useful process in itself, the products of ion exchange reactions have also found use in catalysis. In altering the identity of the charge-balancing cations in a zeolite, properties such as pore sizes, adsorptive behaviour and catalytically active sites can also be affected. By reducing an included metal ion, metal bifunctional catalysts can be produced, which can then be used in de/hydrogenation reactions. Other metals, for example, can also be introduced to inhibit or pacify a zeolite-supported catalyst.

Modification for catalytic purposes, however, isn't restricted to ion substitution; the framework T-atoms can also be substituted either during synthesis or post-synthesis to manipulate the internal electrostatic fields. A simple example of this is

ZSM-5, which can accept B and Ga as T-atoms via a straightforward salt treatment.

Inclusion Chemistry

The very well defined and regular porosity of zeolites have led to the concept of using zeolite pores as supports for other materials in the fields of catalysis, agriculture, medicine, electronics and optical emission. Zeolite support has the potential to improve the performance of many materials with respect to their bulk counterparts; whether this is due to slow release mechanisms, greater surface area, shape selectivity or quantum confinement (See Chapter 1.4). The factors affecting the viability of an occlusion process include the degree of hydration of the inclusion species and zeolite, pore geometry/size, cations present in the zeolite, temperature and the nature of the ion/molecule intended to be occluded.

Many groups have investigated the occlusion of additional species inside the pores of zeolites for a vast range of applications using various methods. For example; Anderson, et al. demonstrated that zinc-cadmium alloy clusters could be formed within zinc-exchanged zeolite A by the adsorption of cadmium vapour^[15, 16] and that zeolite A will also readily absorb zinc vapour,^[17] which may be useful in electronic or catalytic applications. Anderson et al. also demonstrated that extra-zeolite bimetallic nanowires could be produced from copper and silver containing zeolites by irradiating a sample with an electron beam during HRTEM analysis.^[18, 19] In terms of luminescence; Tiseanu, et al. have spent a number of years investigating the photoluminescent properties of lanthanides, in particular terbium, within zeolite hosts.^[20-25] Recently, Meteleva, et al. has moved from investigating CdS semiconductor thin films to zeolite-semiconductor composites in order to further the field of photocatalysts,^[26, 27] joining other groups; such as Yuan, et al. who has also recently moved into zeolite-semiconductor composites with a

particular emphasis on Ag_2S .^[28, 29] A handful of research groups have investigated the capability of zeolites to play host to reactions with harsh conditions, such as those required to form metal nitrides,^[30, 31] although these studies have so far been limited to structural characterisation and catalytic studies.

1.1.6. Zeolites in Electronics

Zeolites are not well known as electronic materials as they themselves don't present many useful electronic properties. However, many research groups have started to turn to zeolites as hosts for electronic materials. Due to the regular and defined arrays of pore networks and the extensive range of pore geometries and sizes available, zeolites are becoming increasingly attractive as 'molecular scaffolds' for other species. The driving force for the increase in research in this area is not only the potential for developing nanoscale conduction pathways and circuits with the recent popularity of 'nanomaterials' promising to further the efforts of device miniaturisation, but also the promise of altered and sometimes improved properties with respect to bulk materials upon size reduction.

In terms of zeolites themselves, they show very little electronic conductivity. In some cases the cations present within the structure can be mobile and are thus allowed to migrate through the framework. This process is highly dependent on the cation and channel sizes. To date, the conductivity of zeolites has not been applied to any device or application.

There is, however, intensive research into the occlusion of electronic materials within zeolite cavities. ^[26, 28, 29, 32-38] Many groups have investigated the possibility of producing nanoscale, conductive, metallic wires within zeolites, with some success. The properties of these zeolite/metal composites in comparison to bulk metal wires has not yet been fully investigated due to the technical difficulties involved in comparing such complex 3 dimensional structures to the bulk counterparts. Unfortunately, the zeolites with so-called 'one-dimensional' channel

structures also contain main-channel connecting pores and exhibit intra-cavity interactions.

The encapsulation of semiconducting materials, such as sulphides, oxides and phosphides within zeolite cavities has also been under scrutiny. ^[17, 26, 28, 37, 39] A particular reason for wanting to encapsulate semiconductors within nanostructures is the potential of changing the optoelectronic properties of semiconducting material with respect to the bulk; a phenomenon that is described further in Chapter 1.4.

1.2. Metal Nitrides and Oxides

1.2.1. Nitrides

Metal nitrides are a class of chemicals with the general formula M_xN_y , where M is a metal and N (nitrogen) occupies the -3 oxidation state and is covalently bonded to the metal, making nitrides useful as very hard materials. Metal nitrides can be synthesised in a number of ways, but in general harsh reaction conditions are required, such as high temperatures, long reaction times and, in some cases, high pressures. Also, many nitrides or the intermediate products formed during the synthesis are sensitive to oxygen and moisture; therefore many syntheses must be performed in an inert atmosphere. As N_2 is relatively unreactive alternative nitrogen sources have been investigated, such as solid sodium azide, NaN_3 , which can be used in conjunction with a molten Na flux to produce highly pure and crystalline nitrides. ^[40, 41] Another approach to nitride synthesis is the ammonolysis of metals or their compounds; such as oxides, halides and sulphides. This process involves heating the precursor at high temperatures in an ammonia atmosphere. ^[42-47]

The emergence of synthetic nitrides started in the 1920s and '30s, thus nitrides are a relatively young class of compounds, which is largely attributed to the difficult synthetic methods and the complicated analytical techniques required in nitride chemistry. During the last century, however, nitrides have found uses in a variety of applications: such as high temperature refractory ceramics and coatings, semiconductors and ionic conductors. Due to limitations in synthetic hardware and analytical techniques, it wasn't until the 1990s that ternary and higher order

nitrides started to be investigated, resulting in the current plethora of fully characterised nitride materials reported to date.

Nitrides, and especially group 13 nitrides, are important in the semiconductor industry. Group 13 nitrides have wide ranging band gap energies, i.e. 0.7eV for InN, 3.4eV for GaN and 6.2eV for AlN. GaN has attracted a significant amount of attention in recent years as a blue light emitter, thus promising real progress in high density optical memory storage and solid state lighting (i.e. LEDs). The actual wavelength at which GaN emits can be tuned by doping with other metals, such as In, As and Mg. Unfortunately, bulk GaN powders, and other nitride materials often suffer from impurities, such as oxygen and carbon, which affects the emission spectrum significantly, thus making them inefficient at emitting at specified wavelengths. ^[48] Current research efforts in the field of nitride semiconductors is focussed mainly on the synthesis of colloidal quantum dots; particles of reduced dimensionality, in order to reduce the levels of impurities and control crystal growth by capping crystals with organic chemicals. ^[49]

1.2.2. Oxides

Oxides, in comparison to nitrides, are a well investigated class of materials. Oxides have the general formula M_xO_y and are generally synthesised in the laboratory by heating a metal or non-oxide metal compound in air at temperatures from as low as 100°C to as high as current furnace technology allows (>2000°C). New phases may also be reached using different pressures and heating techniques; such as microwaves. Oxides are also abundant in nature, in fact, many metals will oxidise at ambient conditions, given time, which is why metal will rust, or oxidise when left untreated. Oxides are generally stable at ambient conditions, which make the practicality of synthesis and characterisation of such materials fairly trivial. Due to the comparatively facile synthesis of metal oxides, they have been studied for centuries; therefore there is a lot more information available regarding oxides compared to nitrides.

Metal oxides have found use in a vast range of applications ranging from paints, coatings and cosmetics to catalysts, semiconductors and fuel cells.

1.3. Semiconductors

Semiconductors are materials that possess an electronic band structure, which allows the movement of electrons (negative charge carriers) and/or 'holes' (lack of electrons – positive charge carriers) to occur. In order to explain the mechanism by which semiconductors conduct electricity, an understanding of Band Theory is required. In a single atom the electrons surrounding the nucleus occupy well-defined energy levels and according to Pauli's exclusion principle, no two electrons may occupy the same quantum state in a potential system and thus no more than two electrons may occupy the same energy level as long as they have opposite spins. Therefore when several identical atoms, with identical electron energy levels, come together to form a solid the energy levels sub-divide into levels with slightly different energies to satisfy Pauli's principle. The number of energy level divisions is equal to the number of atoms in the system, therefore for a relatively small piece of semiconductor there can be a very large number of divided energy levels (for example, a 1cm^3 piece of silicon contains 4.93×10^{22} atoms and therefore 4.93×10^{22} energy level divisions). The difference in energy between these levels is so small that it is more convenient to consider them as continuous bands. A physical representation is shown in Figure 11 .

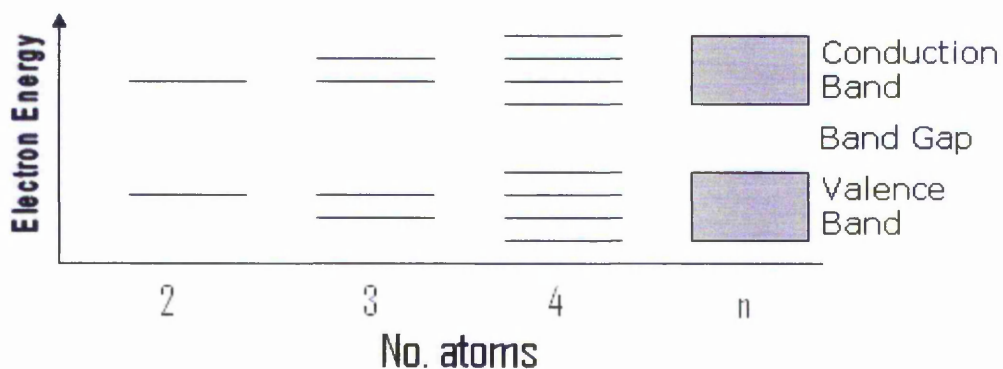


Figure 11: Schematic representation of Band Structure Formation.

The collection of energy states occupied by the electrons at the ground state is termed the 'valence band'. Upon absorption of energy the electrons are promoted to a higher energy state called the 'conduction band'. The energy between the valence and conduction bands is an area of energies forbidden by quantum mechanics; known as the 'band gap'. The difference between semiconductors and insulators is the size of the band gap, i.e. a large band gap (>4 eV) material is usually an insulator at room temperature. When an electron is promoted into the conduction band it then has the freedom to move within that partially occupied band. The electrons that remain in the valence band can also then move within the band due to the vacancy (hole) formed by the departure of the promoted electron. Upon recombination of promoted electrons with holes energy is released in the form of lattice vibrations (phonons) or light (photon) emission, hence the use of semiconductors in LEDs.

One of the many factors that define a semiconductor and its properties is the band gap energy (E_g). This determines the energy required to activate the semiconducting properties (i.e. promote a valence band electron to the conduction band) and the wavelength of any emitted light upon electron-hole recombination in the case of intrinsic semiconductors (i.e. a single semiconducting phase with one band structure).

The band gap of a semiconducting material can be estimated by employing a number of different methods. Photoluminescence (PL) (described in Section 4.5) involves using a laser of energy high enough to excite all ground state electrons and a spectrometer to measure the light emitted as a result of electron-hole recombination; thus giving a value for E_g . UV-visible spectroscopy is used to

measure the absorption of energy (as opposed to emission in PL). The sample is subjected to a beam of light, the wavelength of which is varied across the UV-visible range, and a spectrometer measures the intensity of the beam at each wavelength after it has encountered the sample, thus providing information on the wavelengths of light that are absorbed by the sample. If a semiconducting material is analysed an absorption 'edge' or 'step' will be produced rather than a peak. The band gap can be estimated by taking the 1st derivative of the data and determining the position of the peak maximum.

In characterising the absorption/emission properties of a semiconductor there will usually be a discrepancy between the observed band gaps when comparing both techniques. This is known as Stokes or anti-Stokes shift. Stokes shift occurs when the observed emission energy is less than the absorbed energy and anti-Stokes shift is the reverse. The differences in energy result from dissipation of heat by thermal phonons (lattice vibrations) within the crystal lattice.

A number of semiconducting materials were investigated in this project. The band gaps of all materials were investigated using UV-vis spectroscopy and by PL using a Nd:YAG laser with an exciting emission wavelength of 266nm for a select few.

1.4. Quantum Confinement

By reducing the size of semiconducting particles, a number of improvements in the operation of semiconductor quantum dot laser devices is expected, some of which are given below with explanations:

- Lower threshold currents
 - o The minimum electrical current required to activate a semiconductor. Reducing this allows semiconducting action to occur with less energy input.
- Higher characteristic threshold current temperatures
 - o The dependence of the threshold current on temperature. Some materials only semiconduct at low temperatures. Increasing this may allow the use of some of these at room temperatures.
- Higher modulation bandwidths
 - o The maximum rate of change in the frequency of emission. Increasing this can allow the transmission of data at faster rates.
- Narrower linewidths
 - o The distribution of wavelengths emitted during the emission of light. Narrowing the linewidths can increase the efficiency of a semiconductor when a narrow output wavelength range is desired.

These can all contribute to more efficient operation of semiconductor devices and are possible by reducing the freedom of movement of the charge carriers (i.e. confinement) and the consequentially modifying the density of states of the carriers (an indication of the maximum number of carriers that can occupy an

energy range).^[50-55] Decreasing the dimensionality of free carrier motion results in the density of states (DOS) being modified, as shown in Figure 12.

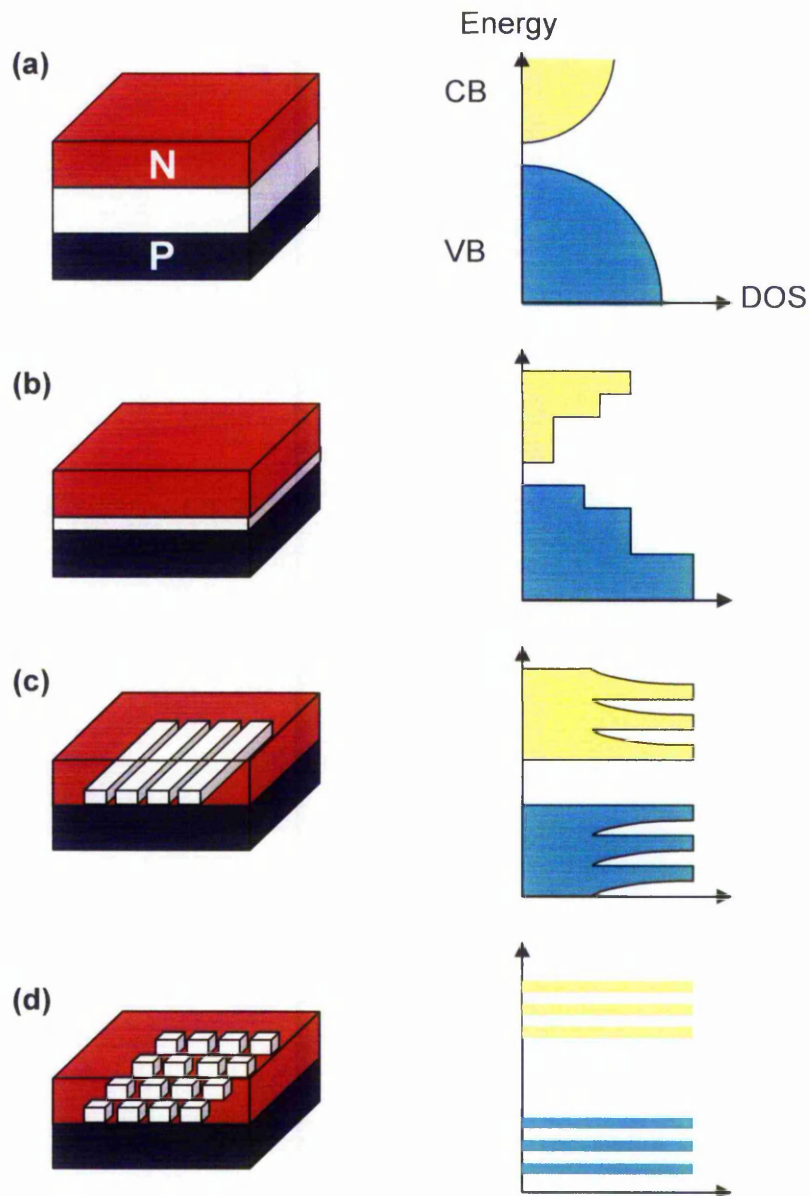


Figure 12: DOS diagrams for (a) double heterostructure (b) quantum well (c) quantum wire and (d) quantum box lasers.

When taking the active region of a double heterostructure (DH) laser as an example (Figure 12a), it can be seen that the DOS is smallest near the edges of the conduction and valence bands (CB and VB, respectively). By reducing the

thickness of the active region to the order of the De Broglie wavelength, i.e. producing a quantum well (QW) (Figure 12b), the charge carriers are confined in the z-direction, therefore producing the DOS distribution shown, with a step-like shape. This offers an improvement on the DH laser as the populations of holes and electrons are now larger near the edges of the bands, the energy of optical transitions can be controlled by the well thickness and the move towards discrete energy levels means sharper optical transitions. Upon further confinement, quantum wires (Figure 12c - QWi - 1-dimensional charge carrier freedom) and quantum boxes or dots (Figure 12d - QB/D – 0-dimensional charge carrier freedom) can be realised, each providing further improvement on the DH laser's DOS shape. As can be seen, upon increasing carrier confinement the DOS moves further towards truly discrete energy levels, providing sharper emission linewidths and thus more efficient emission at desired, discrete wavelengths and also reducing the threshold current density and its temperature dependence and giving greater control over optical transitions.

In 1984 L.E. Brus attempted to quantify the particle size dependence of the band gap of a semiconductor, which resulted in Equation 1.

Equation 1: The Brus Equation. ^[56]

$$\Delta E = \frac{h^2}{8\mu R^2} - \frac{1.8e^2}{4\pi\epsilon_0\epsilon_\infty R}$$

This relates the size of a particle, R , to the change in band gap from the bulk value, ΔE . This equation does, however, assume the particles are spherical. The other limitation of the equation is that it only applies to a finite size range, which has not

been defined and may be different for each material. This is, however, the best estimation of the effect of size on the electronic properties of semiconducting materials to date, and thus is used in this work.

2. Aims

2.1. Zeolite Encapsulation of Metal Nitride Clusters

There are currently no documented investigations into the formation of nitrides within zeolite frameworks that venture beyond structural characterisation and catalytic capability. ^[30, 31] However, the vast array of framework geometries provided by zeolites has led to the idea of quantum dots (QDs) and wires (QWs) (small clusters (QDs) or long thin wires (QWs) of atoms with dimensions in the nanometre range) with electronic properties being synthesised using the templating effect of zeolite pores. ^[32, 57] Therefore, the aim of this project was to produce relatively simple metal nitride and oxide materials with optoelectronic properties within the pores systems of various zeolites and to assess the effect of zeolite occlusion, and thus quantum confinement, on the optoelectronic properties with respect to bulk samples.

The main guest materials investigated during the course of the project were the nitrides and oxides of Ga and Zn. Other materials included a selection of lanthanide and transition metal nitrides and a series of $\text{In}_x\text{Ga}_{1-x}\text{N}$ materials. The nitrides and oxides of Ga and Zn formed the majority of the work in this project; allowing a focussed approach to the effect of several zeolites and synthetic approaches to be assessed using the relatively wide band-gap materials GaN and ZnO ($E_g = 3.44$ ^[58] and 3.37 eV, respectively ^[59]).

In theory, all zeolites possess potential with regard to the aims of the project. However, the suitability of a zeolite to the work involved was assessed on a

number of factors, such as commercial availability, stability under ion-exchange processes, thermal stability and resistance to certain harsh reaction conditions. Investigating a comprehensive range of geometries was necessary to provide a significant study into any effect a zeolite may have on the optoelectronic properties of encapsulated clusters. In order to explore the effect of zeolite characteristics on quantum confinement a range of pore configurations and sizes were explored. Therefore the three zeolites shown in Table 1 were investigated.

Table 1: Zeolites used in this work.

Zeolite	Pore System	Main Pore Sizes (nm)	Expected Guest Configuration
Faujasite	0-D Cages	0.74 x 0.74	Quantum Dots
ZSM-5	1-D Channels. Straight channels intersecting zigzag channels	0.56 x 0.53	Quantum Wires
Ferrierite	1-D Channels. Layers of intersecting, perpendicular channels	0.54 x 0.42	Quantum Wires

Although Faujasite may not seem a wise choice as it can be unstable under ion exchange conditions and high temperatures, a highly siliceous Faujasite was used in this work, reducing the amount of dealumination that could occur under the proposed preparation conditions.

The intention of the work of this project was to build on the work being carried out by other groups working on producing metallic and metal oxide clusters within zeolites by performing well documented bulk nitridation reactions^[60-76] within the pores of zeolites.

2.2. Structural Characterisation

A number of complimentary methods were employed in order to characterise the materials.

Powder X-ray Diffraction (XRD) was used to assess the integrity of the zeolite frameworks and to verify the absence of large (>200 nm), extra-zeolite species. This technique, however, could not be used to reliably confirm the presence and/or identity of the included phases. As XRD is a long range order technique, little or no structural data relating to the guest phases were available due to short range order upon encapsulation within the zeolite pores. Well defined XRD data relating to guest phases were indicative of external crystal growth.

X-ray Photoelectron Spectroscopy (XPS) was used to characterise the guest phases. As XPS is a surface technique, this was coupled with a depth profiling process in order to probe the internal structure of the zeolite frameworks. The resolution of the technique, however, is not great enough to be able to determine whether the guest phases were present within the pores or on surfaces.

Microscopic investigations included Scanning Electron Microscopy (SEM), which provided images of material topology at high magnifications and High Resolution Transmission Electron Microscopy (HRTEM); providing transmission images at a much higher magnification than SEM and confirming the inclusion of material within zeolite pores. These two techniques were coupled with Energy Dispersive X-ray spectroscopy (EDX), providing elemental analysis of the imaged areas.

2.3. Optoelectronic Investigation

The optical properties of the materials were characterised by two techniques: UV-Visible diffuse-reflectance spectroscopy and photoluminescence (PL). UV-Vis spectroscopy allowed the determination of absorption properties, in particular the band gaps, of guest phases. PL was used to characterise emission spectra; aiding in the determination of band gaps and other emission properties. The combination of these techniques also allowed the determination of Stokes shifts.

3. Experimental Techniques

3.1. Ion Exchange

Zeolites are composed of Si and Al tetrahedra connected by bridging O atoms. This results in a charge imbalance where Al atoms are present (AlO_2^- cf. SiO_2), which must be compensated for by the presence of charge balancing cations, such as NH_4^+ , H^+ , Na^+ , K^+ , Ca^{2+} , etc. Ion exchange reactions are well documented and widely used. ^[1] These reactions replace the charge balancing cations present within the as-synthesised zeolites with others, in particular those that may be of interest in the area of semiconductors (denoted M hereafter).

A known quantity of zeolite is dried under vacuum at $\sim 100^\circ\text{C}$, thus removing any degree of hydration and enabling the sample to be weighed accurately. The zeolite is then stirred in an aqueous solution of a salt of M at a concentration much greater than that required to fully exchange the zeolite cations. This solution is refluxed overnight. The zeolite is then filtered, washed thoroughly and dried. This process is repeated several times in order to achieve maximum loading of M .

Protonated zeolites, with H^+ ions, can also be produced. This is achieved by heating an ammonium form of the zeolite (NH_4^+) to above 400°C for several hours in air. ^[30]

3.2. Precursor Impregnation

In order to produce dense clusters of metal nitrides and oxides, the zeolite pores need to be impregnated with a precursor, in addition to any ion exchange processes that may have been carried out previously. This precursor is usually a salt of the metal with properties that lends itself to the route of impregnation, as described in the next two sections.

3.2.1. Aqueous Solution Impregnation

In this method of impregnating the zeolite pores with a metal salt the zeolite is stirred for several hours in an aqueous solution of a metal salt whilst gently heating. Over this period the solvent evaporates, leaving the solid zeolite impregnated with the salt. If there is any excess salt that is unable to be taken up by the zeolite this remains as a separate solid phase to the zeolite/salt composite. This may seem counter-intuitive; however, by not washing away any excess the expected guest phase is seen in the powder diffraction patterns for those samples with high loadings, thus confirming the nitridation/oxidation products. Also, a clear difference should be seen between not only the structural characterisation results of the high- and low-loaded samples, but also in the optoelectronic properties.

In a typical solution impregnation process a small volume (~100 mL) of aqueous solution with a known concentration of a salt of M (i.e. $\text{Ga}(\text{NO}_3)_3$, EuCl_3 , etc.) is prepared. A known amount of a dried zeolite is stirred for several hours in the solution with gentle heating until all of the solvent is evaporated. The salt concentration to zeolite mass ratio is such that a known loading of the zeolite with the metal is achieved, typically 5-50 wt%. The purpose of this wide range of loadings is to give scope for the identification of the point of maximum pore filling

by the various analysis techniques used and to confirm the success of nitride/oxide synthesis at high loadings at which large nitride/oxide crystals are expected, allowing them to be analysed by powder XRD. The product is then dried under vacuum for several hours.

3.2.2. Molten Salt Impregnation

This is a very simple process in which a liquid metal salt is allowed to seep into the pores of a zeolite by using a combination of capillary forces and inter-zeolite pore charge separation in which the exposed, charged surfaces of the cations located on opposing sides of the inner walls of the pores draw polar species into the pore structure. This provides a nitride or oxide precursor; the metal salt, inside the zeolite with no need for the use of solvents.

In a typical molten salt impregnation process a known amount of dried zeolite is manually ground together with a known, excess amount of a salt of M with a relatively low melting point (e.g. $\text{Zn}(\text{NO}_3)_2 \cdot 6\text{H}_2\text{O}$, melting point = 36°C). The ground mixture is then heated to above the melting point of the salt (above 100°C in order to drive off any water of hydration of the salt, allowing a truly non-aqueous impregnation to occur) for several hours under nitrogen to prevent oxidation of the salt before it has had the opportunity to impregnate the zeolite. The sample is then washed quickly with a small amount of distilled water to remove the excess salt.

3.3. Nitridation and Oxidation

Nitridation of a sample is performed in a tubular furnace under a constant flow of $\text{NH}_{3(g)}$ with the temperature increasing at $1^{\circ}\text{C min}^{-1}$ from room temperature to 800°C . The temperature is held for 5 hours and then returned to room temperature at $1^{\circ}\text{C min}^{-1}$. The tube is then purged with $\text{N}_{2(g)}$ for several hours to remove any residual $\text{NH}_{3(g)}$.

Oxidations are performed at the same temperatures and temperature ramp rates as the nitridation reactions, but in this process the reaction is carried out in air instead of ammonia and there is no need for purging with $\text{N}_{2(g)}$.

4. Analytical Techniques

4.1. X-ray Diffraction

4.1.1. Introduction

X-ray diffraction (XRD) is a fundamental technique in chemistry and is also extremely useful in other branches of science. XRD is used to determine the arrangement of atoms in crystalline material by measuring the scattering angles and intensities of X-rays scattered by a crystal, relative to the incident beam.

It was only relatively recently; in the 1890s, that the modern idea of crystals was suggested. The theory suggested that atoms, assumed to be spherical entities, would pack together in close, regular arrays to form crystals. This proposal coincided by chance with the discovery of X-rays in 1895 by the German physicist Wilhelm Conrad Röntgen. The link between X-rays and crystals, however, was not to be found until 1912 when another German physicist, Max Theodor Felix von Laue realised that the wavelengths of X-rays, which lie in the region of 0.01–10nm, lend themselves to be diffracted by crystals. The founders of modern X-ray diffraction, however, are widely accepted to be William Henry Bragg and his son, William Lawrence Bragg. The Braggs were the first to use monochromatic X-rays in order to determine that the crystal structures of KCl and NaCl were both related to face-centred cubic packed spheres. ^[77, 78]

4.1.2. X-ray Generation

X-rays are a form of electromagnetic radiation with wavelength, λ , in the range of 0.01 – 10 nm. X-rays are produced by two different processes that occur when high energy electrons (1-100 keV) are incident on a metal target. The first process produces so called “white radiation” or *Bremstrahlung*: X-rays with a wide range of wavelengths. This form of radiation is produced when the impacting electrons lose energy and rapidly slow down due to collisions with the metal target, thus ejecting electrons from a variety of energy levels. The second process, which happens simultaneously with the first, creates X-rays of discrete wavelengths that are characteristic of the metal target. These discrete peaks in the X-ray spectrum occur when electrons are ejected from core quantum levels and an ensuing cascading effect takes place when electrons in higher energy levels drop down to fill the deficit, a process that takes 10^{-14} to 10^{-6} seconds. The emitted radiation is named after the core electron level that is initially vacated and consequently filled, such that the energy levels $n = 1, 2, 3, \dots$ correspond to the K, L, M, ... shells. This is followed by a term to distinguish between the most favourable electron transitions (alpha) from those less favourable (beta, gamma, ...). The final term is one that defines the transitions within this subset, so that as there are two distinct electron states in the L shell available to fill the vacant K shell, the two most favourable transitions are $K_{\alpha 1}$ and $K_{\alpha 2}$ and a less favourable transition, that which an electron from the higher energy M shell replaces the lost K shell electron, is denoted $K_{\beta 1}$, which is more energetic, yet less intense due to the reduced probability of the transition. The X-ray spectrum resulting from these two processes using a copper target is shown in Figure 13. ^[77]

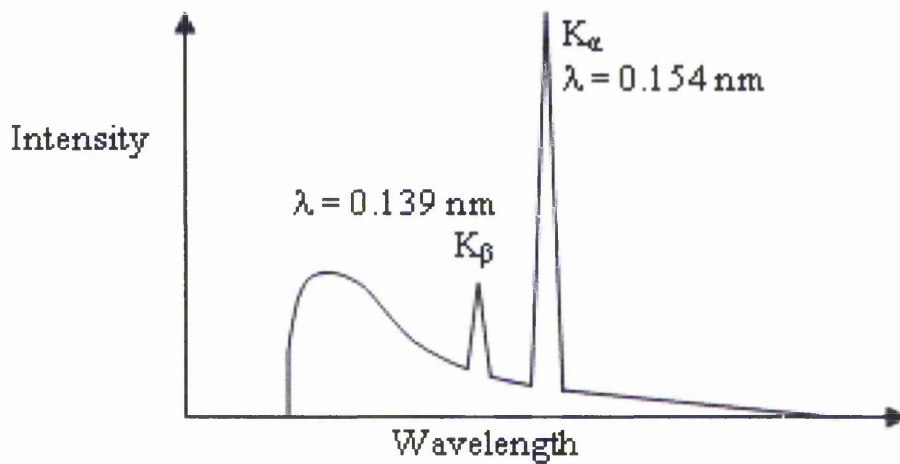


Figure 13: X-ray spectrum of copper.

The most widely used source of X-rays is an X-ray tube, which consists of a glass and metal casing, containing a wire filament, through which a high electrical current is passed to produce polychromatic electrons. An electrical potential of 40 – 60 kV then accelerates the electrons over a short space to a water-cooled metal target. Here, the majority of the energy is wasted through heat, but a small fraction creates X-rays by the processes explained previously. A schematic of a typical laboratory X-ray tube is shown in Figure 14.

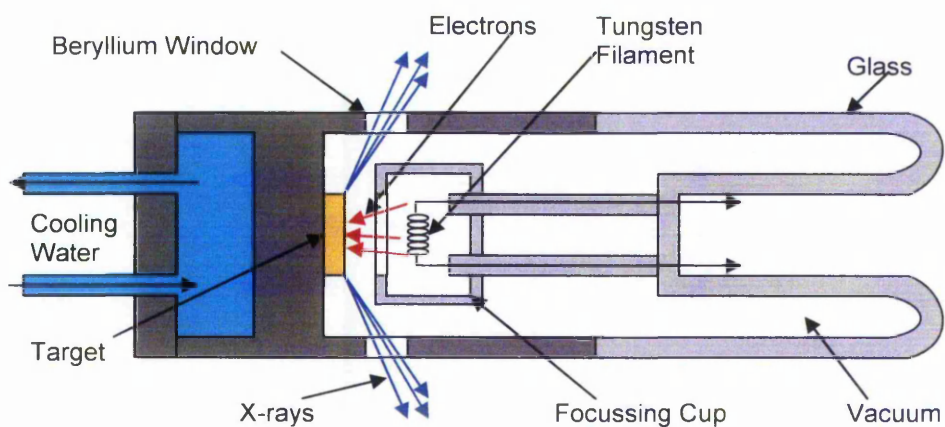


Figure 14: A schematic diagram of a laboratory X-ray tube.

In order to use X-rays of a defined wavelength from the complete spectrum, such as that shown in Figure 13, a monochromating crystal is used as a diffraction grating to “filter” out unwanted wavelengths. A single crystal of known crystal structure is oriented such that the Bragg equation (see Equation 2) is satisfied by the required wavelength, thus allowing X-rays of this wavelength to be diffracted and all others to pass through the crystal. ^[79]

Equation 2: The Bragg Equation.

$$n\lambda = 2d \sin \theta$$

Here n is an integer giving the order of diffraction, λ is the wavelength of the incident X-rays, d is the interlayer spacing of the diffracting planes of atoms and 2θ is the angle between the incident beam and the diffracted beam.

4.1.3. Crystal Symmetry

A crystal is a solid material consisting of atoms and/or molecules that are regularly and repeatedly arranged symmetrically in three dimensions. In the analysis of a material by X-ray diffraction a crucial step is to determine the nature of the symmetry adopted by the regularly arranged atoms. This is achieved by assigning a 'unit cell', which is the smallest repeating unit that contains each lattice point. The unit cell can be manipulated by a symmetry operation to build a picture of the complete crystal structure. The possible crystal systems available for crystals to adopt are limited to seven unique types: namely *triclinic*, *monoclinic*, *orthorhombic*, *hexagonal*, *rhombohedral*, *cubic* and *tetragonal* (Figure 15).

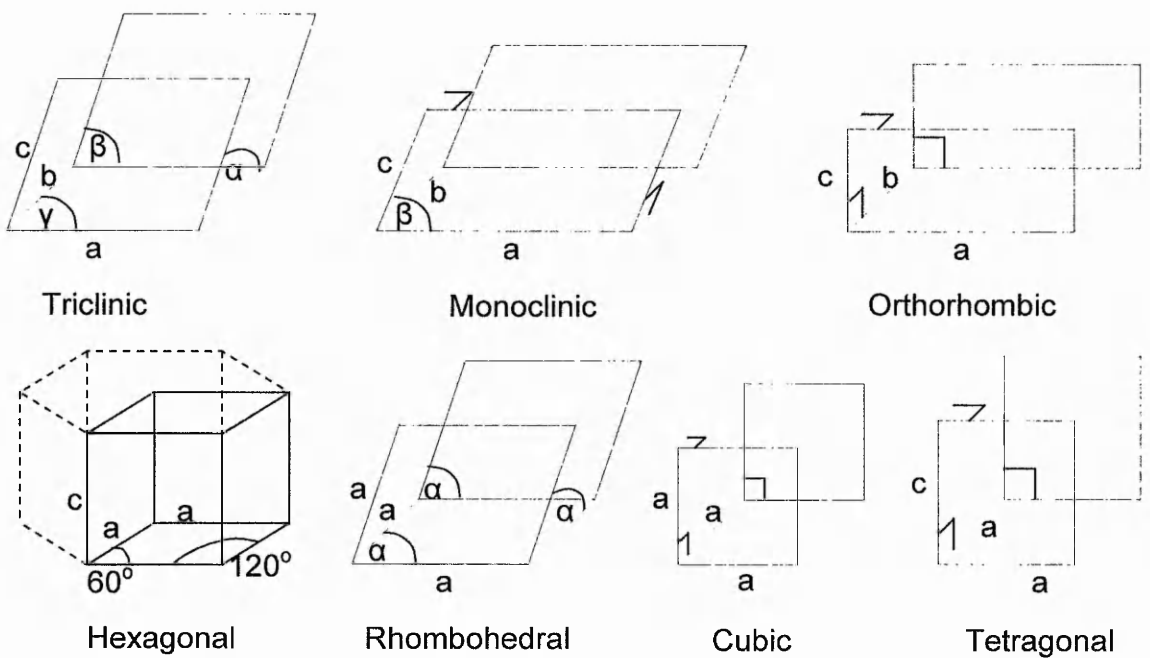


Figure 15: The Seven Crystal Systems.

The unit cell can be repeated on a 3D lattice to create the complete structure of the crystal, giving one lattice point per unit cell; a so-called primitive lattice, denoted *P*. Sometimes, however, it is more convenient to use more than 1 lattice point per unit cell, which leads to centred lattices such as face-centred (*F*), side-centred (*C*) and body-centred (*I*). This gives a total of 14 Bravais lattices from all of the possible centring configurations, discounting all equivalent combinations (i.e. with isomorphic symmetry groups).

In order to complete the crystal system from a lattice point a symmetry operation (or collection of operations) about “symmetry elements” is required. A symmetry element is a physical point, line or plane in 3D space about which a symmetry operation may be applied. A symmetry operation can be a plane reflection, line rotation or point inversion which leaves the object identical in appearance as before the operation was applied, with a different spatial position and/or orientation. The crystallographic symmetry operations can be classified as either proper rotations (rotations about an axis by a fraction of 360°) or an improper rotation (a combination of a rotation with a reflection in a plane perpendicular to that of the axis passing through the centre of the molecule). A combination of a rotation or a reflection with a translation operation results in screw axes and glide planes, respectively.

The sum of all the symmetry operations on a material is called the point group, each of which carries its own characteristic properties and conventional symbol. The symmetry operations combine to give 32 crystallographically different point groups. The combination of a point group with translational symmetry and a Bravais lattice is denoted a space group, of which there are 230.

In crystallographic notation, the Cartesian axes x , y and z are replaced by a , b and c and the respective angles denoted α , β and γ . The notation system used for describing planes of atoms within a unit cell is known as the Miller Index, in which the reciprocals of the fractional intercepts with the axes of the unit cell are used and denoted h, k and l . An example is shown in Figure 16; where the highlighted plane is denoted (100) as the fractional intercept on the a axis is 1, the reciprocal of which is 1 and those on the b and c axes are ∞ , the reciprocal of which is 0.

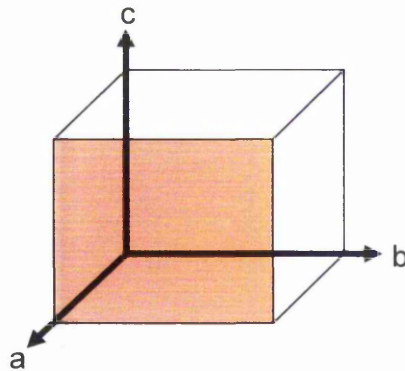


Figure 16: An example of a (100) plane.

4.1.4. Diffraction of X-rays by Crystals

The regularity of atoms within a crystal allows it to act as a diffraction grating for X-rays. When X-rays are incident on a crystal they are scattered. The pattern observed in X-ray Diffraction is the sum of the constructive and destructive interference of the X-rays scattered by the regular array of atoms. As can be expected, only constructive interference is observed as diffraction intensity, which relies on the difference in path length ($2d\sin\theta$, where θ is the incident angle) between scatterings from successive planes of atoms being an integer number of wavelengths ($n\lambda$, where n is the diffraction order 1, 2, 3, etc.). Constructive interference is only observed when Bragg's Law (Equation 2) is satisfied. Diffraction is described pictorially in Figure 17.

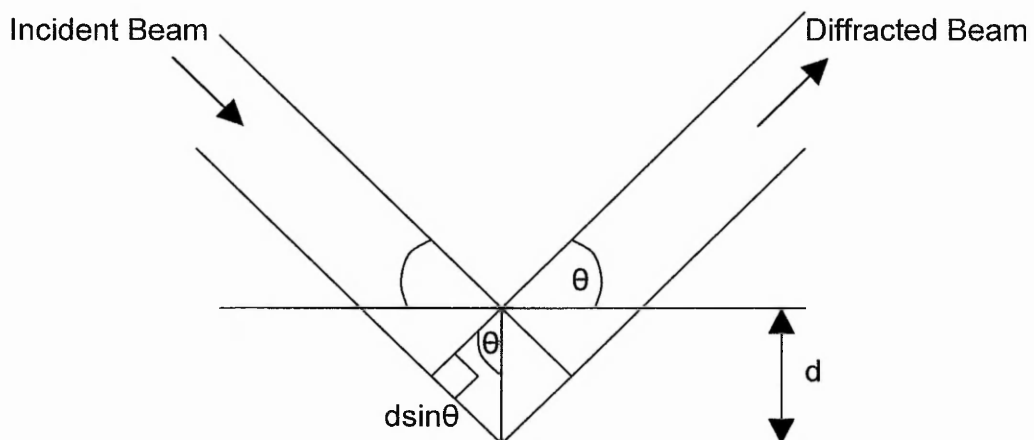


Figure 17: Bragg Diffraction.

The intensity of a peak in an X-ray diffraction pattern is dependent on the scattering factors of the diffracting atoms such that if we take a primitive crystal with one lattice point and therefore one atom per unit cell, the scattered amplitude from one cell, F_{hkl} , is equal to the atomic scattering factor, f_o , of that atom. As more

cells are added to the crystal (or as the diffracted X-rays encounter more cells) all scattering factors and the distances between each lattice plane need to be taken into account, thus the Structure Factor Equation (Equation 3) can be used to calculate the intensity of a diffracted beam from a set of planes with the positions of the atoms in the unit cell and their atomic scattering factors, but more importantly can also be applied in reverse to calculate the atom positions in the unit cell.

Equation 3: The Structure Factor Equation. ^[80]

$$F_{hkl} = \sum_{n=0}^{n=N} f_n \exp 2\pi i(hu_n + kv_n + lw_n)$$

- Where:
- F_{hkl} = The scattered intensity
 - f_n = The atomic scattering factor of atom, n
 - $2\pi(hu_n+kv_n+lw_n)$ = The phase angle, φ_n , of the n th atom with unit cell fractional coordinates $(u_n v_n w_n)$

The inclusion of the phase angle in the structure factor equation takes account of constructive and destructive interference; for example if $(hu_n+kv_n+lw_n) = 0$ (all atoms lying within the (hkl) planes) complete constructive interference occurs, however, when $(hu_n+kv_n+lw_n) = 0.5$ (with a plane of atoms lying between the (hkl) planes), destructive interference occurs and no intensity is observed.

4.1.5. *Single Crystal X-ray Diffraction*

Single crystal X-ray diffraction has become a fundamental technique in synthetic chemistry and other areas of molecular science. The technique has benefited greatly from the ever increasing computing power and the introduction of charge coupled device (CCD) detectors, which use X-ray sensitive phosphors to convert X-rays into visible light that can then be amplified and recorded. In recording reflections from a single crystal, it is possible to rotate the crystal and detector in order to obtain a complete, 3D sphere of diffraction patterns, thus allowing the elucidation of a complete crystal structure. By using modern techniques it is now possible to obtain a full crystal structure in several hours.

4.1.6. Powder X-ray Diffraction

Microcrystalline powders can also be analysed by X-ray diffraction, but require slightly different methods. In a crystalline powder, consisting of several millions of microcrystals arranged at random where there is no preferential orientation, the atomic planes in each crystal are completely randomly oriented in comparison to others in the sample. Therefore, Bragg diffraction will occur for each individual crystal orientation simultaneously, thus producing concentric rings of superimposed diffraction spots as opposed to discrete spots, as in single crystal diffraction, as described in Figure 18.

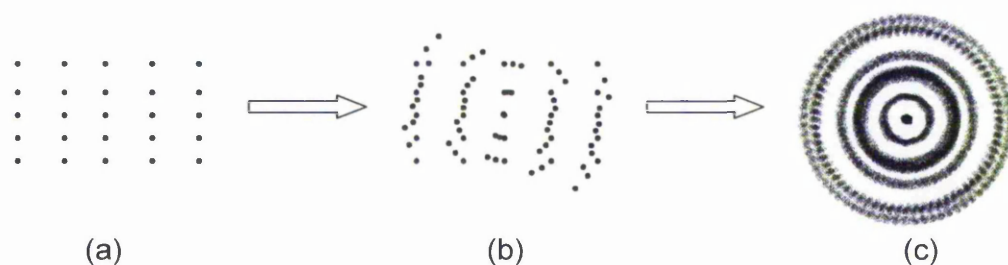


Figure 18: Production of diffraction rings. (a) Single orientation diffraction pattern, (b) Superimposition of 3 orientations of the same diffraction pattern and (c) 'Complete' set of orientations of the same diffraction pattern.

The data obtained from powder diffraction is therefore a 2D plot of diffraction angle, θ , against intensity of a radial 'slice' of the circular diffraction pattern. Due to the superimposition of a 3D collection of diffraction patterns into a 2D diffraction pattern, powder diffraction data does not lend itself easily to complete structure solution as much as single crystal diffraction. Structures can, however, be solved via a least squares refinement technique named Rietveld Refinement, which is discussed in Chapter 4.1.7.

4.1.7. Rietveld Refinement

Rietveld refinement uses a least squares approach to compare a theoretical diffraction profile to a measured profile of a sample. The basic principle of the technique can be described with Equation 4:

Equation 4: The equation used in Rietveld refinement to determine the fit of the theoretical profile with that of the measured profile.

$$M = \sum_i W_i \left\{ y_i^{obs} - \frac{1}{c} y_i^{calc} \right\}^2$$

Here M is a function that describes the fit between the observed and calculated profiles; a value the Rietveld method aims to reduce, W_i is a statistical weighting factor and c is an overall scale factor, such that $y^{calc} = cy^{obs}$. [81]

The Rietveld method uses many factors to determine the calculated profile, including instrument and beam parameters, strain, crystalline size and shape and preferred orientation to name a few. Rietveld refinement of materials with large unit cells, such as zeolites, requires a high degree of computing power and a considerable amount of time.

There are many computer programs available to perform Rietveld refinement. In the course of this work Topas Academic V4.1 was used. [82]

XRD experiments conducted during this project were performed on a Phillips X'Pert Pro diffractometer in Bragg-Brentano geometry with variable divergence slits using a back-filled stainless steel sample holder on a spinning sample stage.

Measurements were taken at room temperature using Ge (111) monochromated $\text{CuK}_{\alpha 1}$ radiation with a wavelength of 1.54056 Å with voltage and amperage set to 45kV and 40mA respectively. Data were typically collected over the range 3-90° in 2θ with a step size of 0.02°. In all zeolite-guest permutations a selection of samples were analysed in duplicate to verify the unit cell parameters within experimental error.

The following parameters were refined and experimental standard deviations calculated:

- Lattice Parameters
- Scale Factors
- Background Polynomials
- Si and Al Occupancies
- Equivalent Isotropic Temperature Factors for all atomic sites
- Phase Densities
- Peak Asymmetry due to Axial Divergence
- Mass Absorption Coefficients for Mixtures
- Mixture Densities
- Linear Absorption Coefficients for Mixtures
- Thompson-Cox-Hastings pseudo-Voigt (TCHZ) Peak Type Parameters:

$$\eta = 1.36603 q - 0.47719 q^2 + 0.1116 q^3$$

where:

$$q = \Gamma_L / \Gamma$$

$$\Gamma = (\Gamma_G^5 + A\Gamma_G^4\Gamma_L + B\Gamma_G^3\Gamma_L^2 + C\Gamma_G^2\Gamma_L^3 + D\Gamma_G\Gamma_L^4 + \Gamma_L^5)^{0.2} = \text{fwhm}$$

$$A = 2.69269, B = 2.42843, C = 4.47163, D = 0.07842$$

$$\Gamma_G = (U \tan^2\theta + V \tan \theta + W + Z / \cos^2\theta)^{0.5}$$

$$\Gamma_L = X \tan \theta + Y / \cos \theta$$

with U, V, W, X, Y, Z as refineable parameters.

Figure 19 shows a typical Rietveld analysis plot, in this case of ZSM-5 treated by the molten salt method to produce GaN. The blue line shows the experimental data, the red line is the calculated diffraction profile and the grey line below is the difference between the two. The tick marks at the bottom of the graph show the calculated positions of peaks from the two phases; the blue tick marks represent those from ZSM-5 and the black tick marks show those from GaN.

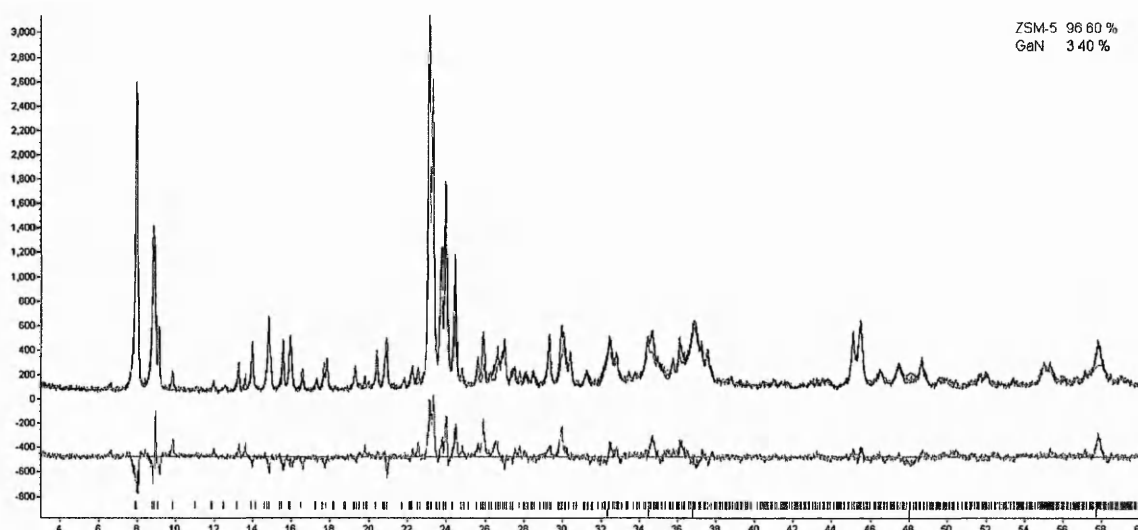


Figure 19: Rietveld analysis of ZSM-5 with GaN treated by the molten salt method.

This profile shows that although GaN peaks are clearly visible, they are relatively broad in comparison to those from ZSM-5. This suggests GaN is present, but as very small clusters. Size analysis using Topas Academic gives a value of 332nm

using a Lorentzian peak model. This method, however assumes the particles are spherical and is calculated using the FWHM, the accuracy of which is debatable given that these measurements were taken at room temperature and the convolution of GaN diffraction peaks by numerous peaks from ZSM-5. Therefore, these calculated values are not presented in this work as conclusive results.

Figure 20 shows the profile for ZSM-5 treated with the solution impregnation method with a Ga loading of 50wt%. It is clear in this profile that there is a significantly higher GaN component (10.2% of 3.4% for the molten salt treated sample), producing larger diffraction peaks, but which are still very broad. Size analysis using Topas Academic gives a value of 1186nm for these crystals, which is approximately four times that measured in the sample above.

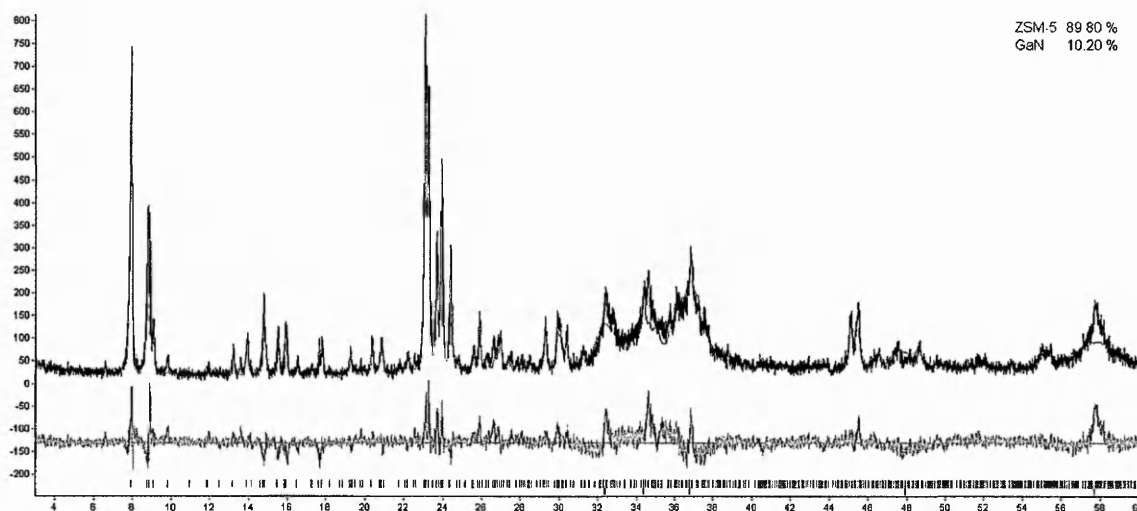


Figure 20: Rietveld analysis of ZSM-5 with GaN treated by the solution impregnation method with 50wt% loading of Ga.

As these two profiles show, although the inherent complexity of zeolite structures make complete structure solution by Rietveld refinement an intricate and arduous

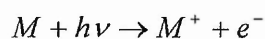
task, determining many crystal parameters is fairly straightforward as the diffraction peaks are sharp and numerous, therefore relatively accurate analysis can be performed with little interference from the guest phase. Analysis of the guest phase, however, is more problematic. As they are simple structures in comparison to zeolites, they have significantly fewer diffraction peaks which can be masked by the peaks from the zeolite phase. Also, given the task of this project requires the synthesis of nano-sized clusters of these phases, any detectable diffraction peaks from successfully occluded phases will be broad and poorly resolved.

4.2. X-ray Photoelectron Spectroscopy

4.2.1. Introduction

XPS (also known as ESCA – Electron Spectroscopy for Chemical Analysis) is a spectroscopic technique that is used to probe the chemical environment of surface atoms of a material. In a typical measurement, the sample is placed under UHV (Ultra High Vacuum) and irradiated with X-rays from an aluminium (monochromatic K_{α} X-rays with a wavelength of 0.83386 nm and a photon energy of 1486.7 eV) or magnesium (polychromatic X-rays with a wavelength of 0.989 nm and a photon energy of 1253 eV) source, causing electrons to be ejected from the sample due to the photoelectric effect, in which electrons are emitted from a material on the absorption of photons with a short enough wavelength, i.e. X-rays, according to Equation 5.

Equation 5: The Photoelectric Effect.



There are three mechanisms of electron ejection by photon impact ^[83]:

1. Direct Ionisation

In direct ionisation a photon impacts and ejects an electron from a valence orbital, as in Figure 21.

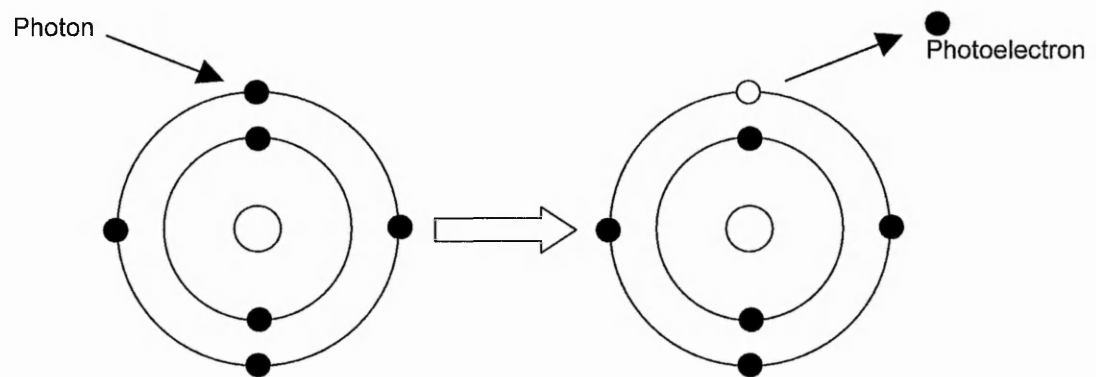


Figure 21: Direct Ionisation.

2. Auger Electrons

An Auger electron is ejected when an electron from an inner orbital is ionised, which is followed by an electron from a filled, higher level dropping down to fill the hole, which provides sufficient energy to eject a second electron, producing a divalent ion, as in Figure 22.

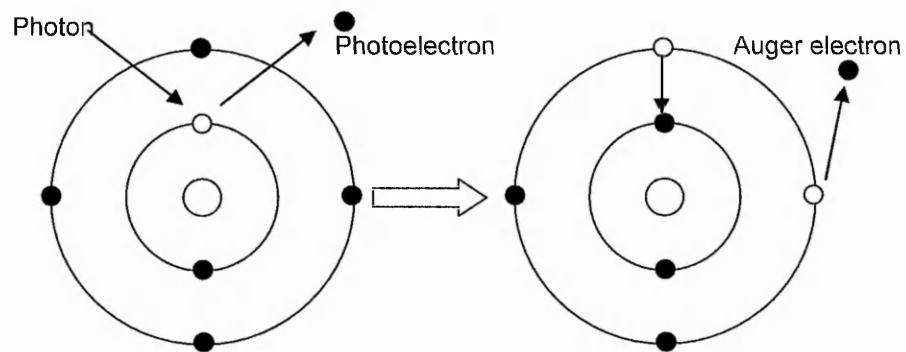


Figure 22: Auger Electron Ejection.

3. Autoionisation

In this mechanism of ionisation, a core electron is promoted to an higher energy level, producing an excited state. If the energy of the excitation is sufficient to then ionise the promoted electron a rearrangement occurs and the electron is expelled, creating an ion, as in Figure 23.

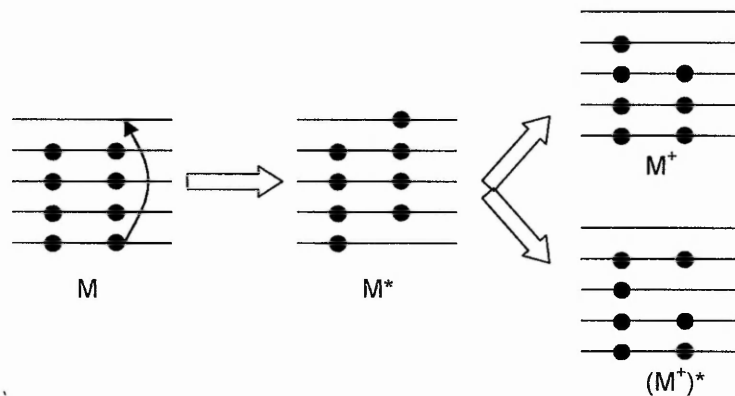


Figure 23: Autoionisation.

Upon ionisation, the kinetic energy and amount of the ejected photoelectrons is recorded. The kinetic energy of the photoelectron is characteristic of the element, orbital and charge of the atom from which it was ejected and the number of electrons detected is an indication of the population of the specific atomic species, allowing surface chemical composition to be determined.

4.2.2. Data Analysis

The data obtained from XPS measurements is plotted as Binding or Kinetic Energy against Counts per Second. The binding/kinetic energy of the ejected electron is only dependent on the wavelength of the impacting photon, not the intensity, and is characteristic of the element, its charge, bonding environment, geometry, aromaticity, etc. and the orbital from which the electron was ejected. The number of electrons ejected is directly related to the population of a certain element. The technique is, however, limited to atoms of molecular weight greater than 3 (i.e. not H, He or Li).

In using a known energy of X-ray, the kinetic energy of the emitted electrons can be determined by applying the corrected Einstein's Photoelectric Law, Equation 6.

Equation 6: Einstein's Photoelectric Law.

$$E_n = h\nu - I_n - E_{vib} - E_{rot}$$

Here E_n is the kinetic energy of the electron, $h\nu$ is the energy of the X-ray photon in use, I_n is the ionisation potential of the electron E_{vib} is the energy absorbed by the molecule/atom in order to excite vibrations and E_{rot} is the energy absorbed to induce rotations in the molecule/atom. ^[83]

In this work, the XPS facility at Cardiff University was used to provide information on the elements present in various samples and to probe the chemical environment of specific elements, thus confirming the identity of the metal oxides and nitrides. As XPS is a surface analysis technique (typically measuring the

uppermost 1-10 nm of a sample), a depth profiling system, using an argon ion gun, was used to probe the internal structure of the materials in order to elucidate any differences between surface and bulk composition, in particular, whether the metal oxides and nitrides were present on the surface of the materials or within the pores.

4.3. Electron Microscopy

Electron microscopy is a method of imaging specimens at up to 1,000,000 times magnification. An electron microscope uses a beam of electrons, as opposed to visible light in a conventional microscope, to illuminate the specimen. As the wavelengths of electrons are approximately 100,000 times shorter than those for visible light, a greater magnification is achievable.

Instead of using optical, glass lenses in order to focus the beam, an electron microscope uses electrostatic and electromagnetic "lenses".

4.3.1. *Transmission Electron Microscopy*

In Transmission Electron Microscopy (TEM) the electron beam is partly transmitted through the material and onto a screen coated with a phosphor, such as zinc sulphide, creating an image of the transmitted electron beam in contrast to the 'shadow' created by the material scattering parts of the beam. This resultant image can be photographed or recorded by a CCD.

Traditionally, TEM was limited in its applications due to the resolution being hampered by spherical aberration. Fortunately, modern aberration correctors have come a long way to overcoming this problem and increasing resolution. Now, HRTEM (High Resolution Transmission Electron Microscopy) possesses far increased resolution, allowing the positions of individual atoms within a material to be found with resolutions up to 0.05 nm with >50 million times magnification.

4.3.2. Scanning Electron Microscopy

Scanning Electron Microscopy (SEM) is a surface imaging technique with much less resolution than TEM. Unlike TEM, in which a wide electron beam is transmitted through the sample, in SEM a focused, narrow electron beam is rastered across the sample and it is the processes that occur on the surface that are detected. When the electrons impact the surface, they lose energy in the forms of heat, secondary, low energy electron emission, luminescence and X-ray emission and it is the sum of all of these processes that is recorded in SEM, mapping the variation in intensity with respect to the position of the beam, producing an image of the 3D topography of a material.

4.3.3. *Energy Dispersive X-ray Spectroscopy*

Energy Dispersive X-ray Spectroscopy (EDX) is an elemental analysis technique that is usually coupled with TEM or SEM in order to determine the location of specific elements within a sample. The principles of the technique are similar to those of XPS (see Chapter 4.2), in which an impacting electron of high energy causes the ejection of a core electron, which leaves a hole that is filled by an electron in a higher energy level. The difference in energy between the higher energy level and the newly occupied level may be released as X-rays, the energy of which is characteristic of the element from which it was ejected.

4.4. UV-Visible Spectroscopy

4.4.1. Introduction

UV-Vis spectroscopy uses light in the visible and ultraviolet regions of the spectrum to induce electronic transitions in molecules. The incident wavelength is varied from the near-infrared to the UV range and the transmitted light is recorded, with any loss of light representing an absorption inducing an electronic transition. In the visible region, any absorbance of energy directly influences the colour the human eye perceives the material to be.

In analysing the absorption properties of solid powders, it is not practical to measure the transmitted light. Therefore, a method called "Diffuse Reflectance Spectroscopy" is used. As light is incident on a granular surface, reflection of the light will occur at many different angles (diffuse reflection). Attempting to analyse a single angle of reflection is impractical as the intensity of the reflection will be insignificant in comparison to the incident beam and attempting to align a detector with a single, significant reflection with each sample analysed would not be trivial. Therefore to analyse the absorption spectrum of a powdered solid, the powder must first be pressed, either into a self-supporting pellet or between two materials. In pressing between two materials, one of the materials must transmit all wavelengths of the incident beam (i.e. quartz) and the other must absorb all wavelengths of the beam. Therefore the only measured intensity is that reflected from the sample. Then, the diffuse-reflected light at all angles must be focussed. This is achieved with the use of an "integrating sphere". This is a sphere with an inner coating of a material that completely reflects all possible wavelengths of the reflected beam, such as BaSO₄ and 3 apertures; one for the incident beam to

enter the sphere, one for the incident beam to come into contact with the sample and one for the diffuse-reflected light to enter the detector, such as that shown in Figure 24.

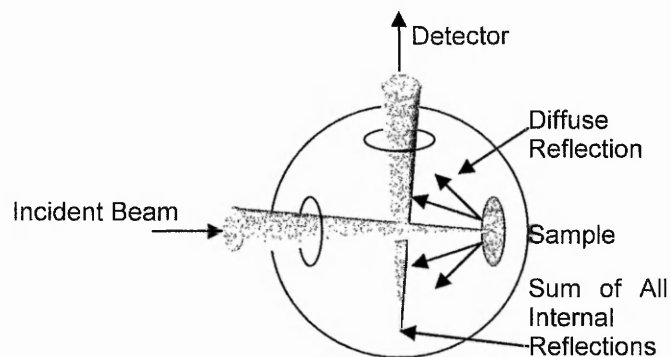


Figure 24: An integrating sphere for diffuse-reflectance spectroscopy.

The UV-Visible spectra presented in this work were measured using diffuse-reflectance spectroscopy with an integrating sphere.

4.4.2. Band Structure Determination

In the case of semiconductors, the wavelength of absorption in the UV-Visible region can be used to determine the band gap of the material if the light absorbed is of sufficient energy to induce a promotion of an electron from the valence band to the conduction band.

In order to obtain the band-gap of a semiconductor with diffuse-reflection spectroscopy data, the following steps are performed; the diffuse-reflectance spectrum of ZnO is used as an example, as shown in Figure 25:

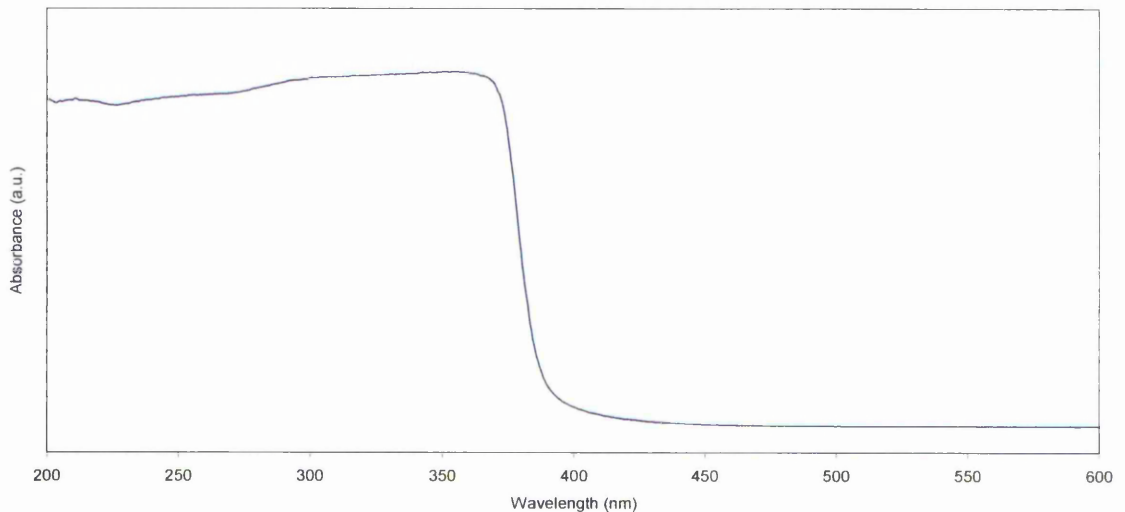


Figure 25: UV-Visible Diffuse-Reflectance Spectrum of ZnO.

- The units of the x-axis are converted from wavelength (λ in nm) to energy (eV):

$$\circ \quad h\nu = \frac{1240}{\lambda}$$

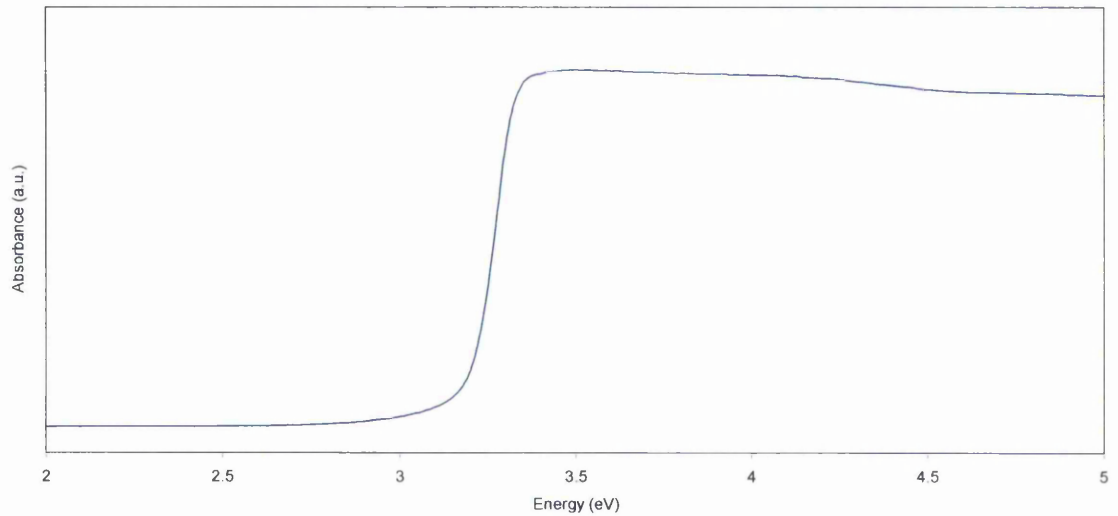


Figure 26: ZnO spectrum converted from wavelength to energy.

- The first derivative of the y-data is then taken. The x-position of the maximum in the resultant curve provides the band-gap energy in eV.

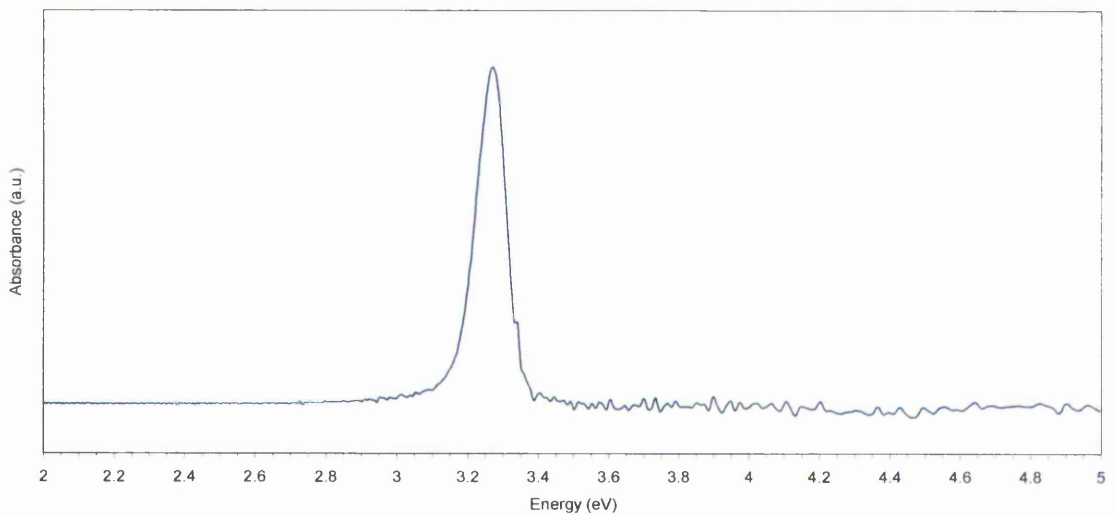


Figure 27: ZnO spectrum first derivative curve.

- In some cases the second derivative of the data can be taken to determine the band gap more accurately by using the intercept at the x-axis. However, this method requires a sharp edge in the original data, which is not always the case in mixed systems.

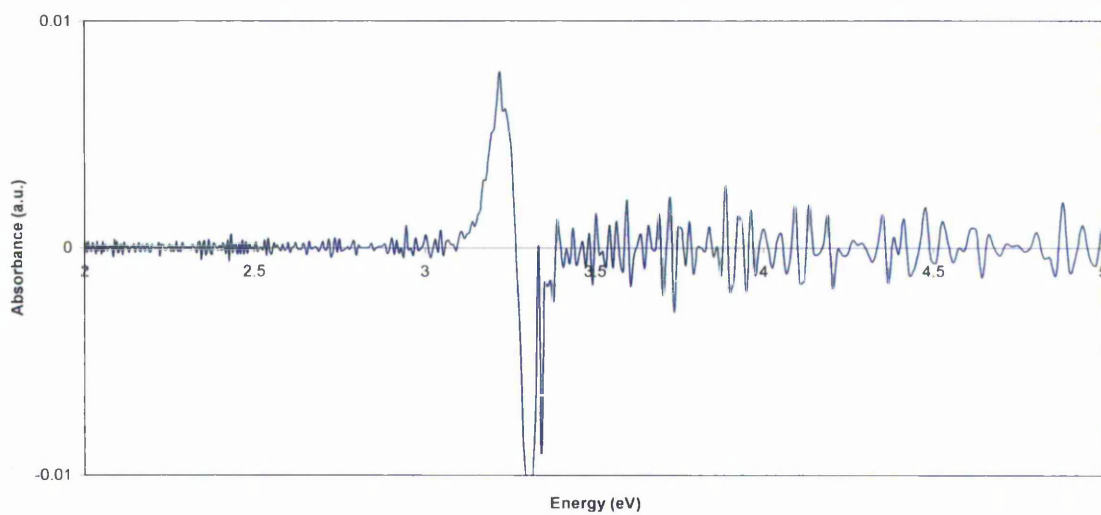


Figure 28: ZnO spectrum second derivative curve.

In this work, band-gap measurements provide the basis of comparison between bulk and zeolite-encapsulated materials. Estimation of the band gaps of zeolites are beyond the analytical capabilities of the instruments used in this work.

4.5. Photoluminescence

Photoluminescence (PL) is used to investigate the optical properties of a material. Typically a laser with a specific wavelength is used to excite a sample, which induces an electronic transition to a higher energy level. As the electron relaxes back to its ground state, photons are emitted by luminescent or fluorescent pathways. The resultant spectra can be used to ascertain the presence of discrete energy levels or band structures in quantum dots and wells. The technique can also provide information on impurity levels and the quality of materials.

The wavelength of an emission is characteristic of a specific energy level transition, which is governed by the laws of quantum mechanics. Thus, the PL spectrum of a material is a measure of the available electron transitions, and therefore the electronic configuration or the molecular orbitals of a sample.

The most basic of photoluminescent processes is the absorption of a photon at a specific wavelength followed by the emission of an equivalent photon. This process requires no significant internal energy transfer, resulting in the emission of a photon with identical energy to the incident photon. More complicated luminescence occurs when there is internal energy transfer between energy levels within the material prior to re-emission. In this case the emitted photon will be lower in energy to that of the incident photon and is said to be "red-shifted".

In terms of semiconductor analysis, PL is used to determine the band gap energy of a material and whether there are impurities, resulting in dopant energy levels within the band gap. ^[84]

The PL spectra presented were obtained using a Nd:YAG laser at an excitation wavelength of 266 nm.

5. Gallium Nitride

Gallium nitride (GaN) is a wide band-gap semiconductor with a band-gap of 3.44 eV. ^[58] GaN can occupy two different crystal habits: namely the wurtzite and zinc blende structures. The structure of interest in this project is the wurtzite structure, shown in Figure 29. Wurtzite GaN is relatively easily synthesised by high temperature ammonolysis of Gallium salts at ambient pressure and is the most widely used form of GaN in electronic materials due to its stability at high temperatures and voltages.

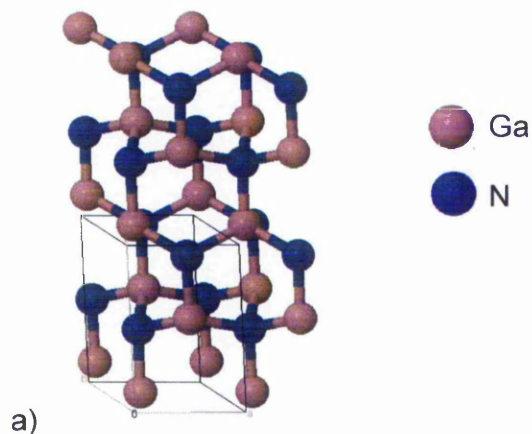


Figure 29: The unit cell of wurtzite GaN. ^[85]

The wurtzite form of GaN generally has the following crystallographic parameters:

Space Group: $P6_3mc$

$a = 3.095 \text{ \AA}$ $b = 3.095 \text{ \AA}$ $c = 5.000 \text{ \AA}$

$\alpha = 90^\circ$ $\beta = 90^\circ$ $\gamma = 120^\circ$

Wurtzite GaN can be synthesised by high temperature ammonolysis of gallium compounds, such as gallium arsenide or gallium oxide, or gallium salts, such as $\text{Ga}(\text{NO}_3)_3$ at temperatures as high as 1200°C . Gallium nitride is a yellow powder that is very hard and stable in air at room temperature and pressure with a melting point of $>2500^\circ\text{C}$.

Many groups have investigated the properties of GaN nanostructures, such as nanowires, but only a handful of groups have investigated occlusion of GaN within mesoporous materials, such as the silicates MCM-41 and SBA-15 and carbon nanotubes.^[34, 86-88] None have used microporous zeolites. In this work, GaN was occluded within the zeolites ZSM-5, ferrierite and faujasite using both the molten salt and salt solution impregnation methods using $\text{Ga}(\text{NO}_3)_3$ (described in Chapters 3.2.1 and 3.2.2).

5.1. Results

5.1.1. ZSM-5

Diffraction profiles were refined using Topas Academic V4.1 against the ZSM-5 structure reported by Li, et al.^[89] and GaN structure reported by Kaminski, et al.^[90]. The XRD and Rietveld profiles from solution-treated samples are shown in Figure 30 to Figure 36.

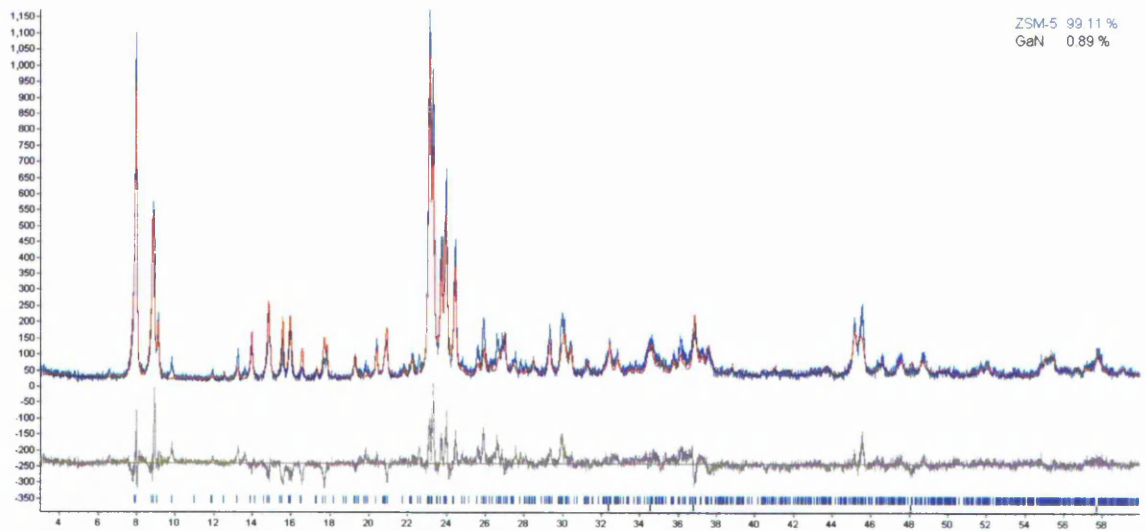


Figure 30: Rietveld fit for solution-treated ZSM-5 with 5wt% Ga as GaN.

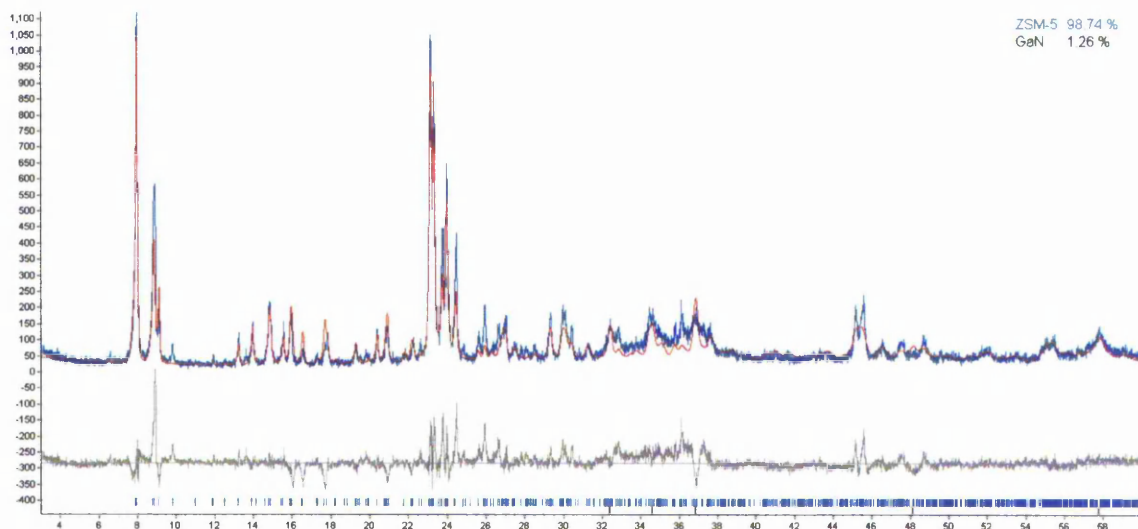


Figure 31: Rietveld fit for solution-treated ZSM-5 with 10wt% Ga as GaN.

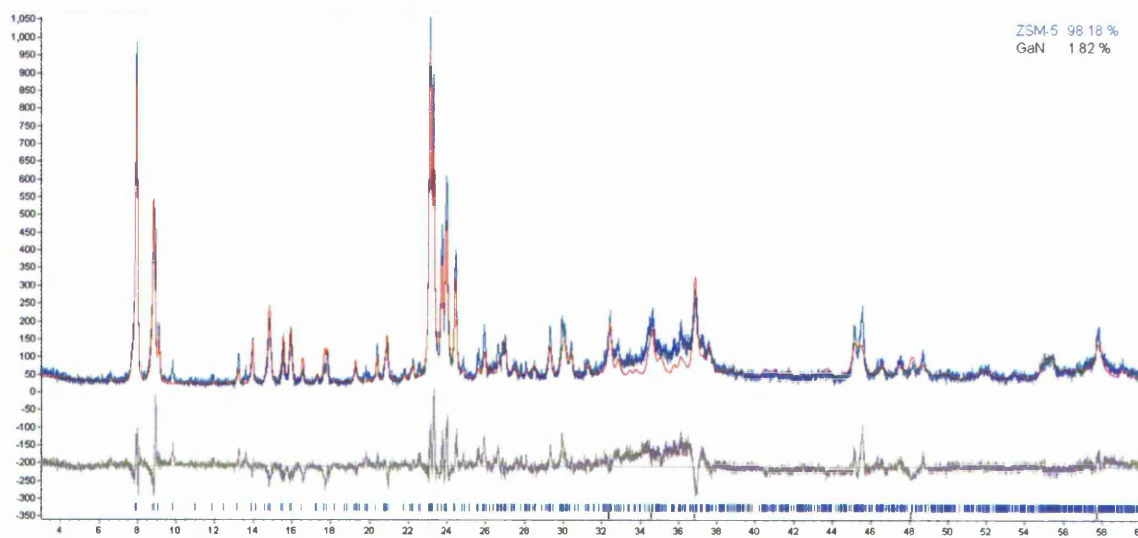


Figure 32: Rietveld fit for solution-treated ZSM-5 with 15wt% Ga as GaN.

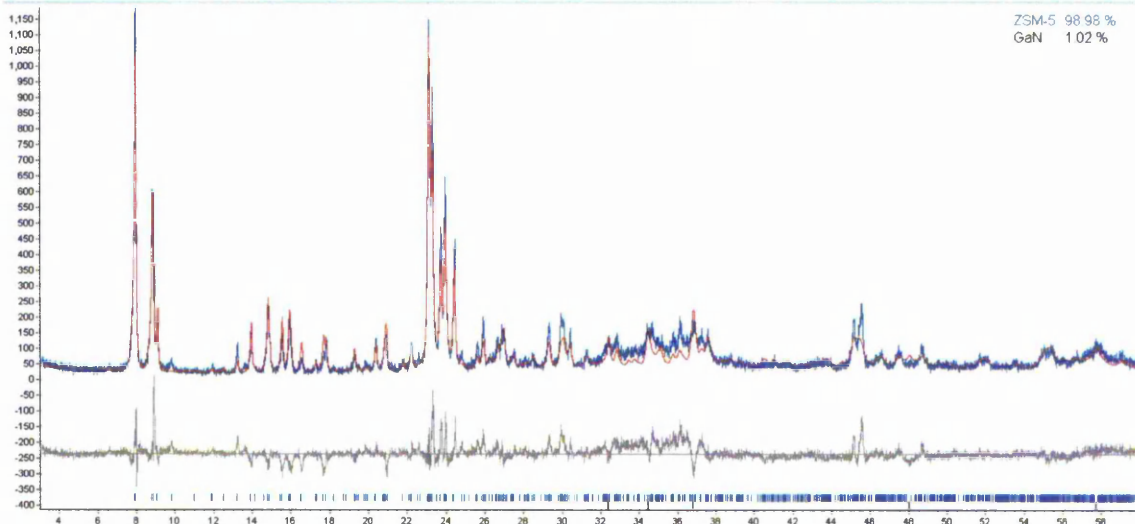


Figure 33: Rietveld fit for solution-treated ZSM-5 with 20wt% Ga as GaN.

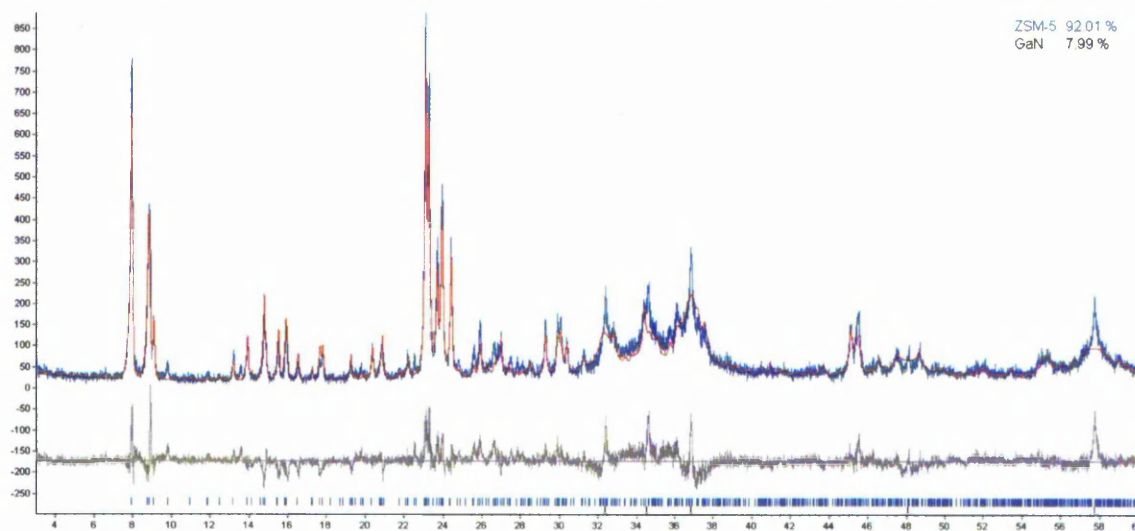


Figure 34: Rietveld fit for solution-treated ZSM-5 with 30wt% Ga as GaN.

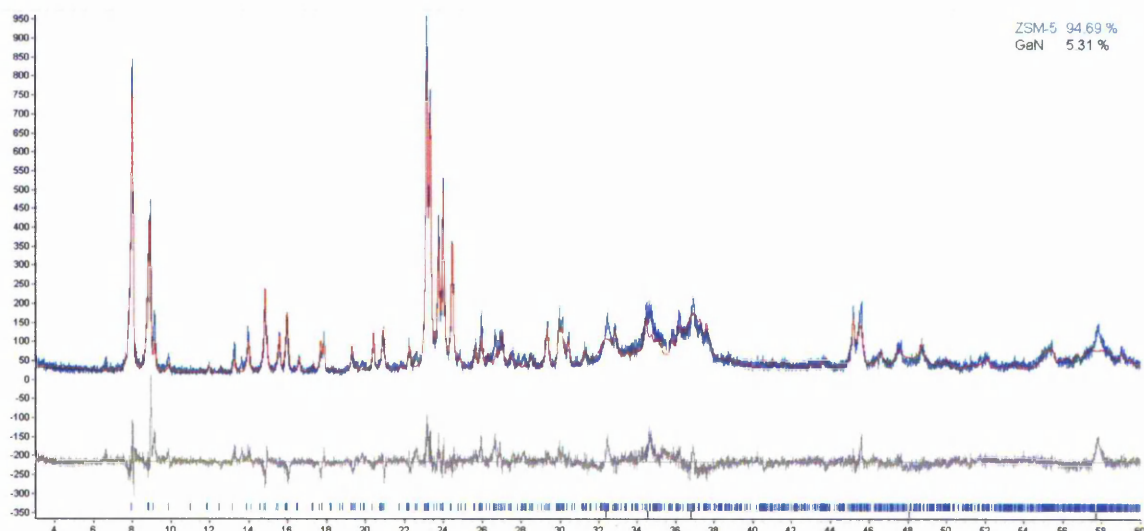


Figure 35: Rietveld fit for solution-treated ZSM-5 with 40wt% Ga as GaN.

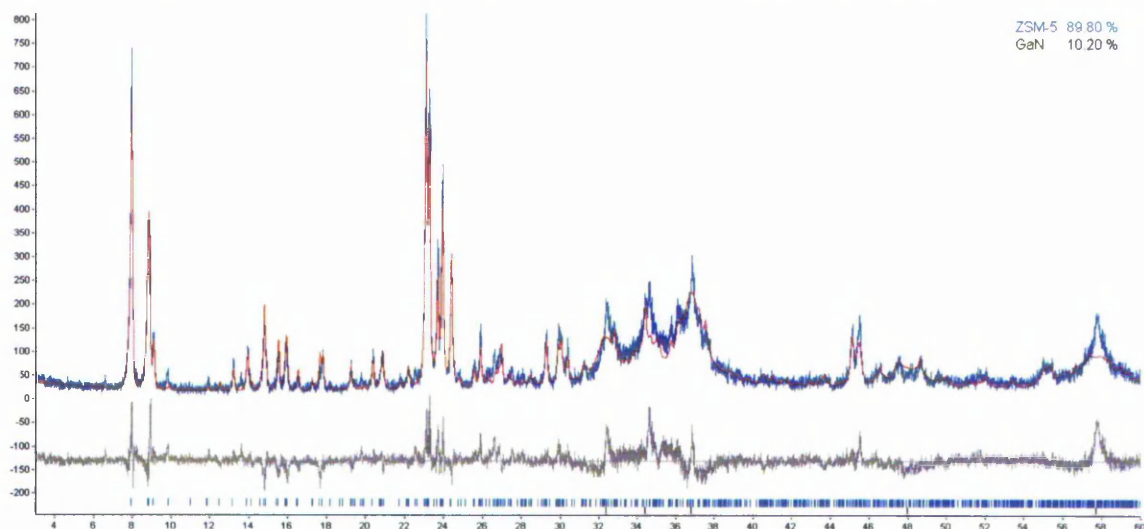


Figure 36: Rietveld fit for solution-treated ZSM-5 with 50wt% Ga as GaN.

The Rietveld profiles shown in Figure 30 to Figure 36 show that the process of GaN inclusion has little effect on the crystallinity of the host zeolite as the ZSM-5 diffraction peaks remain sharp. The peaks related to GaN, in particular the three peaks between $2\theta = 32$ to 37° , ([010], [002] and [011]) become more prevalent with increasing Ga content, which is to be expected. These peaks become significantly sharper between Ga loadings of 20 – 30wt%, at which the calculated GaN content from Rietveld refinement of measurable GaN diffraction increases

from 1.02 to 7.99%. This coincides with an approximated maximum main pore-filling Ga loading of 19.34 wt% using the following calculations assuming 1 main channel per unit cell:

- Main channel dimensions: 0.56 x 0.53 x 1.974 nm
- GaN unit cell dimensions (2GaN): 0.3197 x 0.3197 x 0.5207 nm
- Approx. Ga atoms per channel: 16
- Total Ga mass: 1115.57 a.m.u.
- Zeolite Unit Cell Mass: 5766.76 a.m.u.
- (Ga Mass/Zeolite Mass) x 100: 19.34 wt%

Therefore the data suggests that at Ga loadings of 20 wt% and less the GaN present, as confirmed by XRD data, is present as smaller crystallites than at more than 20wt% of Ga. This is likely to be due to GaN existing within the pore structure of the zeolite at the lower loadings. At the higher loadings the pores are fully occupied, thus the surplus GaN exists outside the zeolite crystals as bulk phase GaN of larger crystal size.

The Rietveld fit shown in Figure 37 was taken from the molten salt-treated sample.

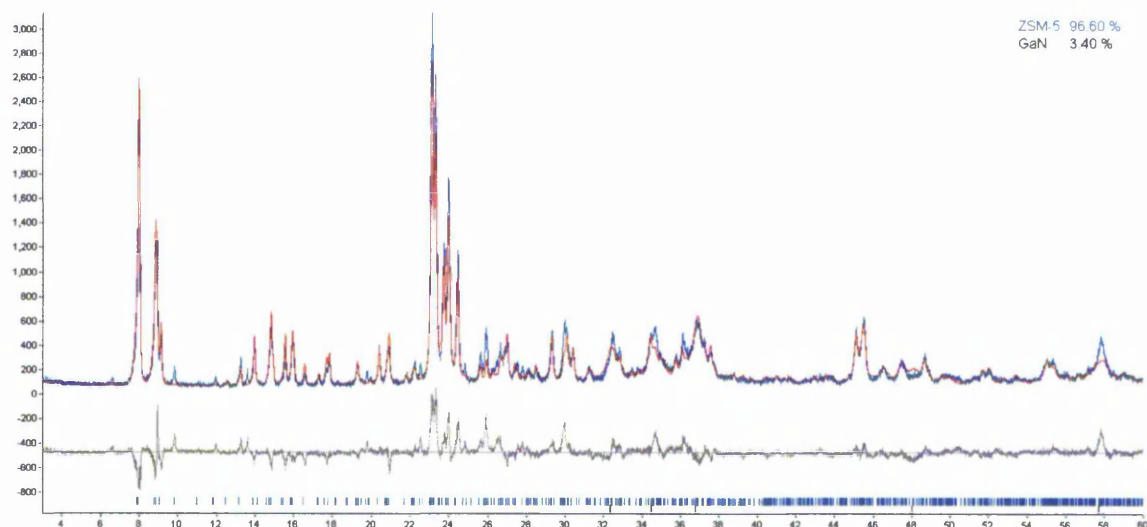


Figure 37: Rietveld fit for molten salt-treated ZSM-5 with GaN.

The broad GaN diffraction peaks in Figure 37 shows that by employing the molten salt method of impregnation the GaN exists as small crystallites. The calculated GaN content lies between the values obtained for 20-30wt% Ga loaded solution-treated samples, which suggests there is a large portion of zeolite-occluded GaN, but also a minor portion of larger, extra-zeolite GaN crystals.

The lattice parameters from ZSM-5 (Si:Al = 80) samples with GaN using both the solution and molten salt impregnation methods derived from Rietveld analysis are shown graphically in Figure 38.

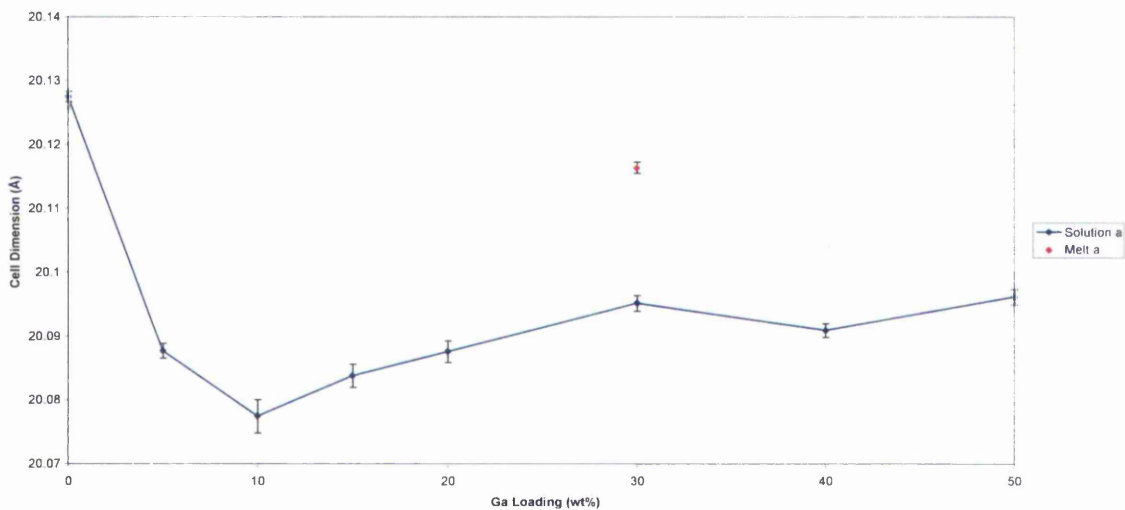


Figure 38: Unit Cell Parameter a for ZSM-5 with GaN.

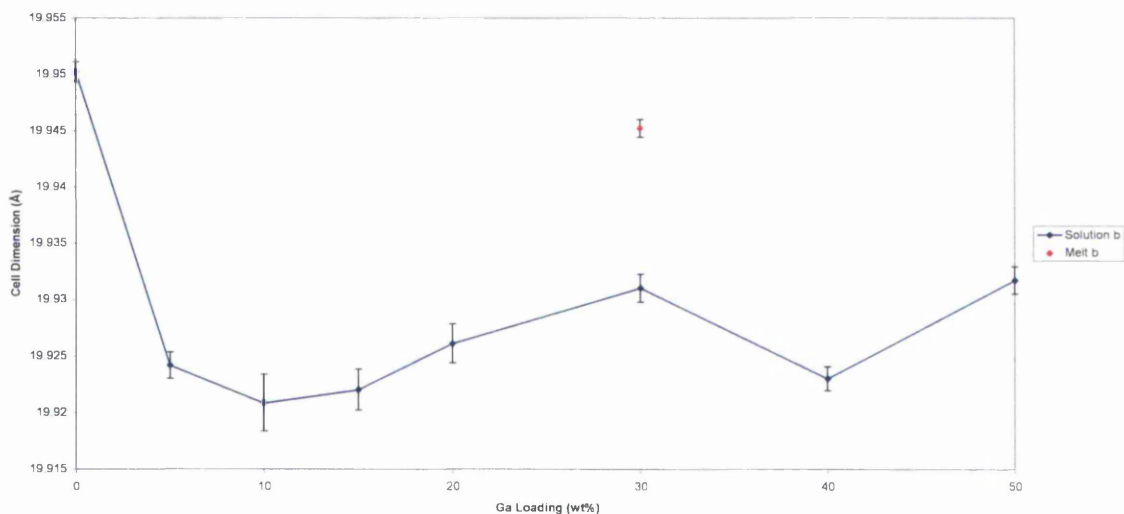


Figure 39: Unit Cell Parameter b for ZSM-5 with GaN.

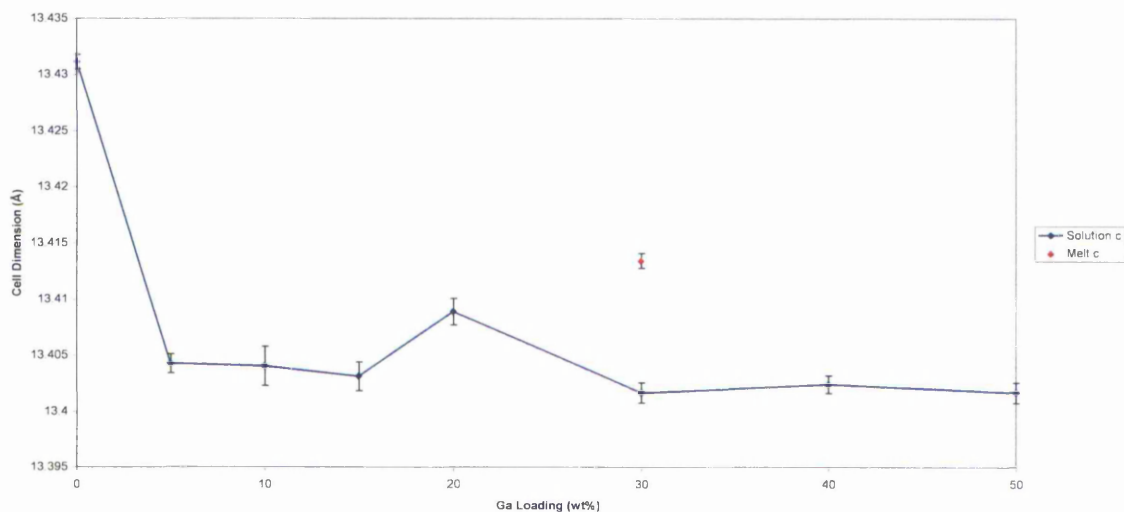


Figure 40: Unit Cell Parameter c for ZSM-5 with GaN.

It can be seen that compared to the salt solution treated samples, ZSM-5 treated by the molten salt impregnation method has a larger cell size in all three directions within experimental error. The dimensions are smaller than the parent zeolite in all instances. This suggests a change in the zeolite pore structure, which is more significant in the solution treated samples than for the molten-salt treated sample.

The XPS spectra for the ZSM-5 sample treated by the salt solution method with a 15% loading of Ga and the molten salt method were recorded without the use of an argon ion gun for depth profiling (i.e. only the surface was analysed). The data for the solution-treated samples are shown in Figure 41.

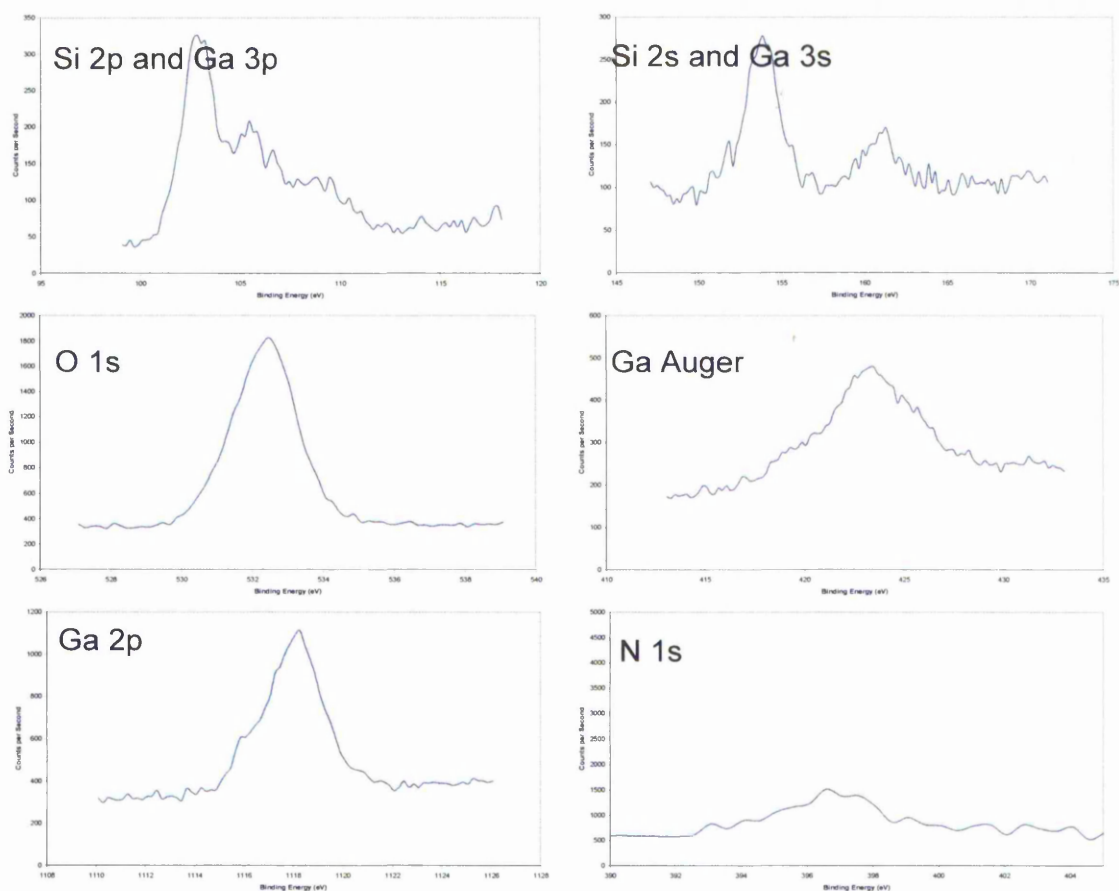


Figure 41: XPS spectra for ZSM-5 with 15% GaN.

The Ga spectra in this series of measurements were recorded using an Mg source. The rest of the measurements were recorded using an Al source.

The data for the molten salt-treated sample are shown in Figure 42. All spectra were recorded using an Al source.

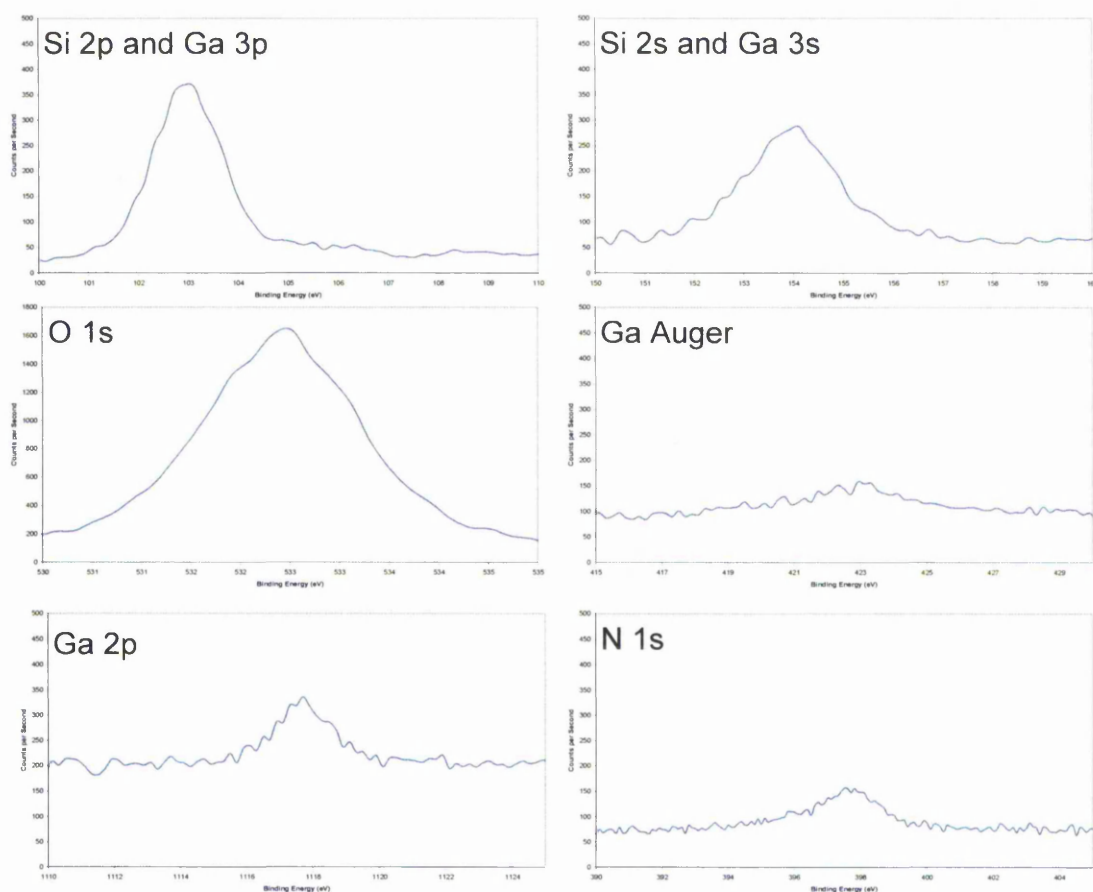


Figure 42: XPS spectra for ZSM-5 with GaN via the molten salt method.

As the XPS spectra for the two samples show, the Si 2s and 2p spectra are similar for both samples, as are the O 1s, which is to be expected. The Ga 2p spectrum for the solution-treated sample shows a distinctly more pronounced peak than that for the sample treated with the molten salt; suggesting less surface (uppermost 1-10 nm) Ga content in the molten salt treated sample. The N 1s spectra show similar profiles, which are mainly attributed to surface adsorbed NH_x species arising from the ammonolysis process.

Figure 43 shows the SEM/EDX analysis of ZSM-5 with 15% GaN.

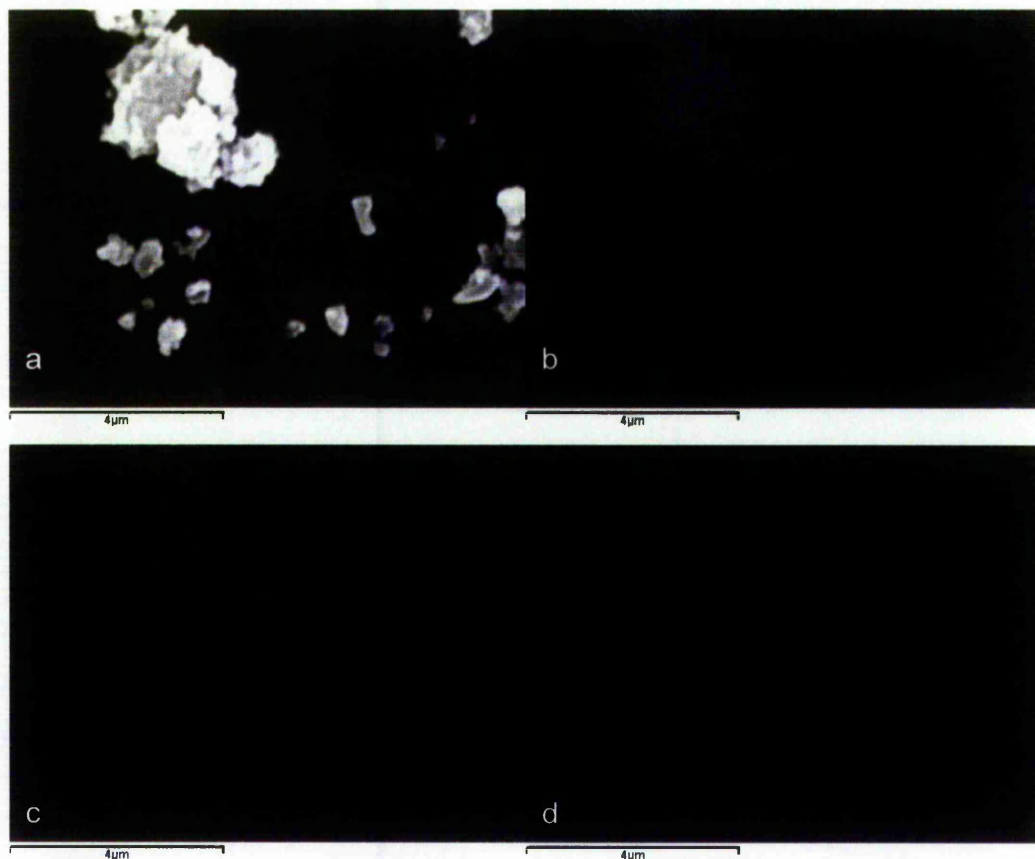


Figure 43: SEM/EDX images for ZSM-5 with 15% GaN. a) SEM Image, b) Si EDX map, c) O EDX map and d) Ga EDX map.

As EDX analysis shows; the ZSM-5 sample with 15% GaN shows very little trace of Ga from the surface to a depth of approximately 2 μ m of the zeolite crystals, which exhibit significant Si and O responses in EDX.

Figure 44 shows the SEM/EDX analysis of ZSM-5 with 50% GaN.

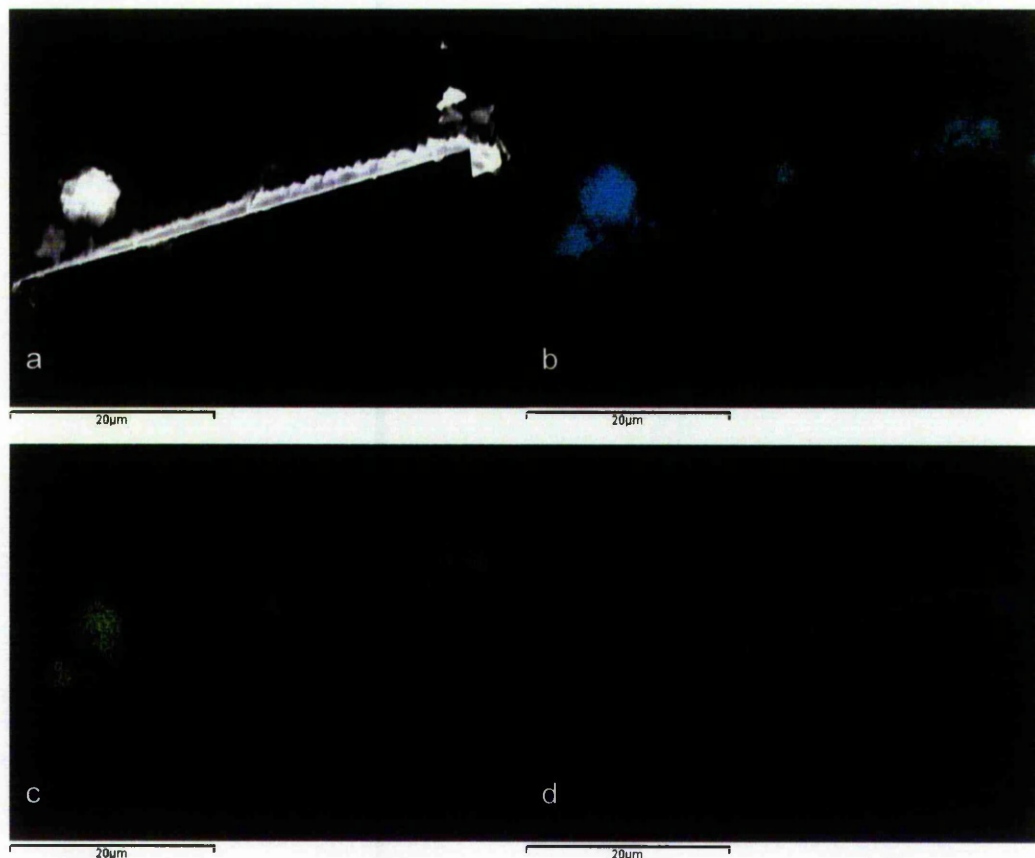


Figure 44: SEM/EDX images for ZSM-5 with 50% GaN. a) SEM Image, b) Si EDX map, c) O EDX map and d) Ga EDX map.

At a loading of 50% GaN of ZSM-5 there is a clear indication of extra-zeolite growth of GaN as there are distinct crystals of zeolite (Figure 44b and c; where Si and O EDX signals are strongest) and GaN; shown in Figure 44d as a long, thin, needle-shaped crystal.

Figure 45 shows the SEM/EDX analysis of ZSM-5 with GaN treated with the molten salt impregnation process.

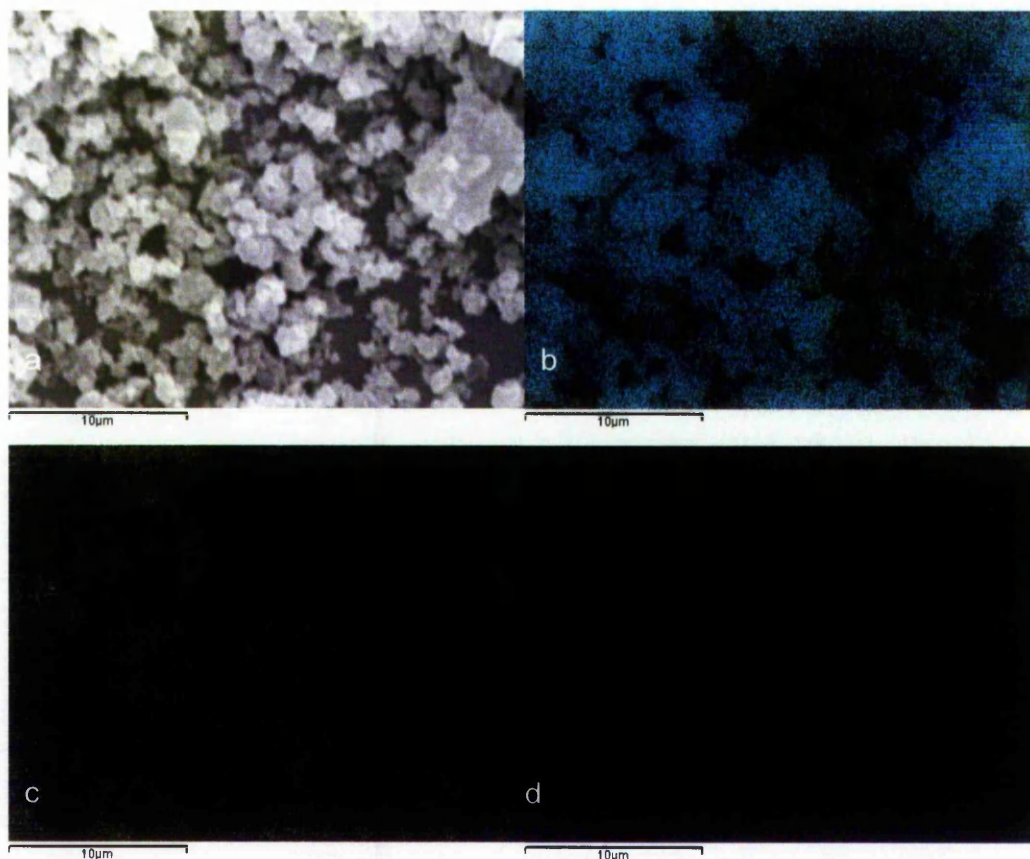


Figure 45: SEM/EDX images for ZSM-5 with GaN using the molten salt method. a) SEM Image, b) Si EDX map, c) O EDX map and d) Ga EDX map.

EDX analysis shows the absence of surface and extra-zeolite GaN crystallites in the ZSM-5/GaN sample prepared using the molten salt method (Figure 45d).

In the HRTEM image in Figure 46, the parallel lines show that the zeolite pore structure is left intact, in concurrence with XRD data, and there are no extra-zeolite phases of GaN, which would appear as hexagonal crystals. The presence of Ga distributed through the pores is shown by the dark ridges of the image as Ga scatters electrons more strongly than Si, Al and O.

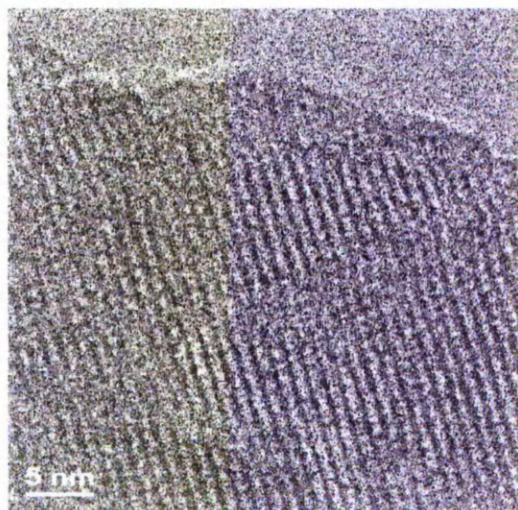


Figure 46: HRTEM image of ZSM-5 with 15% GaN.

The EDX spectrum (Figure 47) confirms the presence of Ga, as well as Si and O from the zeolite and Cu from the sample holder.

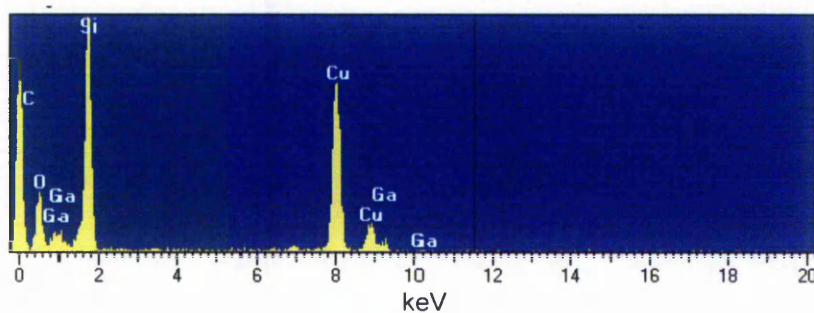


Figure 47: EDX spectrum of ZSM-5 with 15% GaN.

The HRTEM images in Figure 48 show that by employing the molten salt method in forming GaN, crystalline, extra-zeolite GaN nanowires are formed with widths of ~17 nm (Figure 48c) that appear to emerge from the zeolite crystals (Figure 48b), which retain their pore structure, in agreement with XRD data. The hexagonal nature of the wires suggests these consist of GaN. The dark ridges in Figure 48d also show that there is still GaN dispersed throughout the zeolite pore structure.

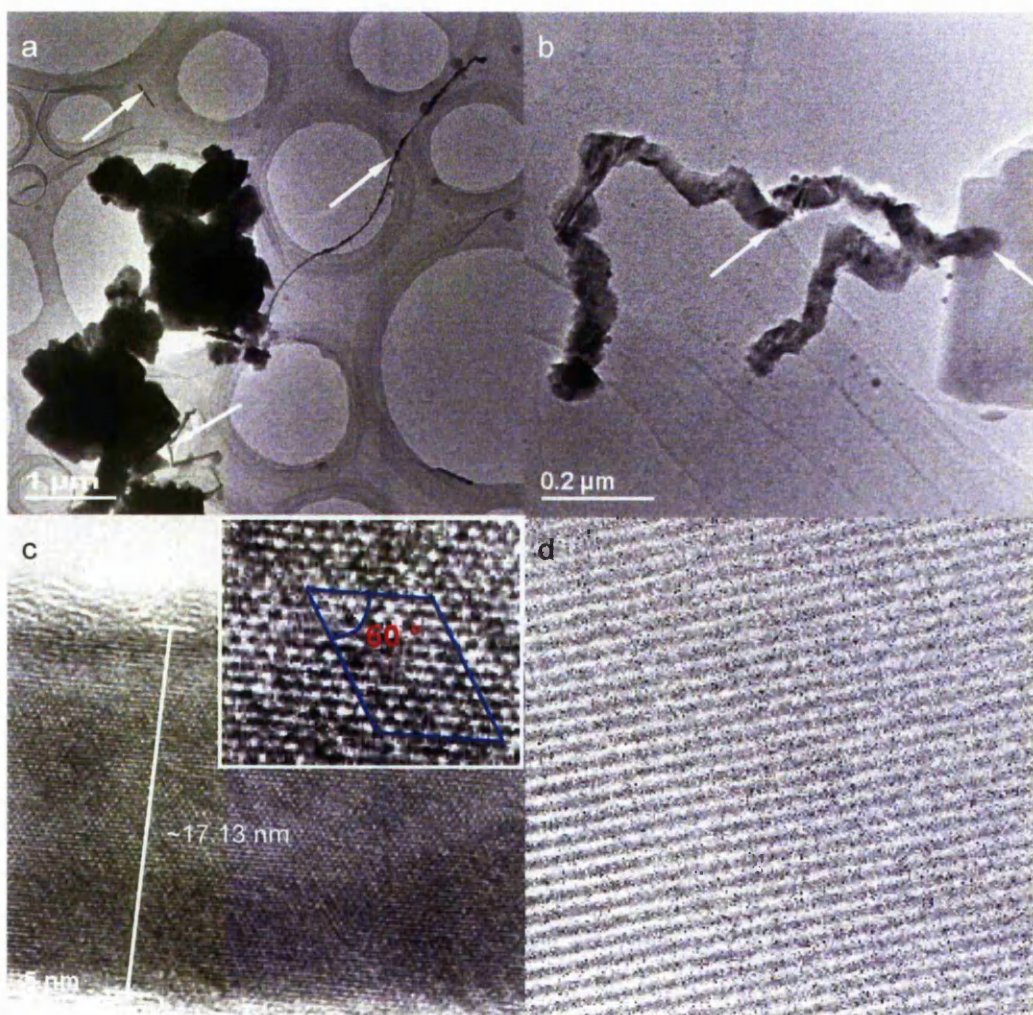


Figure 48: HRTEM images of ZSM-5 with GaN via the molten salt method. Arrows indicate GaN nanowires/clusters. (a) Several ZSM-5 crystals with GaN nanowires highlighted by arrows. (b) GaN nanowires emanating from a ZSM-5 crystal. (c) View of nanowire cross-section. Inset highlights the hexagonal structure of the nanowires. (d) GaN clusters within the ZSM-5 pore system highlighted by arrows.

The EDX spectra of the areas containing the nanowires (Figure 50) show significantly more Ga content than that of the zeolite crystals alone (Figure 49), confirming the Ga content of the wires. Since the crystal habit of the wires is hexagonal, which suggests the wires are composed of wurtzite GaN, also in agreement with the XRD data that provides a Ga content of 3.40%, as shown in Figure 19.

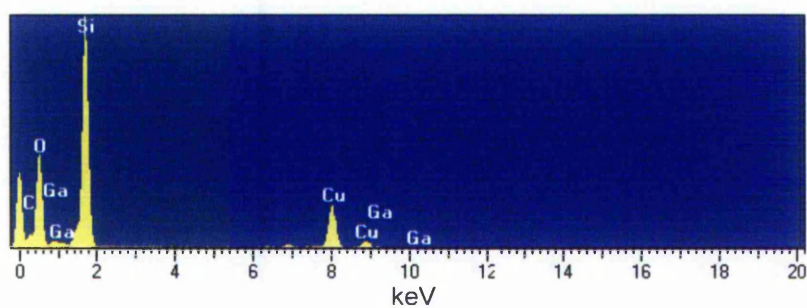


Figure 49: EDX spectrum of ZSM-5 with GaN via the molten salt method (zeolite area).

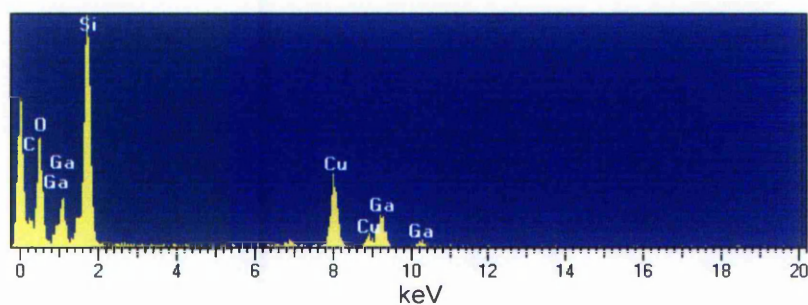


Figure 50: EDX spectrum of ZSM-5 with GaN via the molten salt method (Ga nanowire area).

Figure 51 shows the UV-visible diffuse reflectance curves obtained for all ZSM-5 samples impregnated with GaN, the parent zeolite and bulk GaN. By taking the 1st derivative of the data, the band gaps can be read at the curve maxima, giving the values shown in Table 2 and Figure 52.

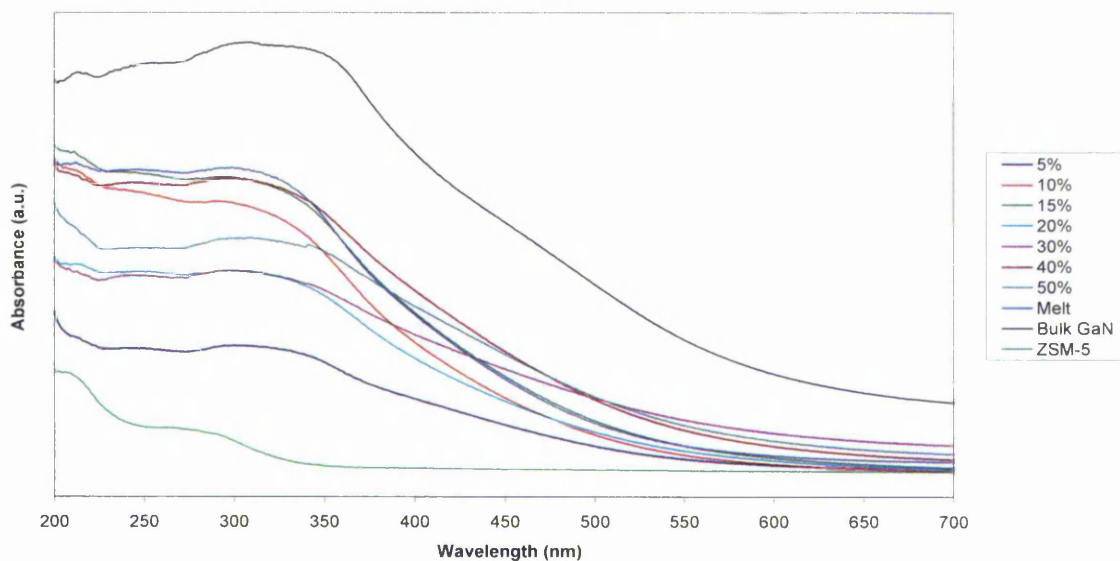


Figure 51: UV Vis Data for ZSM-5 samples with GaN.

Table 2: Band gap values for ZSM-5 samples with GaN.

Impregnation Method	Band Gap (eV)
Molten Salt	3.51
5% Solution	3.51
10% Solution	3.46
15% Solution	3.46
20% Solution	3.4
30% Solution	3.43
40% Solution	3.46
50% Solution	3.43
Bulk GaN	3.37

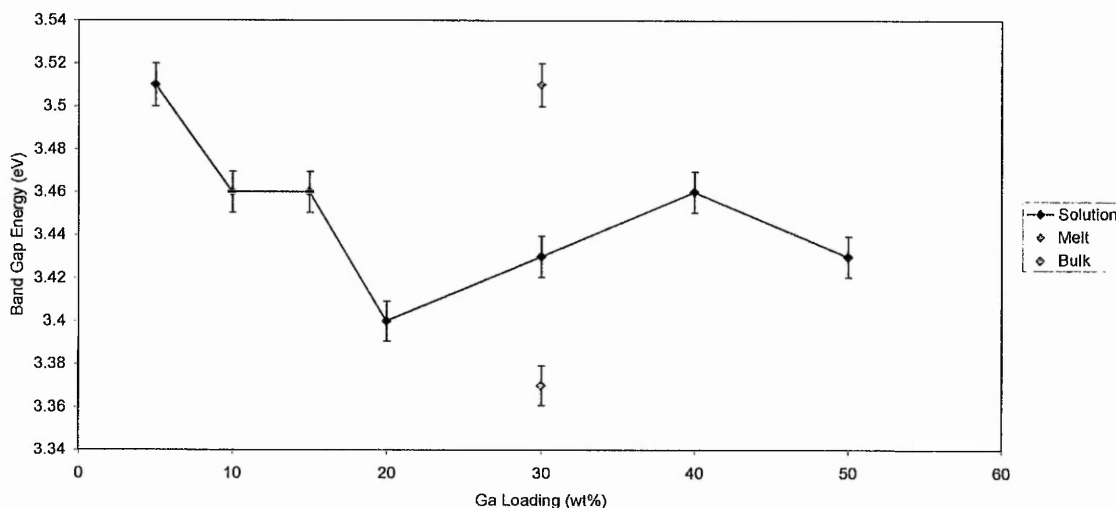


Figure 52: Band gap values for ZSM-5 samples with GaN. The position of the Melt and Bulk GaN points in the centre of the x-axis are for illustration only and does not imply Ga loadings of 30 wt% are present in these samples.

It is clear that, within experimental error, the band gap of GaN is increased on solution impregnation into ZSM-5 in comparison to bulk GaN; the extent to which

varies across the loading range of 5 – 50 wt% Ga, and that by adopting the molten salt approach the band gap is increased to the maximum value obtainable by using solution impregnation, which occurs at a loading of 5% Ga.

5.1.2. Faujasite

Diffraction profiles were refined using Topas Academic V4.1 against the faujasite structure reported by Parise, et al.^[91] and GaN structure reported by Kaminski, et al.^[90]. The refinement of the data from the solution-treated sample with 50wt% Ga loading, in which the zeolite structure was destroyed, includes a 2-direction preferred orientation factor in the [010] and [002] directions for the GaN phase. The XRD and Rietveld profiles from solution-treated samples are shown in Figure 53 to Figure 59.

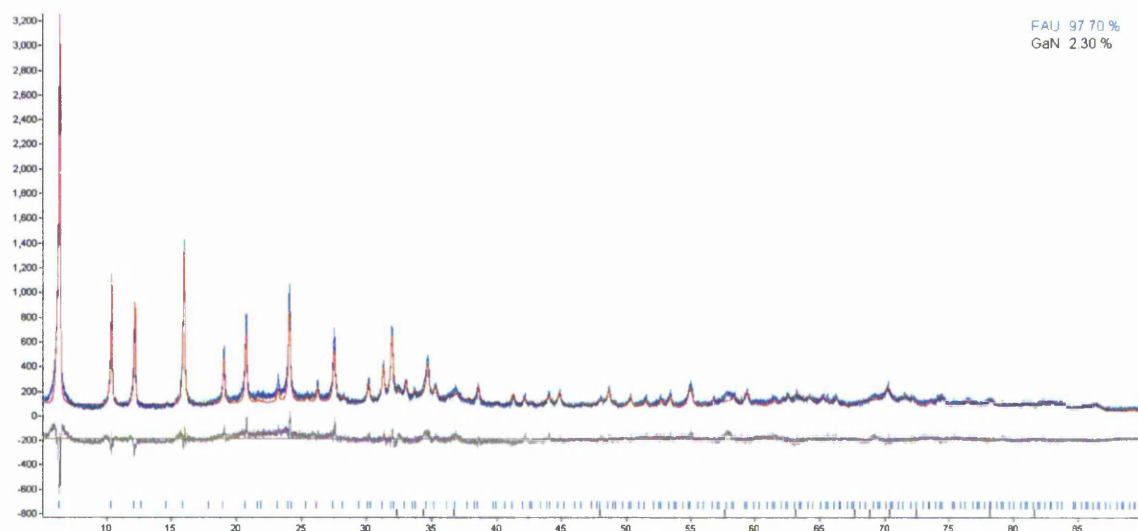


Figure 53: Rietveld fit for solution-treated FAU with 5wt% Ga as GaN.

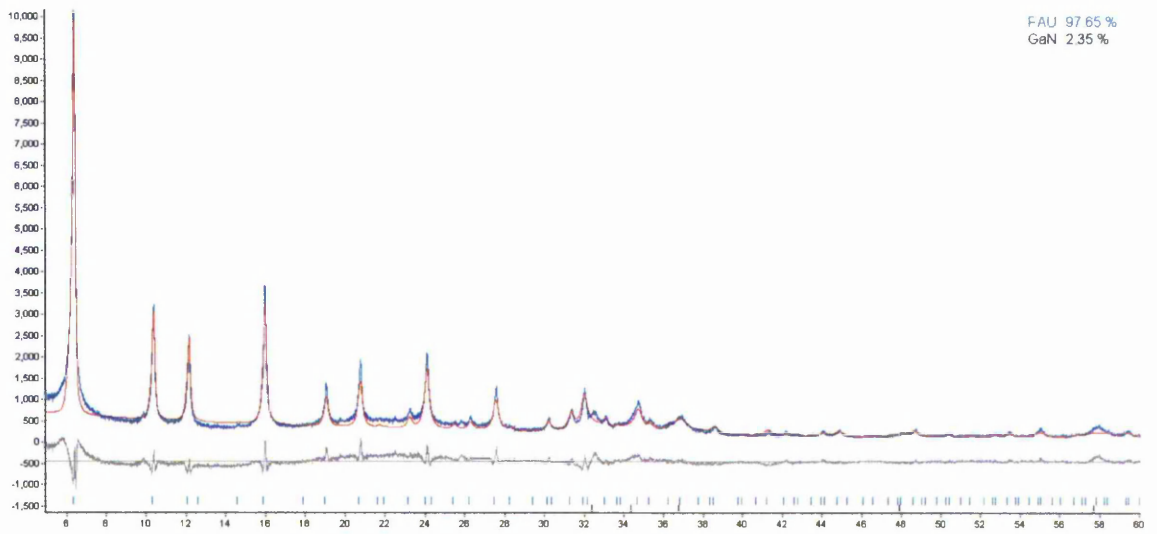


Figure 54: Rietveld fit for solution-treated FAU with 10wt% Ga as GaN.

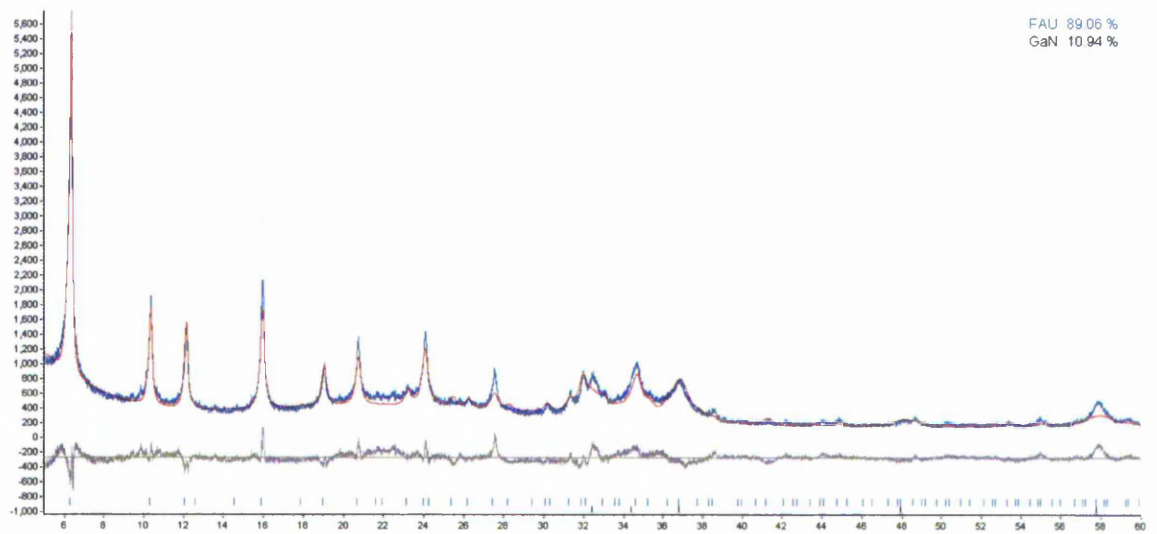


Figure 55: Rietveld fit for solution-treated FAU with 15wt% Ga as GaN.

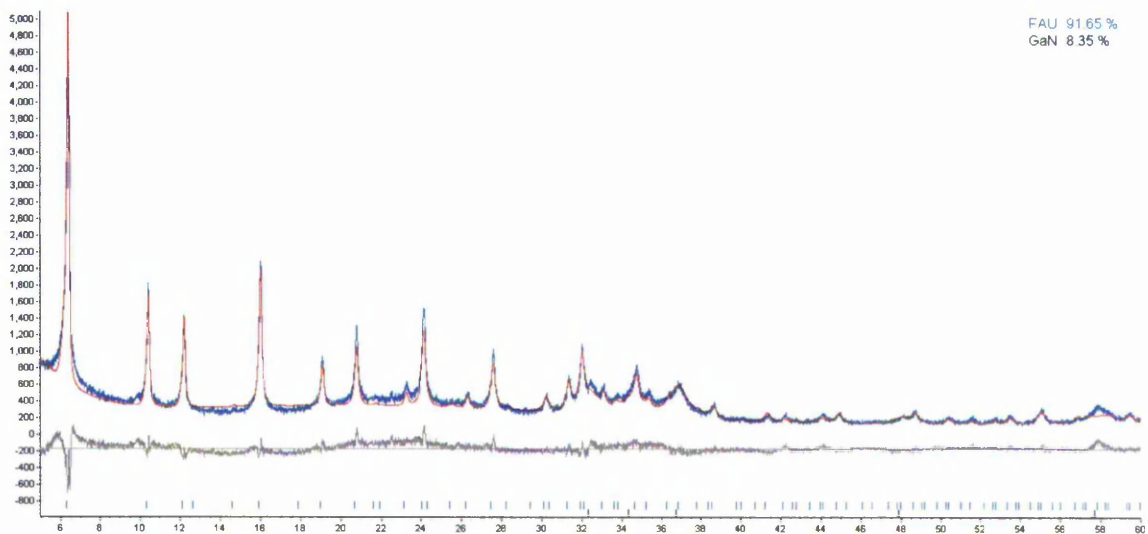


Figure 56: Rietveld fit for solution-treated FAU with 20wt% Ga as GaN.

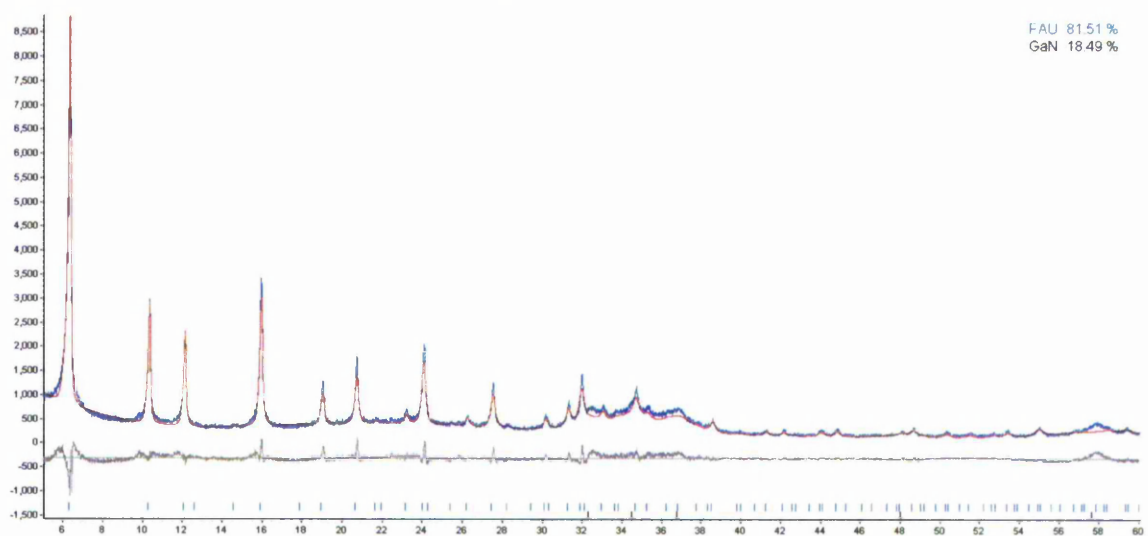


Figure 57: Rietveld fit for solution-treated FAU with 30wt% Ga as GaN.

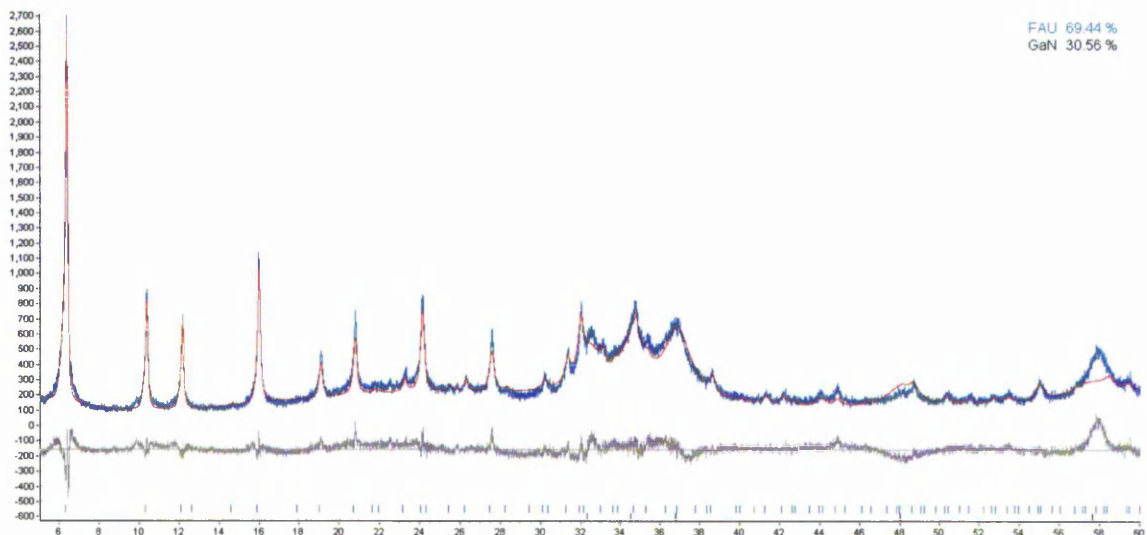


Figure 58: Rietveld fit for solution-treated FAU with 40wt% Ga as GaN.

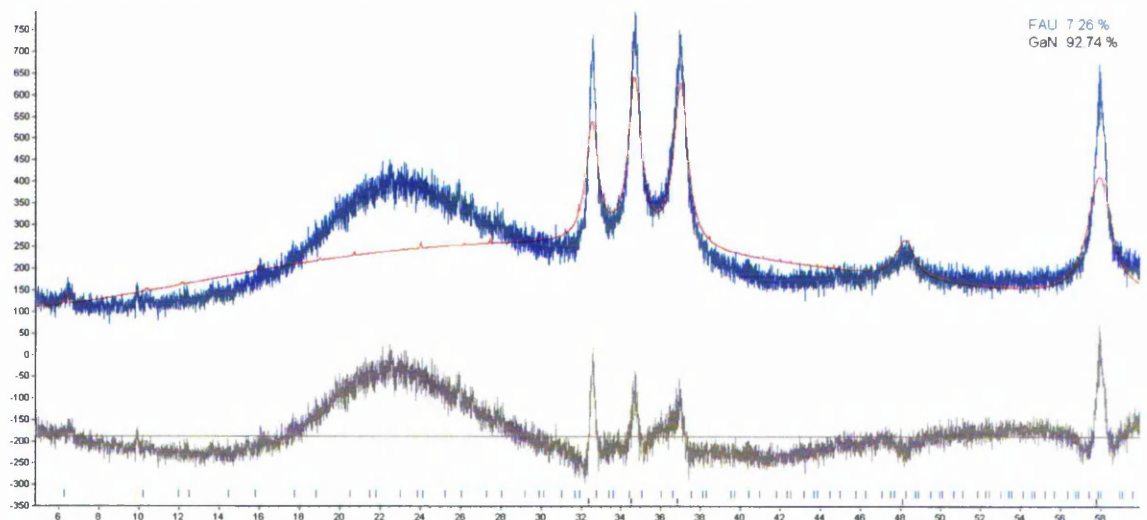


Figure 59: Rietveld fit for solution-treated FAU with 50wt% Ga as GaN.

The Rietveld profiles shown in Figure 53 to Figure 59 show that the process of GaN inclusion has little effect on the crystallinity of the host zeolite at Ga loadings below 50wt%. At 50wt% Ga loading the zeolite structure is destroyed, producing a mostly amorphous XRD profile with the only discernible peaks being that of a poorly crystalline GaN phase with bidirectional preferred orientation. In the profiles from samples containing less than 50wt% Ga the peaks related to GaN, in particular the three peaks between $2\theta = 32$ to 37° , ([010], [002] and [011]) become

more prevalent with increasing Ga content, which is to be expected. These peaks become significantly sharper between Ga loadings of 10 – 15wt% and then again between 30 – 40wt%, at which the calculated GaN content from Rietveld refinement of measurable GaN diffraction increases from 2.35 to 10.94% and 18.49 to 30.56%. The first increase coincides with an approximated maximum main cage-filling Ga loading of 12.09 wt% using the following calculations assuming 1 cage per unit cell:

- Cage dimensions: 1.304 x 1.304 x 1.304 nm
- GaN unit cell dimensions (2GaN): 0.3197 x 0.3197 x 0.5207 nm
- Approx. Ga atoms per cage: 20
- Total Ga mass: 1394.46 a.m.u.
- Zeolite Unit Cell Mass: 11533.51 a.m.u.
- (Ga Mass/Zeolite Mass) x 100: 12.09 wt%

The second increase after 30wt% Ga loading coincides with the filling of the smaller, secondary cages (sodalite cages) of which there are approximately 5 per unit cell:

- Cage dimensions: 0.604 x 0.604 x 0.604 nm
- GaN unit cell dimensions (2GaN): 0.3197 x 0.3197 x 0.5207 nm
- Approx. Ga atoms per cage: 9
- Total Ga mass: 3137.54 a.m.u.
- Zeolite Unit Cell Mass: 11533.51 a.m.u.
- (Ga Mass/Zeolite Mass) x 100: 27.20 wt%

Thus the total Ga loading is 39.29 wt%. Therefore the data suggests that at Ga loadings of 15 wt% and less the GaN present, as confirmed by XRD data, is present as small crystallites occupying the main cages of the zeolite structure and

that at loadings between 15 and 40wt% the smaller sodalite cages are filled. It is not until 40wt% of Ga is present that extra-zeolite phases of GaN exist.

The Rietveld fit shown in Figure 60 was taken from the molten salt-treated sample.

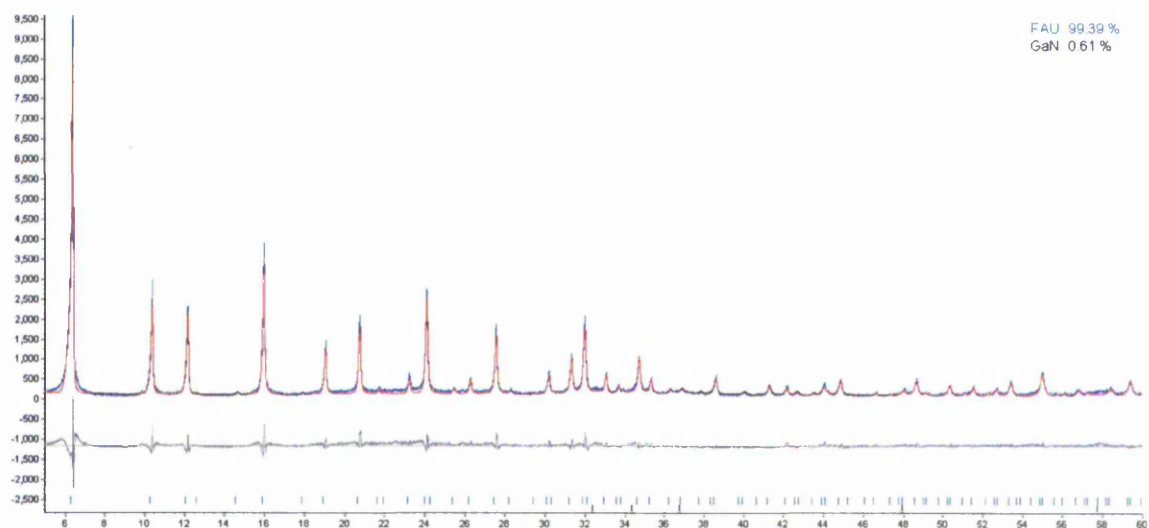


Figure 60: Rietveld fit for molten salt-treated FAU with GaN.

The relatively small calculated GaN content from the molten salt-treated sample shows that the majority of GaN formed is very much smaller than the XRD technique is able to detect. It is also clear that the zeolite structure is still intact. The absence of significant diffraction from GaN suggests there may not be any GaN phase present at all, yet the UV-Vis data suggests a band structure similar to that of GaN is present.

The lattice parameter from FAU (Si:Al = 80) samples with GaN using both the solution and molten salt impregnation methods derived from Rietveld analysis of the XRD data are shown graphically in Figure 61.

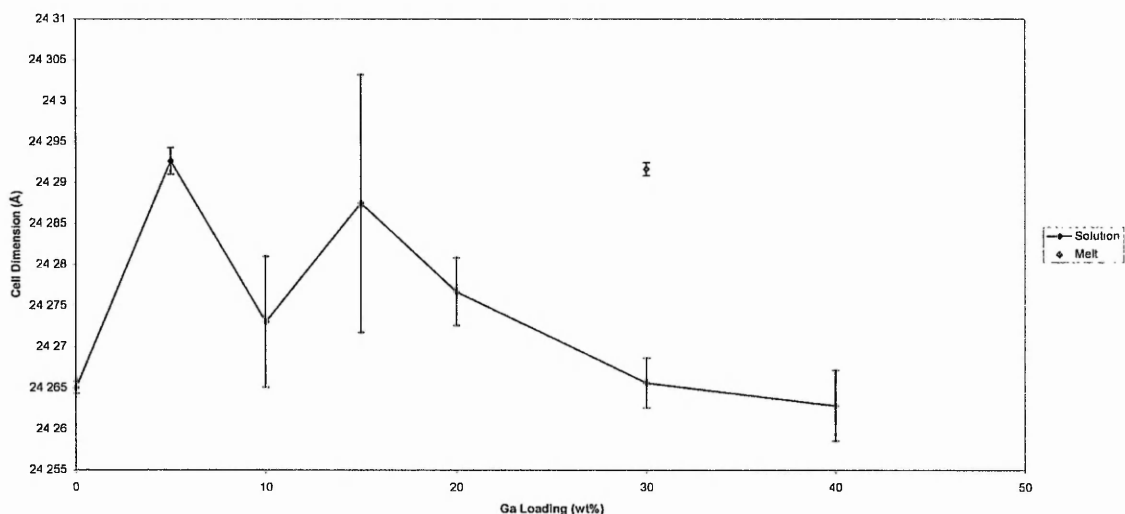


Figure 61: Unit cell parameter for FAU with GaN.

As Figure 61 shows, the unit cell parameter for FAU generally decreases from 5 – 40 wt% within experimental error. Figure 61 also shows that the unit cell parameter for FAU upon treatment with the $\text{Ga}(\text{NO}_3)_3$ melt is large in comparison to many of the solution-treated samples. At a loading of 50 wt% of Ga the zeolite framework is destroyed during the nitridation process yet is still present upon oxidation of the same nitrate-loaded sample (see section 6.1.2). This suggests that at this higher loading the zeolite structure is sufficiently weakened, most likely by dealumination, to be susceptible to attack by NH_3 at these temperatures yet resistant to thermal shock during calcination.

Figure 62 shows the UV-Visible diffuse-reflectance curves obtained for all FAU samples impregnated with GaN, the parent zeolite and bulk GaN.

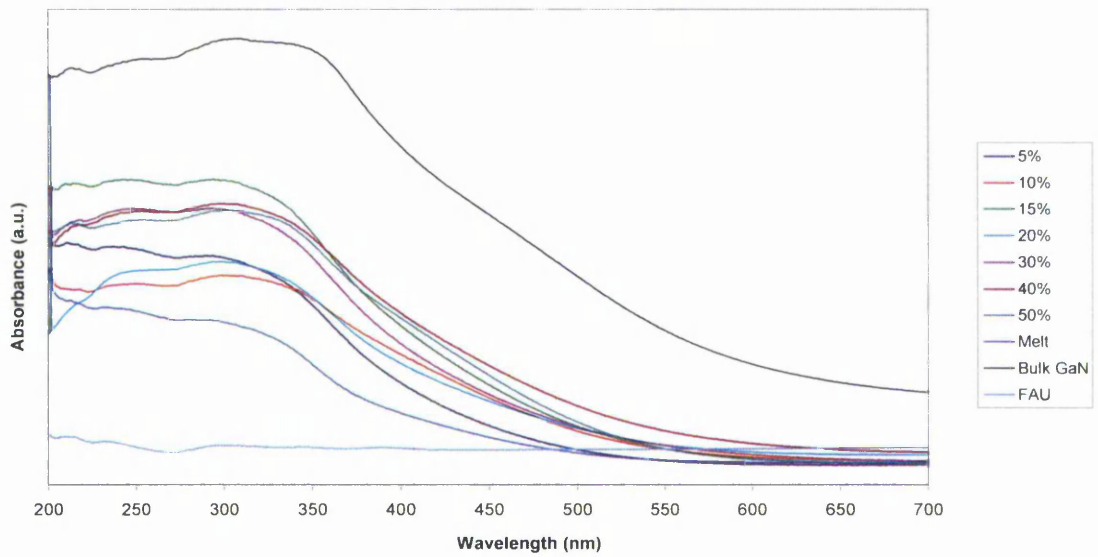


Figure 62: UV Vis data for FAU samples with GaN.

By taking the 1st derivative of the data, the band gaps can be read at the curve maxima, giving the values shown in Table 3 and Figure 63.

Table 3: Band gap values for FAU samples with GaN.

Impregnation Method	Band Gap (eV)
Molten Salt	3.625
5% Solution	3.54
10% Solution	3.54
15% Solution	3.57
20% Solution	3.525
30% Solution	3.525
40% Solution	3.47
50% Solution	3.55
Bulk GaN	3.4

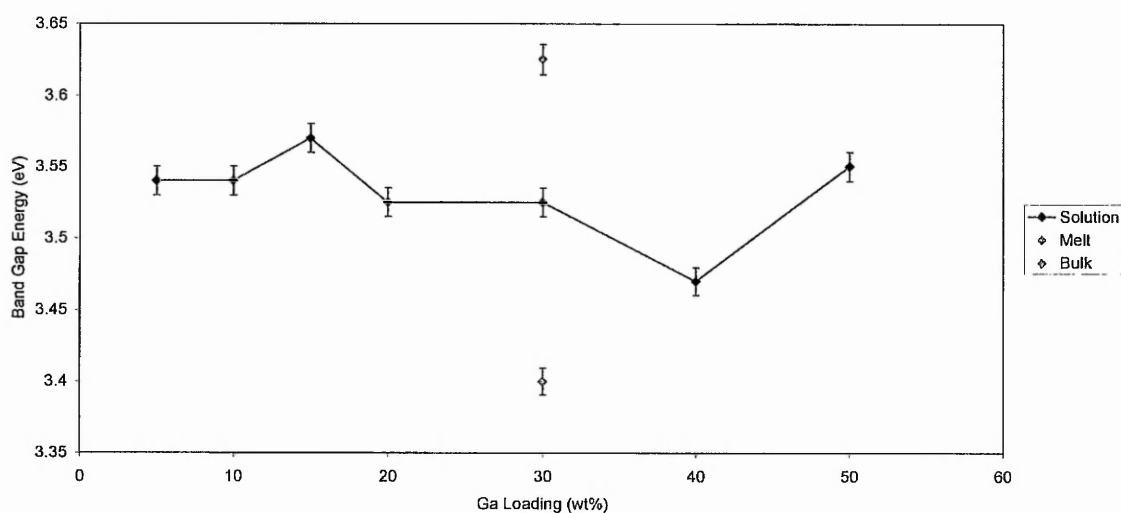


Figure 63: Band gap values for FAU samples with GaN. The position of the Melt and Bulk GaN points in the centre of the x-axis are for illustration only and does not imply Ga loadings of 30 wt% are present in these samples.

It is clear that, within experimental error, the band gap of GaN is increased upon solution impregnation into FAU in comparison to bulk GaN, the extent of which varies slightly across the loading range of 5 – 50 wt% Ga, and that by adopting the molten salt approach the band gap is increased 0.055 eV beyond the maximum value obtainable by using solution impregnation, which occurs at a loading of 15% Ga.

5.1.3. Ferrierite

Diffraction profiles were refined using Topas Academic V4.1 against the ferrierite structure reported by Bull, et al.^[92] and GaN structure reported by Kaminski, et al.^[90]. The XRD and Rietveld profiles from solution-treated samples are shown in Figure 64 to Figure 70.

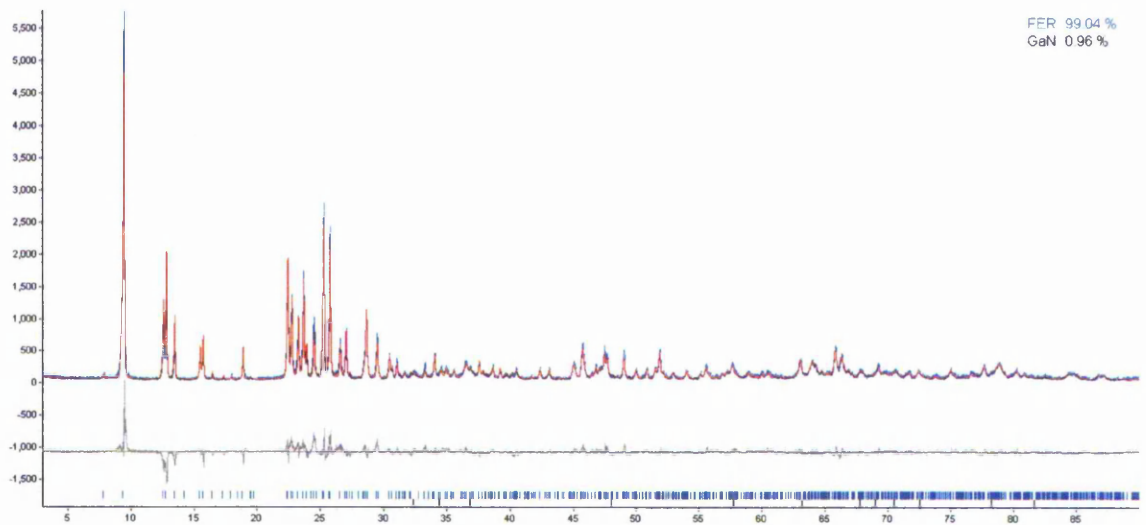


Figure 64: Rietveld fit for solution-treated FER with 5wt% Ga as GaN.

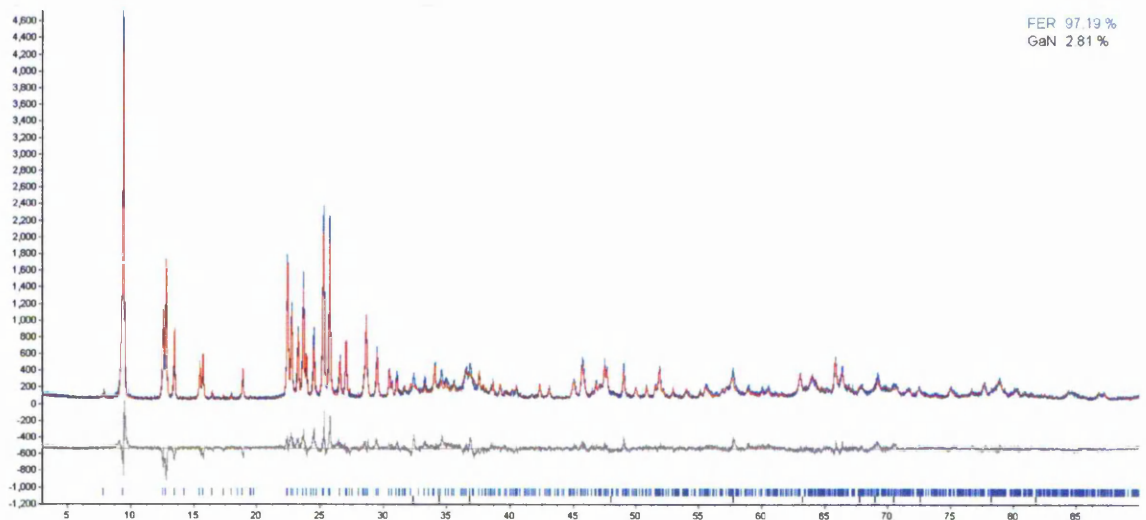


Figure 65: Rietveld fit for solution-treated FER with 10wt% Ga as GaN.

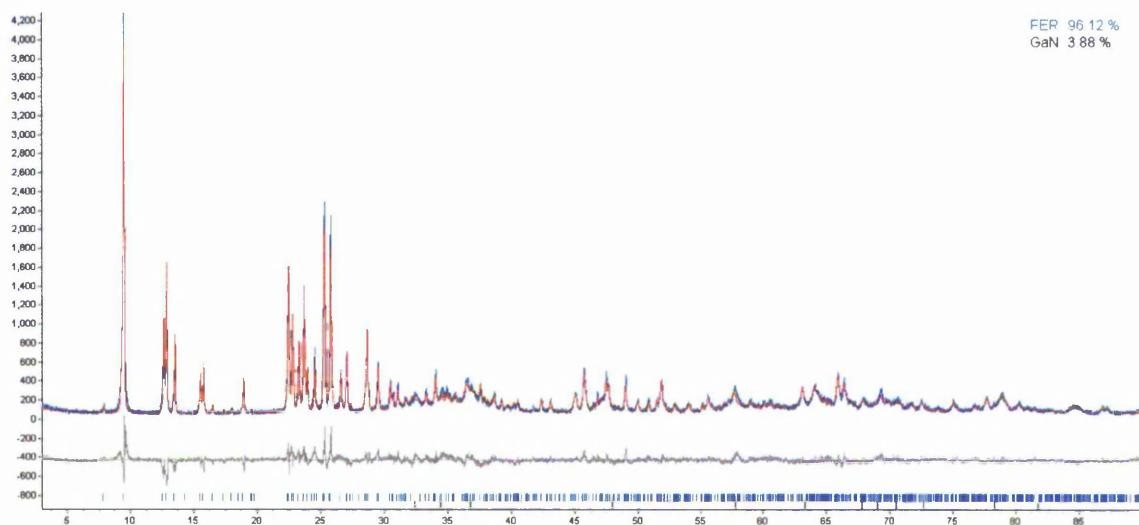


Figure 66: Rietveld fit for solution-treated FER with 15wt% Ga as GaN.

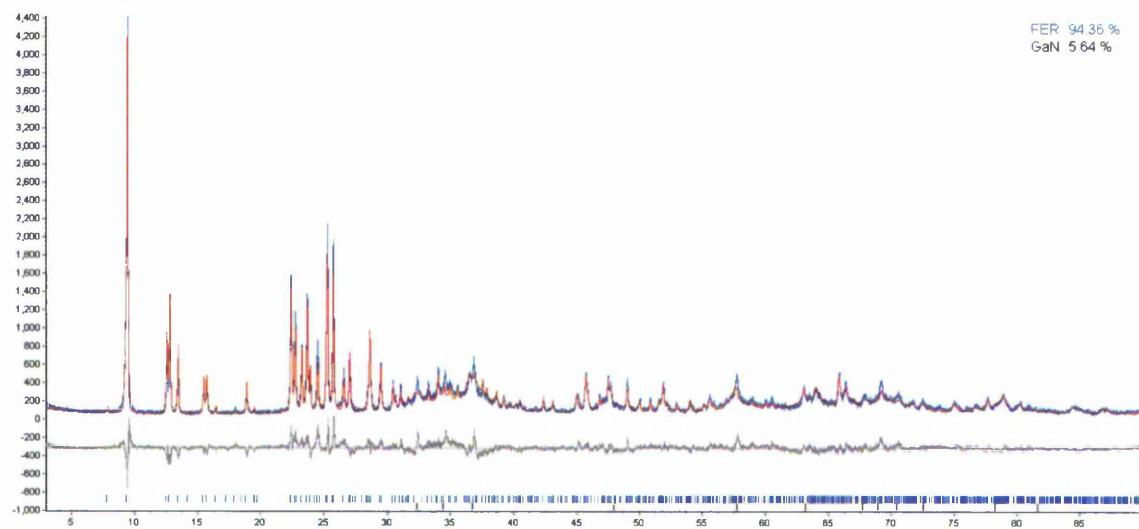


Figure 67: Rietveld fit for solution-treated FER with 20wt% Ga as GaN.

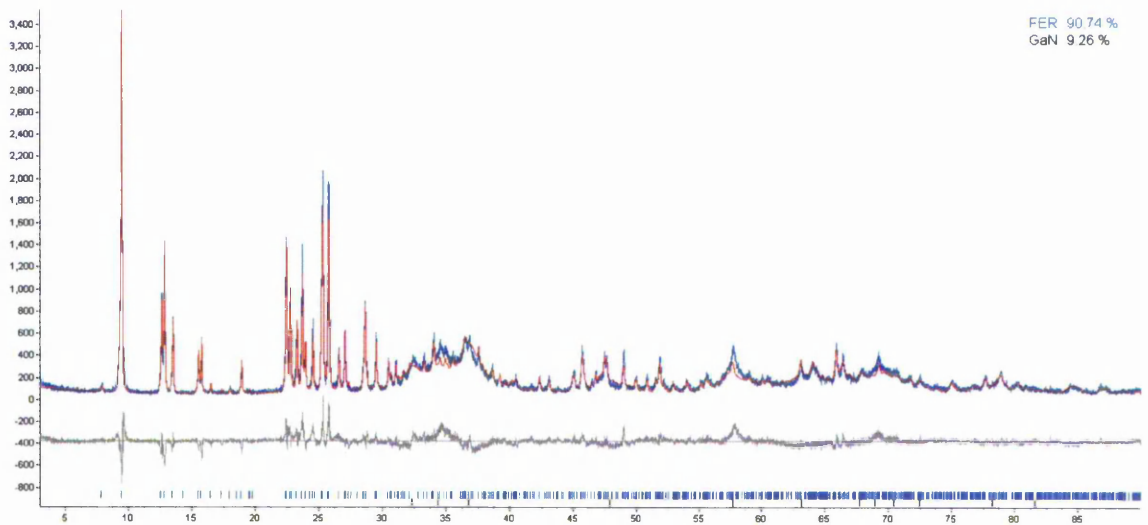


Figure 68: Rietveld fit for solution-treated FER with 30wt% Ga as GaN.

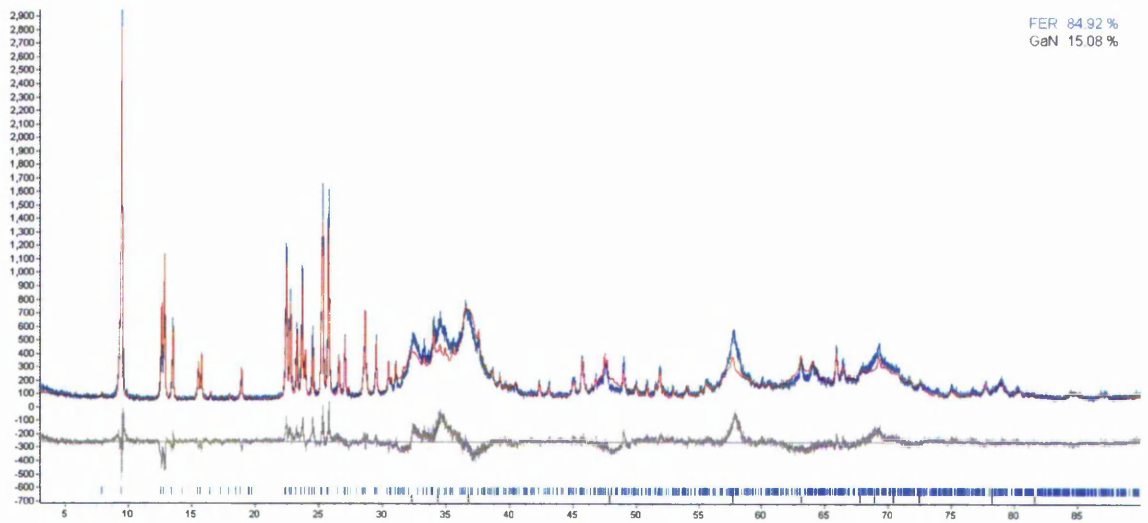


Figure 69: Rietveld fit for solution-treated FER with 40wt% Ga as GaN.

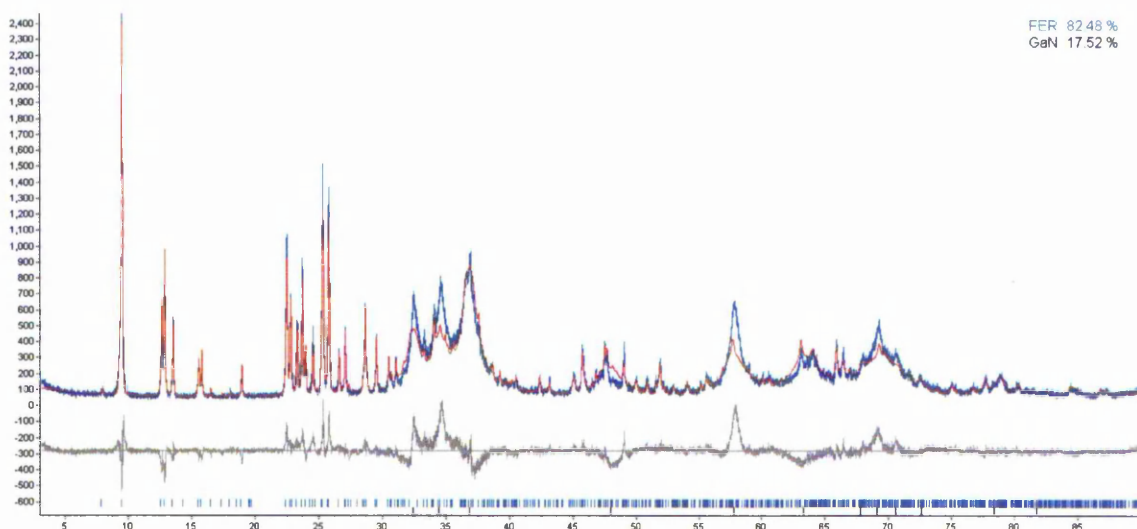


Figure 70: Rietveld fit for solution-treated FER with 50wt% Ga as GaN.

The Rietveld profiles shown in Figure 64 to Figure 70 show that the process of GaN inclusion has little effect on the crystallinity of the host zeolite at Ga loadings below 50wt%. The peaks related to GaN, in particular the three peaks between $2\theta = 32$ to 37° , ([010], [002] and [011]) become more prevalent with increasing Ga content, which is to be expected. These peaks become significantly sharper between Ga loadings of 20 - 30wt%, at which the calculated GaN content from Rietveld refinement of measurable GaN diffraction increases from 5.64 to 9.26%. This coincides with an approximated maximum main pore-filling Ga loading of 25.81 wt% using the following calculations assuming 1 pore per unit cell:

- Pore dimensions: 0.54 x 0.42 x 0.754 nm
- GaN unit cell dimensions (2GaN): 0.3197 x 0.3197 x 0.5207 nm
- Approx. Ga atoms per cage: 8
- Total Ga mass: 557.78 a.m.u.
- Zeolite Unit Cell Mass: 2161.13 a.m.u.
- (Ga Mass/Zeolite Mass) x 100: 25.81 wt%

Therefore the data suggests that at Ga loadings of 20 wt% and less the GaN present, as confirmed by XRD data, is present as small crystallites occupying the main pores of the zeolite structure and that at loadings above 30 wt% extra-zeolite phases of GaN exist.

The Rietveld fit shown in Figure 71 was taken from the molten salt-treated sample.

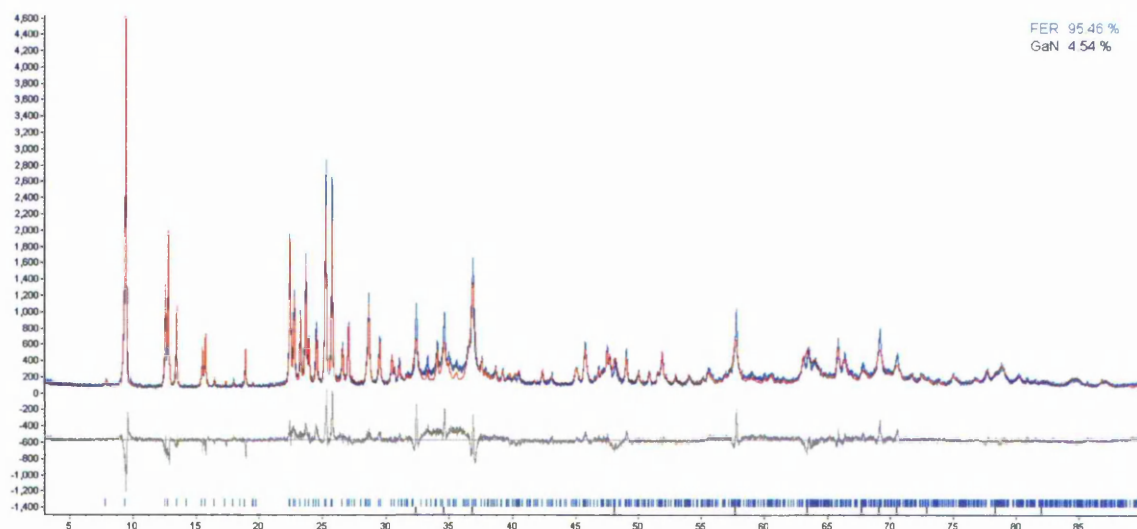


Figure 71: Rietveld fit for molten salt-treated FER with GaN.

The relatively small calculated GaN content from the molten salt-treated sample shows that the majority of GaN formed is very much smaller than the XRD technique is able to detect. It is also clear that the zeolite structure is still intact.

The absence of significant diffraction from GaN suggests there may not be any GaN phase present at all, yet the UV-Vis data suggests a band structure similar to that of GaN is present.

The lattice parameters from FER (Si:Al = 20) samples with GaN using both the solution and molten salt impregnation methods derived from Rietveld analysis of the XRD data are shown graphically in Figure 72 to Figure 74.

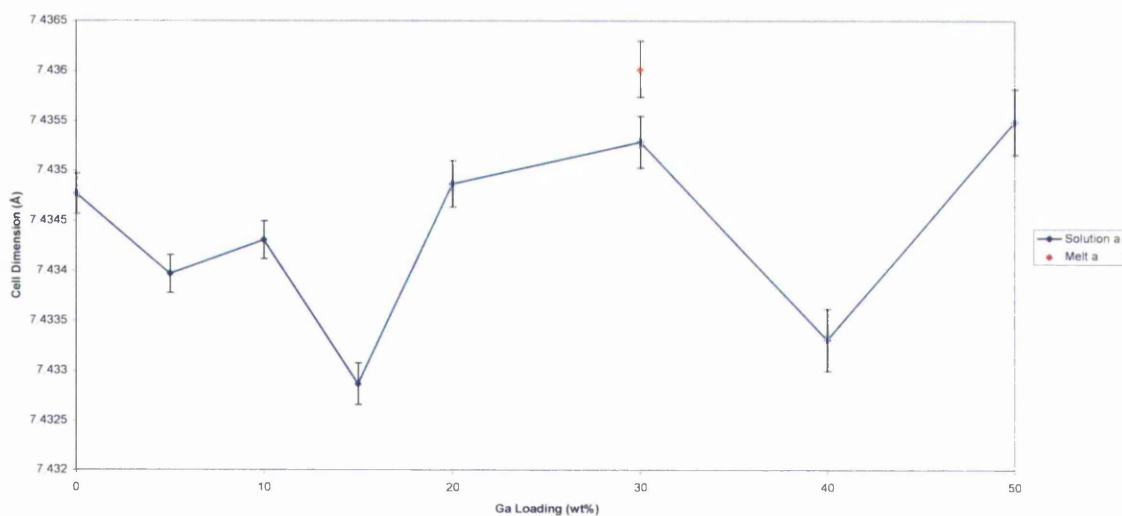


Figure 72: Unit cell parameter a for FER with GaN.

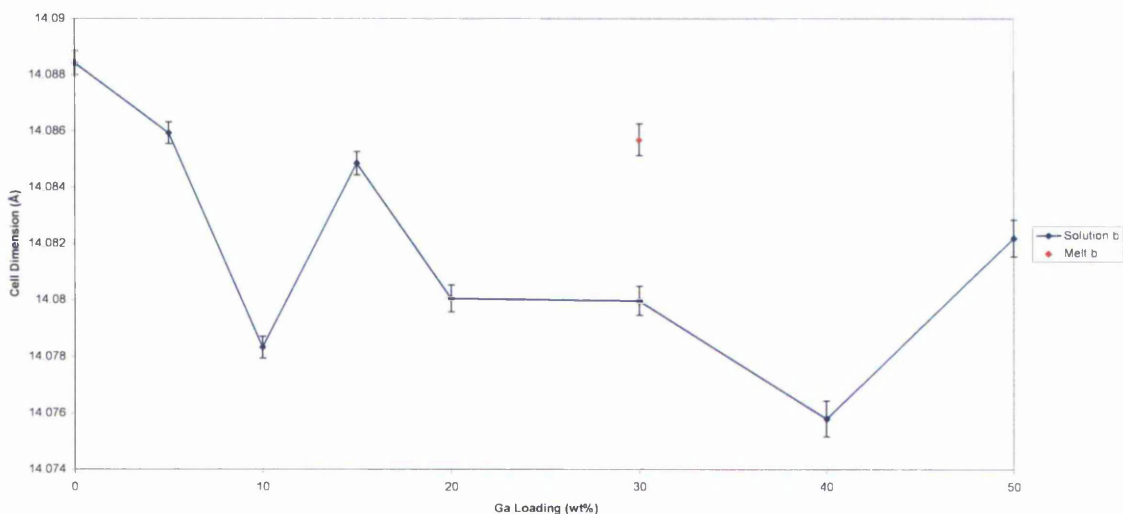


Figure 73: Unit cell parameter *b* for FER with GaN.

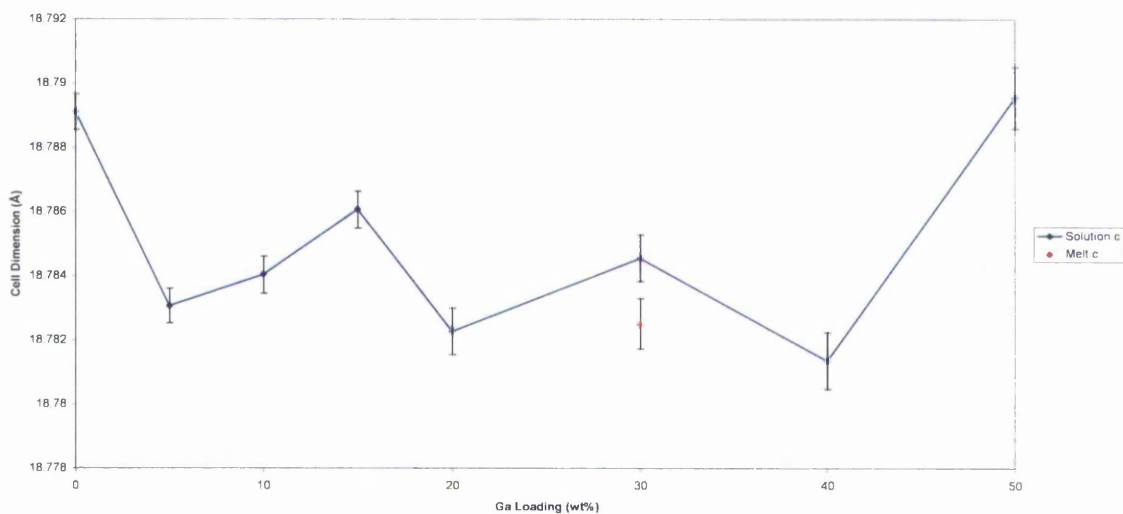


Figure 74: Unit cell parameter *c* for FER with GaN.

These data show that the unit parameters of FER are variable across the Ga loading range. In the *a* and *b* directions the unit cell parameter for the molten salt-treated sample is larger than that of the solution-treated samples, within experimental error. Otherwise, the unit cell values for the parent zeolite and those of the solution-treated samples are comparable to each other. In the *c* direction (perpendicular to the lengths of both the main and the secondary channels) the values for the solution-treated samples with a Ga loading of less than 50 wt% are

less than that of the parent zeolite, whereas the sample with 50 wt% loading of Ga has a value slightly larger than that of the parent zeolite. The value for the molten salt-treated sample lies among the values found for the samples treated with less than 50 wt% Ga solution.

Figure 75 shows the UV-Visible diffuse-reflectance curves obtained for all FER samples impregnated with GaN, the parent zeolite and bulk GaN.

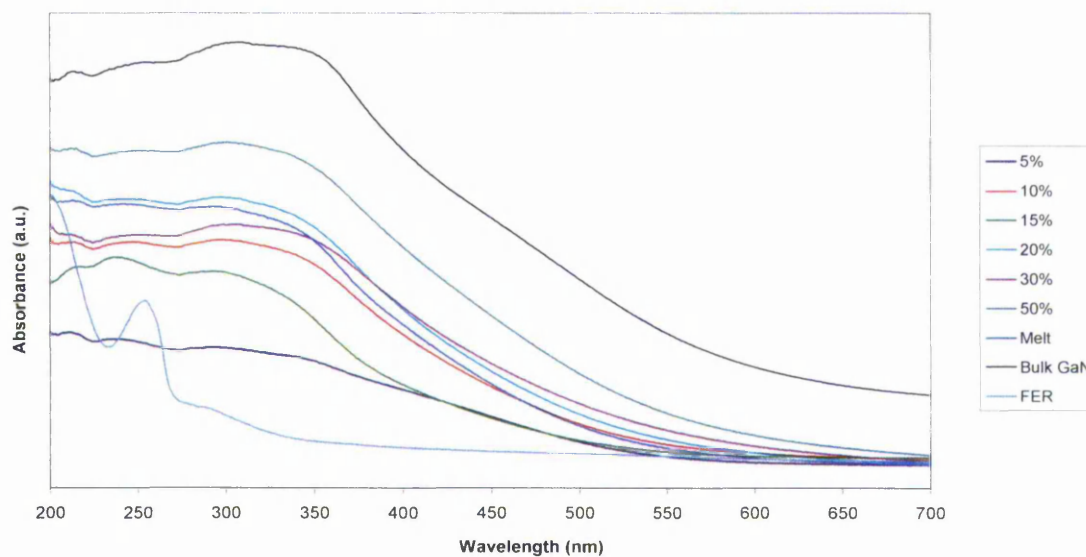


Figure 75: UV Vis data for FER samples with GaN.

By taking the 1st derivative of the UV-Vis diffuse reflectance data, the band gaps can be read at the curve maxima, giving the values shown in Table 4 and Figure 76.

Table 4: Band gap values for FER samples with GaN.

Impregnation Method	Band Gap (eV)
Molten Salt	3.49
5% Solution	3.51
10% Solution	3.44
15% Solution	3.56
20% Solution	3.41
30% Solution	3.37
50% Solution	3.4
Bulk GaN	3.4

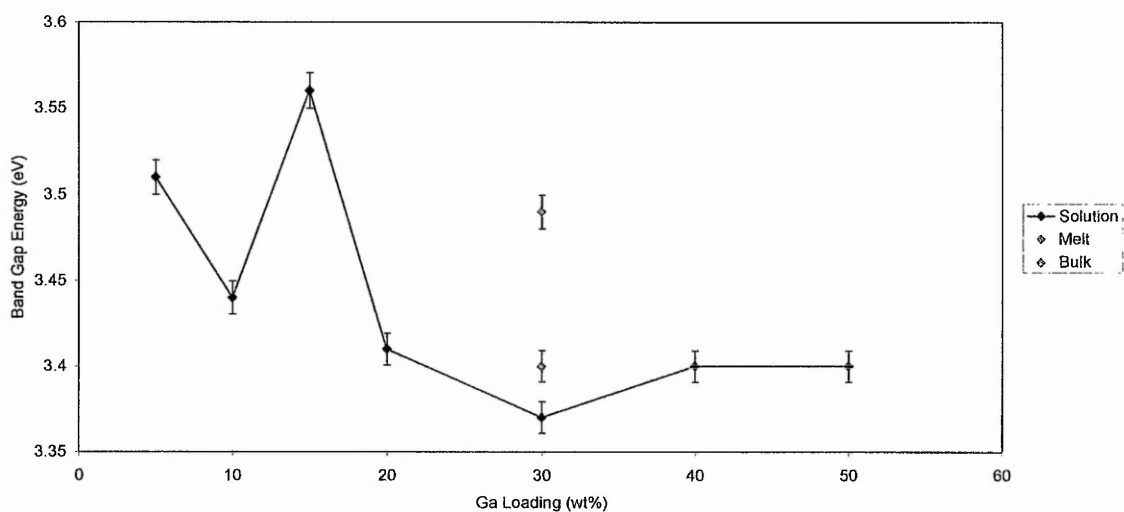


Figure 76: Band gap values for FER samples with GaN. The position of the Melt and Bulk GaN points in the centre of the x-axis are for illustration only and does not imply Ga loadings of 30 wt% are present in these samples.

It is clear that within experimental error the band gap of GaN is increased on solution impregnation into FER at Ga loadings of <20wt%, in comparison to bulk

GaN, and that by adopting the molten salt approach the band gap value is comparable to that obtained with a 5 wt% solution impregnation.

5.2. Discussion and Conclusions

The consistent differences in unit cell parameters in all cases between zeolites treated by the molten salt and salt solution impregnation methods implies that the zeolite framework is enlarged upon treatment with the molten salt, allowing pore filling to occur with greater ease. This may be due to the differences in the mechanism of impregnation between the two methods. The salt solution impregnation method uses a diffusion of disperse ionic species in the aqueous medium to deposit the metal species within the framework, whereas the molten salt method makes use of a combination of capillary forces and inter-zeolite pore charge separation in which the exposed, charged surfaces of the cations located on opposing sides of the inner walls of the pores draw polar species into the pore structure. Therefore, upon nitridation the crystallisation of the GaN phase may have a swelling effect within the pore structure, which may be a negligible effect when the metal salt phase is present as highly disperse nanoclusters, but when there is a dense metal salt phase, this may be more pronounced, creating pressure on the inside walls of the pores.

Upon nitridation an interesting difference between the two groups of materials is noticed, especially when viewed under HRTEM. The emergence of GaN nanowires from molten salt-treated ZSM-5 crystallites further highlights the differences between the two impregnation methods. By introducing a dense metal salt phase to the zeolite pores, the formation of discrete and disperse nitride crystals within the pore structure is difficult. Instead, it seems the metal salt particles agglomerate and crystallise within the zeolite crystal and eventually break through the crystal, forming extra-zeolite nanowires. This phenomenon was not

present in the sample treated with the 15 wt% solution, suggesting a high dispersion of metal particles within the zeolite prevents this from happening, and thus contains the nitride crystallites within the pore structure.

In terms of optoelectronic properties, it is clear that by adopting the molten salt treatment method a GaN band gap that is higher than that of the bulk value is achieved in all zeolite types tested. This value is also generally higher than those obtained for materials treated by the salt solution method. This is true for the FAU-impregnated GaN, but not for both ZSM-5 and FER, the two zeolites with 1-D channels. In ZSM-5 and FER the band gap value obtained for the molten salt treated materials is comparable to the values achieved with lower metal loadings using the salt solution method. This could be an initial indication of the dependence of the band gap value on the geometry of the templating framework (i.e. channels vs. cages or QWs vs. QDs).

6. Gallium Oxide

Gallium oxide can occupy 5 different crystal habits; namely α , β , γ , δ and ϵ . The structure of interest in this project is β - Ga_2O_3 , which is shown in Figure 77. β - Ga_2O_3 is of interest because it is synthesised at atmospheric pressure in air, is stable at ambient conditions and is a wide band-gap semiconductor with a band-gap of 4.23 – 4.75 eV at 300 K. ^[93, 94]

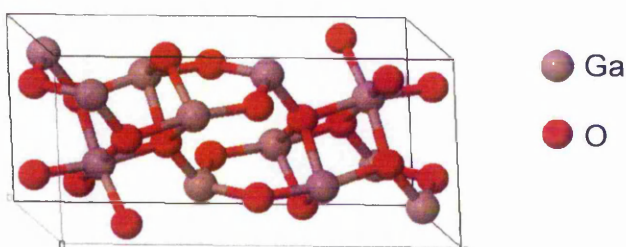


Figure 77: The crystal structure of β - Ga_2O_3 . ^[95]

β - Ga_2O_3 generally has the following crystallographic parameters:

Space Group: C2/M

$a = 12.214 \text{ \AA}$ $b = 3.0371 \text{ \AA}$ $c = 5.7981 \text{ \AA}$

$\alpha = 90^\circ$ $\beta = 103.83^\circ$ $\gamma = 90^\circ$

β - Ga_2O_3 can be synthesised by high temperature ($>800^\circ\text{C}$) oxidation of Ga metal ^[96] and Ga compounds, such as GaN ^[97] and $\text{Ga}(\text{NO}_3)_3$ ^[98]. Gallium oxide is a white crystalline powder that is stable in ambient conditions, insoluble in water, soluble in acids and has a melting point of 1725°C .

Many groups have investigated the properties of Ga₂O₃ nanostructures; such as thin films^[93, 94] and rods.^[98] There is a lot of work devoted to metal oxide/zeolite composites, but this is mainly limited to catalytic applications.^[99-104] In this work, Ga₂O₃ was occluded within the zeolites ZSM-5, ferrierite and faujasite using both the molten salt and salt solution impregnation methods using Ga(NO₃)₃.

6.1. Results

6.1.1. ZSM-5

Diffraction profiles were refined using Topas Academic V4.1 against the ZSM-5 structure reported by Li, et al.^[89] and Ga_2O_3 structure reported by Ahman, et al.^[95]. The XRD and Rietveld profiles from solution-treated samples are shown in Figure 78 to Figure 84.

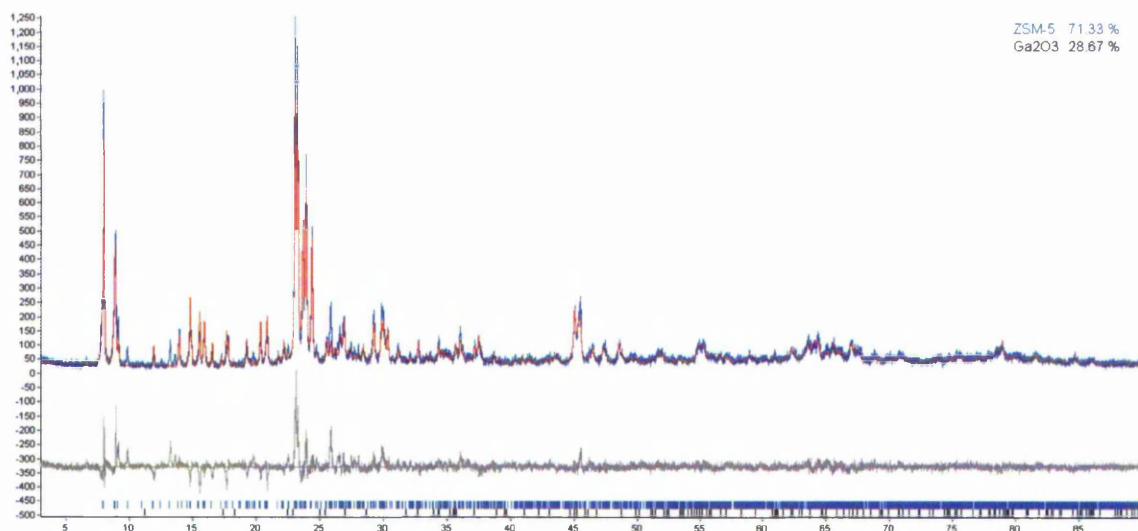


Figure 78: Rietveld fit for solution-treated ZSM-5 with 5wt% Ga as Ga_2O_3 .

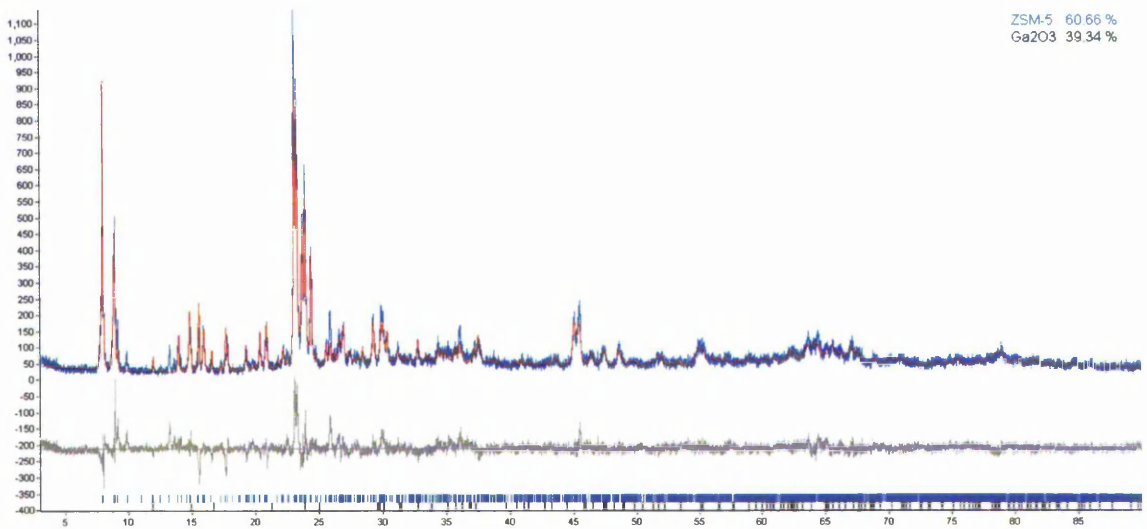


Figure 79: Rietveld fit for solution-treated ZSM-5 with 10wt% Ga as Ga₂O₃.

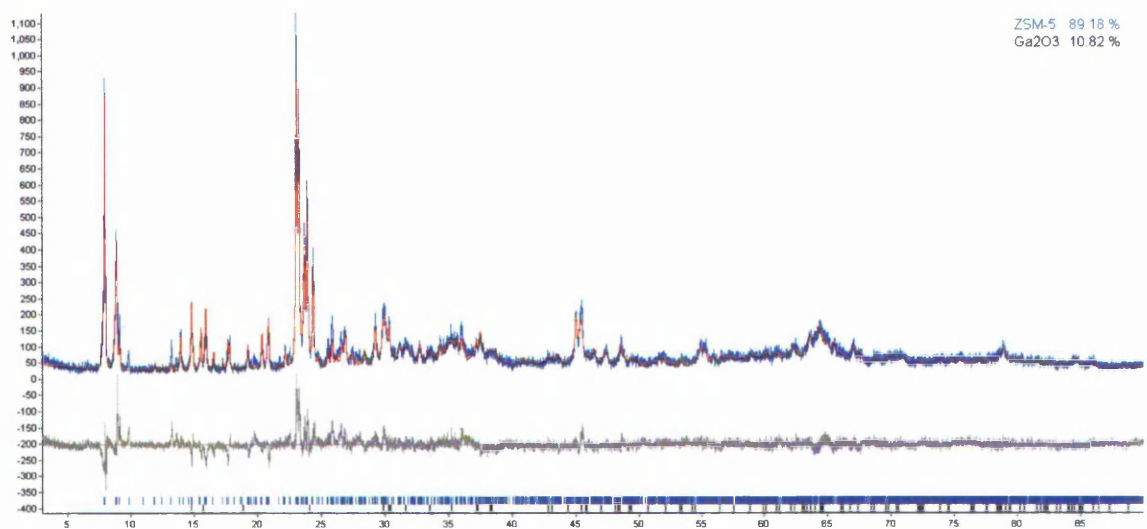


Figure 80: Rietveld fit for solution-treated ZSM-5 with 15wt% Ga as Ga₂O₃.

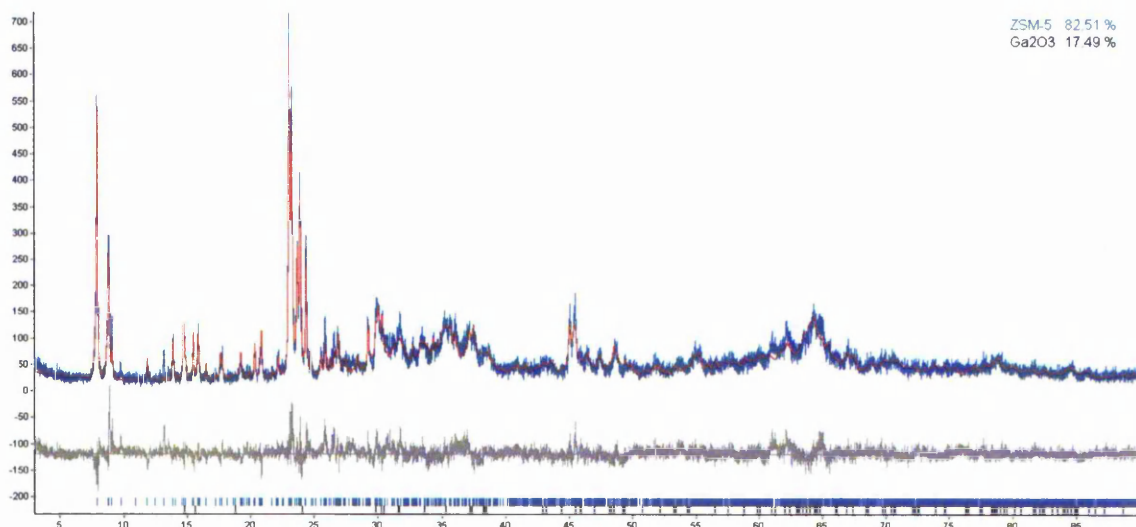


Figure 81: Rietveld fit for solution-treated ZSM-5 with 20wt% Ga as Ga₂O₃.

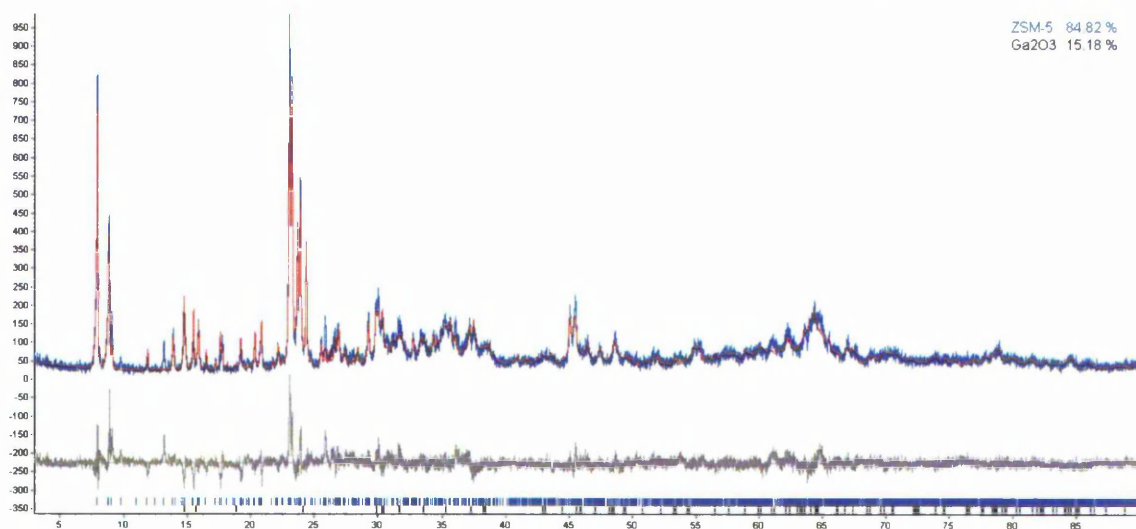


Figure 82: Rietveld fit for solution-treated ZSM-5 with 30wt% Ga as Ga₂O₃.

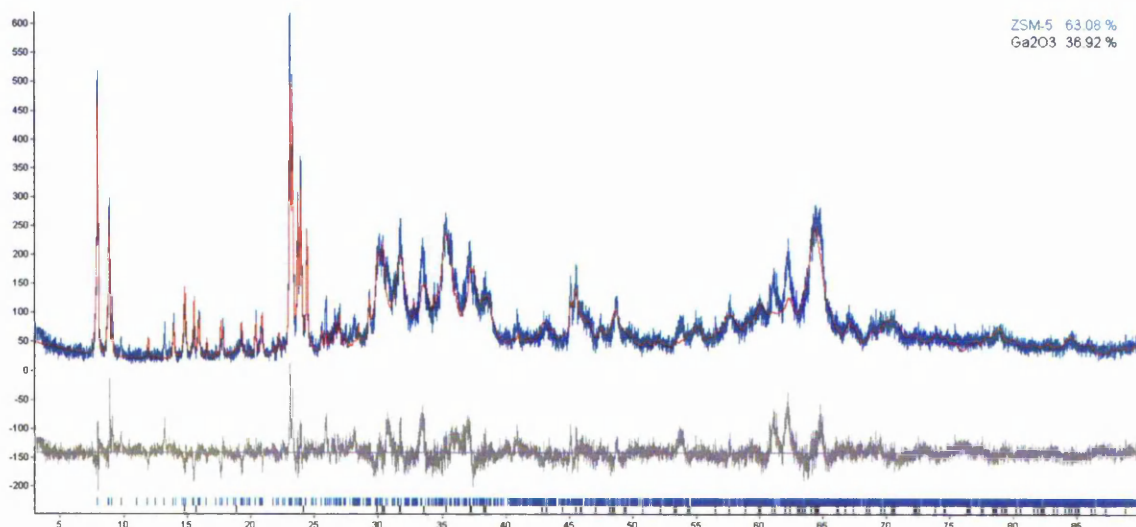


Figure 83: Rietveld fit for solution-treated ZSM-5 with 40wt% Ga as Ga_2O_3 .

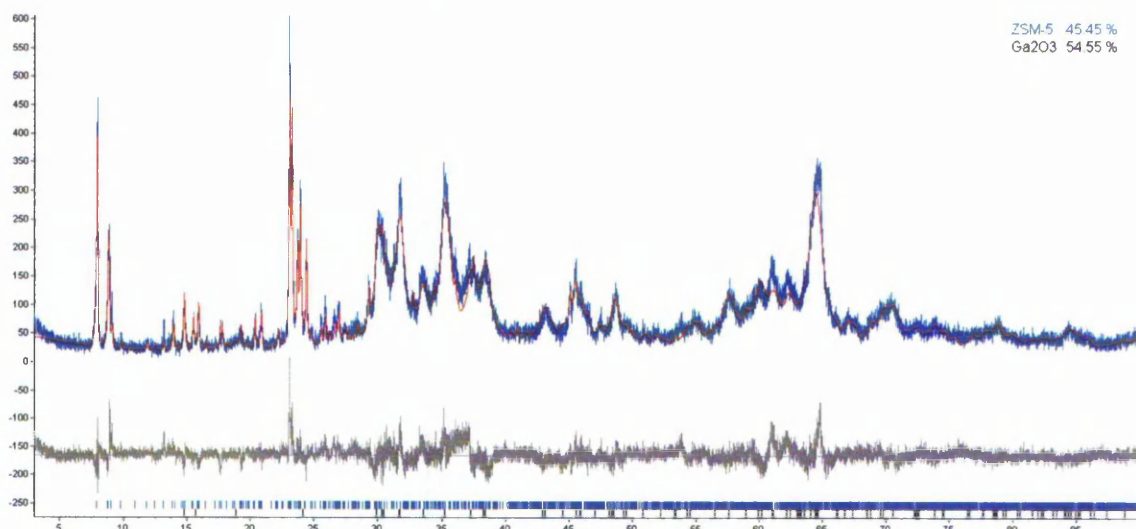


Figure 84: Rietveld fit for solution-treated ZSM-5 with 50wt% Ga as Ga_2O_3 .

The Rietveld profiles shown in Figure 78 to Figure 84 show that the process of Ga_2O_3 inclusion has little effect on the crystallinity of the host zeolite. The peaks related to Ga_2O_3 become more prevalent with increasing Ga content, which is to be expected. These peaks become significantly sharper between Ga loadings of 30 - 40wt%, at which the calculated Ga_2O_3 content from Rietveld refinement of measurable Ga_2O_3 diffraction increases from 15.18 to 36.92%. This coincides with

an approximated maximum main pore-filling Ga loading of 36.27 wt% using the following calculations assuming 1 pore per unit cell:

- Pore dimensions: 0.53 x 0.56 x 1.974 nm
- Ga₂O₃ unit cell dimensions (6Ga₂O₃): 0.3037 x 0.5798 x 1.2214 nm
- Approx. Ga atoms per channel: 30
- Total Ga mass: 2091.69 a.m.u.
- Zeolite Unit Cell Mass: 5766.76 a.m.u.
- (Ga Mass/Zeolite Mass) x 100: 36.27 wt%

Therefore the data suggests that at Ga loadings of 30 wt% and less the Ga₂O₃ present, as confirmed by XRD data, is present as small crystallites occupying the main pores of the zeolite structure and that at loadings above 30 wt% extra-zeolite phases of Ga₂O₃ exist. The relatively large calculated values of Ga₂O₃ content, given the lack of visible diffraction from the Ga₂O₃ phase at low loadings, may be related to the inherent inaccuracies discussed in 4.1.7, in particular the overlap of host and guest diffraction lines.

The Rietveld fit shown in Figure 85 was taken from the molten salt-treated sample.

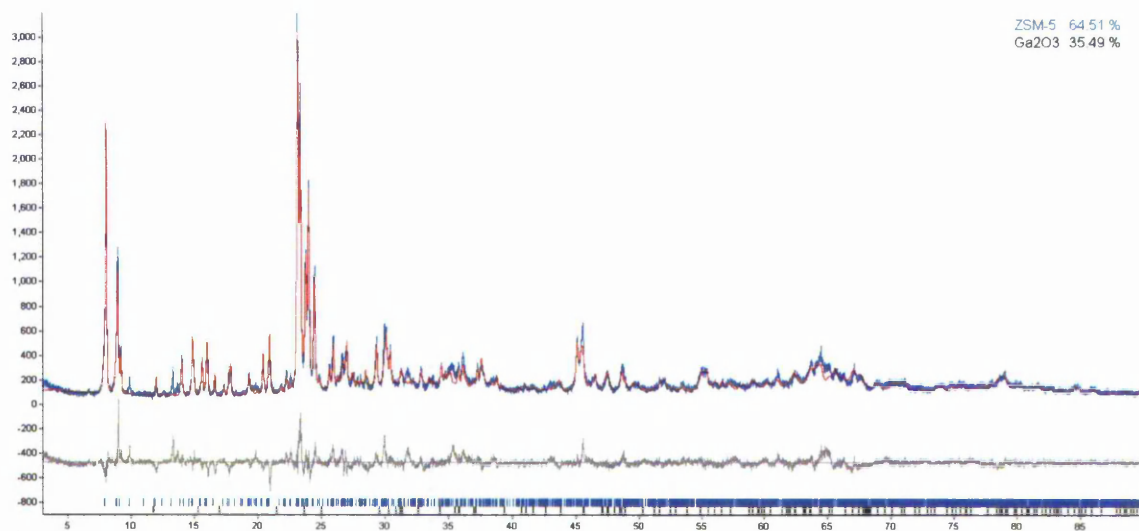


Figure 85: Rietveld fit for molten salt-treated ZSM-5 with Ga_2O_3 .

It is clear from Figure 85 that the zeolite structure is still intact upon molten salt impregnation and subsequent calcination. The absence of significant, discernible diffraction peaks from Ga_2O_3 suggests that any Ga_2O_3 phase is present as small crystallites.

The lattice parameters from ZSM-5 (Si:Al = 80) samples with Ga_2O_3 using both the solution and molten salt impregnation methods derived from Rietveld analysis of the XRD data are shown graphically in Figure 86 to Figure 88.

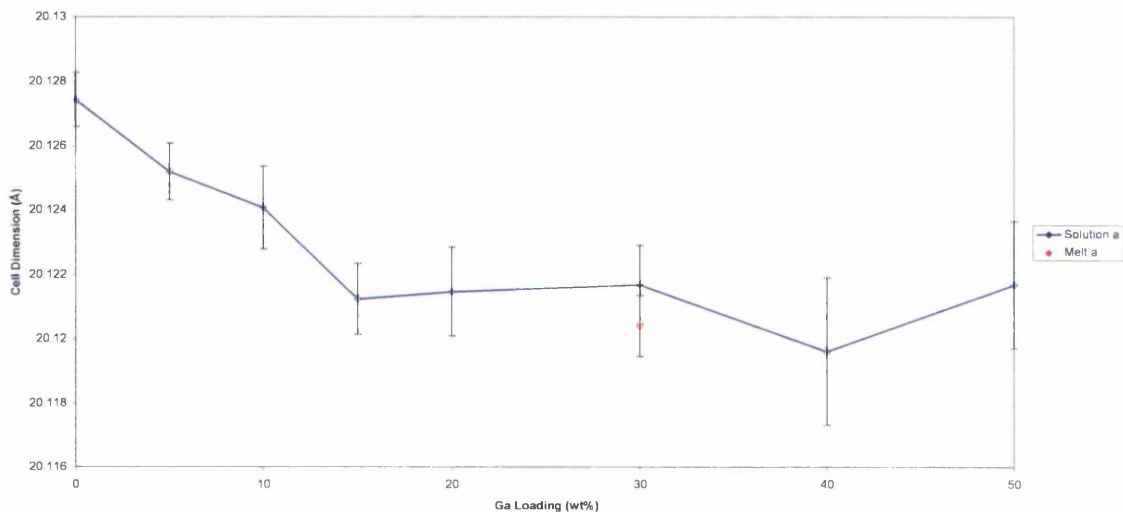


Figure 86: Unit cell parameter a for ZSM-5 with Ga_2O_3 .

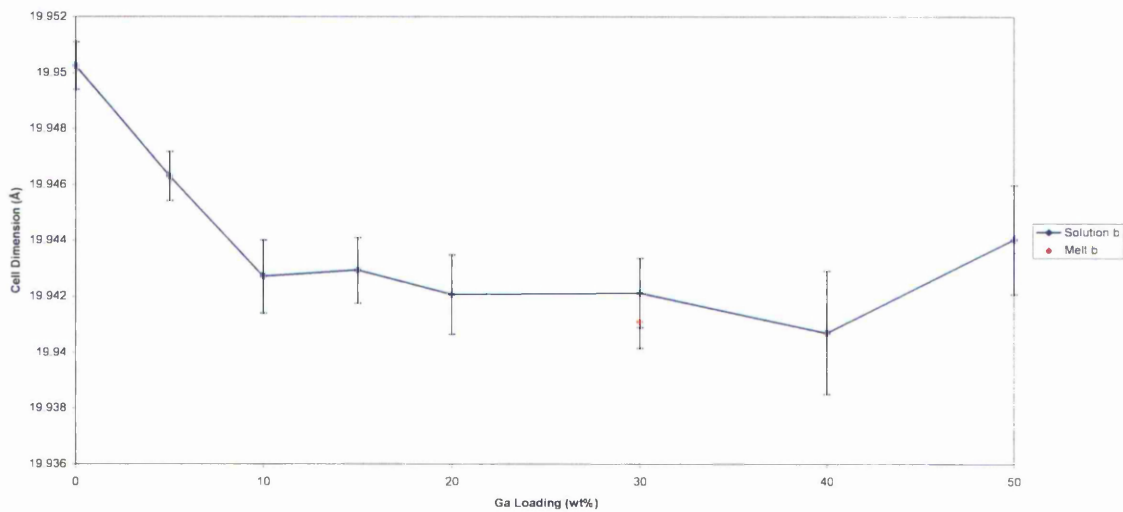


Figure 87: Unit cell parameter b for ZSM-5 with Ga_2O_3 .

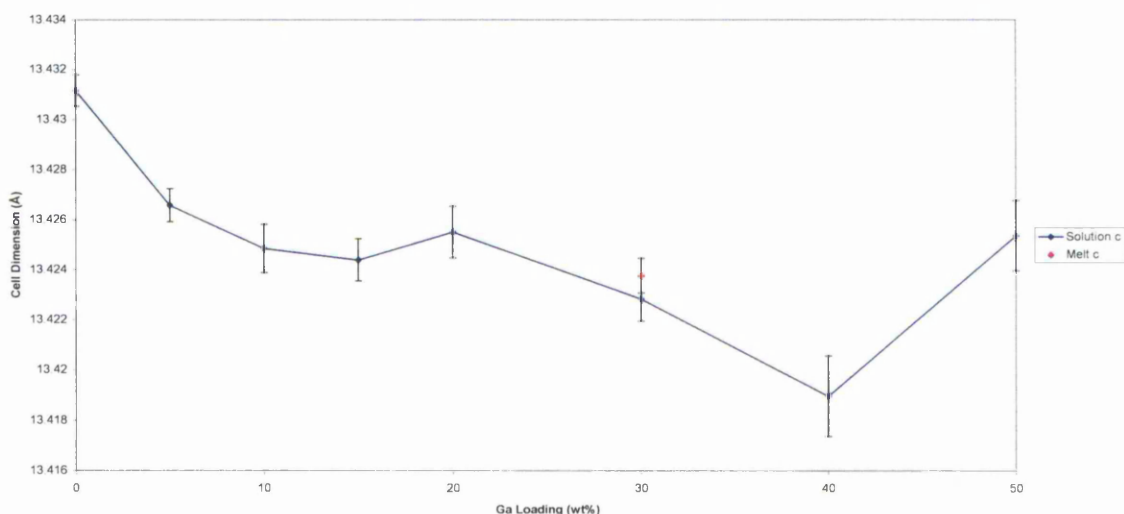


Figure 88: Unit cell parameter c for ZSM-5 with Ga_2O_3 .

These data show that the unit cell values in all three directions is reduced with respect to the parent zeolite upon introduction of the guest phase using both impregnation methods. They also show that there is no significant difference between the values found for the samples treated with the salt solution and the molten salt impregnation methods as the values lie within the ranges and error found for solution treated samples.

As Figure 86 to Figure 88 show; the unit cell dimensions of ZSM-5 decrease significantly upon inclusion of Ga_2O_3 and remain similar across the solution impregnated range of 5 – 50 wt%. What is also clear is that the sample impregnated by the molten salt process has unit cell dimensions comparable to that of the solution-treated samples. Also, in all cases the unit cell parameters are significantly smaller than that of the parent zeolite.

Figure 89 shows the UV-Visible diffuse-reflectance curves obtained for all ZSM-5 samples impregnated with Ga_2O_3 , the parent zeolite and bulk Ga_2O_3 . The solution treated samples with Ga loadings of 5wt% and >10wt% have very similar profiles to that of bulk Ga_2O_3 , with varied band gap energies. The sample with 10wt% Ga has a very different absorption profile. This profile has a peak at approximately 240nm, representing a band gap energy of 5.17eV (± 0.021556) and a second peak at approximately 300nm, which represents a band gap energy of 4.13eV (± 0.013756). This may be an example of band gap shift due to zeolite occlusion. The increased absorbance with respect to the other samples may also be a sign of zeolite occlusion leading to narrower linewidths, thus more efficient absorption at band gap energies.

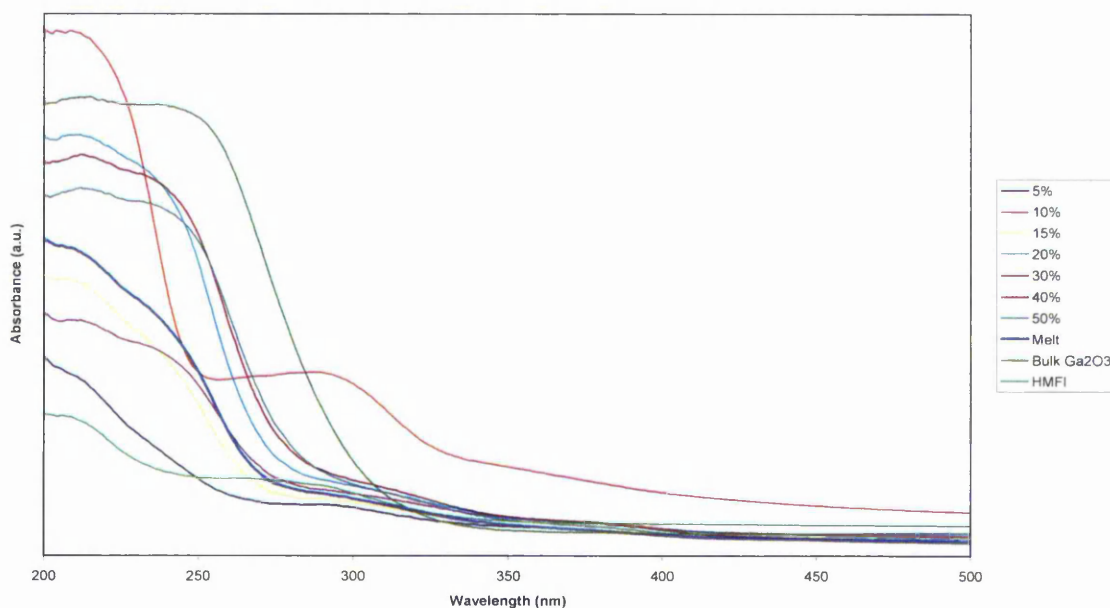


Figure 89: UV Vis data for ZSM-5 samples with Ga_2O_3 .

By taking the 1st derivative of the data, the band gaps can be read at the curve maxima, giving the values shown in Table 5 and Figure 90.

Table 5: Band gap values for ZSM-5 samples with Ga₂O₃.

Impregnation Method	Band Gap (eV)
Molten Salt	4.86
5% Solution	5.3
10% Solution	5.27
15% Solution	4.9
20% Solution	4.9
30% Solution	4.85
50% Solution	4.8
Bulk Ga ₂ O ₃	4.75

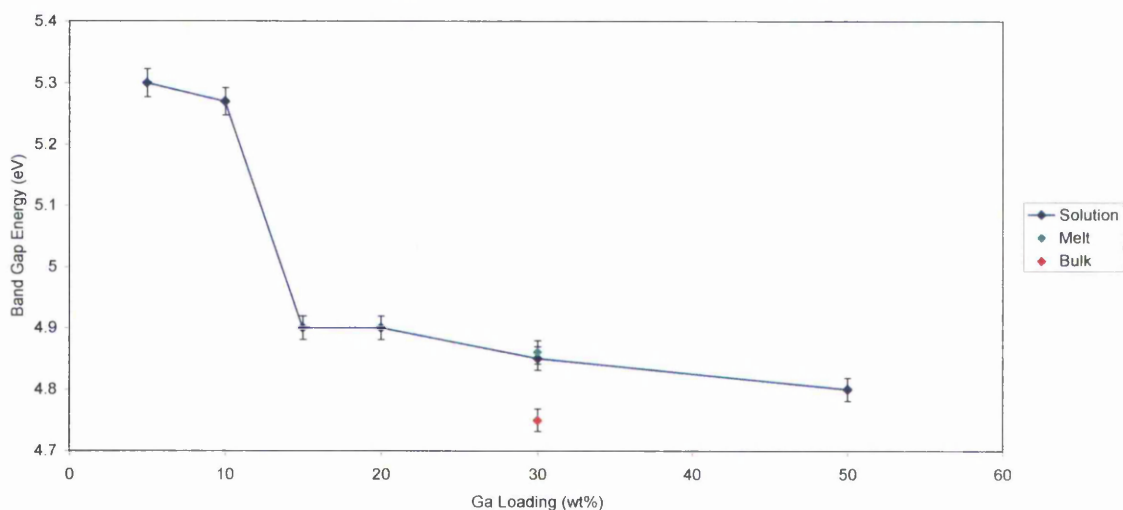


Figure 90: Band gap values for ZSM-5 samples with Ga₂O₃. The position of the Melt and Bulk Ga₂O₃ points in the centre of the x-axis are for illustration only and does not imply Ga loadings of 30 wt% are present in these samples..

It is clear that the band gap of Ga_2O_3 is increased on solution impregnation into ZSM-5 in comparison to bulk Ga_2O_3 , the extent of which is dramatic at a loading ≤ 10 wt%, but less so and with slight variation across the loading range of 10 – 50 wt% Ga. The band gap generally decreases with increasing loading. By adopting the molten salt approach the band gap is increased with respect to the bulk value, but is comparable to the band gaps obtained from the samples treated with the solution method. The errors related to the data are insignificant when compared to the differences in the values.

6.1.2. Faujasite

Diffraction profiles were refined using Topas Academic V4.1 against the faujasite structure reported by Parise, et al. [91] and Ga₂O₃ structure reported by Ahman et al. [95] The XRD and Rietveld profiles from solution-treated samples are shown in Figure 91 to Figure 97.

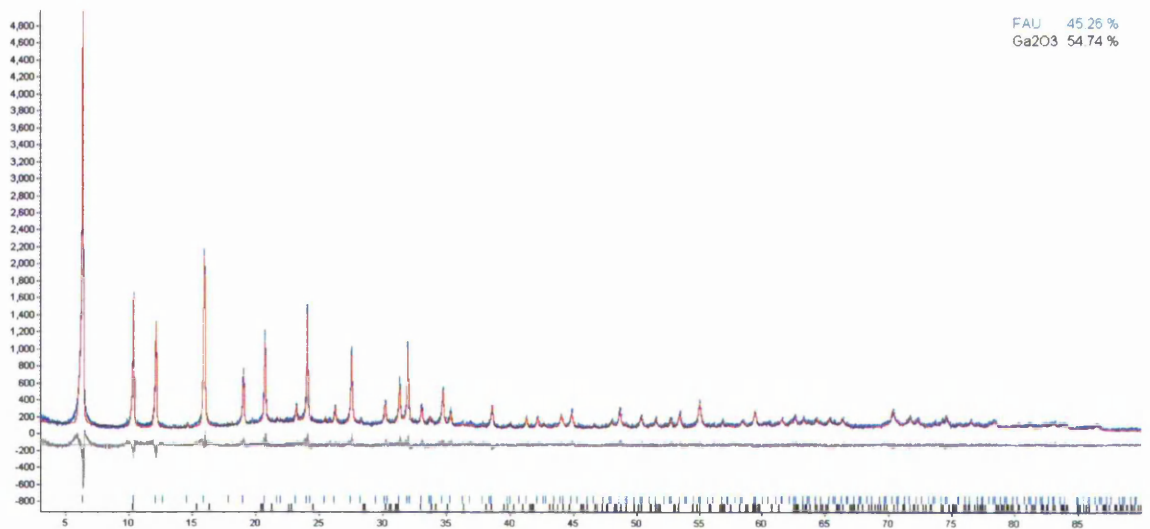


Figure 91: Rietveld fit for solution-treated FAU with 5wt% Ga as Ga₂O₃.

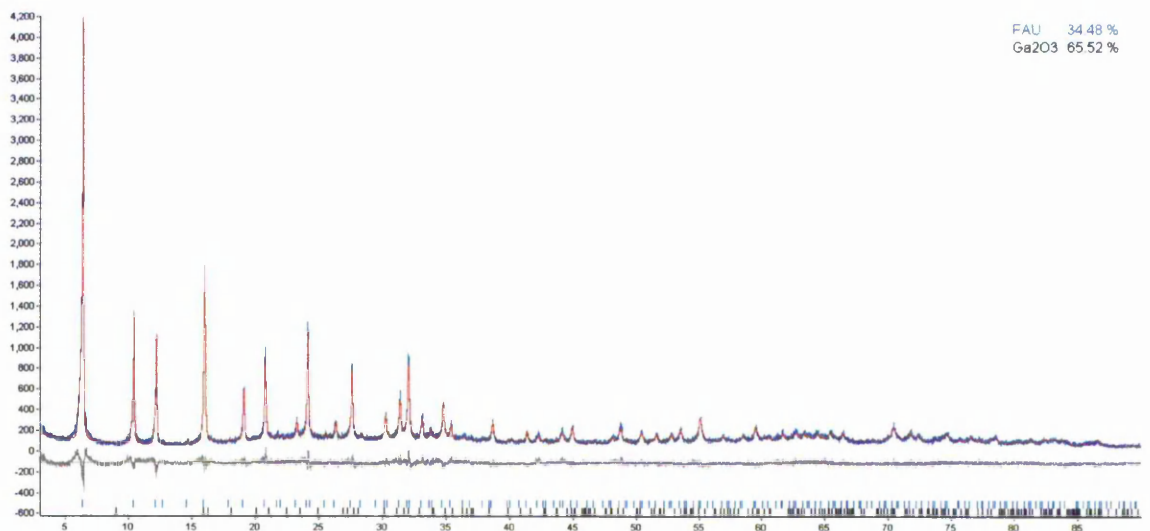


Figure 92: Rietveld fit for solution-treated FAU with 10wt% Ga as Ga₂O₃.

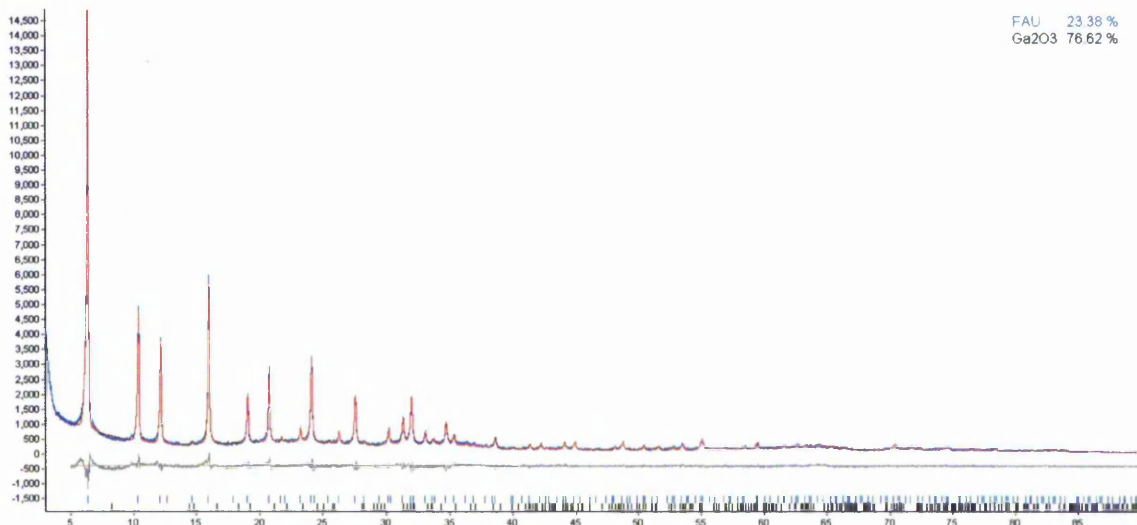


Figure 93: Rietveld fit for solution-treated FAU with 15wt% Ga as Ga₂O₃.

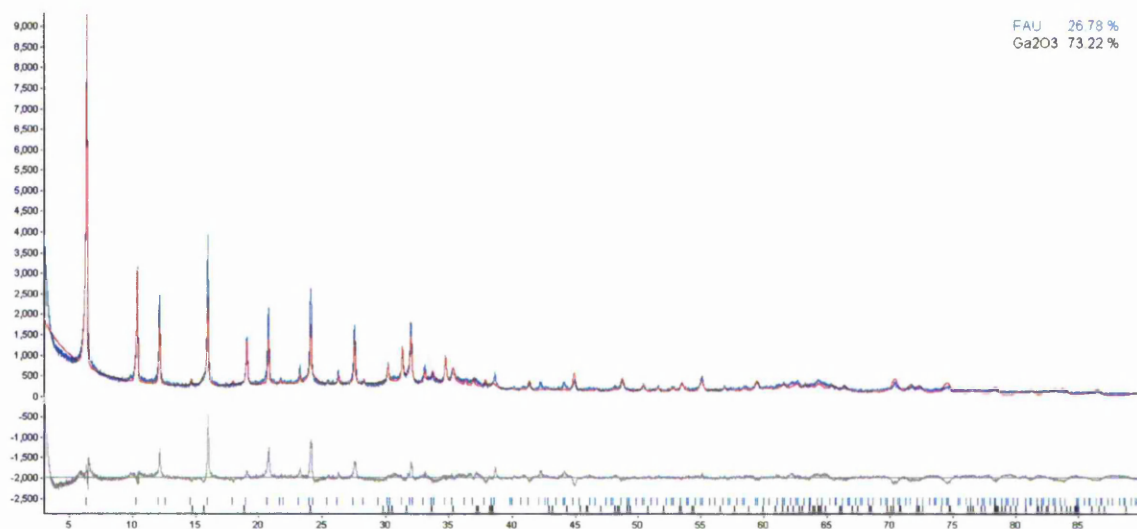


Figure 94: Rietveld fit for solution-treated FAU with 20wt% Ga as Ga₂O₃.

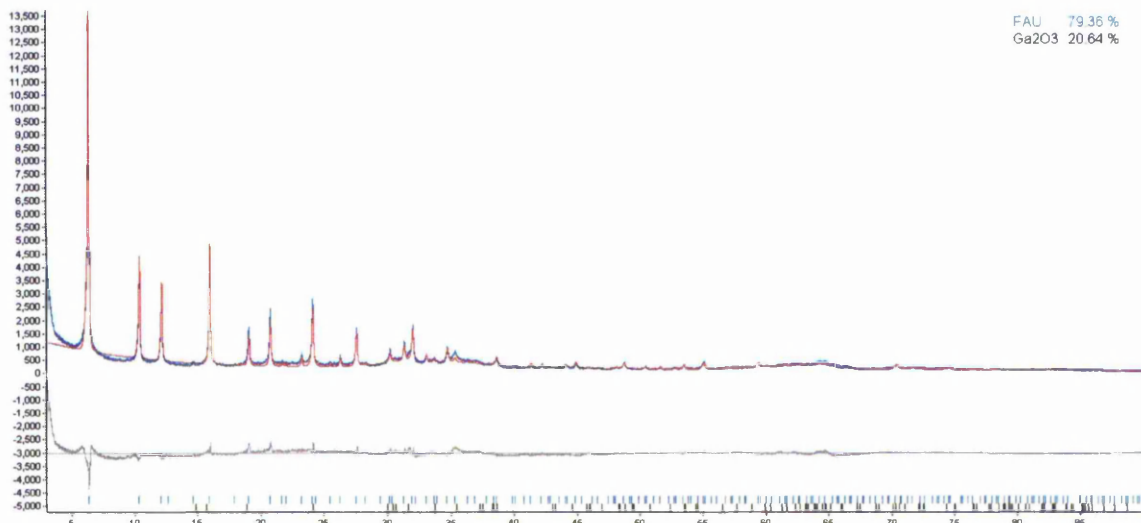


Figure 95: Rietveld fit for solution-treated FAU with 30wt% Ga as Ga_2O_3 .

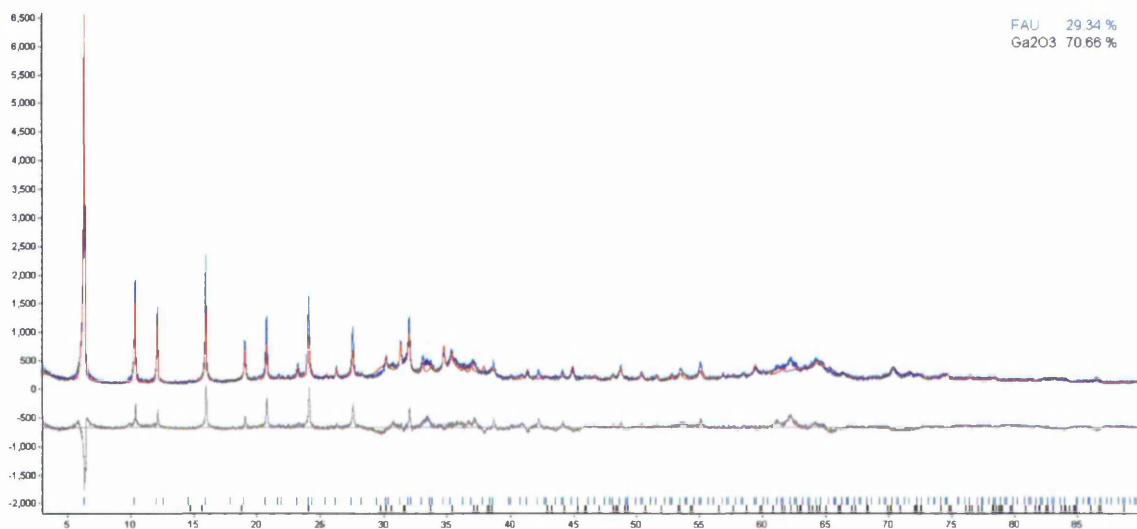


Figure 96: Rietveld fit for solution-treated FAU with 40wt% Ga as Ga_2O_3 .

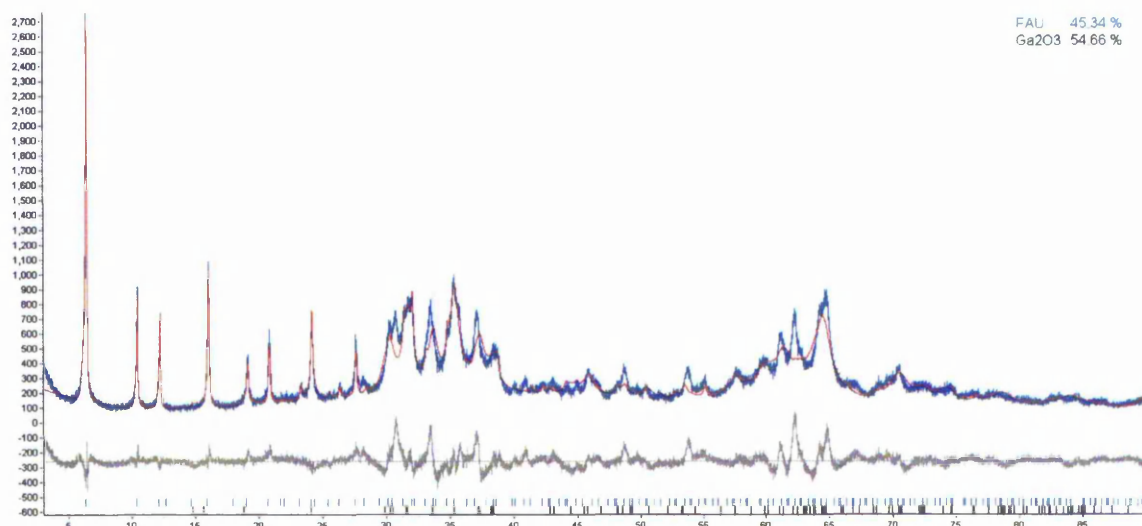


Figure 97: Rietveld fit for solution-treated FAU with 50wt% Ga as Ga_2O_3 .

The Rietveld profiles shown in Figure 91 to Figure 97 show that the process of Ga_2O_3 inclusion has little effect on the crystallinity of the host zeolite. The peaks related to Ga_2O_3 become more prevalent with increasing Ga content, which is to be expected. These peaks become significantly larger between Ga loadings of 40 - 50wt%, at which the calculated Ga_2O_3 content from Rietveld refinement of measurable Ga_2O_3 diffraction decreases from 70.66 and then to 54.66%, yet it is clear from the diffraction profile that the Ga_2O_3 content is increased yet has significant amorphous character, which may lead to inaccurate refinement. This coincides with an approximated maximum main cage-filling Ga loading of 48.36 wt% using the following calculations assuming 1 cage per unit cell:

- Cage dimensions: 1.304 x 1.304 x 1.304 nm
- Ga_2O_3 unit cell dimensions ($6\text{Ga}_2\text{O}_3$): 0.3037 x 0.5798 x 1.2214 nm
- Approx. Ga atoms per cage: 80
- Total Ga mass: 5577.84 a.m.u.
- Zeolite Unit Cell Mass: 5766.76 a.m.u.
- (Ga Mass/Zeolite Mass) x 100: 48.36 wt%

Therefore the data suggests that at Ga loadings of 40 wt% and less the Ga_2O_3 present, as confirmed by XRD data, is present as small crystallites occupying the main cages of the zeolite structure and that at loadings above 40 wt% extra-zeolite phases of Ga_2O_3 exist. The relatively large calculated values of Ga_2O_3 content, given the lack of visible diffraction from the Ga_2O_3 phase at low loadings, may be related to the inherent inaccuracies discussed in 4.1.7, in particular the overlap of host and guest diffraction lines.

The Rietveld fit shown in Figure 98 was taken from the molten salt-treated sample.

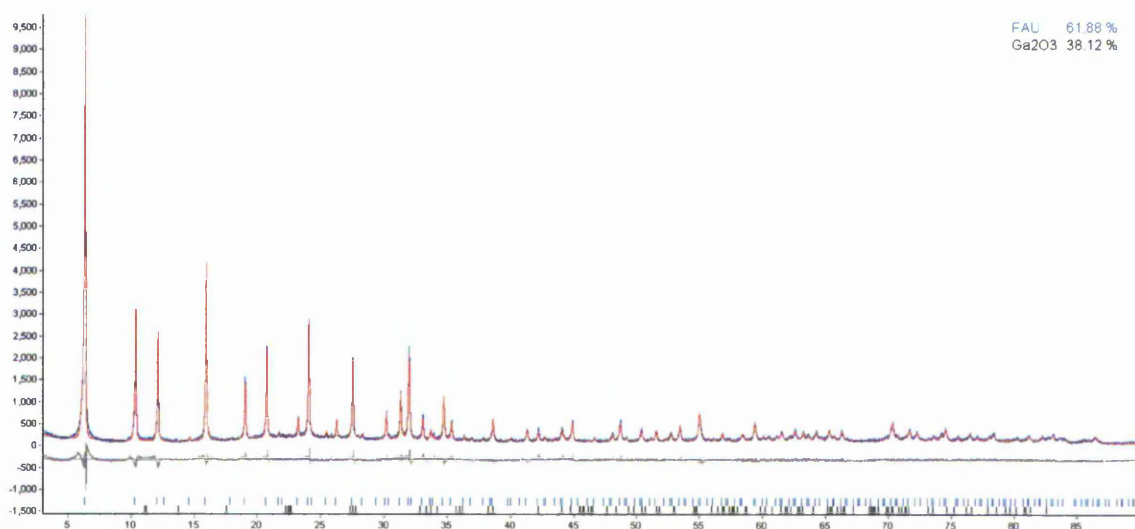


Figure 98: Rietveld fit for molten salt-treated FAU with Ga_2O_3 .

It is clear from Figure 98 that the zeolite structure is still intact upon molten salt impregnation and subsequent calcination. The absence of significant, discernible diffraction peaks from Ga_2O_3 suggests that any Ga_2O_3 phase is present as small crystallites.

The lattice parameters from FAU samples with Ga_2O_3 using both the solution and molten salt impregnation methods derived from Rietveld analysis of the XRD data are shown graphically in Figure 99.

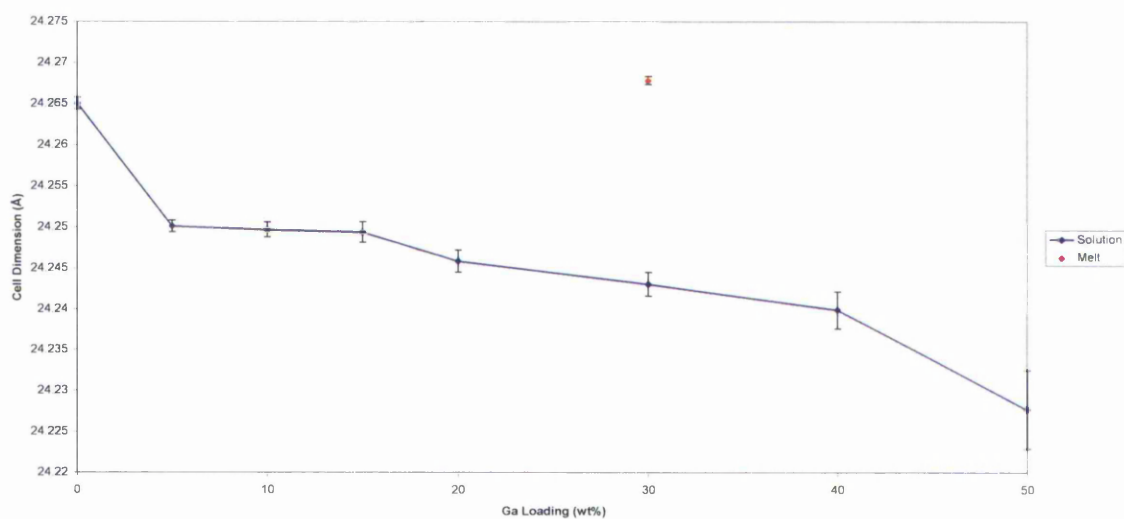


Figure 99: Unit cell parameter for FAU with Ga_2O_3 .

As Figure 99 shows there is a steady decrease in the unit cell parameter of FAU upon increasing loading of Ga when using the solution-based impregnation method, yet by using the molten salt method the unit cell parameter is not reduced and is, in fact, slightly increased with respect to the parent zeolite. The errors are insignificant in comparison to this rate of change.

Figure 100 shows the UV-Visible diffuse-reflectance curves from all FAU samples impregnated with Ga_2O_3 , the parent zeolite and bulk Ga_2O_3 . The curves of the solution treated samples with $>10\text{wt}\%$ Ga and that of bulk Ga_2O_3 have similar profiles, which suggests Ga_2O_3 is present in the solution treated samples. As the profiles for HFAU and the molten salt treated sample are similar, it is fair to assume no significant, measurable band formation has occurred. The solution treated sample with $5\text{wt}\%$ Ga shows an extra peak, however, centred around $\sim 320\text{nm}$, but which is very shallow and broad. This could be an indication of a significant shift in band gap energy and the successful occlusion of Ga_2O_3 within the pores of FAU. It may also mean the confines of the zeolite pore structure have induced significant pressure on the system to promote the crystallisation of another Ga_2O_3 polymorph with a different band gap energy. Given the very small quantities involved this would be very difficult to prove with conventional powder XRD.

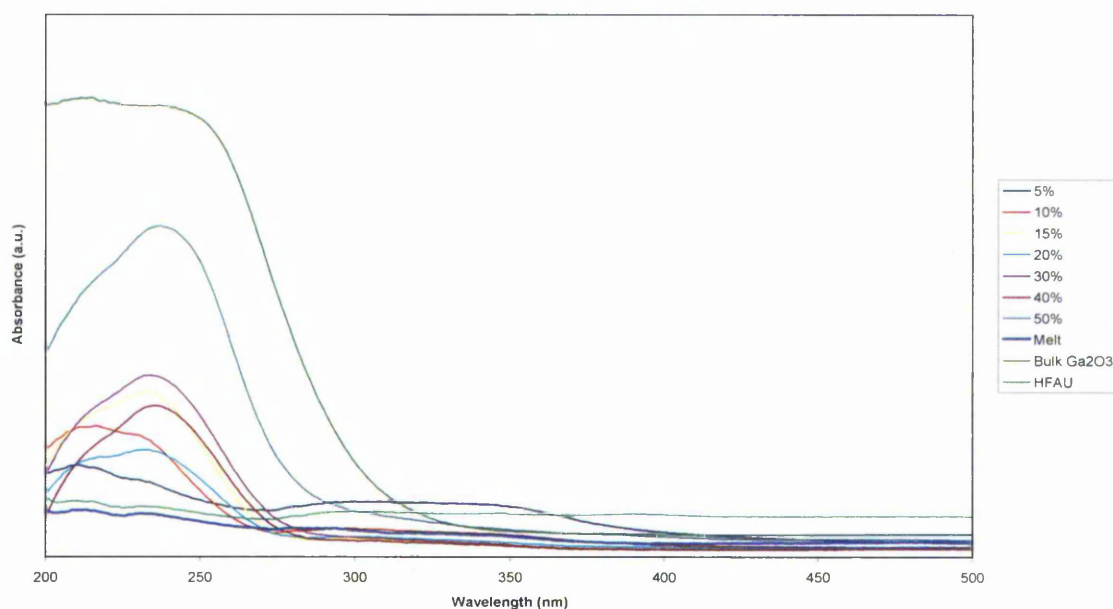


Figure 100: UV-Vis data for FAU samples with Ga_2O_3 .

By taking the 1st derivative of the data, the band gaps can be read at the curve maxima, giving the values shown in

Table 6 and Figure 101. Although the value for the 5wt% Ga loaded sample is quoted in the table, it is not shown in the graph as it may not be representative of a true α -Ga₂O₃ band structure and doing so allows the trend of increasing Ga loading to be observed.

Table 6: Band gap values for FAU samples with Ga₂O₃.

Impregnation Method	Band Gap (eV)
Molten Salt	-
5% Solution	(2.8)
10% Solution	5.08
15% Solution	4.9
20% Solution	4.88
30% Solution	4.83
50% Solution	4.83
Bulk Ga ₂ O ₃	4.75

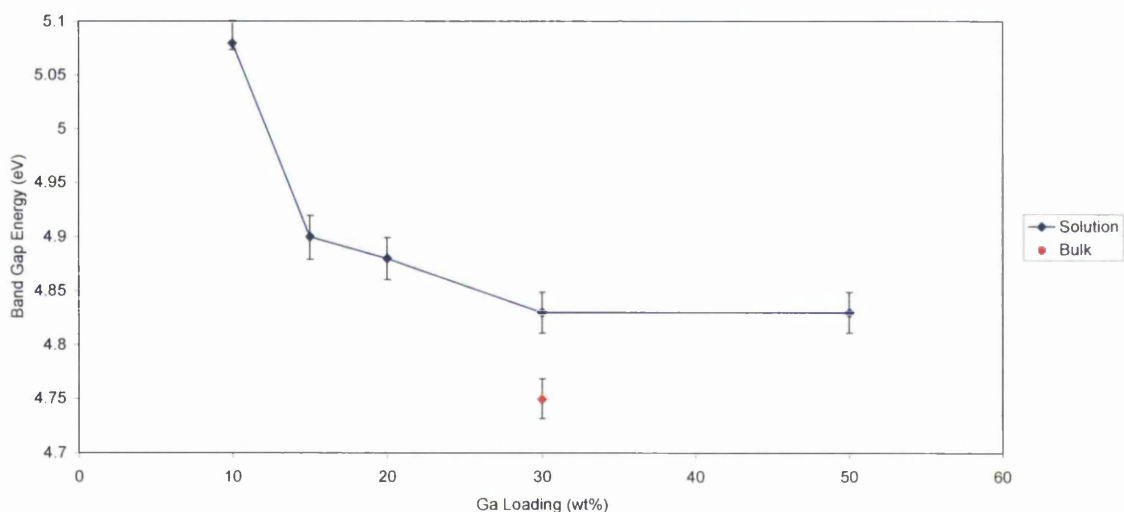


Figure 101: Band gap values for FAU samples with Ga₂O₃. The position of the Melt and Bulk Ga₂O₃ points in the centre of the x-axis are for illustration only and does not imply Ga loadings of 30 wt% are present in these samples.

It is clear that the band gap of Ga₂O₃ is increased on solution impregnation into FAU in comparison to bulk Ga₂O₃, the extent to which varies slightly across the loading range of 10 – 50 wt% Ga and generally decreases with increasing loading. The errors in the measurements are insignificant with respect to the rate of decrease in band gap energy.

6.1.3. Ferrierite

Diffraction profiles were refined using Topas Academic V4.1 against the ferrierite structure reported by Bull, et al^[92] and Ga₂O₃ structure reported by Ahman, et al.^[95] The XRD and Rietveld profiles from solution-treated samples are shown in Figure 102 to Figure 108.

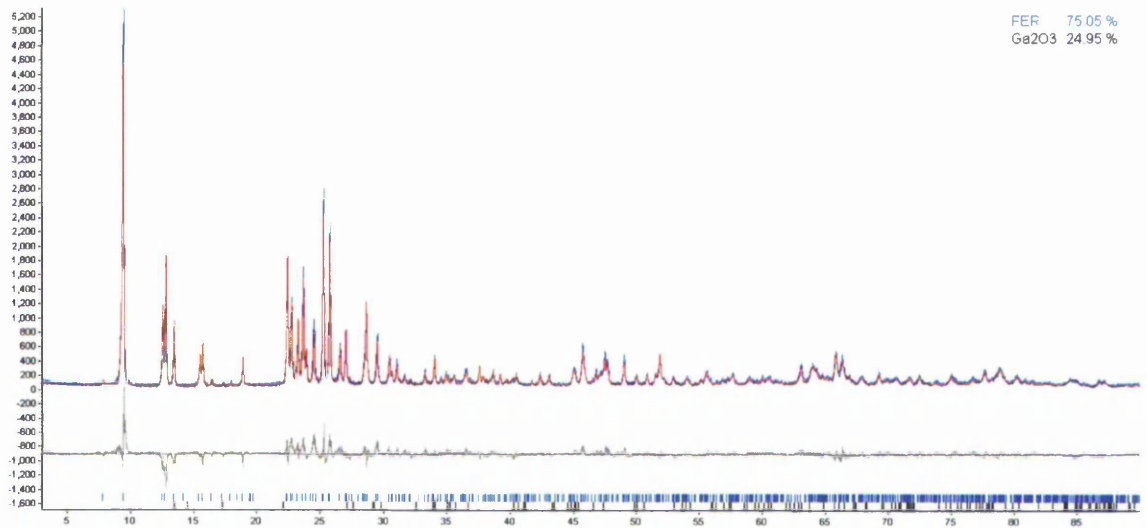


Figure 102: Rietveld fit for solution-treated FER with 5wt% Ga as Ga₂O₃.

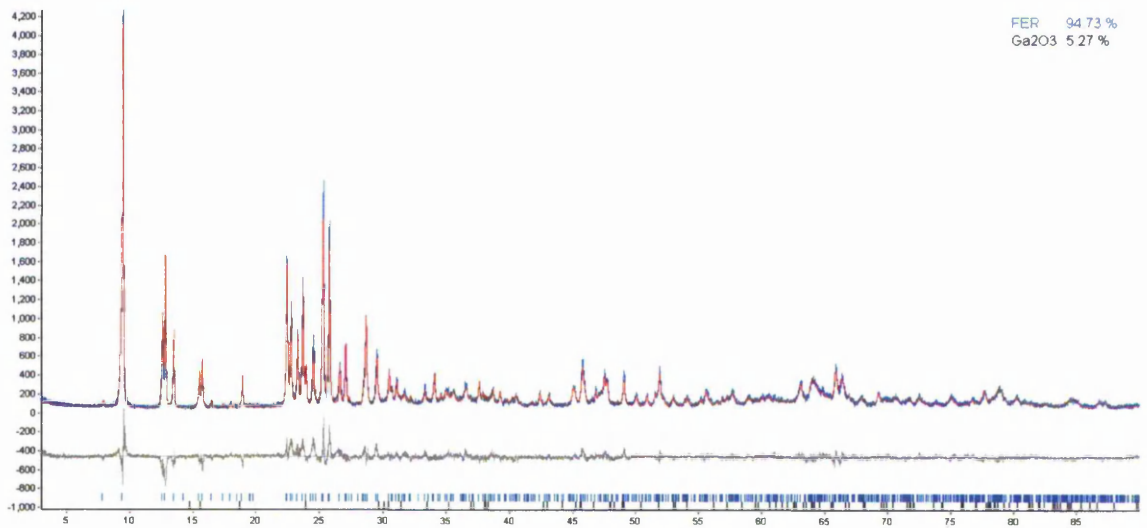


Figure 103: Rietveld fit for solution-treated FER with 10wt% Ga as Ga₂O₃.

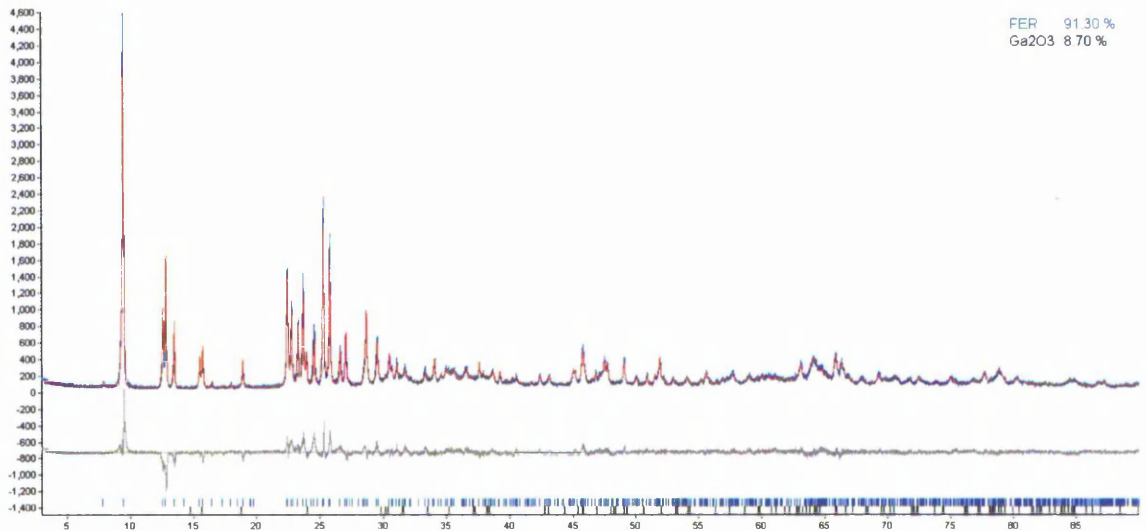


Figure 104: Rietveld fit for solution-treated FER with 15wt% Ga as Ga₂O₃.

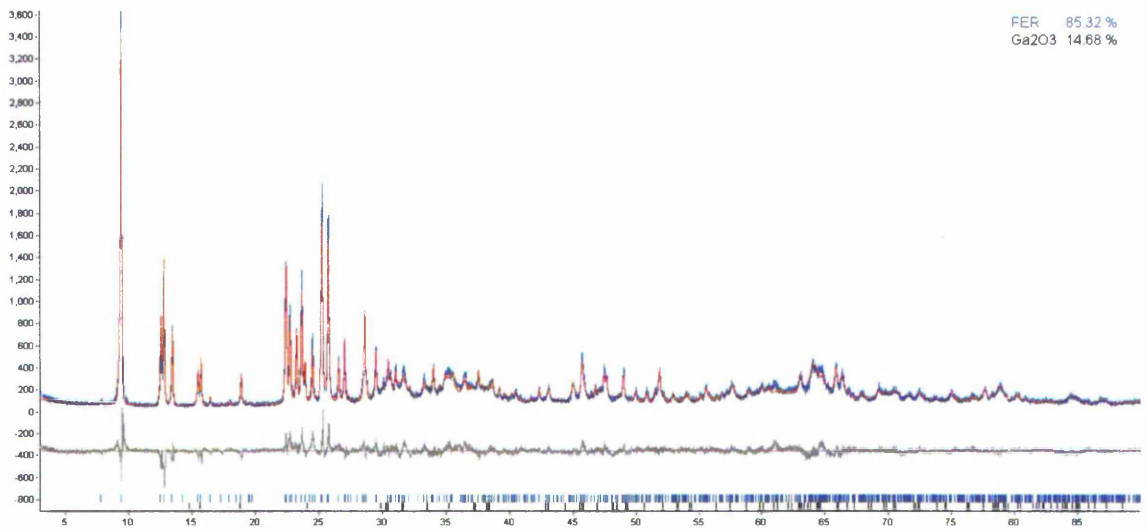


Figure 105: Rietveld fit for solution-treated FER with 20wt% Ga as Ga₂O₃.

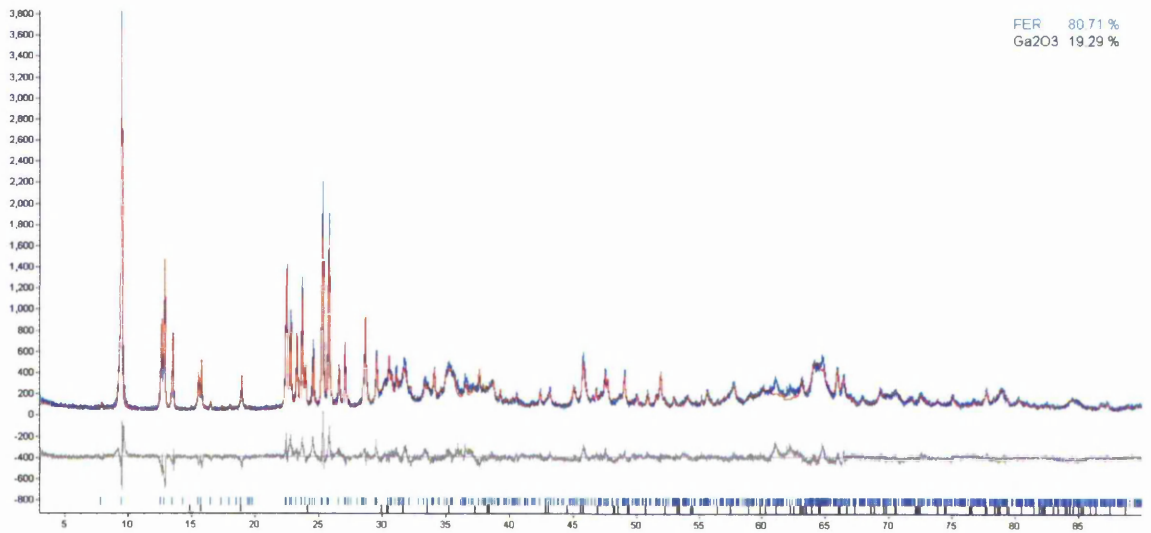


Figure 106: Rietveld fit for solution-treated FER with 30wt% Ga as Ga₂O₃.

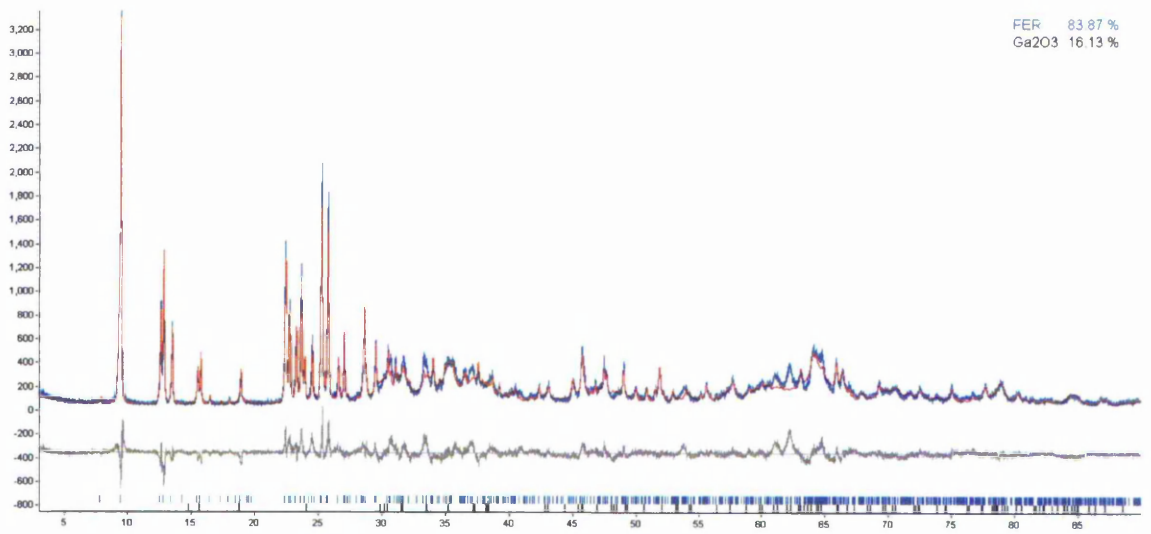


Figure 107: Rietveld fit for solution-treated FER with 40wt% Ga as Ga₂O₃.

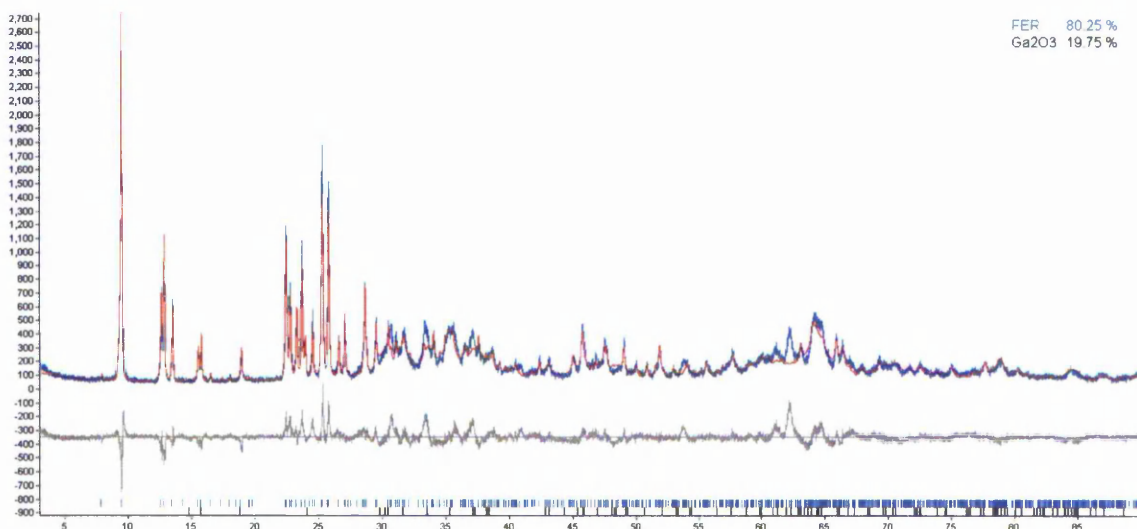


Figure 108: Rietveld fit for solution-treated FER with 50wt% Ga as Ga₂O₃.

The Rietveld profiles shown in Figure 102 to Figure 108 show that the process of Ga₂O₃ inclusion has little effect on the crystallinity of the host zeolite. The peaks related to Ga₂O₃ become gradually more prevalent with increasing Ga content, which is to be expected, yet there is no significant increase, as seen with other host/guest combinations. The calculated Ga loading at which the main pores are filled is 29.04wt%, using the following calculations assuming 1 pore per unit cell:

- Pore dimensions: 0.54 x 0.42 x 0.754 nm
- Ga₂O₃ unit cell dimensions (6Ga₂O₃): 0.3037 x 0.5798 x 1.2214 nm
- Approx. Ga atoms per pore: 9
- Total Ga mass: 627.51 a.m.u.
- Zeolite Unit Cell Mass: 2161.13 a.m.u.
- (Ga Mass/Zeolite Mass) x 100: 29.04 wt%

Therefore the calculations suggest that at Ga loadings of 30 wt% and less the Ga₂O₃ present should be present as small crystallites occupying the main pores of the zeolite structure and that at loadings above 30 wt% extra-zeolite phases of

Ga_2O_3 exist. The fact that this doesn't seem to be the case suggests that the zeolite has taken up more Ga than the calculation suggests is possible. The assumption in the calculations that the main pore is the sole location for Ga absorption may be the reason for this. There is a secondary channel that runs perpendicular to the main channel. The measurements of this channel between intersections with the main channel, therefore treating the secondary channel as a series of cages, are 0.819nm x 0.668 x 0.573 nm. Using the same calculations for this cage provides a pore filling Ga loading of 54.85wt%, for this cage alone. Therefore these cages may have absorbed the extra Ga.

The Rietveld fit shown in Figure 109 was taken from the molten salt-treated sample.

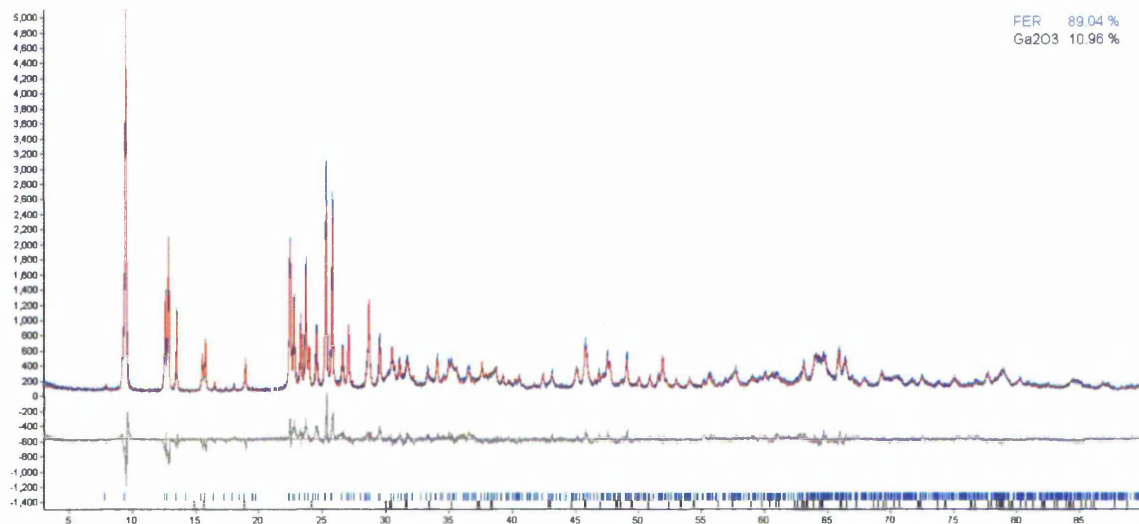


Figure 109: Rietveld fit for molten salt-treated FER with Ga_2O_3 .

It is clear from Figure 109 that the zeolite structure is still intact upon molten salt impregnation and subsequent calcination. The absence of significant, discernible

diffraction peaks from Ga_2O_3 suggests that any Ga_2O_3 phase is present as small crystallites.

The lattice parameters from FER samples with Ga_2O_3 using both the solution and molten salt impregnation methods derived from Rietveld analysis of the XRD data are shown graphically in Figure 110 to Figure 112.

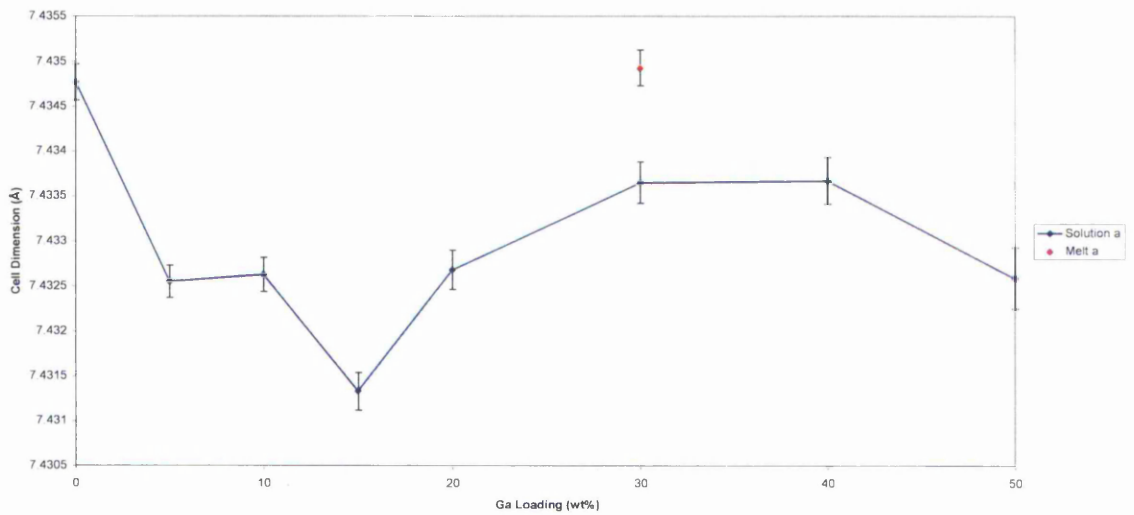


Figure 110: Unit cell parameter a for FER with Ga_2O_3 .

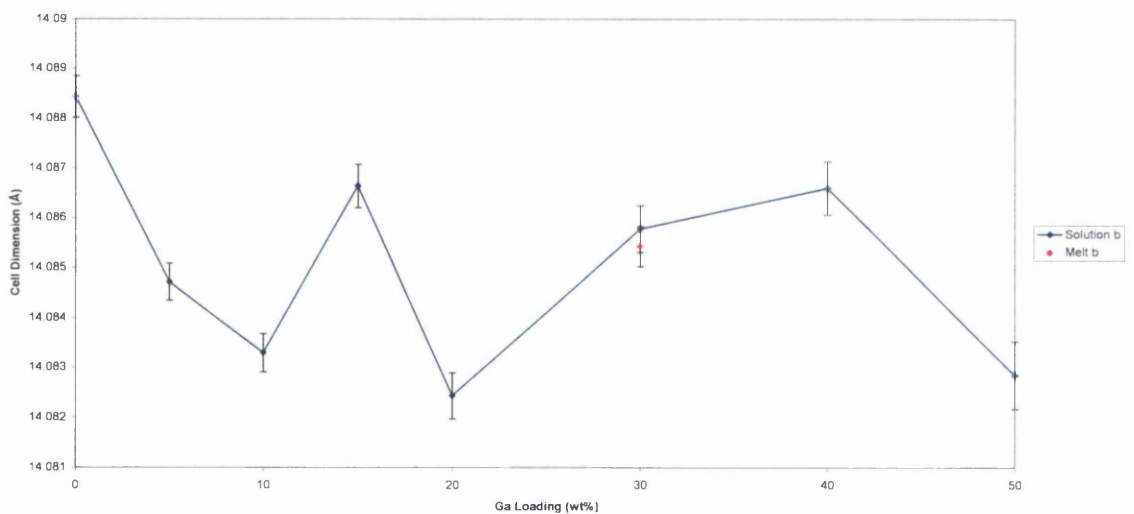


Figure 111: Unit cell parameter b for FER with Ga_2O_3 .

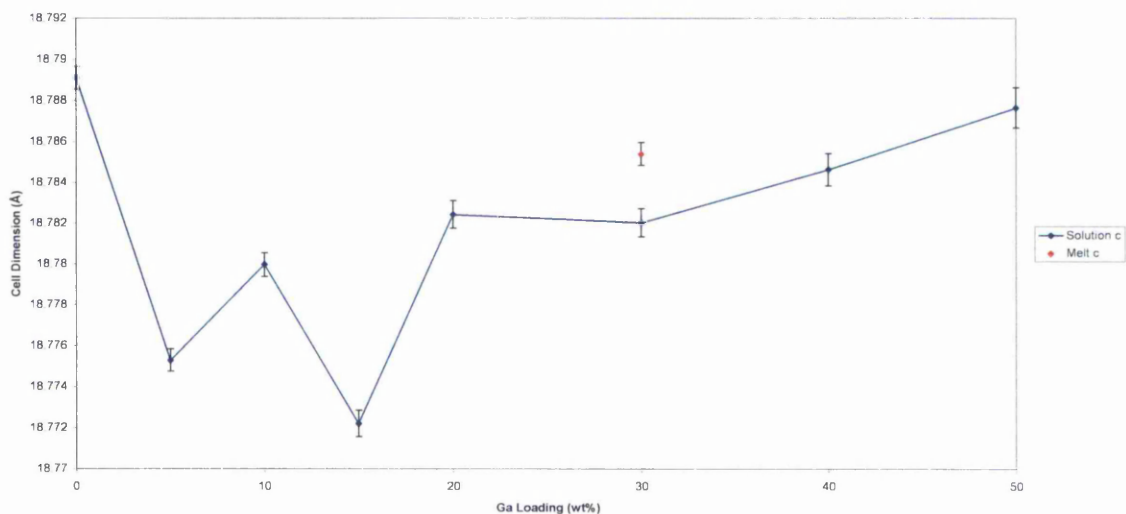


Figure 112: Unit cell parameter *c* for FER with Ga₂O₃.

Figure 110 to Figure 112 show that upon impregnation the unit cell values are generally reduced in all three directions with respect to the parent zeolite. They also show that the values for the molten salt-treated sample are greater in the *a* direction across the entire loading range, greater in the *c* direction for all samples besides the 50 wt% loaded sample and in the *b* direction the value is among the values found for the solution-treated samples, all with taking error analysis into account.

Figure 113 shows the UV-Visible diffuse-reflectance curves obtained for all FER samples impregnated with Ga_2O_3 , the parent zeolite and bulk Ga_2O_3 .

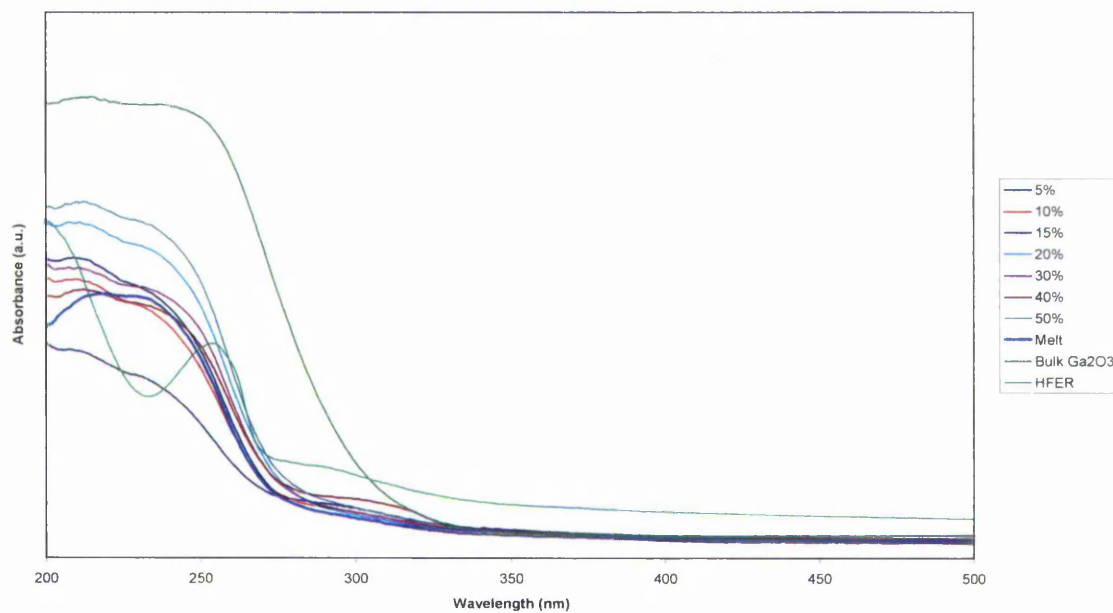


Figure 113: UV-Vis data for FER samples with Ga_2O_3 .

By taking the 1st derivative of the UV-Vis reflectance data, the band gaps can be read at the curve maxima, giving the values shown in Table 7 and Figure 114.

Table 7: Band gap values for FER samples with Ga₂O₃.

Impregnation Method	Band Gap (eV)
Molten Salt	4.82
5% Solution	4.88
10% Solution	4.82
15% Solution	4.82
20% Solution	4.78
30% Solution	4.78
50% Solution	4.76
Bulk Ga ₂ O ₃	4.75

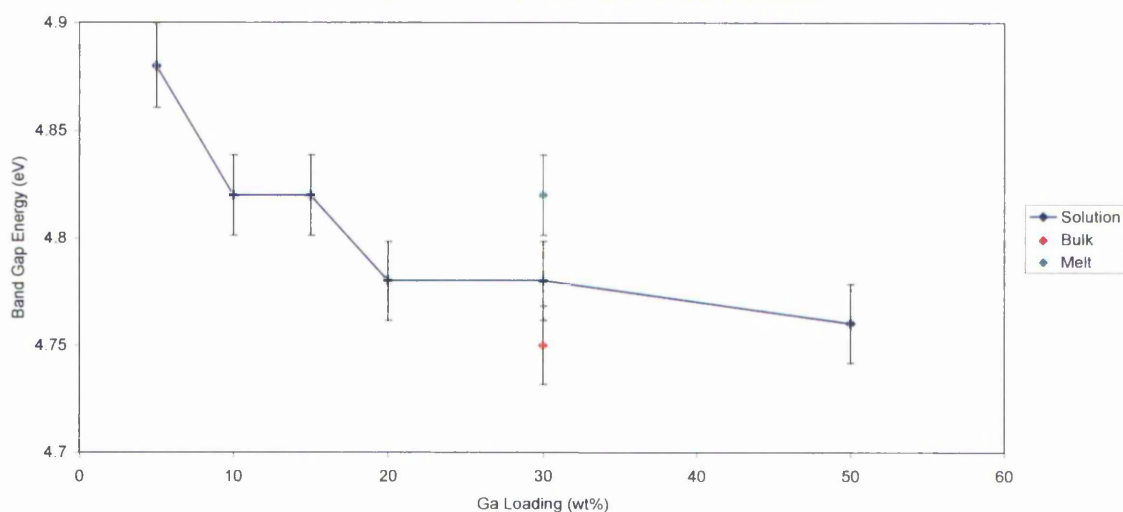


Figure 114: Band gap values for FER samples with Ga₂O₃. The position of the Melt and Bulk Ga₂O₃ points in the centre of the x-axis are for illustration only and does not imply Ga loadings of 30 wt% are present in these samples.

It is clear that the band gap of Ga_2O_3 is increased on solution impregnation into FER at Ga loadings of $\leq 20\text{wt}\%$ in comparison to bulk Ga_2O_3 within error, the extent to which generally decreases with increasing loading. At higher loadings the band gap remains within experimental error of the value for the bulk phase. By adopting the molten salt method the band gap value is comparable to values obtained at Ga loadings of $\leq 15\text{wt}\%$ using the solution impregnation, within experimental error.

6.2. Discussion and Conclusions

The differences in zeolite unit cell parameters noticed in the GaN samples are not present in the samples with Ga_2O_3 within the pores. In these samples the zeolite unit cell parameters for all samples are approximately the same for both the materials treated by the salt solution and molten salt impregnation methods. This suggests the formation of Ga_2O_3 does not exert as much force on the pore walls as with GaN.

The band gap values of the molten salt treated zeolite- Ga_2O_3 materials are not as significantly increased with respect to the bulk and salt solution treated material values as with the zeolite-GaN samples. In all three zeolites a general decrease in E_g is seen with increasing Ga loading in the salt solution impregnated materials, which is attributable to an increase in Ga_2O_3 crystallite size upon increased loading. The band gap of the molten salt treated materials is comparable to that of the solution treated samples, with the exception of the molten salt treated FAU sample, in which no band gap was observed. The difference between the formation of a band gap in the zeolites containing 1-D channels and no band formation in the zeolite with 0-D cages is another indication of the dependence of band structure on the geometry of a semiconducting material. The absence of an absorption step in the FAU sample implies that the pore size may be too small to allow the synthesis of Ga_2O_3 or that the response is too weak to detect.

7. Zinc Nitride

Zinc nitride (Zn_3N_2) is a semiconductor with a band-gap that has a reported range of 1.01 to 3.2 eV, ^[105, 106] which obviously casts over the actual optical properties of the material. Zn_3N_2 occupies a cubic structure, which is shown in Figure 115.

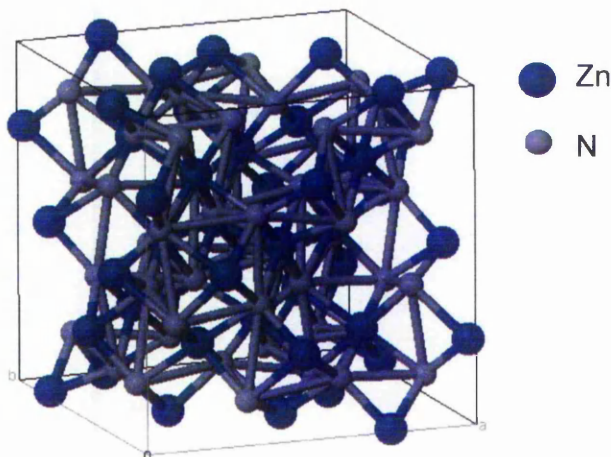


Figure 115: The crystal structure of Zn_3N_2 . ^[107]

Zn_3N_2 generally has the following crystallographic parameters:

Space Group: IA-3

$a = 9.7691 \text{ \AA}$

$\alpha = 90^\circ$

Zn_3N_2 is generally synthesised by heating metallic Zn in flowing ammonia. ^[47, 108]

It is a grey powder that reacts violently with water and has a very high melting point.

Zn_3N_2 is a relatively newly discovered compound, with only one crystal structure reported. ^[107] A group that has studied Zn_3N_2 extensively is that headed by Fujian Zong, ^[109-115] which has endeavoured to fully characterise Zn_3N_2 and has recently ventured into the area of Zn_3N_2 nanowires. In this work, Zn_3N_2 was occluded within the zeolites ZSM-5, ferrierite and faujasite using both the molten salt and salt solution impregnation methods using $Zn(NO_3)_2$.

7.1. Results

7.1.1. ZSM-5

Diffraction profiles were refined using Topas Academic V4.1 against the ZSM-5 structure reported by Li, et al.^[89] and Zn_3N_2 structure reported by Partin, et al.^[89] The XRD and Rietveld profiles from solution-treated samples are shown in Figure 116 to Figure 120.

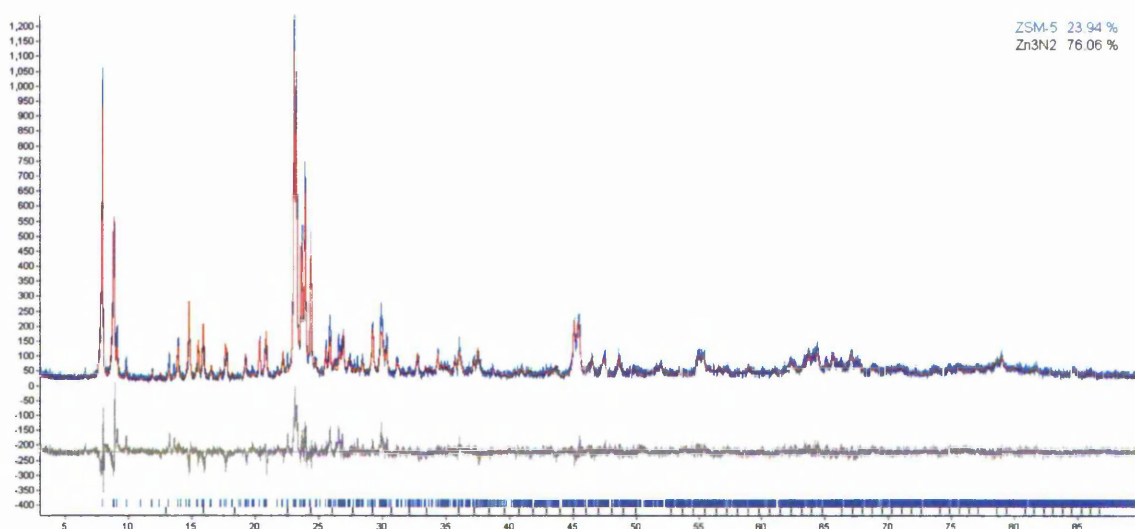


Figure 116: Rietveld fit for solution-treated ZSM-5 with 5wt% Zn as Zn_3N_2 .

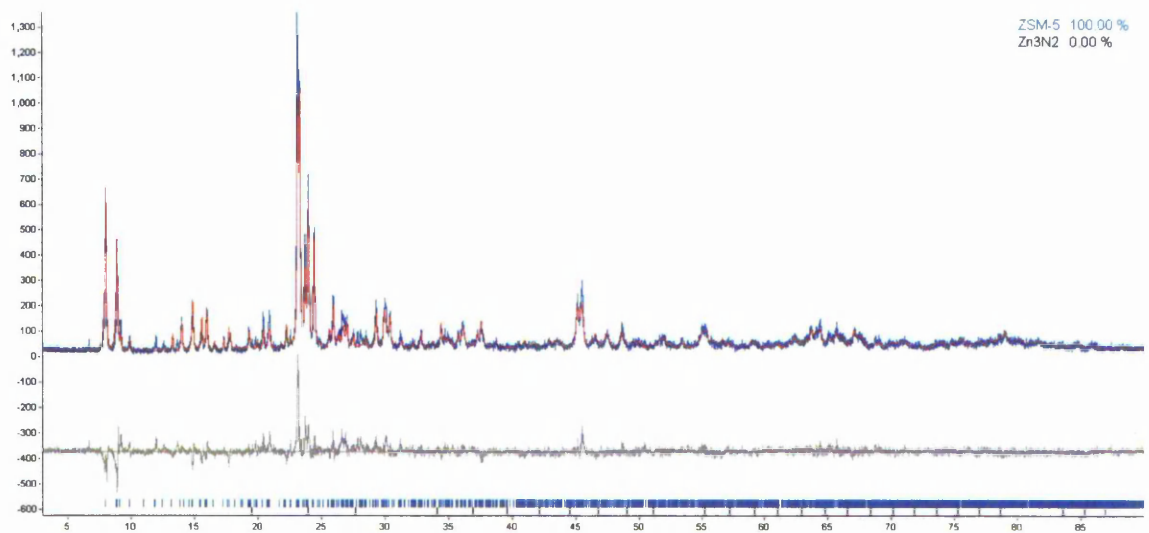


Figure 117: Rietveld fit for solution-treated ZSM-5 with 10wt% Zn as Zn₃N₂.

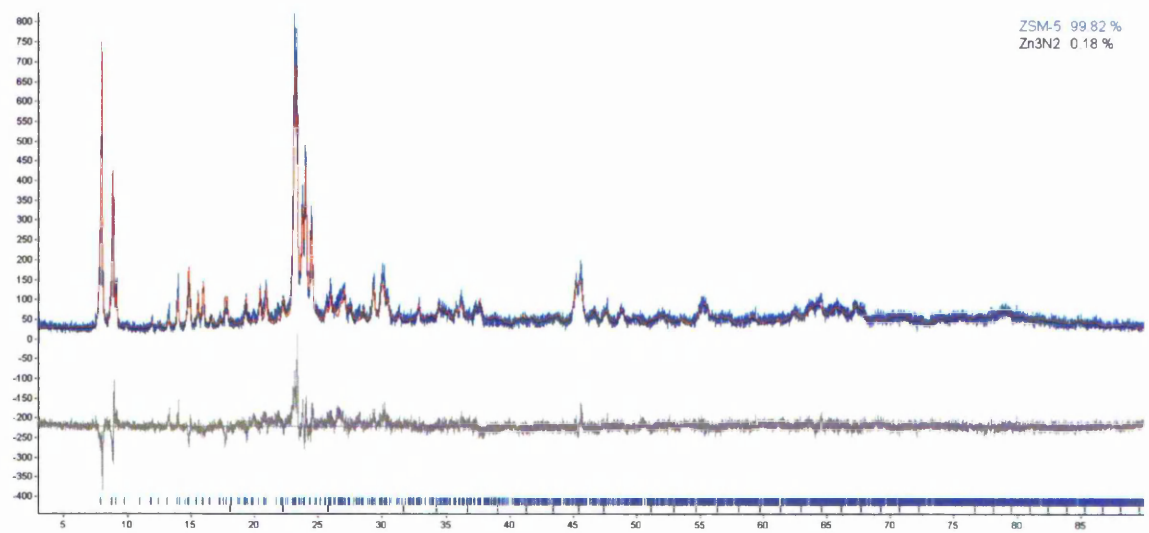


Figure 118: Rietveld fit for solution-treated ZSM-5 with 15wt% Zn as Zn₃N₂.

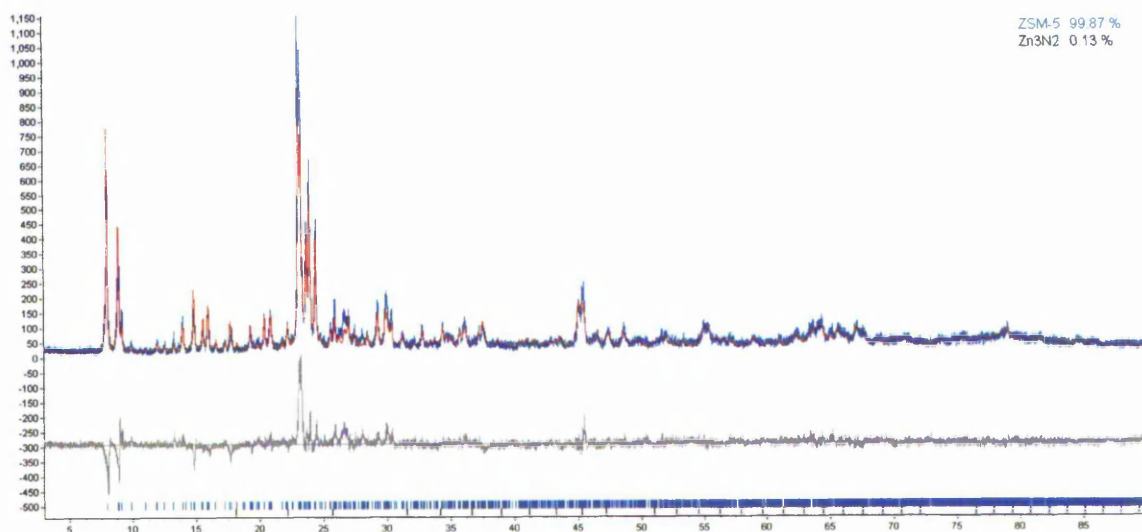


Figure 119: Rietveld fit for solution-treated ZSM-5 with 30wt% Zn as Zn₃N₂.

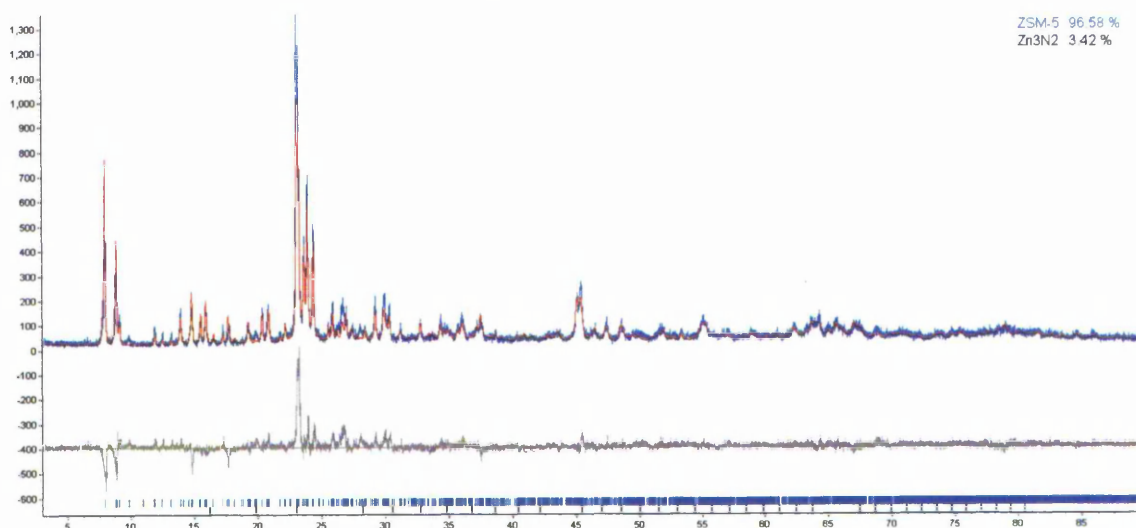


Figure 120: Rietveld fit for solution-treated ZSM-5 with 50wt% Zn as Zn₃N₂.

The Rietveld profiles shown in Figure 116 to Figure 120 show that the process of Zn₃N₂ inclusion has little effect on the crystallinity of the host zeolite. The peaks related to Zn₃N₂ don't become evident even at 50wt% loading of Zn, which suggests that even at these loadings the Zn₃N₂ is present as small crystallites most likely within the zeolite pore structure. This is in contrary to the calculated maximum main pore filling Zn loading of 36.27wt% as per the following calculations:

- Pore dimensions: 0.54 x 0.42 x 0.754 nm
- Zn_3N_2 unit cell dimensions ($16Zn_3N_2$): 0.9769 x 0.9769 x 0.9769 nm
- Approx. Zn atoms per pore: 30
- Total Zn mass: 1961.7 a.m.u.
- Zeolite Unit Cell Mass: 5766.76 a.m.u.
- (Zn Mass/Zeolite Mass) x 100: 34.02 wt%

This may suggest that Zn also occupies the other cavities in the zeolite framework before crystallising outside the structure. Reasons as to why this is not seen in other ZSM-5/guest combinations may be due to hydrated ion radii, ion diffusion kinetics, etc.; the exploration of which is beyond the scope of this project.

The Rietveld fit shown in Figure 121 was taken from the molten salt-treated sample.

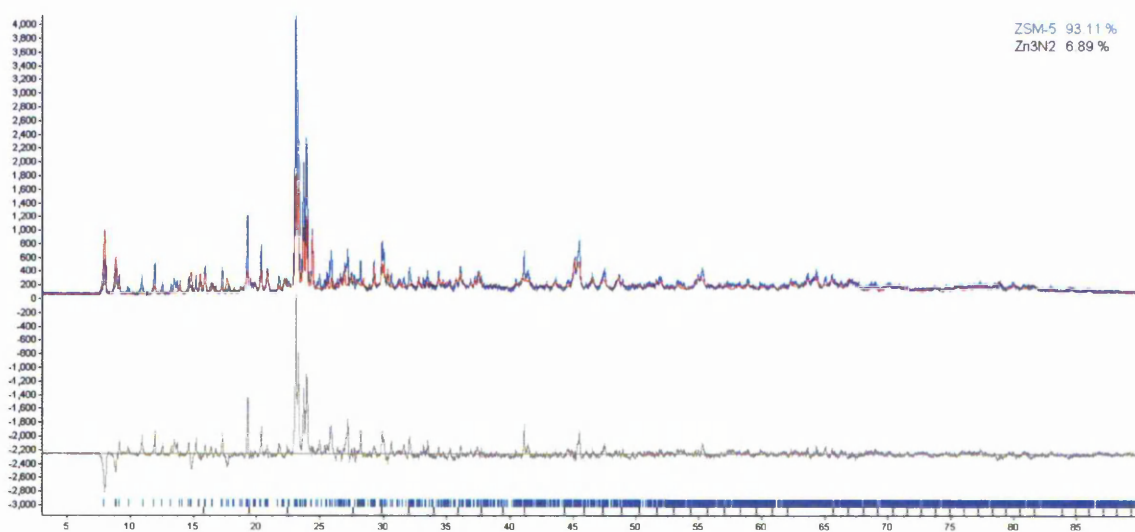


Figure 121: Rietveld fit for molten salt-treated ZSM-5 with Zn_3N_2 .

It is clear from Figure 121 that the zeolite structure is still intact upon molten salt impregnation and subsequent calcination. The absence of significant, discernible

diffraction peaks from Zn_3N_2 suggests that any Zn_3N_2 phase is present as small crystallites.

The lattice parameters from ZSM-5 samples with Zn_3N_2 using both the solution and molten salt impregnation methods derived from Rietveld analysis of the XRD data are shown graphically in Figure 122 to Figure 124.

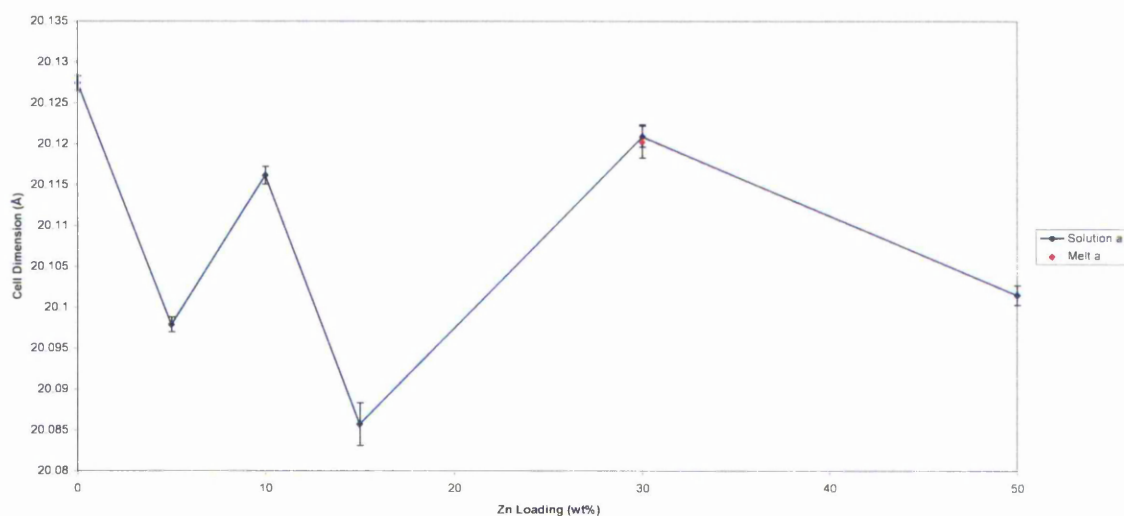


Figure 122: Unit cell parameter *a* for ZSM-5 with Zn_3N_2 .

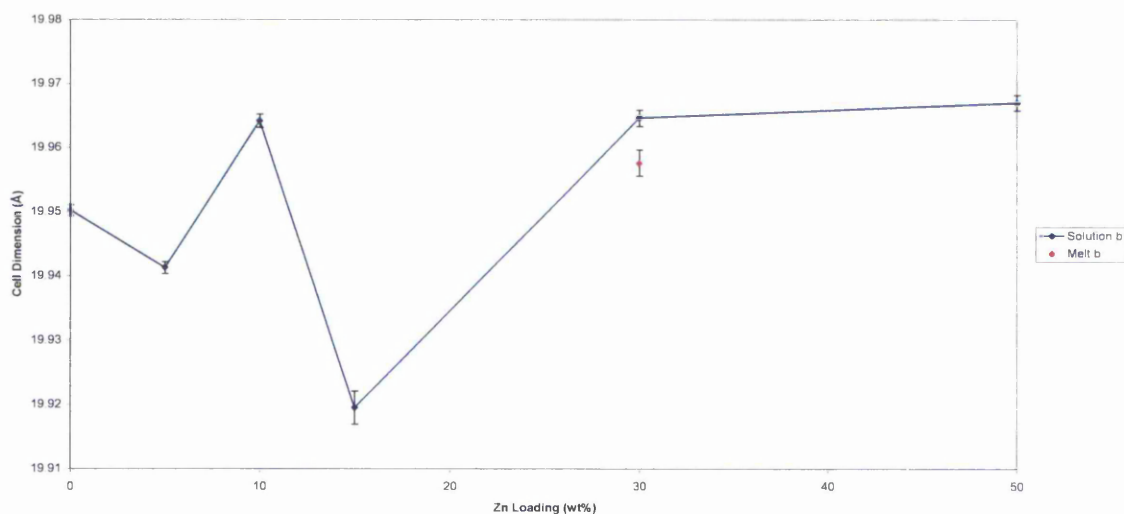


Figure 123: Unit cell parameter *b* for ZSM-5 with Zn_3N_2 .

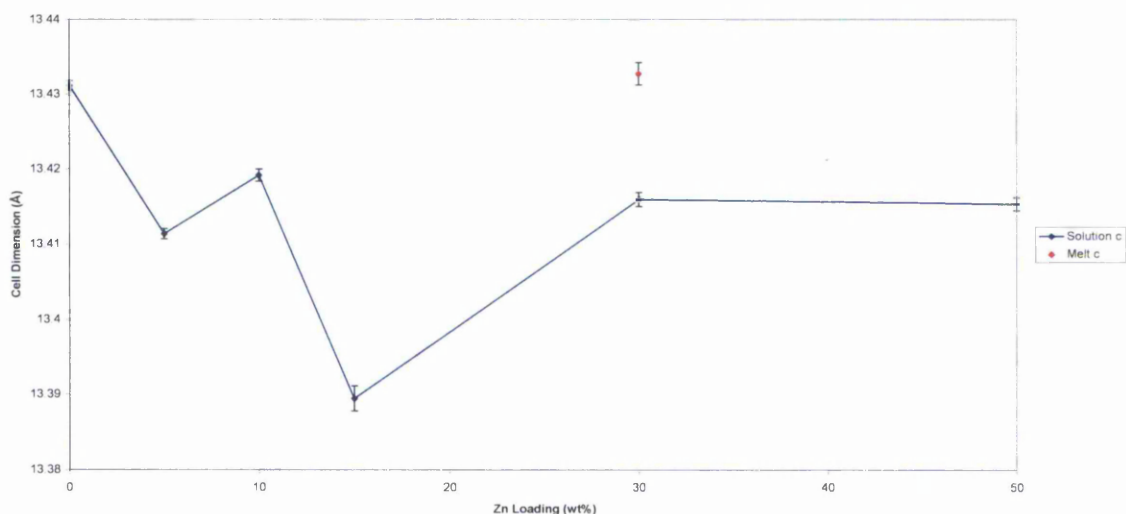


Figure 124: Unit cell parameter c for ZSM-5 with Zn_3N_2 .

The unit cell values shown vary slightly across the Zn solution loading range of 0 – 50 wt%, but are generally smaller than that of the parent zeolite. The value found for the sample treated with the molten salt impregnation method lies among those recorded for the solution-treated samples within experimental error in all but the c direction (perpendicular to the length of the main channel), in which the value is slightly greater, yet comparable within experimental error to that of the parent zeolite.

Figure 125 shows the diffuse reflectance curves obtained for ZSM-5 samples with Zn_3N_2 .

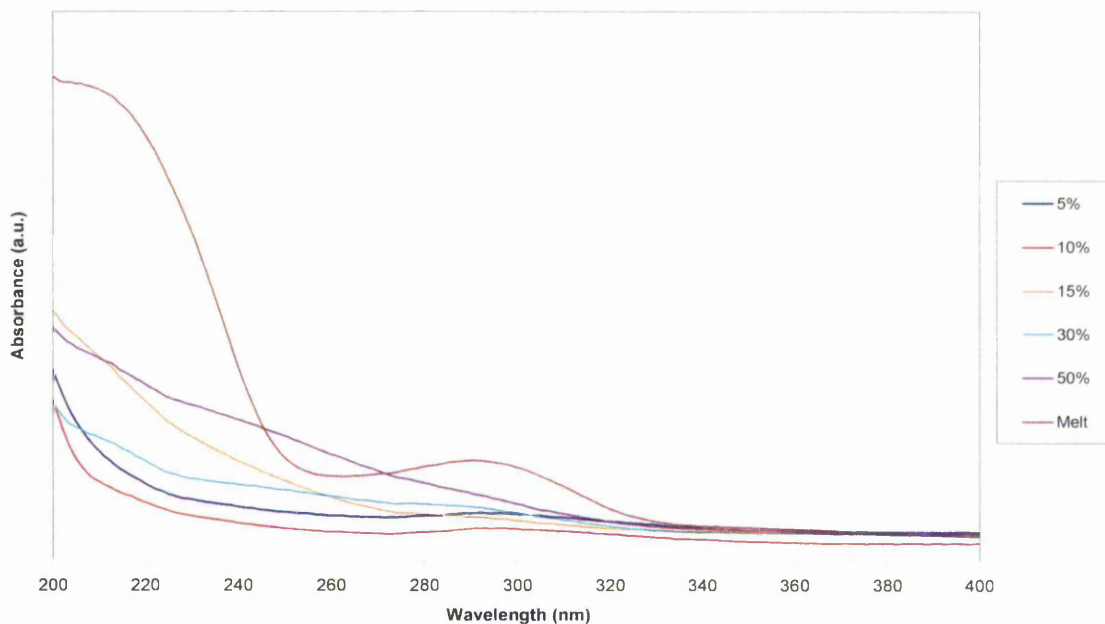


Figure 125: UV Vis data for ZSM-5 samples with Zn_3N_2 .

It is clear that no band structure is formed in any of the samples treated with the solution-based impregnation, yet an absorption edge is obvious in the sample treated with the molten salt impregnation. The band gap of this sample is estimated at 5.22 eV (± 0.021975), with a smaller absorption peak at 3.96 eV (± 0.0127).

As Figure 126 shows, the PL emission peak (E_{PL}) of Zn_3N_2 at 2.5 eV is similar in both the sample impregnated with a 15 % solution and that treated by the molten salt impregnation. There is also a peak that is partly overshadowed at 2.75 eV that is present in both samples. The sharp peak at 2.325 eV is a harmonic from the exciting laser. This data doesn't correlate with the UV-Vis diffuse-reflectance data, which may be due to Stokes shift, but the shift would be very large, at approximately 3eV. This may not be surprising if occlusion was, indeed, successful as both reducing dimensionality and introducing impurities (in this case the zeolite) can increase Stokes shifts.

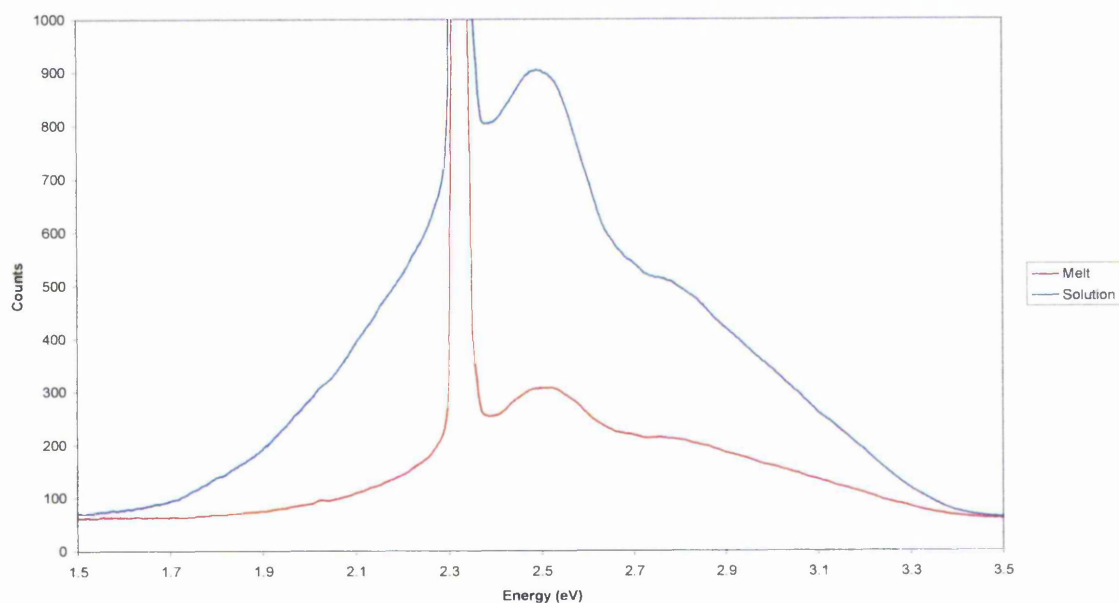


Figure 126: PL spectra for ZSM-5 with Zn_3N_2 .

7.1.2. Faujasite

Diffraction profiles were refined using Topas Academic V4.1 against the faujasite structure reported by Parise, et al. [91] and Zn_3N_2 structure reported by Partin, et al. [107] The XRD and Rietveld profiles from solution-treated samples are shown in Figure 127 to Figure 133.

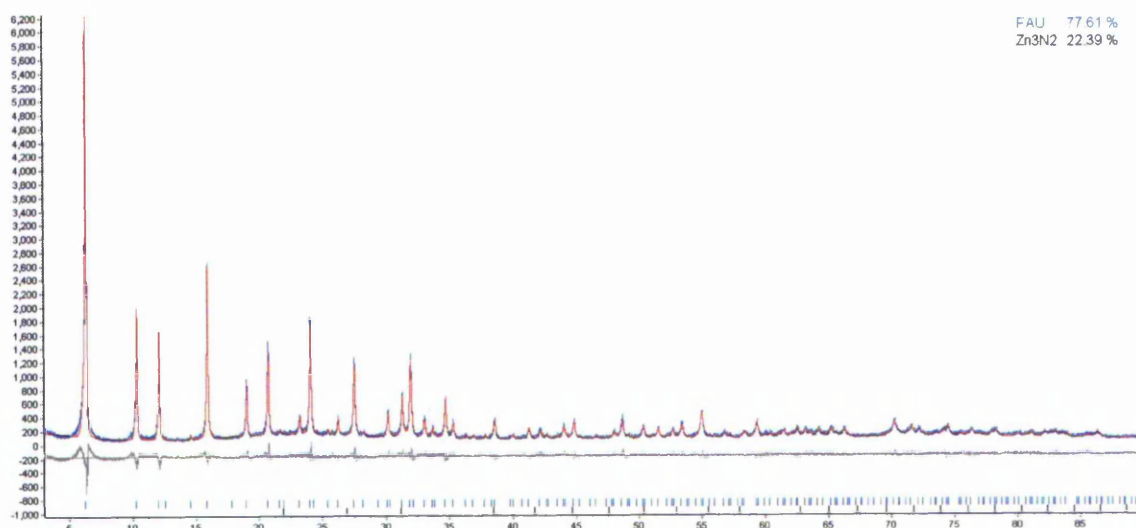


Figure 127: Rietveld fit for solution-treated FAU with 5wt% Zn as Zn_3N_2 .

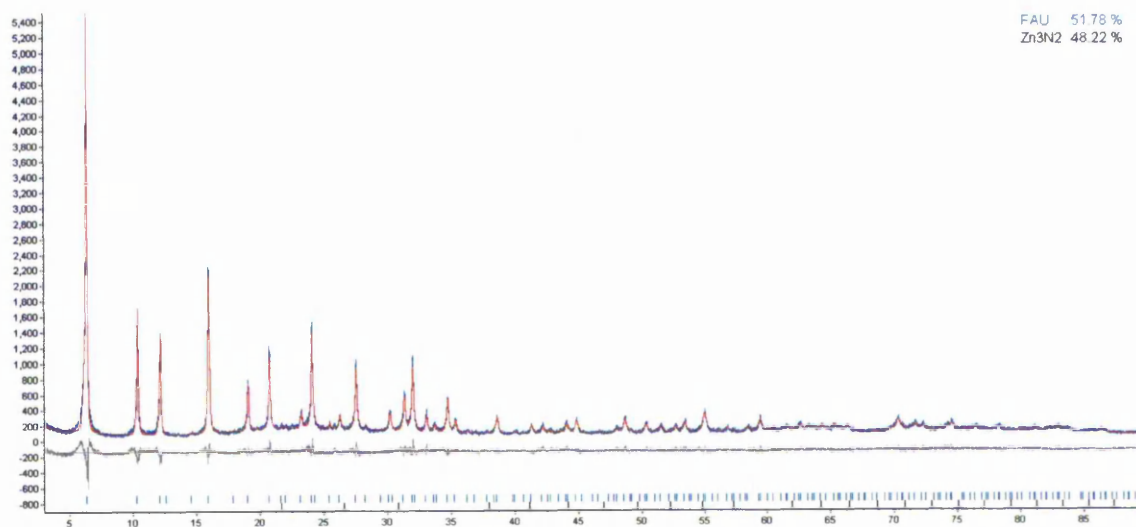


Figure 128: Rietveld fit for solution-treated FAU with 10wt% Zn as Zn_3N_2 .

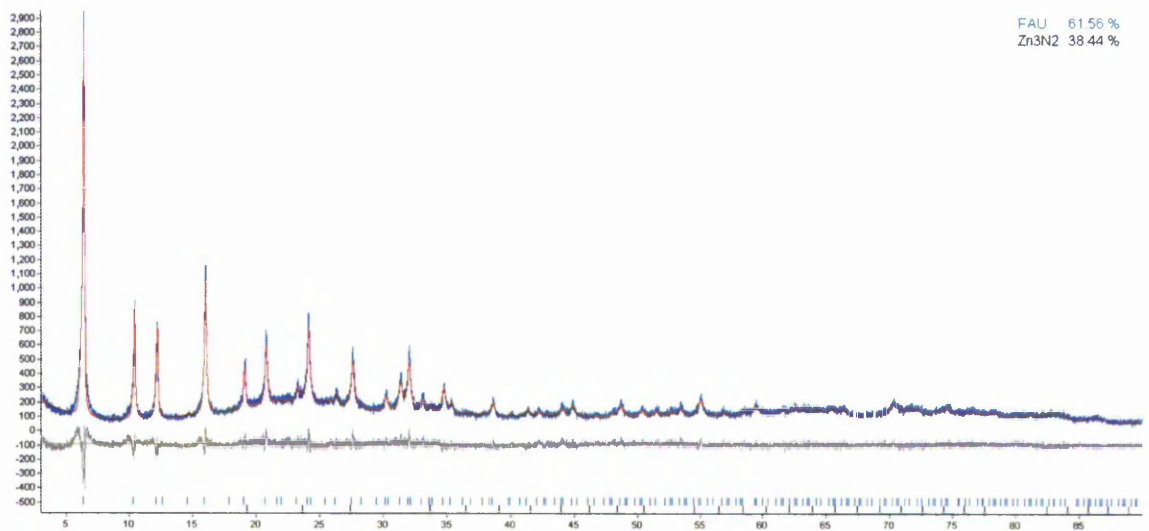


Figure 129: Rietveld fit for solution-treated FAU with 15wt% Zn as Zn₃N₂.

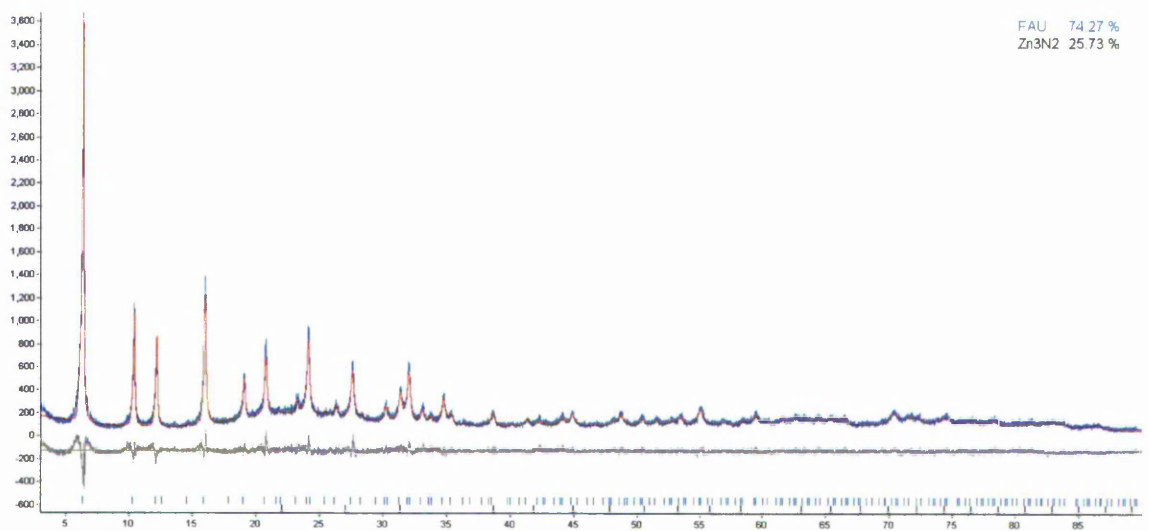


Figure 130: Rietveld fit for solution-treated FAU with 20wt% Zn as Zn₃N₂.

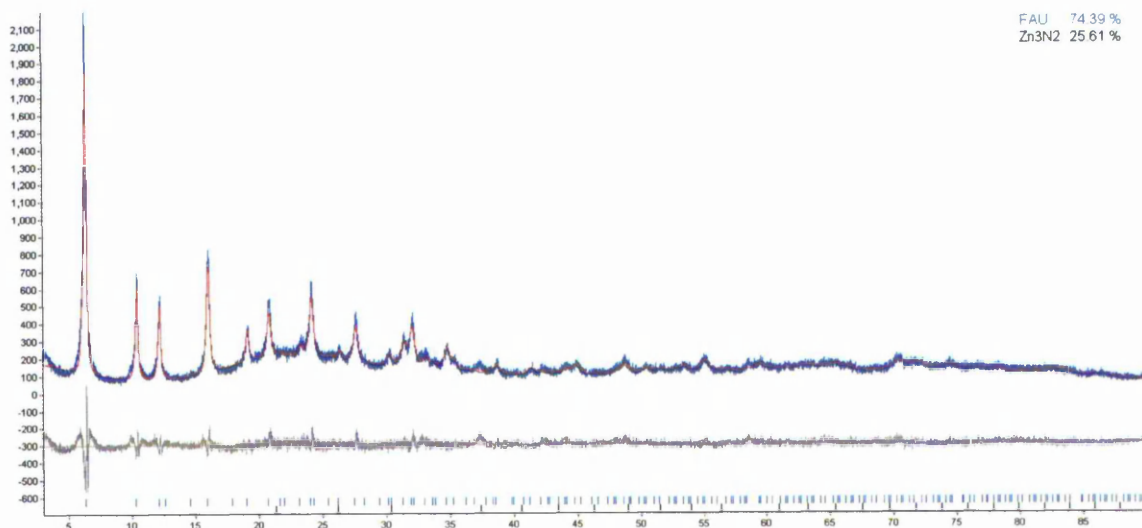


Figure 131: Rietveld fit for solution-treated FAU with 30wt% Zn as Zn₃N₂.

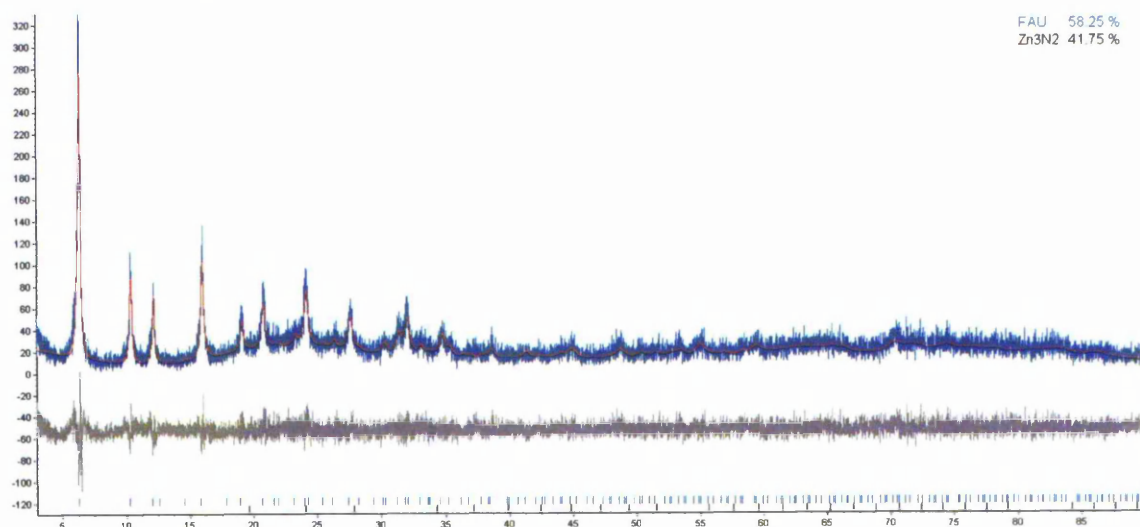


Figure 132: Rietveld fit for solution-treated FAU with 40wt% Zn as Zn₃N₂.

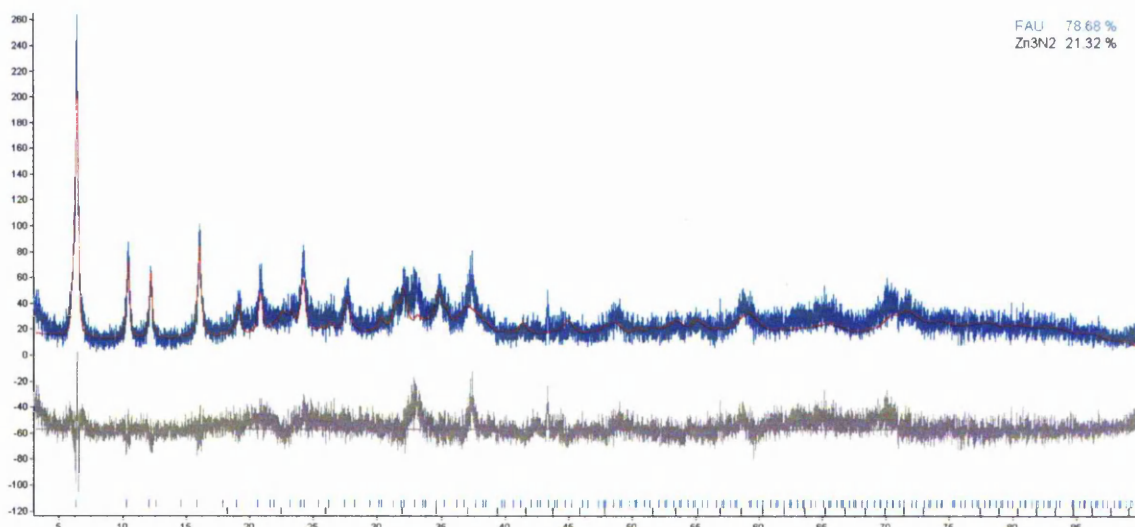


Figure 133: Rietveld fit for solution-treated FAU with 50wt% Zn as Zn_3N_2 .

The Rietveld profiles shown in Figure 127 to Figure 133 show that the process of Zn_3N_2 inclusion does affect the crystallinity of the host zeolite. An increase in amorphous content, as characterised by an increase in profile noise is clear as the loading of Zn increases. The peaks related to Zn_3N_2 don't become noticeable until a Zn loading of 50wt%, suggesting that Zn_3N_2 is present as small crystallites. Given the amorphisation of the host zeolite phase an estimation of maximum possible loading of Zn would not be the best method of understanding this experiment. Calculations do, however, provide a maximum pore filling Zn loading as 56.70wt%:

- Cage dimensions: 1.304 x 1.304 x 1.304 nm
- Zn_3N_2 unit cell dimensions (16 Zn_3N_2): 0.9769 x 0.9769 x 1.9769 nm
- Approx. Zn atoms per cage: 100
- Total Zn mass: 6539.00 a.m.u.
- Zeolite Unit Cell Mass: 11533.51 a.m.u.
- (Zn Mass/Zeolite Mass) x 100: 56.70 wt%

Therefore a noticeable step change in amorphous content may occur at loadings above 50wt%. However, due to the breakdown of the zeolite as Zn loading increases this is unlikely to occur due to the loss of pore structure. The reasons for zeolite amorphisation may be related to the amount of Zn that is available to occupy the pores, effectively increasing the amount of localised charge within the pore structure which could lead to exchange of Al or even Si out of the framework.

The Rietveld fit shown in Figure 134 was taken from the molten salt-treated sample.

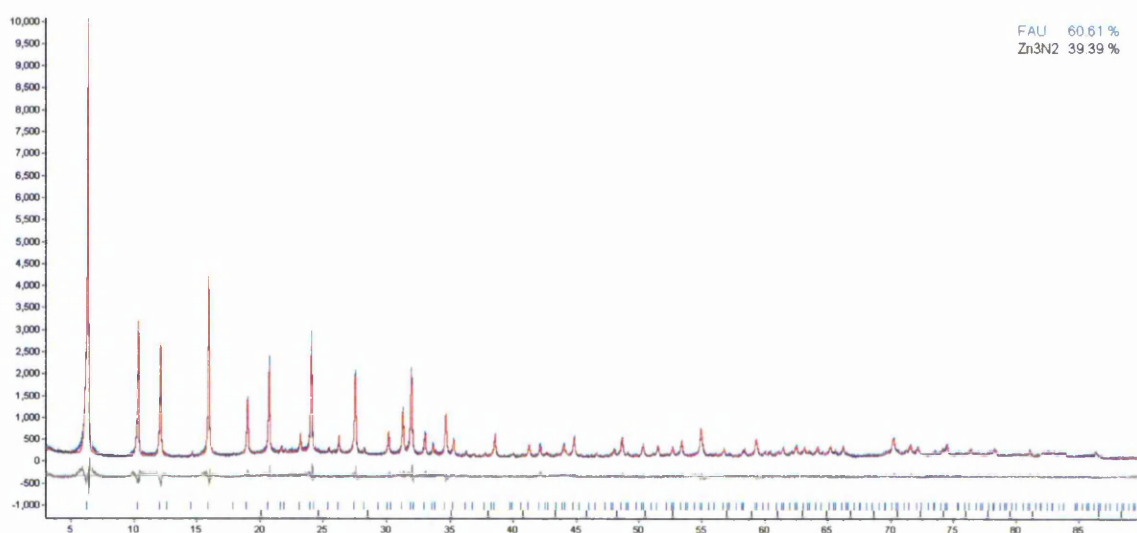


Figure 134: Rietveld fit for molten salt-treated FAU with Zn₃N₂.

It is clear from Figure 134 that the zeolite structure is still intact upon molten salt impregnation and subsequent calcination. The absence of significant, discernible diffraction peaks from Zn₃N₂ suggests that any Zn₃N₂ phase is present as small crystallites.

The lattice parameters from FAU samples with Zn_3N_2 using both the solution and molten salt impregnation methods derived from Rietveld analysis of the XRD data are shown graphically in Figure 135.

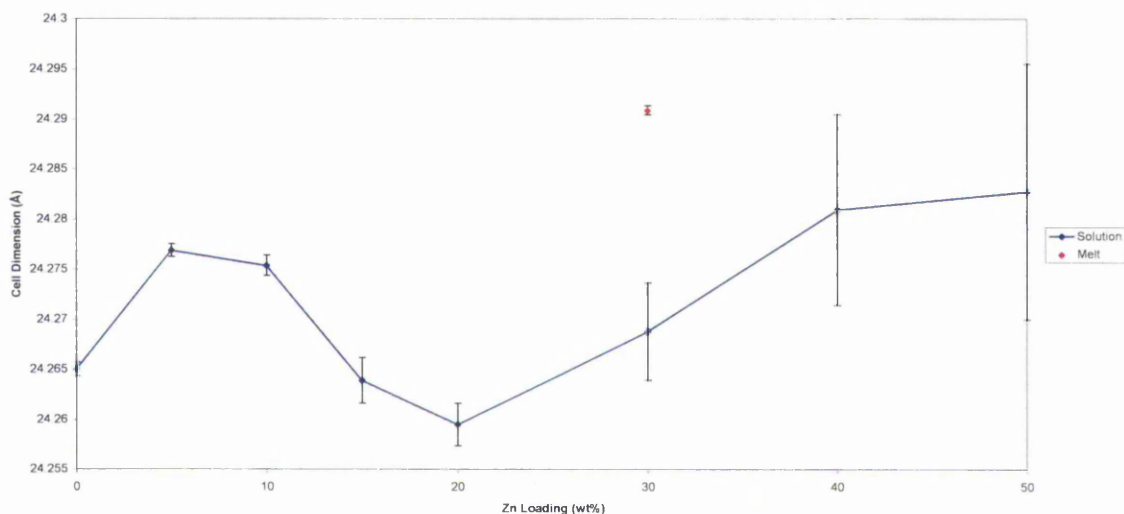


Figure 135: Unit cell parameter for FAU with Zn_3N_2 .

As Figure 135 shows, the unit cell parameter for FAU is variable across the solution-based loading range of 0-50 wt% of Zn with maxima between 5 and 10 wt% and at 50 wt% and a minimum at 20 wt%. Figure 135 shows a general, but slight increase of the unit cell parameter with increased loading of Zn. The unit cell parameter of FAU treated with the molten salt impregnation method, however, is significantly greater than that of the parent zeolite and larger than the solution-treated samples with Zn loadings of ≤ 30 wt% and within the experimental error of the values obtained for the 40 and 50wt% loaded samples.

Figure 136 shows the diffuse reflectance curves obtained for FAU samples with Zn_3N_2 .

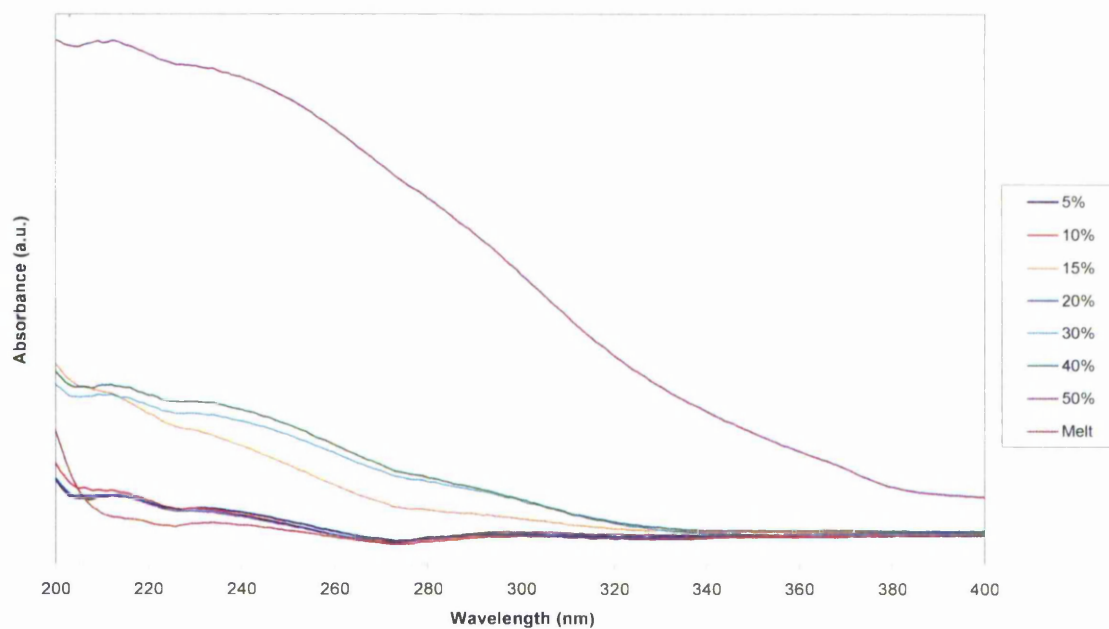


Figure 136: UV Vis data for FAU samples with Zn_3N_2 .

No clear absorption edge is seen in any of the samples, although there is a significant increase in overall absorption when increasing the loading of Zn from 40 to 50 wt%.

Figure 137 shows the PL spectrum of FAU with Zn_3N_2 treated with the molten salt impregnation. E_{PL} in this spectrum is 2.5 eV, with a smaller peak at ~ 2.7 eV. The sharp peak at 2.325 eV is a harmonic from the exciting laser.

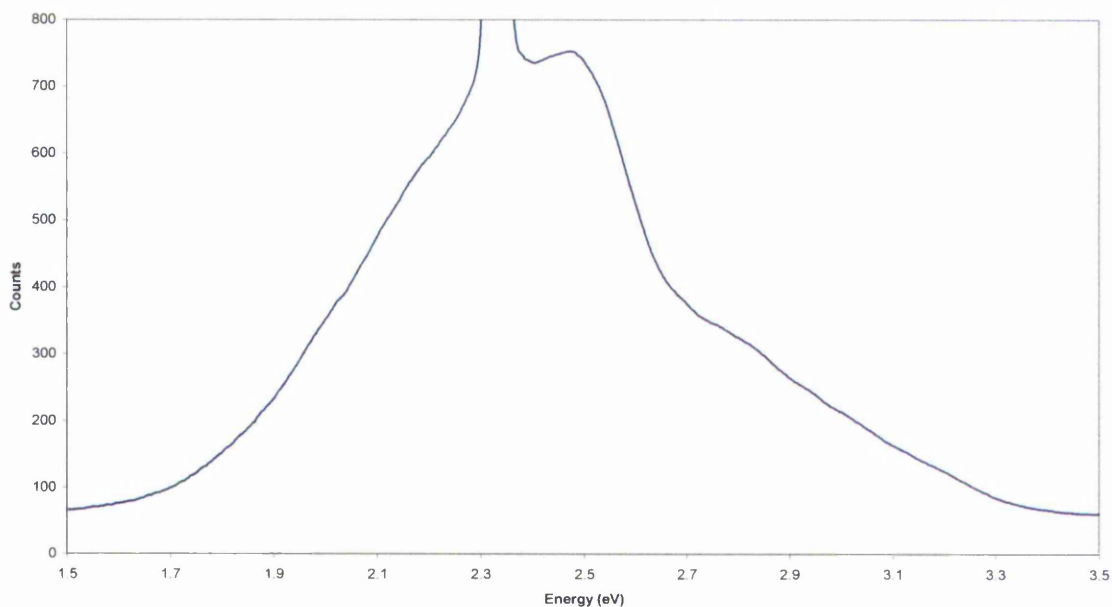


Figure 137: PL Spectrum of FAU with Zn_3N_2 via the molten salt impregnation.

7.1.3. Ferrierite

Diffraction profiles were refined using Topas Academic V4.1 against the ferrierite structure reported by Bull, et al. [92] and Zn_3N_2 structure reported by Partin, et al. [107] The XRD and Rietveld profiles from solution-treated samples are shown in Figure 138 to Figure 144.

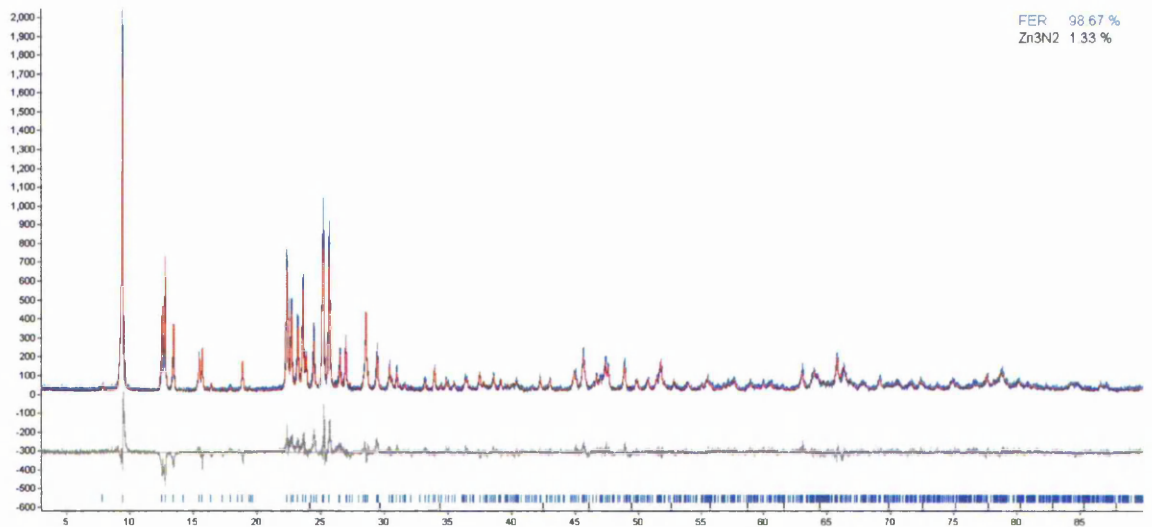


Figure 138: Rietveld fit for solution-treated FER with 5wt% Zn as Zn_3N_2 .

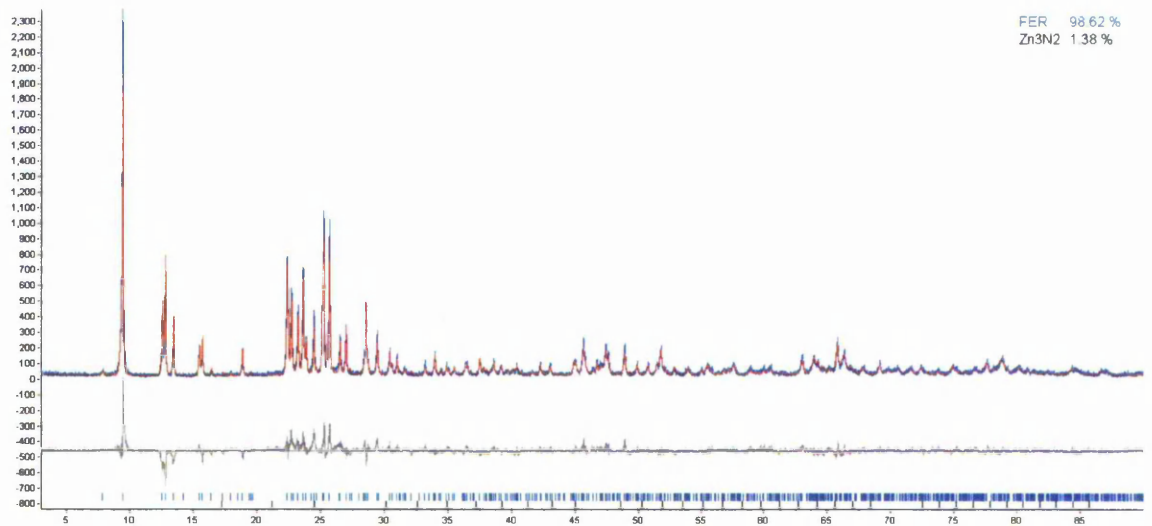


Figure 139: Rietveld fit for solution-treated FER with 10wt% Zn as Zn_3N_2 .

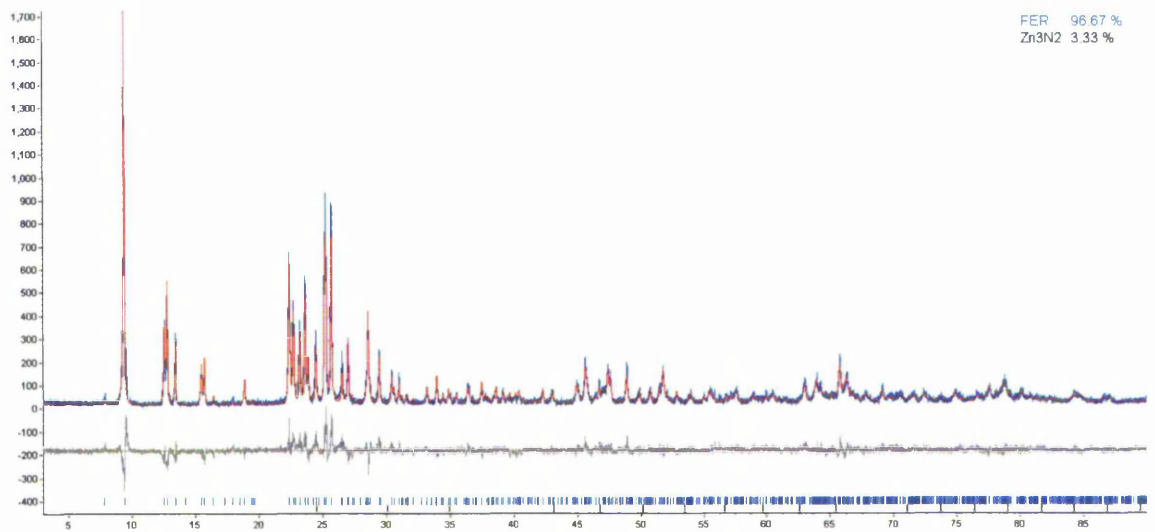


Figure 140: Rietveld fit for solution-treated FER with 15wt% Zn as Zn₃N₂.

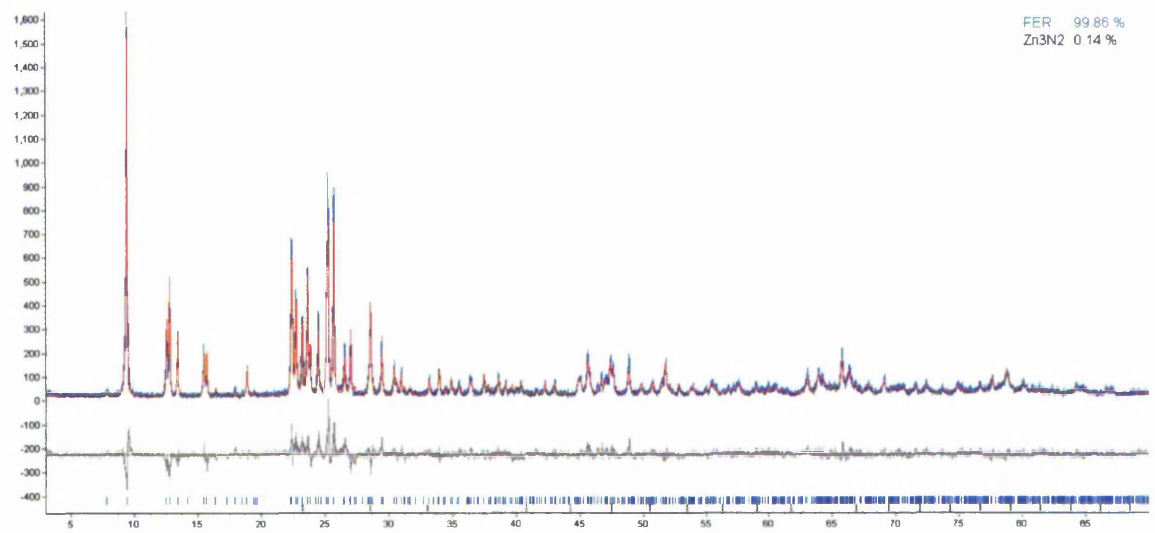


Figure 141: Rietveld fit for solution-treated FER with 20wt% Zn as Zn₃N₂.

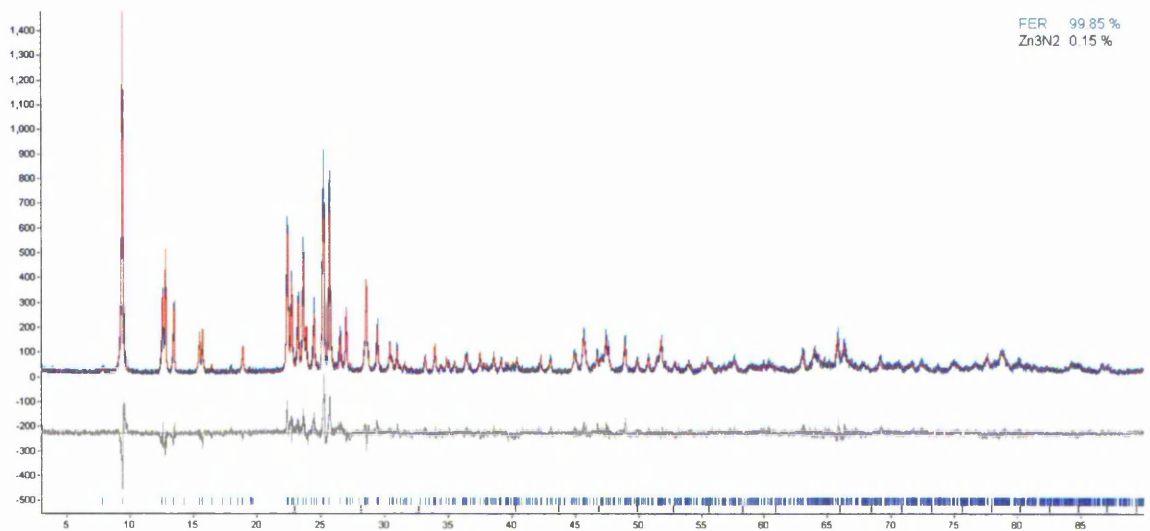


Figure 142: Rietveld fit for solution-treated FER with 30wt% Zn as Zn₃N₂.

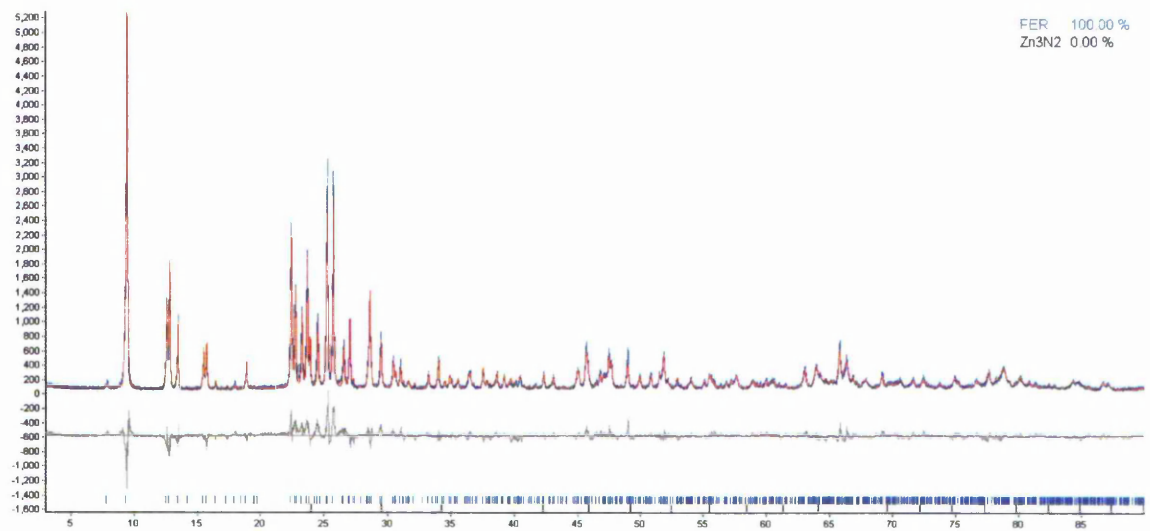


Figure 143: Rietveld fit for solution-treated FER with 40wt% Zn as Zn₃N₂.

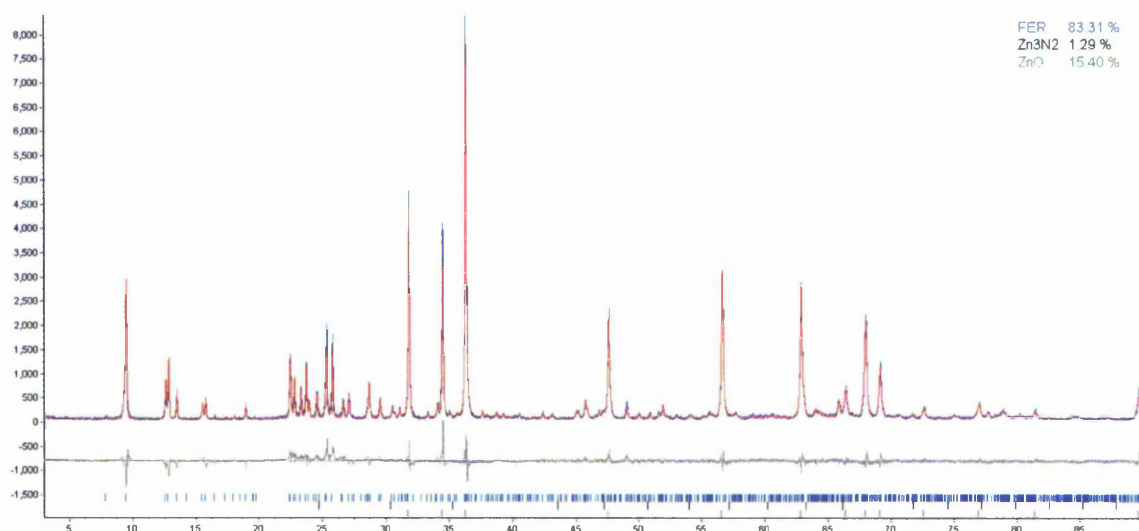


Figure 144: Rietveld fit for solution-treated FER with 50wt% Zn as Zn_3N_2 and ZnO.

The Rietveld profiles shown in Figure 138 to Figure 144 suggest that the process of Zn_3N_2 inclusion does not affect the crystallinity of the host zeolite. No peaks related to Zn_3N_2 become noticeable at any of the tested Zn loadings, suggesting that any Zn_3N_2 present is in the form of small crystallites. At a Zn loading of 50wt%, however, ZnO is present at a calculated 15.40% content. No ZnO peaks were visible in profiles from samples loaded with less Zn and Rietveld refinements showed no sign of diffraction from an oxide phase or any other Zn phases, such as metallic Zn. Repeats of this experiment also showed signs of ZnO content, therefore suggesting no error in experimental setup. As zeolites provide an oxygen-rich environment it is possible that the oxide phase is a symptom of zeolite breakdown, yet no amorphous phase is visible. However, as the ZnO phase diffracts so strongly, as is clear from the diffraction profile in which the zeolite pattern, which makes up the majority of the sample content, is dwarfed by the ZnO profile, a relatively small amount of amorphous material may go unnoticed. Also, the calculated Zn_3N_2 contents that are no higher than 3.33% suggest any Zn_3N_2

phase is present as small crystallites. Again, due to the strong diffracting nature of ZnO any ZnO content would be easily visible at low loadings.

This data suggests FER may be able to accommodate Zn_3N_2 at Zn loadings of up to 40wt% before the Zn content begins to induce amorphisation of the zeolite and form ZnO. A study of higher Zn loadings will be required to confirm this. This coincides with the results seen for FAU, in which the zeolite structure breaks down with increasing Zn loading.

The Rietveld fit shown in Figure 145 was taken from the molten salt-treated sample.

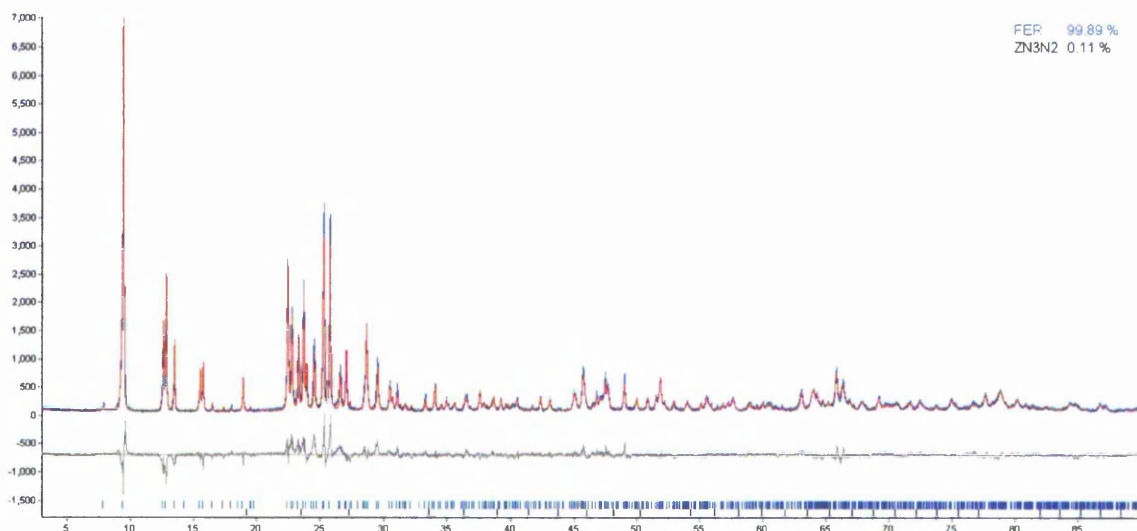


Figure 145: Rietveld fit for molten salt-treated FER with Zn_3N_2 .

It is clear from Figure 145 that the zeolite structure is still intact upon molten salt impregnation and subsequent calcination. The absence of any diffraction peaks from Zn_3N_2 suggests that any Zn_3N_2 phase is present as small crystallites.

The lattice parameters from FER samples with Zn_3N_2 using both the solution and molten salt impregnation methods derived from Rietveld analysis of the XRD data are shown graphically in Figure 146 to Figure 148.

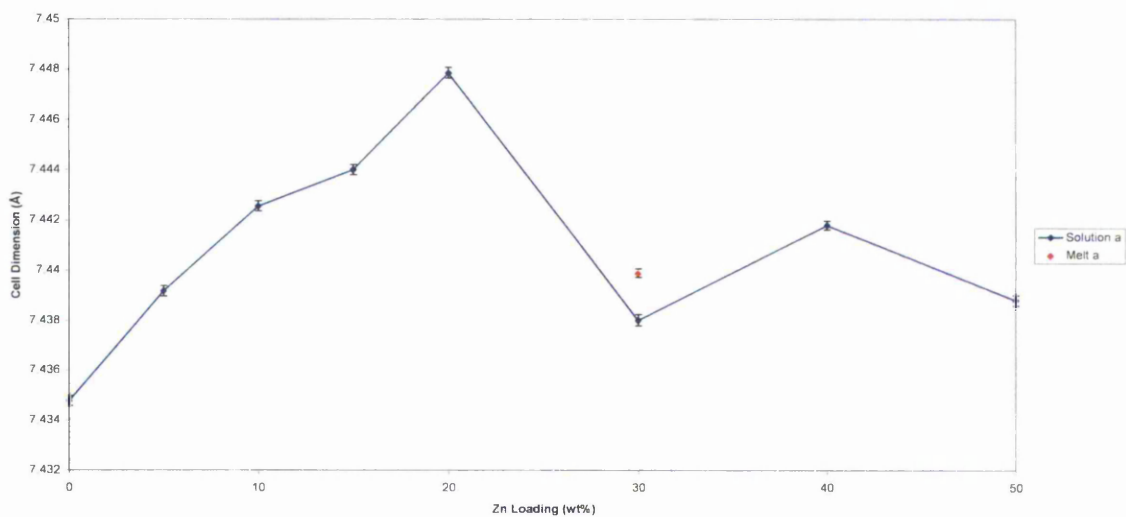


Figure 146: Unit cell parameter *a* for FER with Zn_3N_2 .

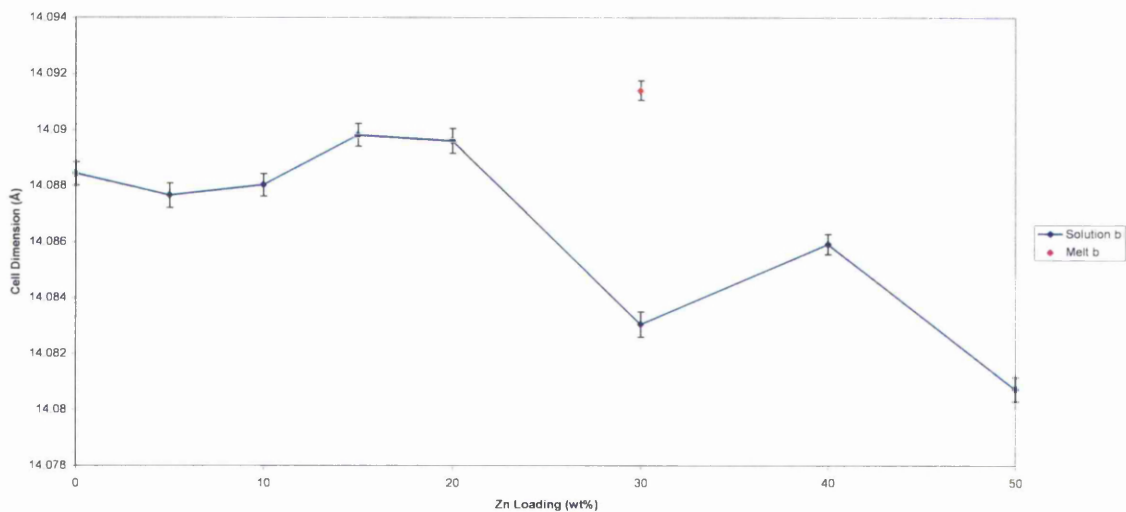


Figure 147: Unit cell parameter *b* for FER with Zn_3N_2 .

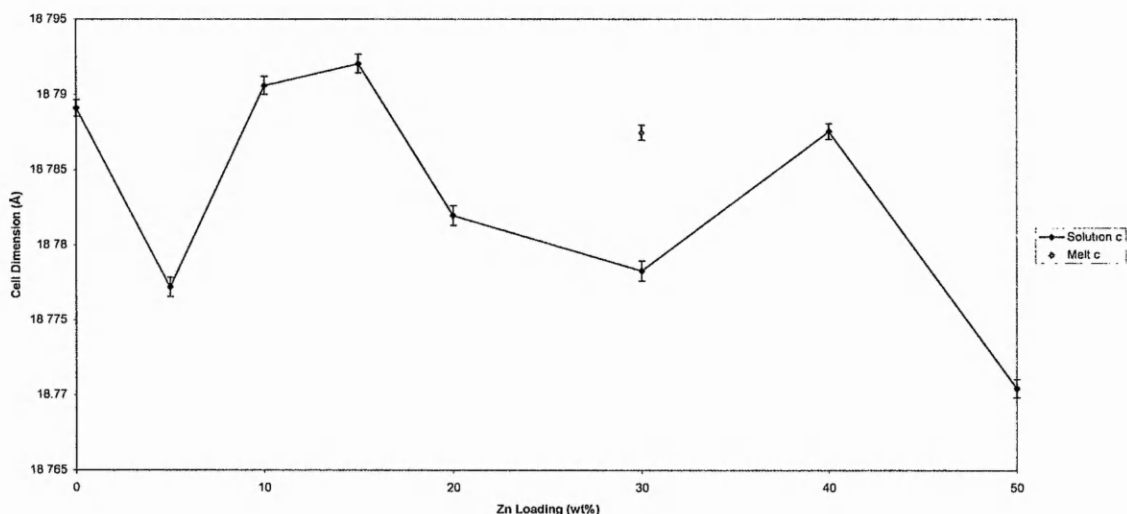


Figure 148: Unit cell parameter c for FER with Zn_3N_2 .

The unit cell parameter a is greater for all samples when compared to the parent zeolite, with the value recorded for the molten salt-treated samples lying among those found for those treated with the solution impregnation. In the b direction there is a general decrease in the unit cell value, which is only significant above a loading of 20 wt%. The b value found for the molten salt sample lies above both the parent zeolite and the entire range of solution-loaded samples. There is no significant change in the c parameter from the value found for the parent zeolite across the solution-loaded range or for the sample treated with the molten salt impregnation method. The experimental errors are insignificant with respect to these trends.

Figure 149 shows the diffuse-reflectance curves obtained for FER samples with Zn_3N_2 .

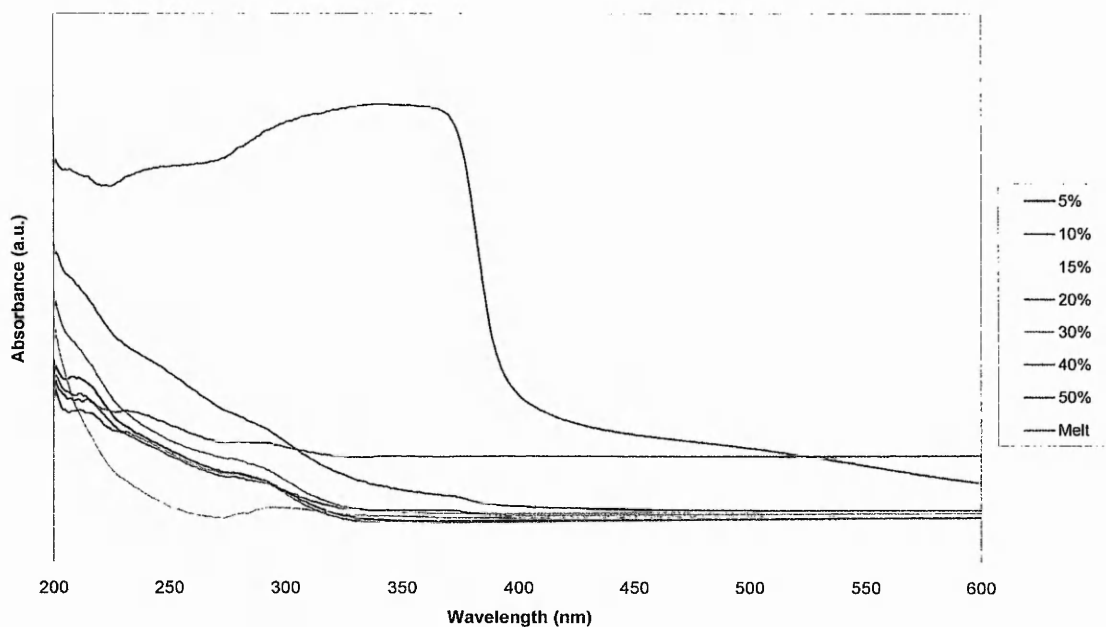


Figure 149: UV Vis data for FER samples with Zn_3N_2 .

No clear absorption edge is seen in all samples, except for that which is loaded with 50 wt% of Zn. The estimated band gap of this sample is 3.24 eV (± 0.0085), which is comparable to the band gap of ZnO.

Figure 150 shows the PL spectra for FER samples with Zn_3N_2 . The E_{PL} values are similar for both samples with a large peak at 2.5 eV, with a smaller peak at ~2.7 eV. The sharp peak at 2.325 eV is a harmonic from the exciting laser. As no Zn_3N_2 absorption was measured by absorption methods this data cannot be compared, yet the values obtained lie within the range of published band gap values for Zn_3N_2 , as discussed in Chapter 7.

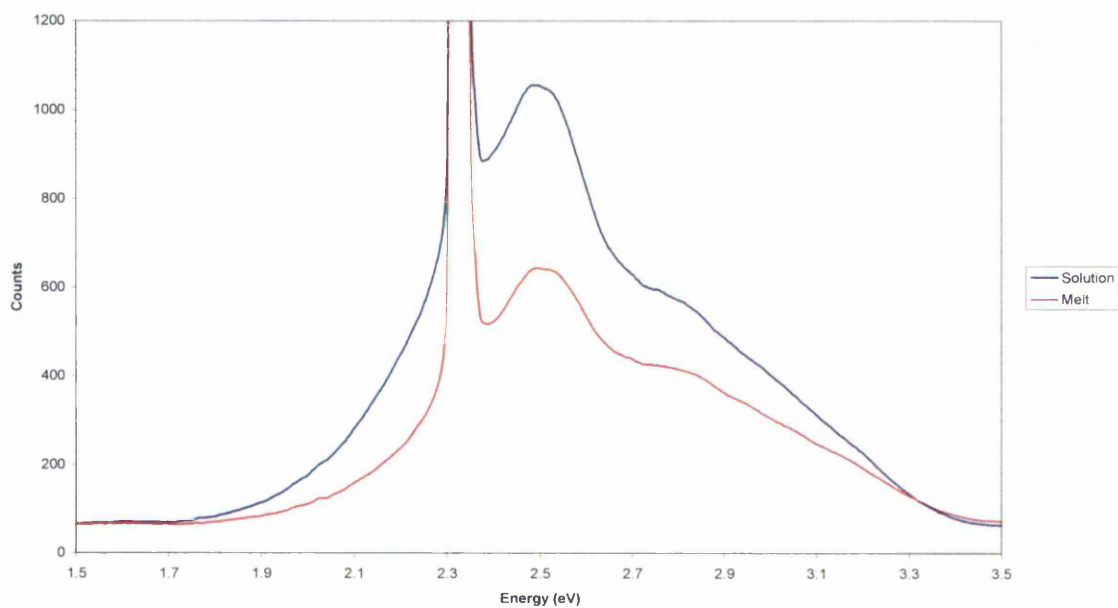


Figure 150: PL Spectra for FER with Zn_3N_2 .

7.2. Discussion and Conclusions

It seems that all three zeolites have withstood the Zn_3N_2 impregnation and synthesis conditions fairly well, with only slight divergences of unit cell parameters across the entire solution-treated loading range and including the molten salt-treated samples.

Unfortunately, however, a band structure was only measured in one sample; FER loaded with 50 wt% Zn.

8. Zinc Oxide

Zinc Oxide (ZnO) is a wide band-gap semiconductor with a band-gap of 3.37 eV.

[59] ZnO occupies both the wurtzite and zinc blende structures. The structure of interest in this project is the wurtzite structure, shown in Figure 151.

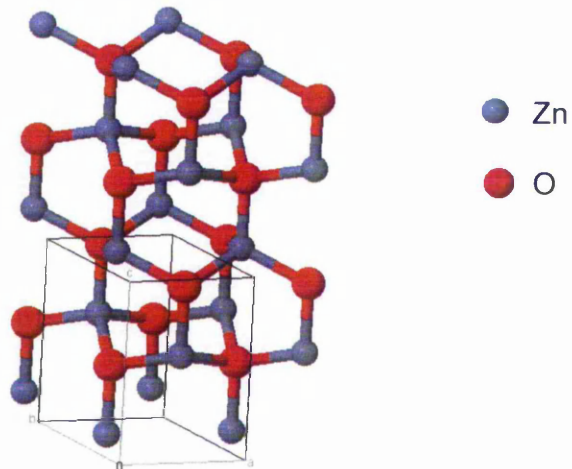


Figure 151: The unit cell of wurtzite ZnO. [116]

The wurtzite form of ZnO generally has the following crystallographic parameters:

Space Group: $P6_3mc$

$a = 3.196 \text{ \AA}$ $b = 3.196 \text{ \AA}$ $c = 5.160 \text{ \AA}$

$\alpha = 90^\circ$ $\beta = 90^\circ$ $\gamma = 120^\circ$

Wurtzite ZnO can be synthesised by oxidising zinc metal, salts or other compounds; such as $Zn(NO_3)_2$ and $ZnCl_2$ at temperatures as high as 1200°C . Zinc Oxide is a white powder that is stable in air at room temperature and pressure and decomposes at 1975°C . ZnO has been used for a very long time as a white pigment in many applications, such as paint, paper and makeup, but has also

been used as an anticorrosive, antibacterial agent and, of course, as a semiconducting material.

ZnO has been extensively studied and is well characterised. Recent research has moved into the formation of nanostructures, such as nanowires and balls and the formation of ZnO clusters within zeolite pores have been characterized. [17, 33, 38, 117, 118] In 2000, Anderson, et al. were able to occlude ZnO within the cage framework of Zn exchanged zeolite A (LTA) by introduction of Zn vapour at 500 °C for 7 days. It was found that there were 9 Zn ions per LTA unit cell; 3 more than were required to balance the charge of the framework. Crystallographically, it was of most interest to see a reduction in the zeolite lattice parameter upon ZnO occlusion, which, in agreement with work done elsewhere, suggests the framework oxygen atoms in the 6-rings being drawn toward the sodalite cage (highlighted in Figure 152)

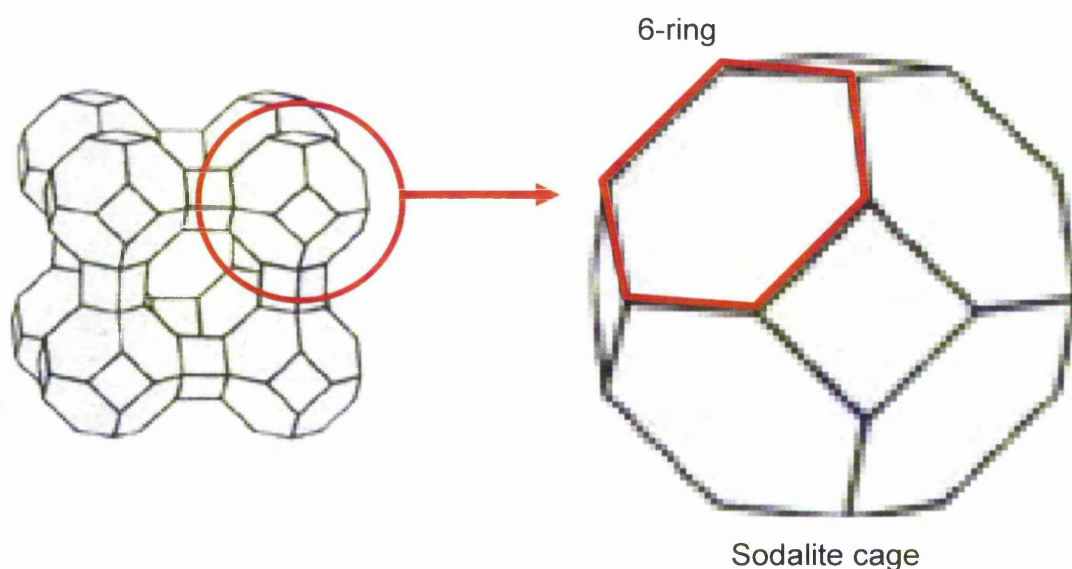


Figure 152: Zeolite A (LTA) with sodalite cage and 6-ring highlighted in red.

Su, et al. reported the introduction of ZnO nanoclusters within faujasite by aqueous impregnation methods in 2006 and presented PL data in which two band gaps larger than that reported for bulk ZnO were recorded (blue-shift). These were attributed to two different sizes of ZnO clusters of 1.7 and 2.5 nm. A compression of the unit cell was also noticed in this work, yet the reason given was due to ion exchange, resulting in a change in crystal symmetry.

In 2009 Song, et al. reported ZnO occlusion in zeolite L also via aqueous impregnation. In this work macrocrystalline ZnO particles were seen on the surface of the zeolite particles as well as within the pore structures. UV-Vis absorption data were recorded and by applying the Brus equation particle diameters were estimated at 0.62 nm, suggesting a portion of ZnO occlusion within the pore structure. Upon increasing loading the absorption peak red-shifted, indicating an increase in particle size. These results were also confirmed by PL data.

8.1. Results

8.1.1. ZSM-5

Diffraction profiles were refined using Topas Academic V4.1 against the ZSM-5 structure reported by Li, et al. ^[89] and ZnO structure reported by Rozale, et al. ^[119]

The XRD and Rietveld profiles from solution-treated samples are shown in Figure 153 to Figure 157.

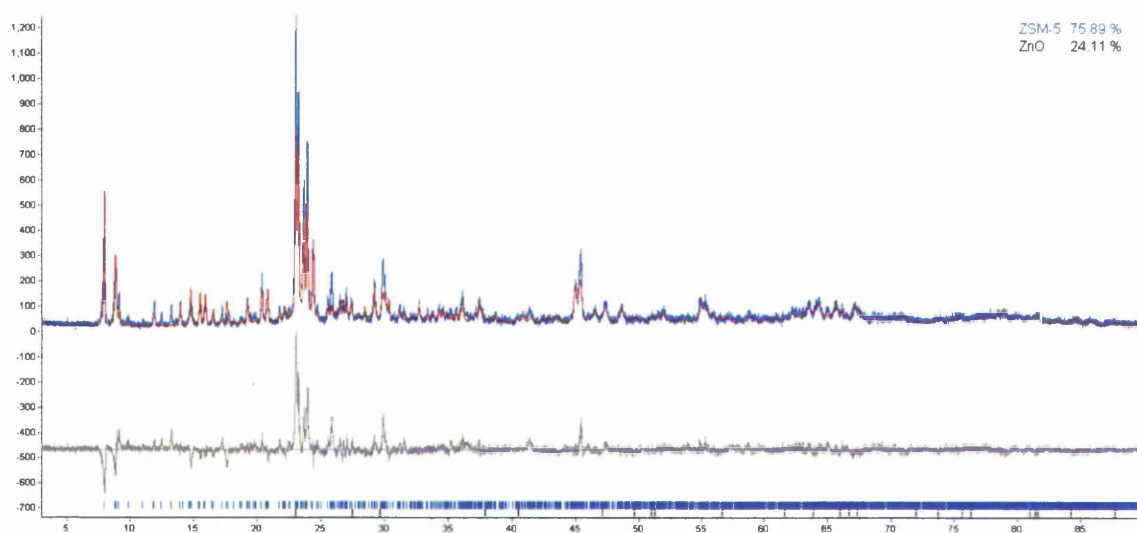


Figure 153: Rietveld fit for solution-treated ZSM-5 with 5wt% Zn as ZnO.

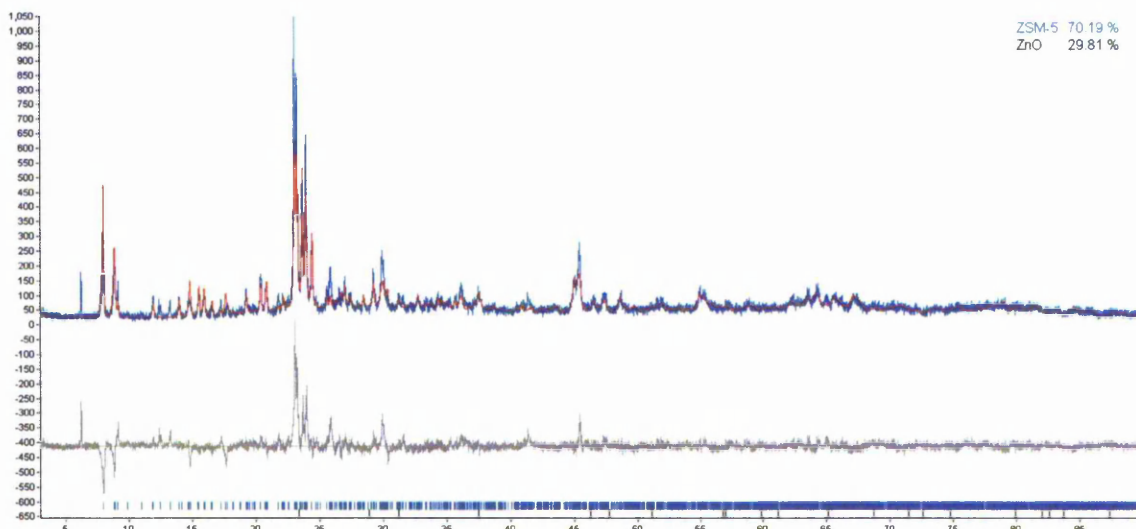


Figure 154: Rietveld fit for solution-treated ZSM-5 with 10wt% Zn as ZnO.

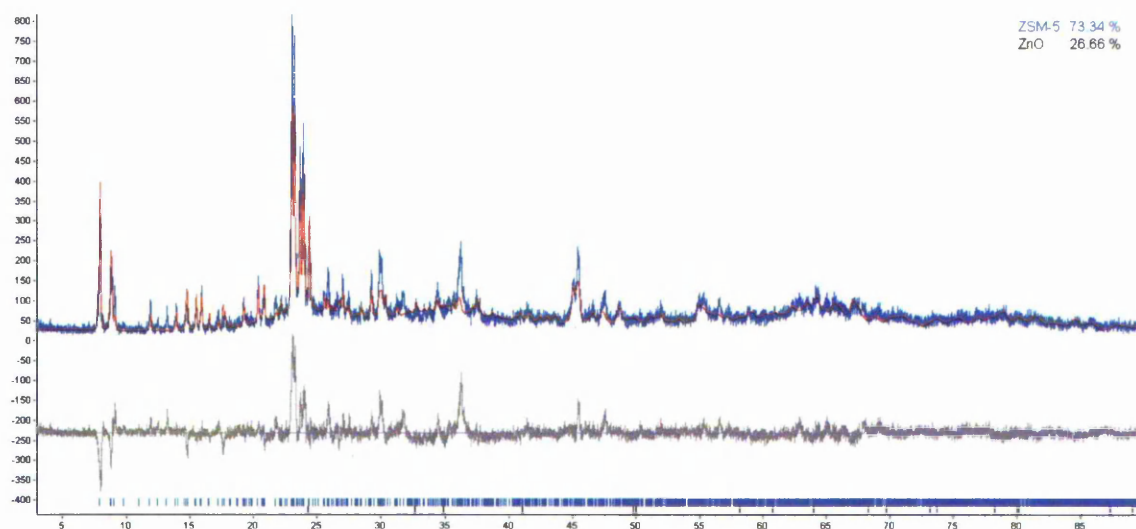


Figure 155: Rietveld fit for solution-treated ZSM-5 with 15wt% Zn as ZnO.

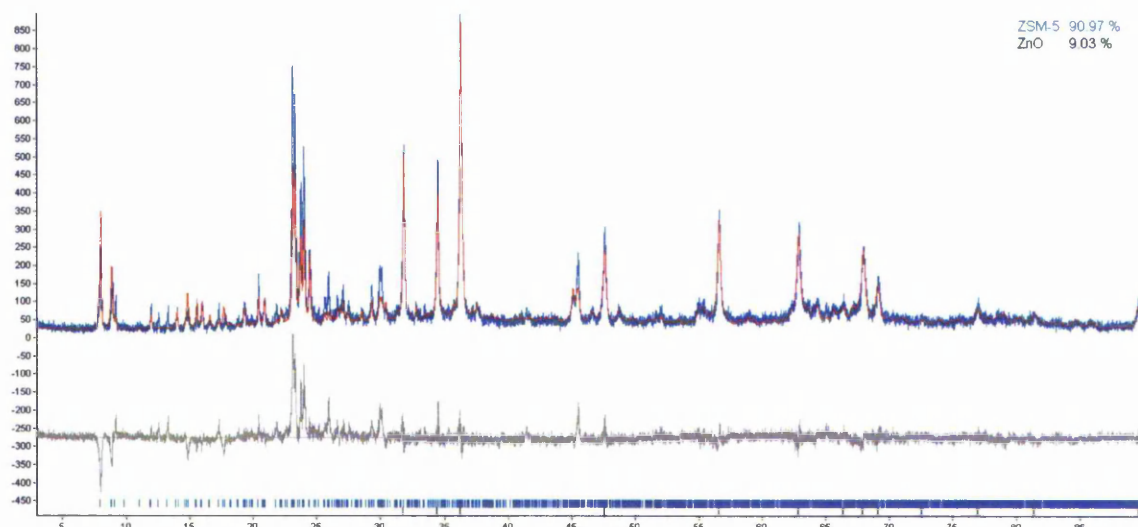


Figure 156: Rietveld fit for solution-treated ZSM-5 with 30wt% Zn as ZnO.

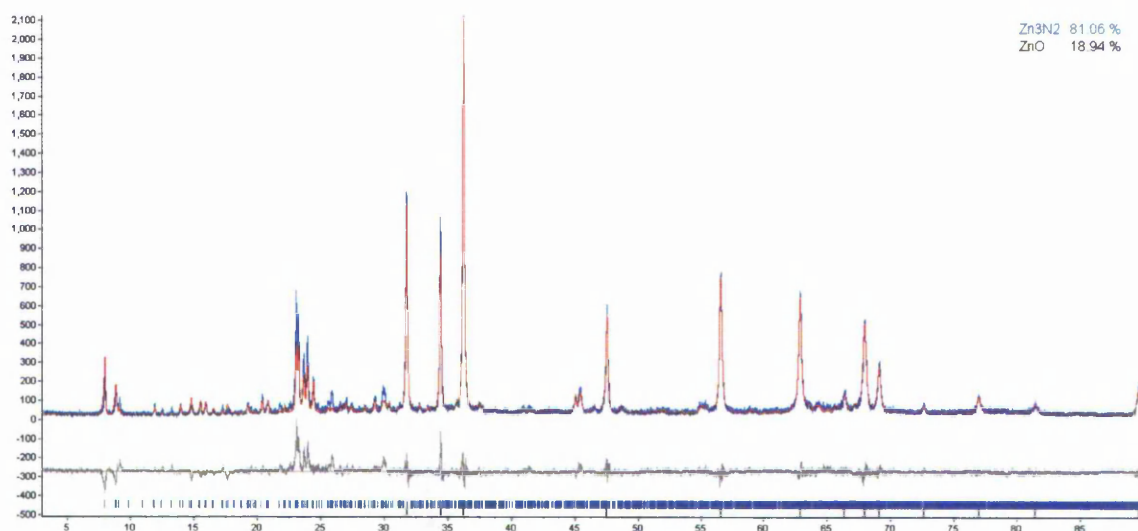


Figure 157: Rietveld fit for solution-treated ZSM-5 with 50wt% Zn as ZnO.

The Rietveld profiles shown in Figure 153 to Figure 157 show that the process of ZnO inclusion slightly reduces the crystallinity of the host zeolite, which is characterised by a gradual increase in profile noise as the Zn loading increases, but which is dwarfed by the emergence of ZnO diffraction. The peaks related to ZnO are evident at 30wt% loading of Zn. This coincides with the calculated maximum main pore filling Zn loading of 23.81wt% as per the following calculations:

- Pore dimensions: 0.53 x 0.56 x 1.974 nm
- ZnO unit cell dimensions (2ZnO): 0.3249 x 0.3249 x 0.5206 nm
- Approx. Zn atoms per pore: 21
- Total Zn mass: 1373.19 a.m.u.
- Zeolite Unit Cell Mass: 5766.76 a.m.u.
- (Zn Mass/Zeolite Mass) x 100: 23.81 wt%

Therefore the data suggests that at loadings of 15wt% and below ZnO is present as small crystallites and at calculated loadings of above 23.81wt% as an extra-zeolite phase.

The Rietveld fit shown in Figure 158 was taken from the molten salt-treated sample.

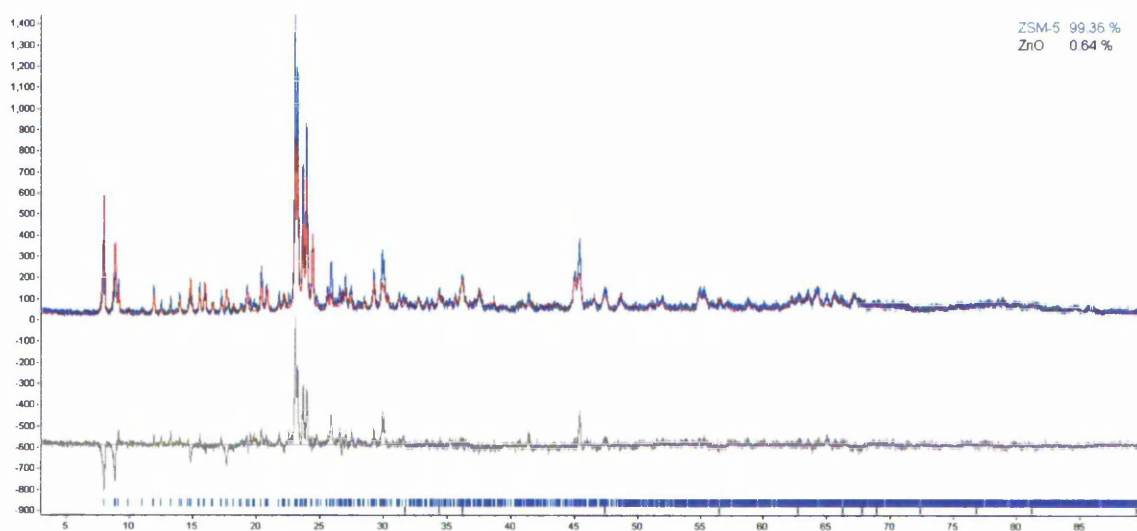


Figure 158: Rietveld fit for molten salt-treated ZSM-5 with ZnO.

It is clear from Figure 158 that the zeolite structure is still intact upon molten salt impregnation and subsequent calcination. The absence of any diffraction peaks from ZnO suggests that any ZnO phase is present as small crystallites.

The lattice parameters from ZSM-5 samples with ZnO using both the solution and molten salt impregnation methods derived from Rietveld analysis of the XRD data are shown graphically in Figure 159.

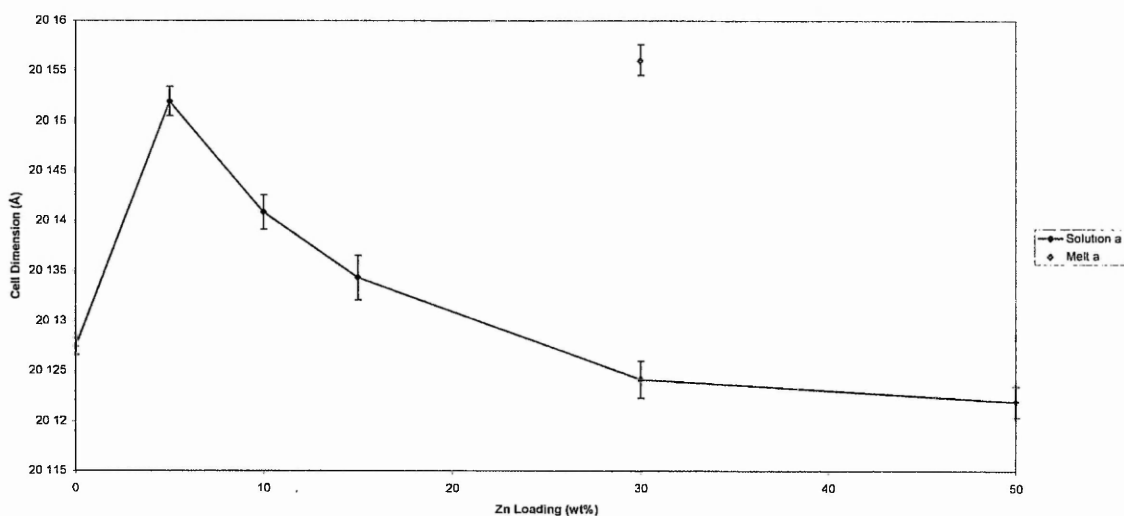


Figure 159: Unit cell parameter a for ZSM-5 with ZnO.

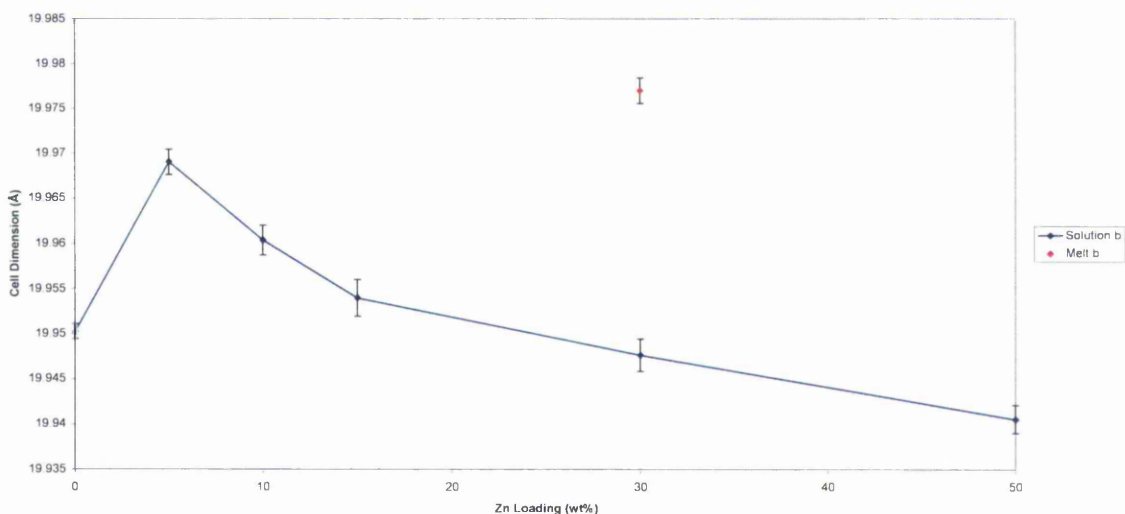


Figure 160: Unit cell parameter *b* for ZSM-5 with ZnO.

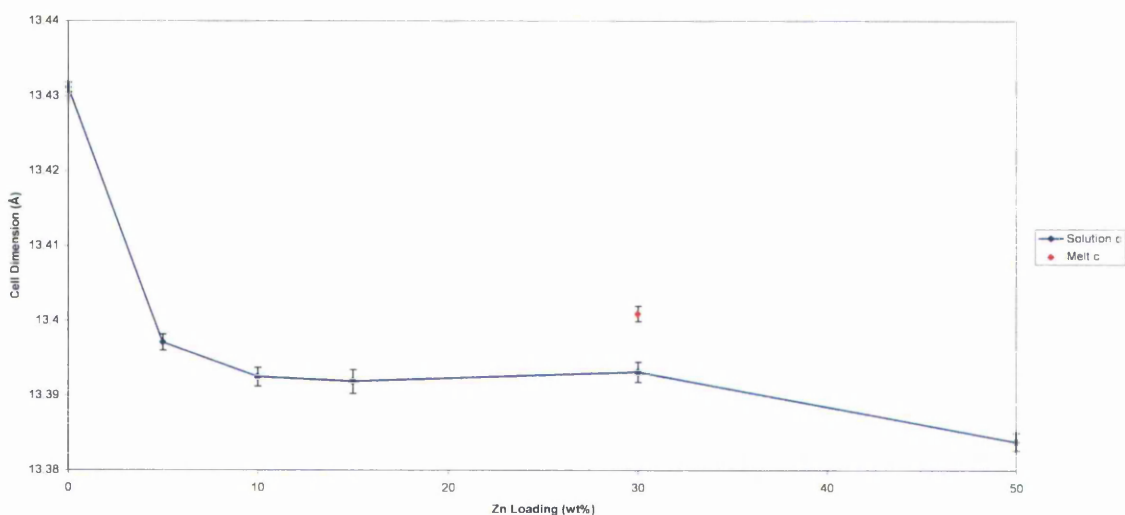


Figure 161: Unit cell parameter *c* for ZSM-5 with ZnO.

The XRD data shows that the unit cell dimensions of the parent zeolite in the *a* and *b* directions are increased upon inclusion of ZnO and that there is a general decrease in cell dimension in all three directions upon increasing Zn loading above 5 wt% of Zn. The *c* parameter (that which runs the length of the main channel) is dramatically decreased upon impregnation and follows the same pattern as *a* and *b* thereafter. The unit cell dimensions in all three directions are greater in the

sample treated by the molten salt impregnation than the salt solution method. This suggests the zeolite pore structure is somehow supported by guest phase when using the molten salt inclusion method. Experimental errors are insignificant with respect to these changes.

In the HRTEM image in Figure 162(a), it is clear that the zeolite pores are left intact and there are no extra-zeolite phases of ZnO; in agreement with XRD studies. Figure 162(b) clearly shows that ZnO nanoparticles are dispersed throughout the pore structure when the molten salt process is employed; which accounts for the very low ZnO content determined by XRD Rietveld analysis (0.64 %). The EDX spectrum in Figure 162(c) confirms the presence of Zn, as well as Si and O from the zeolite and Cu from the sample holder.

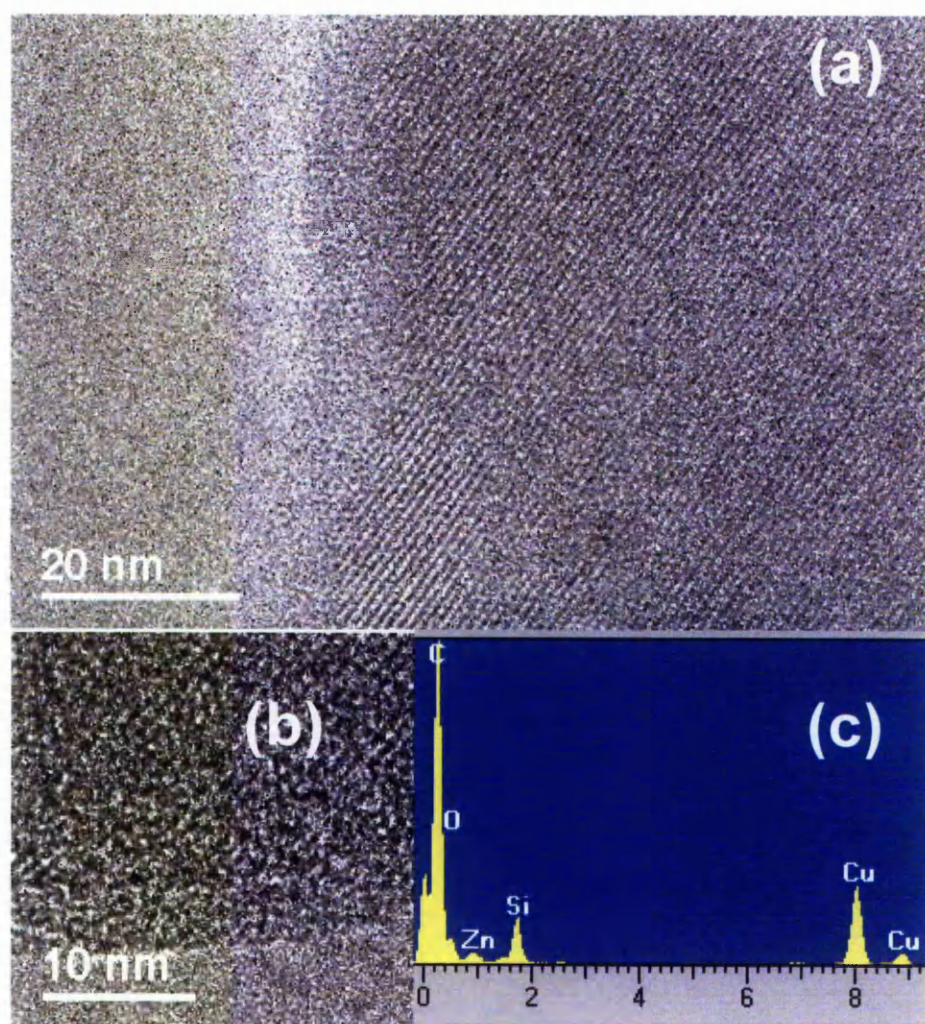


Figure 162: (a) HRTEM image of ZSM-5 with ZnO from the molten salt process. (b) An enlarged HRTEM image showing a rosary pattern of black spots along the principal channels. (c) EDX spectrum showing Zn.

Figure 163 shows the UV-visible diffuse reflectance curves obtained for all ZSM-5 samples impregnated with ZnO.

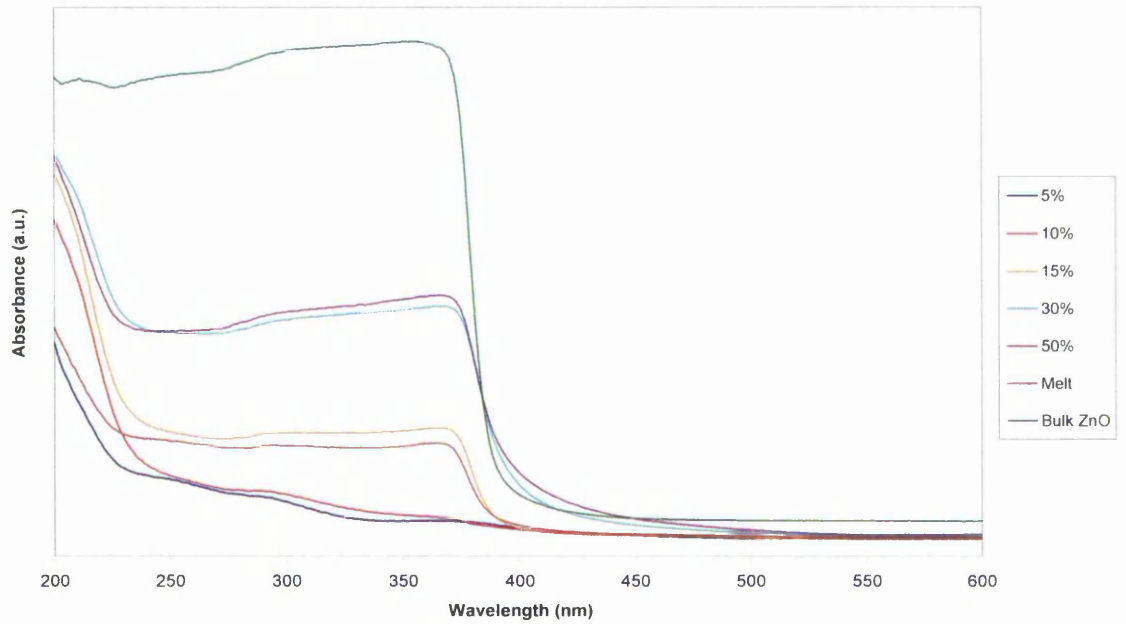


Figure 163: UV Vis Data for ZSM-5 samples with ZnO.

The estimated band gaps are shown in Table 8 and Figure 164, which show that the band gap of ZnO remains relatively similar within experimental error.

Table 8: Band gap values for ZSM-5 samples with ZnO.

Impregnation Method	Band Gap (eV)
Molten Salt	3.275
5% Solution	N/A
10% Solution	N/A
15% Solution	3.266
30% Solution	3.24
50% Solution	3.25
Bulk ZnO	3.265

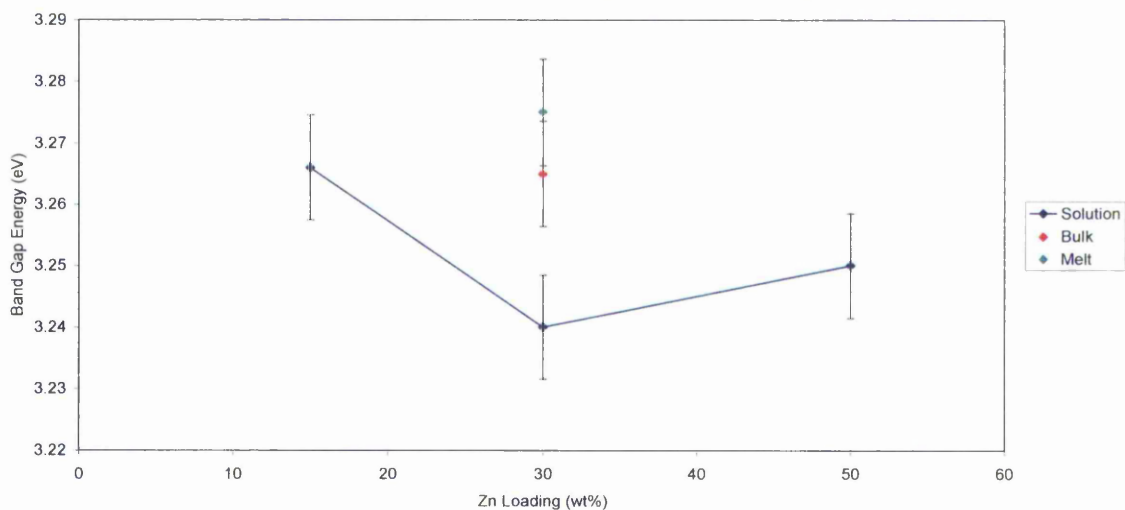


Figure 164: Band gap values for ZSM-5 samples with ZnO.

As Figure 165 shows, the PL emission peak (E_{PL}) of ZnO is slightly blue-shifted upon zeolite inclusion using a 15 % solution with respect to the bulk value and is further shifted by using the melt process, although the emission in the case of the molten salt-treated sample is partly masked by the emission from the zeolite, which can be attributed to the high dispersion of ZnO within the zeolite.

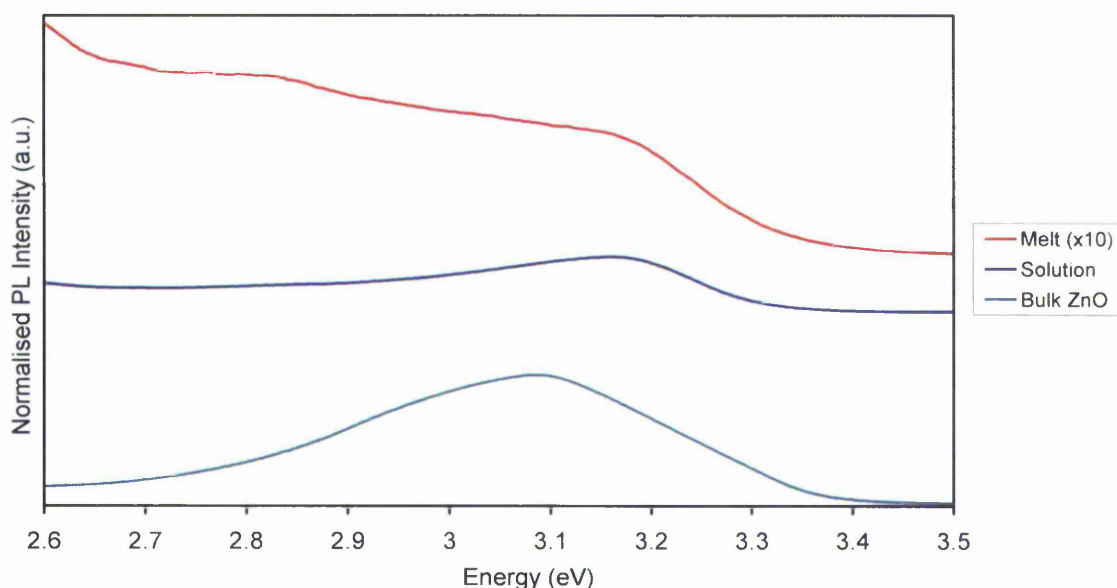


Figure 165: PL spectra for ZSM-5 with ZnO.

The values of E_{PL} are shown in Table 9.

Table 9: E_{PL} values for ZSM-5 with ZnO.

Material	Energy (eV)
ZSM-5/ZnO Melt	3.18 (estimated)
ZSM-5/ZnO 15% Solution	3.161
Bulk ZnO	3.084

8.1.2. Faujasite

Diffraction profiles were refined using Topas Academic V4.1 against the faujasite structure reported by Parise, et al. ^[91] and ZnO structure reported by Rozale, et al. ^[119] Diffraction profiles were refined using Topas Academic V4.1 against the faujasite structure reported by Parise, et al. ^[91] and Zn₃N₂ structure reported by Partin, et al. ^[107] The XRD and Rietveld profiles from solution-treated samples are shown in Figure 166 to Figure 172.

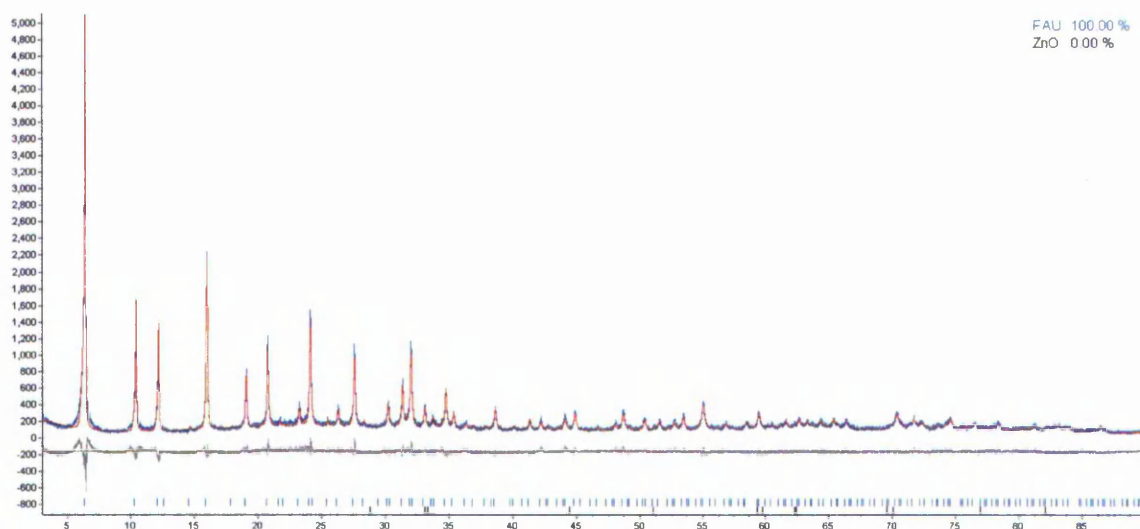


Figure 166: Rietveld fit for solution-treated FAU with 5wt% Zn as ZnO.

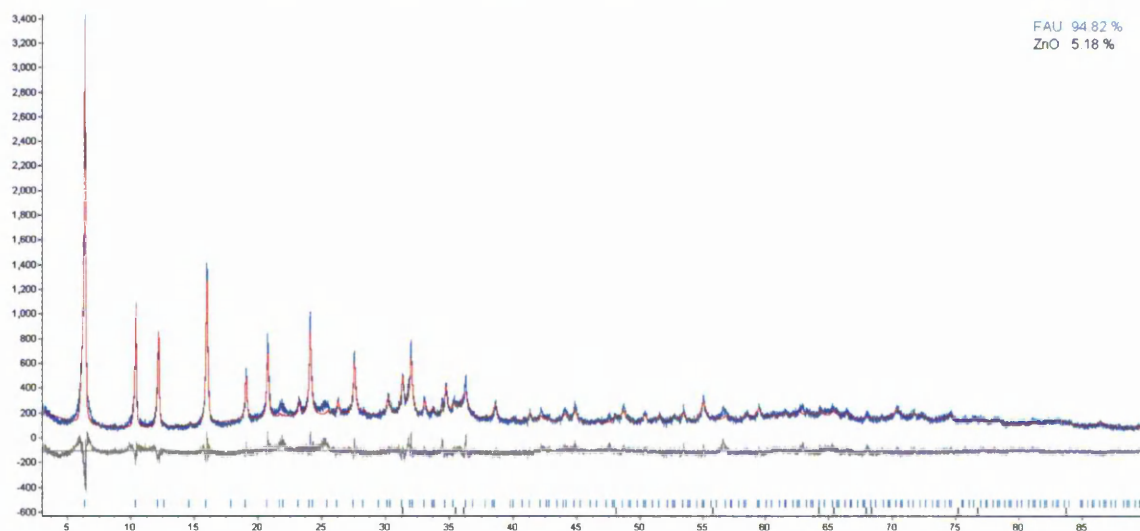


Figure 167: Rietveld fit for solution-treated FAU with 10wt% Zn as ZnO.

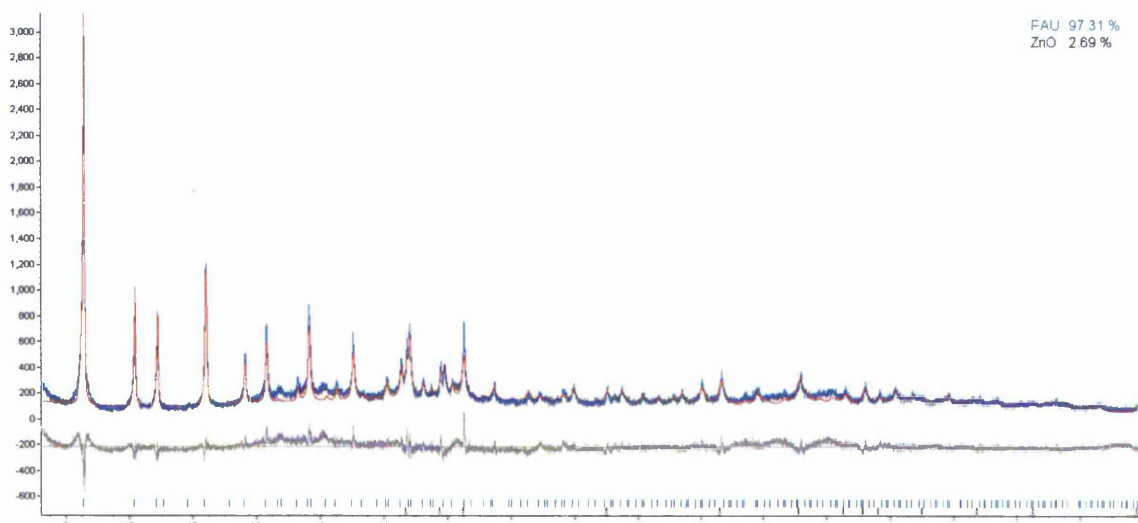


Figure 168: Rietveld fit for solution-treated FAU with 15wt% Zn as ZnO.

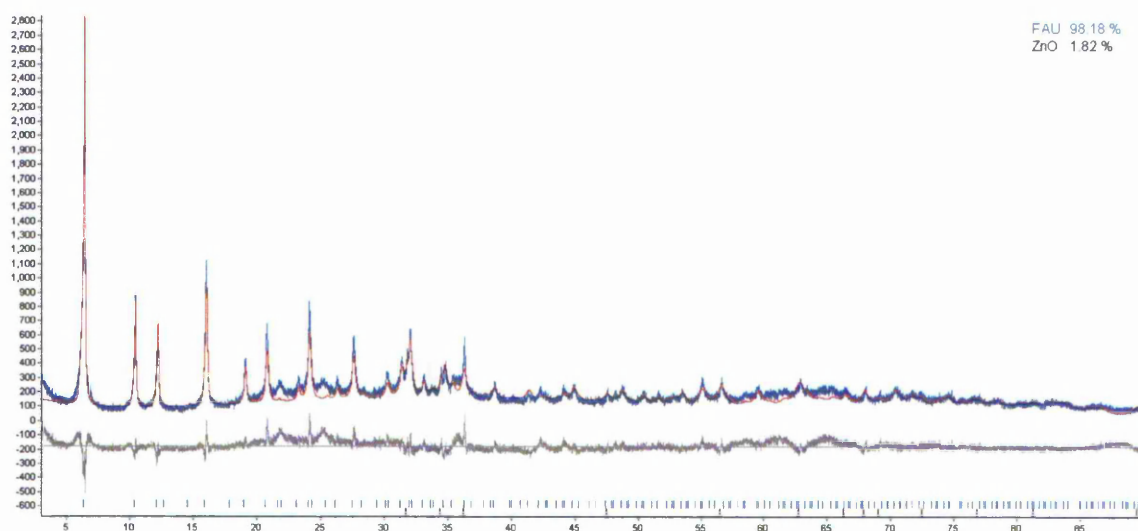


Figure 169: Rietveld fit for solution-treated FAU with 20wt% Zn as ZnO.

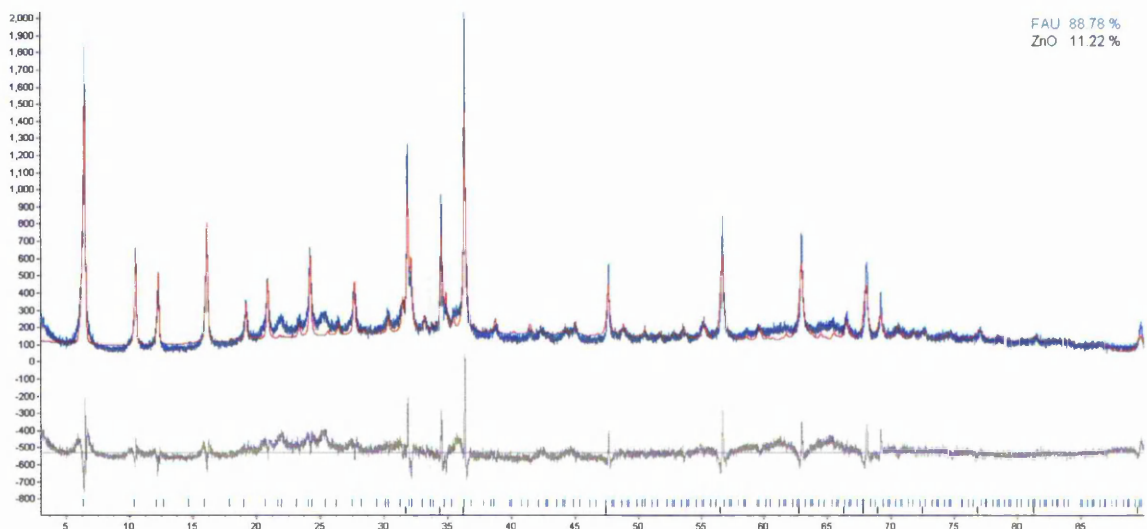


Figure 170: Rietveld fit for solution-treated FAU with 30wt% Zn as ZnO.

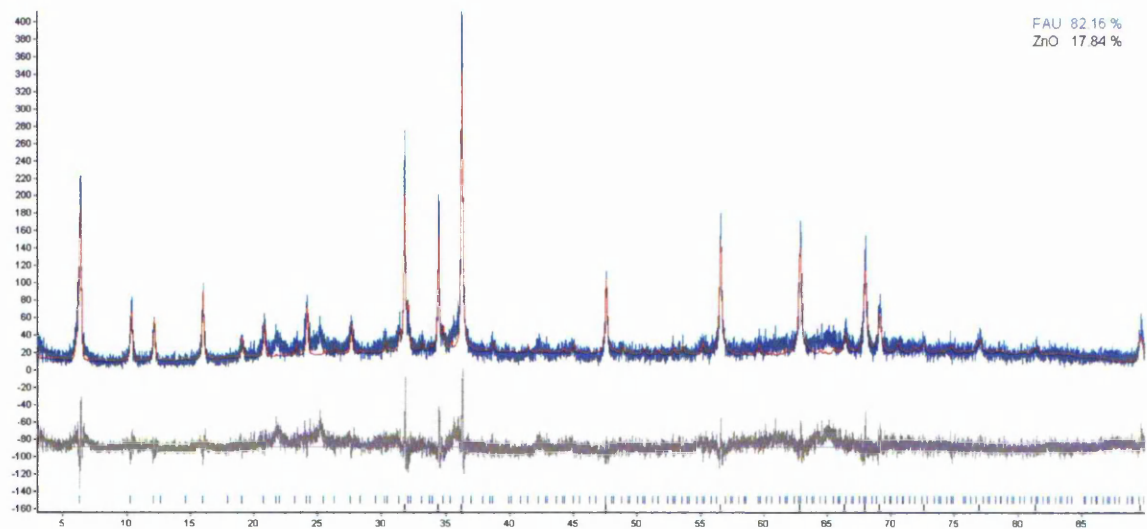


Figure 171: Rietveld fit for solution-treated FAU with 40wt% Zn as ZnO.

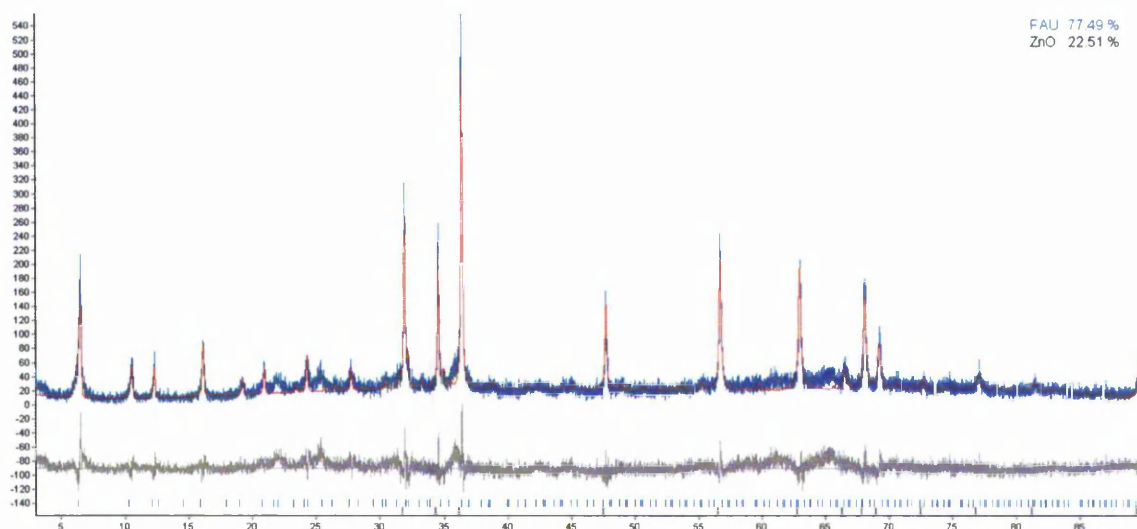


Figure 172: Rietveld fit for solution-treated FAU with 50wt% Zn as ZnO.

The Rietveld profiles shown in Figure 166 to Figure 172 show that the process of ZnO inclusion reduces the crystallinity of the host zeolite, characterised by an increase in profile noise with increasing Zn loading, indicating an increase in amorphous content. The peaks related to ZnO don't become noticeable until a Zn loading of 30wt%, suggesting that ZnO is present as small crystallites. Given the amorphisation of the host zeolite phase an estimation of maximum possible loading of Zn would not be the best method of understanding this experiment. Calculations do, however, provide a maximum pore filling Zn loading as 45.36wt%:

- Cage dimensions: 1.304 x 1.304 x 1.304 nm
- ZnO unit cell dimensions (2ZnO): 0.3249 x 0.3249 x 0.5206 nm
- Approx. Zn atoms per cage: 80
- Total Zn mass: 5231.2 a.m.u.
- Zeolite Unit Cell Mass: 11533.51 a.m.u.
- (Zn Mass/Zeolite Mass) x 100: 45.36 wt%

Due to the breakdown of the zeolite as Zn loading increases this estimation does not fully represent this situation. The reasons for zeolite amorphisation may be related to the amount of Zn that is available to occupy the pores, as mentioned previously.

The Rietveld fit shown in Figure 173 was taken from the molten salt-treated sample.

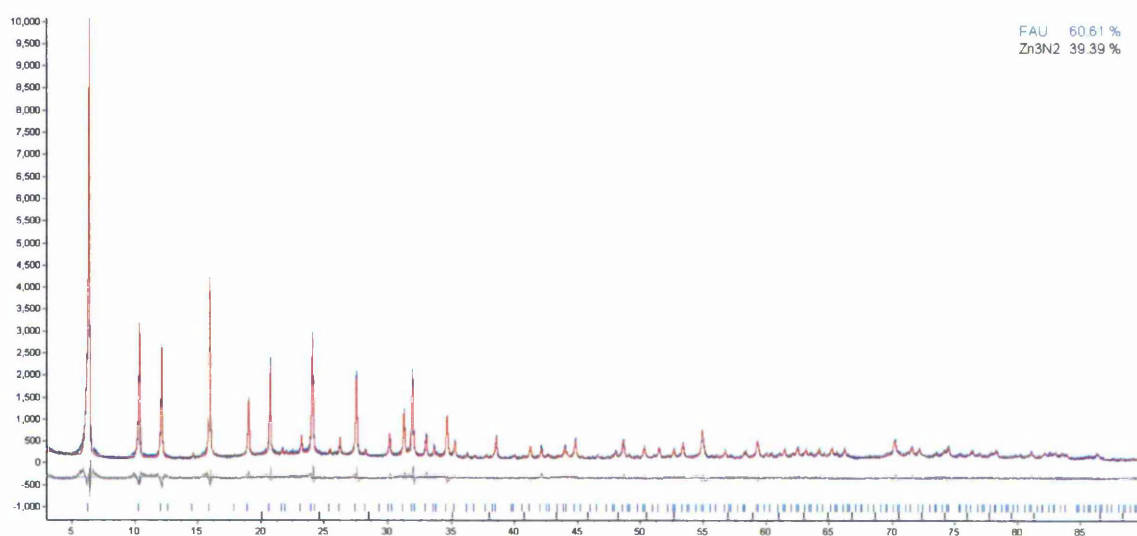


Figure 173: Rietveld fit for molten salt-treated FAU with ZnO.

It is clear from Figure 173 that the zeolite structure is still intact upon molten salt impregnation and subsequent calcination and there is no visible diffraction from ZnO, indicating the ZnO is present as small crystallites that have not destroyed the zeolite framework.

The lattice parameters from FAU samples with ZnO using both the solution and molten salt impregnation methods derived from Rietveld analysis of the XRD data are shown graphically in Figure 174.

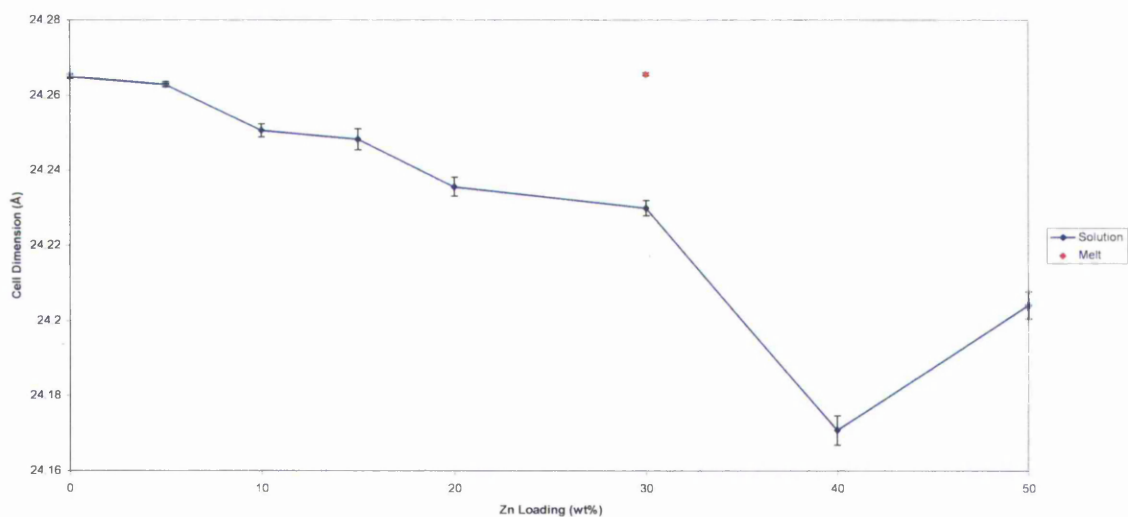


Figure 174: Unit cell parameters for FAU with ZnO.

Figure 174 shows a general decrease in the unit cell parameter of FAU with increased loading of Zn via the solution-based impregnation, with a slight increase from 40 to 50 wt% of Zn. By employing the molten salt method, however, the unit cell parameter is comparable to that of the parent zeolite and is, in fact, very slightly greater than that of the parent zeolite. Experimental errors are insignificant in comparison to these trends.

Figure 175 shows the diffuse-reflectance curves obtained for FAU samples impregnated with ZnO.

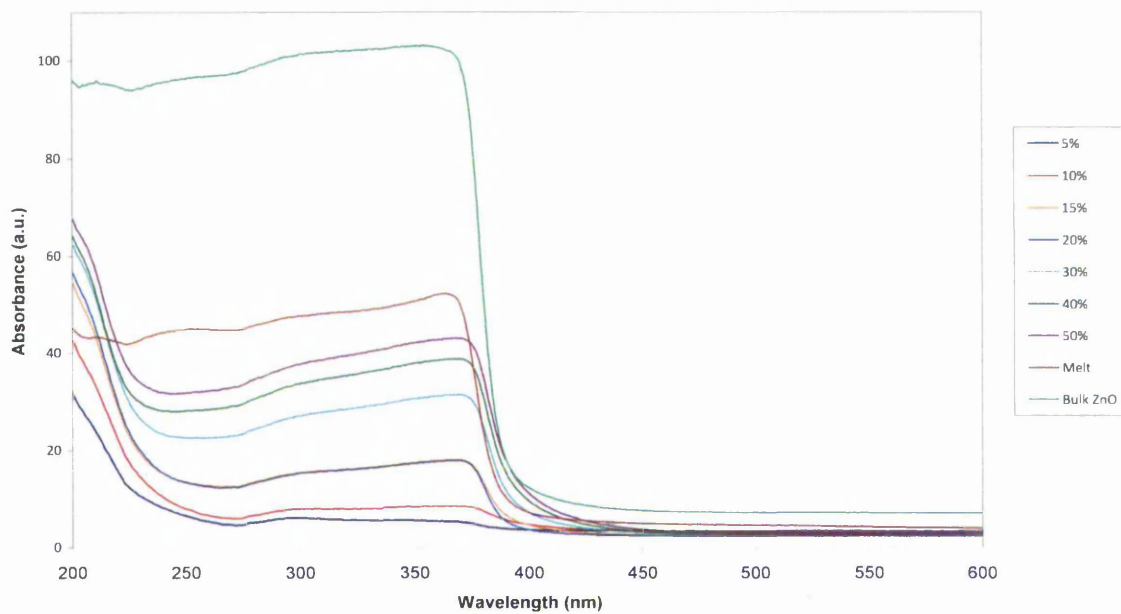


Figure 175: UV Vis Data for FAU samples with ZnO.

As is clear, an estimate of the ZnO band gap in the samples with 5 and 10 wt% is not possible, either due to the low loading or the absence of any ZnO being formed. The band gaps of the other samples, however, are given in Table 10 and displayed graphically in Figure 176.

Table 10: Band gap values for FAU samples with ZnO.

Impregnation Method	Band Gap (eV)
Molten Salt	3.283
5% Solution	N/A
10% Solution	N/A
15% Solution	3.245
20% Solution	3.245
30% Solution	3.24
40% Solution	3.24
50% Solution	3.24
Bulk ZnO	3.265

Figure 176 shows that the band gap of ZnO is significantly reduced, beyond experimental error, with respect to the bulk when impregnated in FAU via the solution-based impregnation and remains fairly constant across the Zn loading range of 15 – 50 wt%. The band gap of the sample treated by the molten salt method, however, increases in comparison to the bulk.

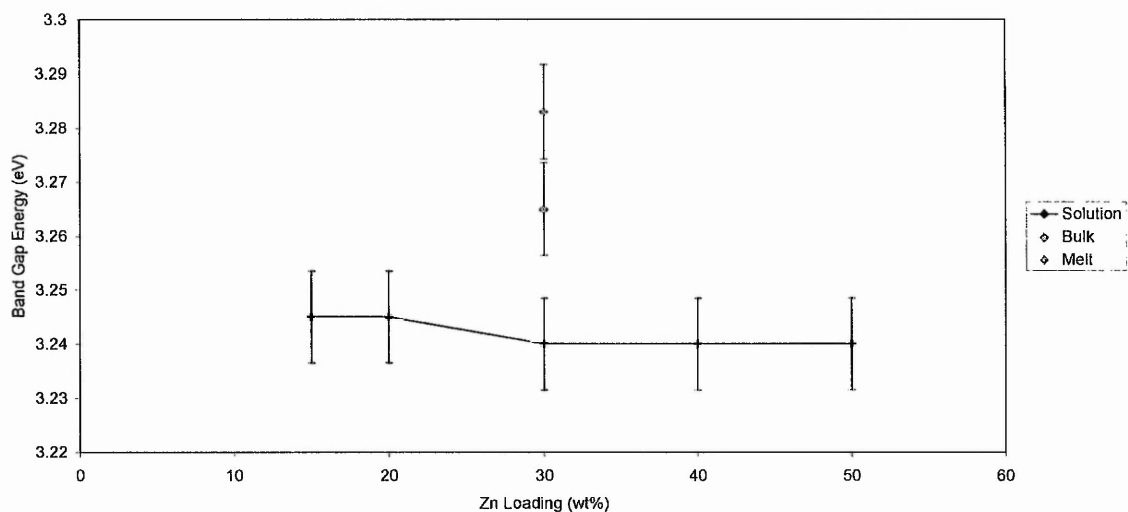


Figure 176: Band gap values for FAU samples with ZnO.

Figure 177 shows the PL spectrum of FAU with ZnO treated with the molten salt impregnation against that of bulk ZnO.

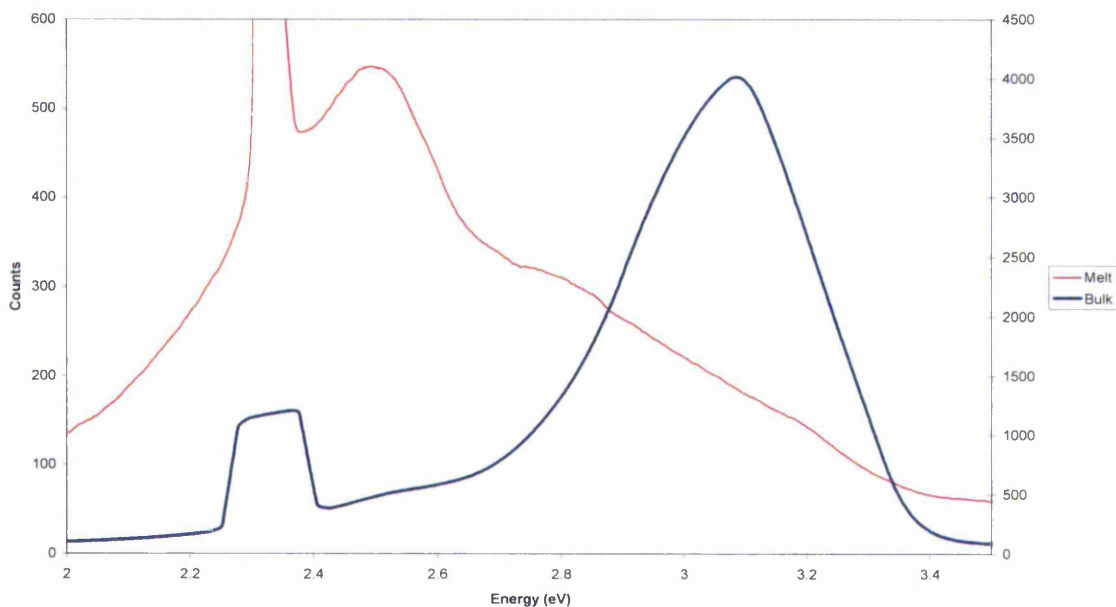


Figure 177: PL spectrum of FAU with ZnO via molten salt impregnation.

It is clear that the major peak in the spectrum of bulk ZnO at 3.1 eV is no longer visible in the spectrum of FAU with ZnO. This may be due to a relatively low loading of ZnO, resulting in the peak by the subtle luminescence from the zeolite framework, which is centred at ~2.5 eV, overshadowing the peak from the ZnO band gap. The sharp (or truncated in the case of the bulk spectrum) peak at 2.325 eV is a harmonic from the exciting laser.

8.1.3. Ferrierite

Diffraction profiles were refined using Topas Academic V4.1 against the ferrierite structure reported by Bull, et al. [92] and ZnO structure reported by Rozale, et al. [119] The XRD and Rietveld profiles from solution-treated samples are shown in Figure 178 to Figure 183.

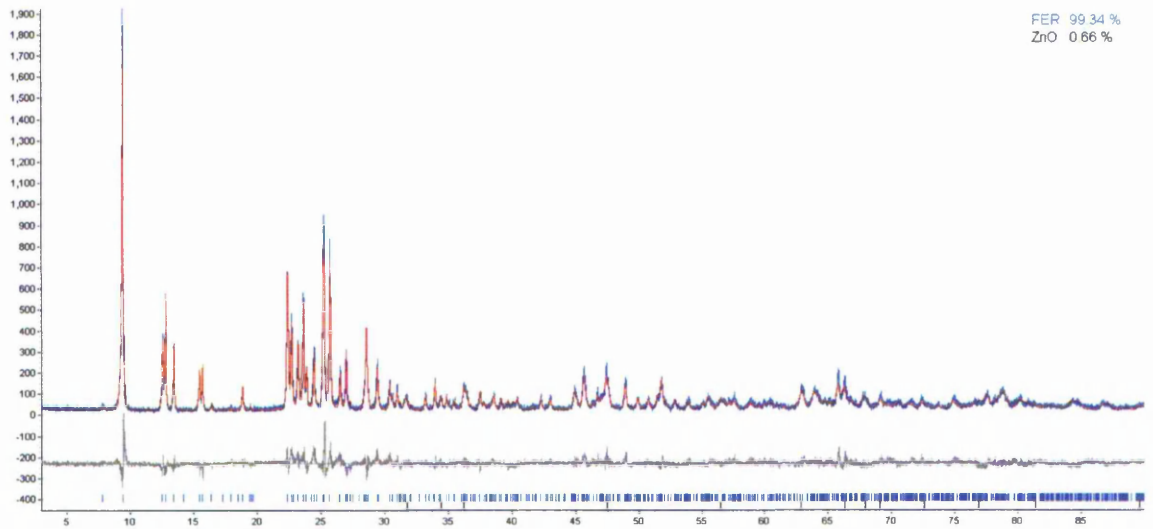


Figure 178: Rietveld fit for solution-treated FER with 5wt% Zn as ZnO.

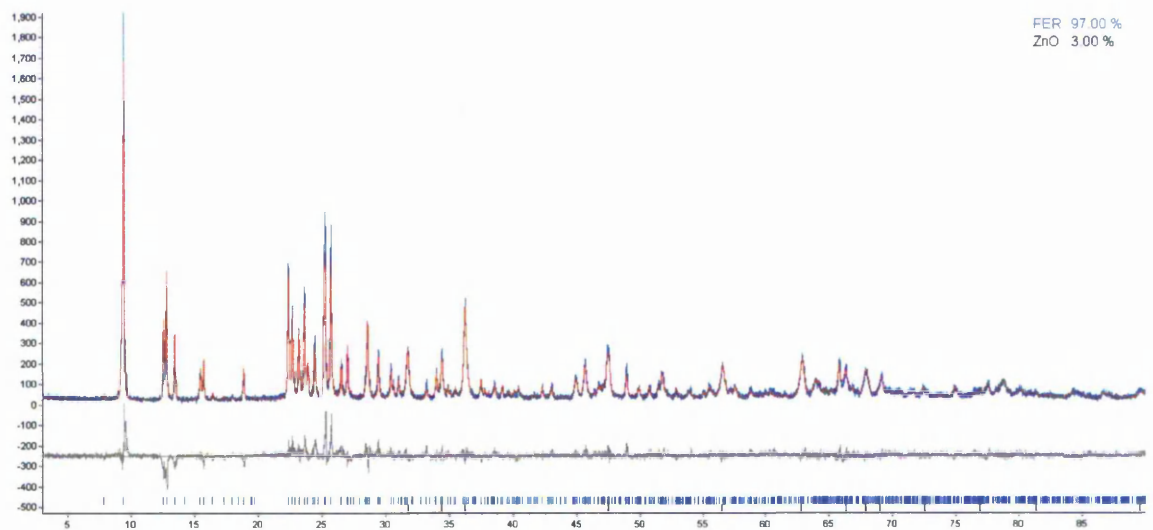


Figure 179: Rietveld fit for solution-treated FER with 10wt% Zn as ZnO.

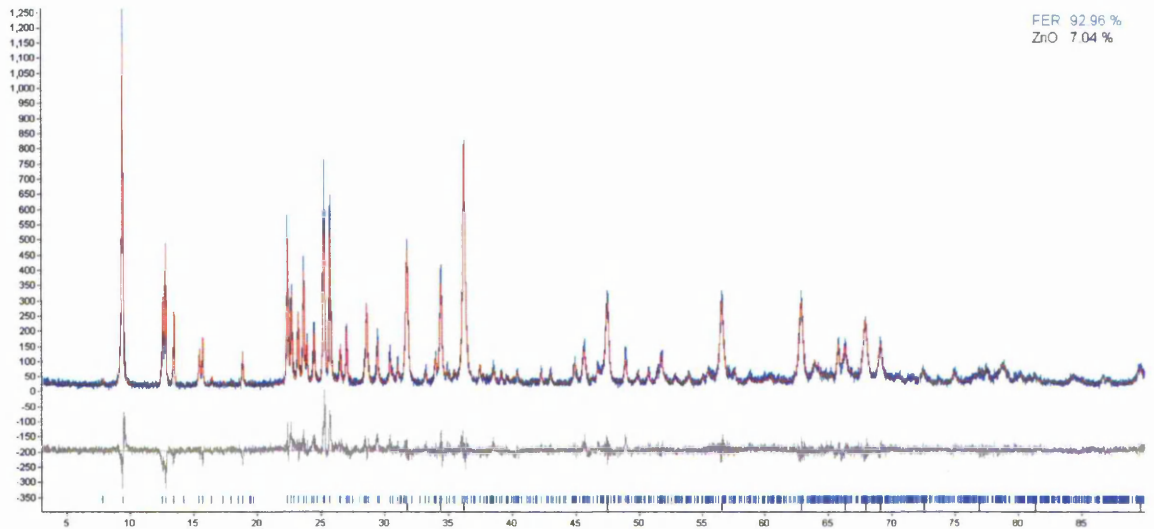


Figure 180: Rietveld fit for solution-treated FER with 20wt% Zn as ZnO.

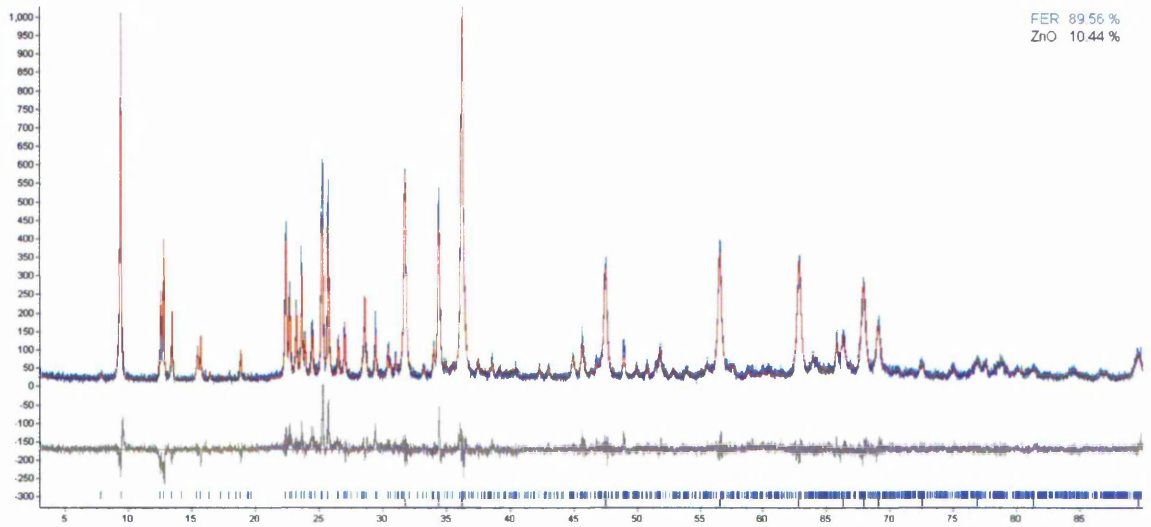


Figure 181: Rietveld fit for solution-treated FER with 30wt% Zn as ZnO.

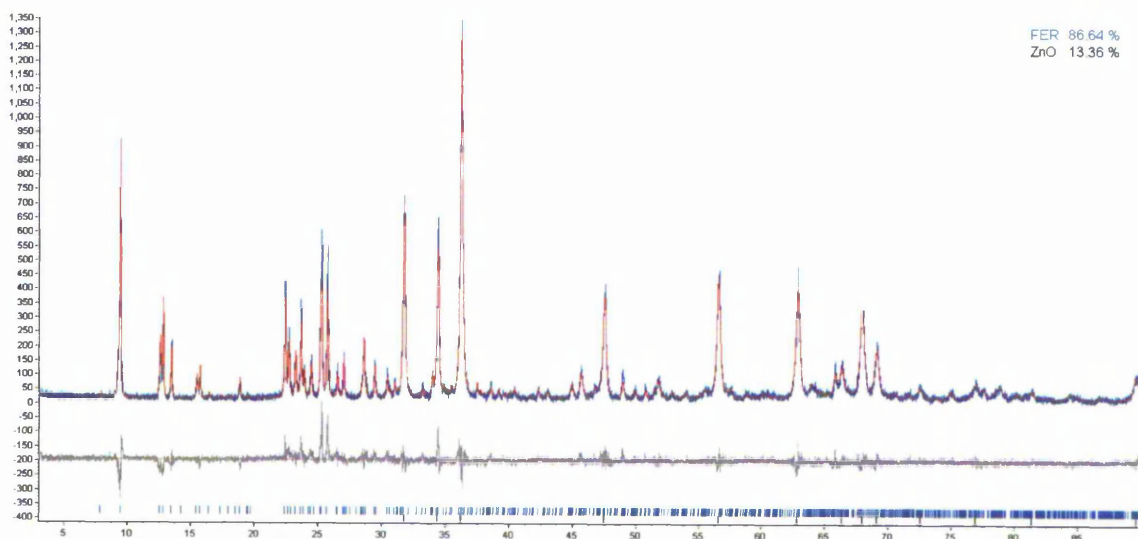


Figure 182: Rietveld fit for solution-treated FER with 40wt% Zn as ZnO.

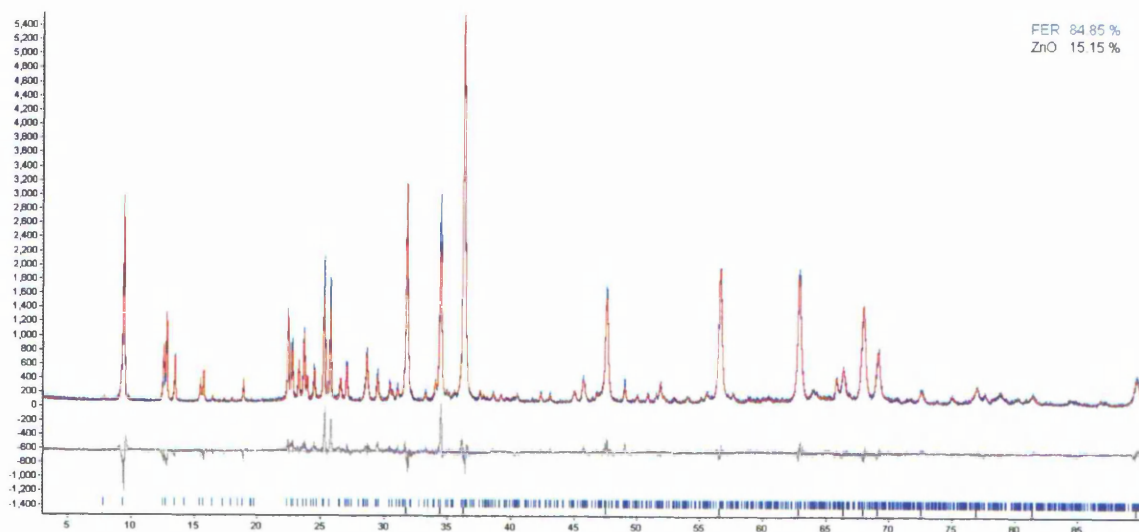


Figure 183: Rietveld fit for solution-treated FER with 50wt% Zn as ZnO.

The Rietveld profiles shown in Figure 178 to Figure 183 suggest that the process of ZnO inclusion does not affect the crystallinity of the host zeolite. Unlike ZnO occlusion in faujasite and ZSM-5, in ferrierite the ZnO peaks increase in intensity gradually with no significant steps in rate of increase. This suggests that ZnO is not occluded within the FER pore structure at Zn loadings of 5wt% and above (approximately 1.7 Zn atoms per unit cell). This, however, does not explain the

changes in unit cell parameters and band gaps of the samples as will be explained later.

The Rietveld fit shown in Figure 184 was taken from the molten salt-treated sample.

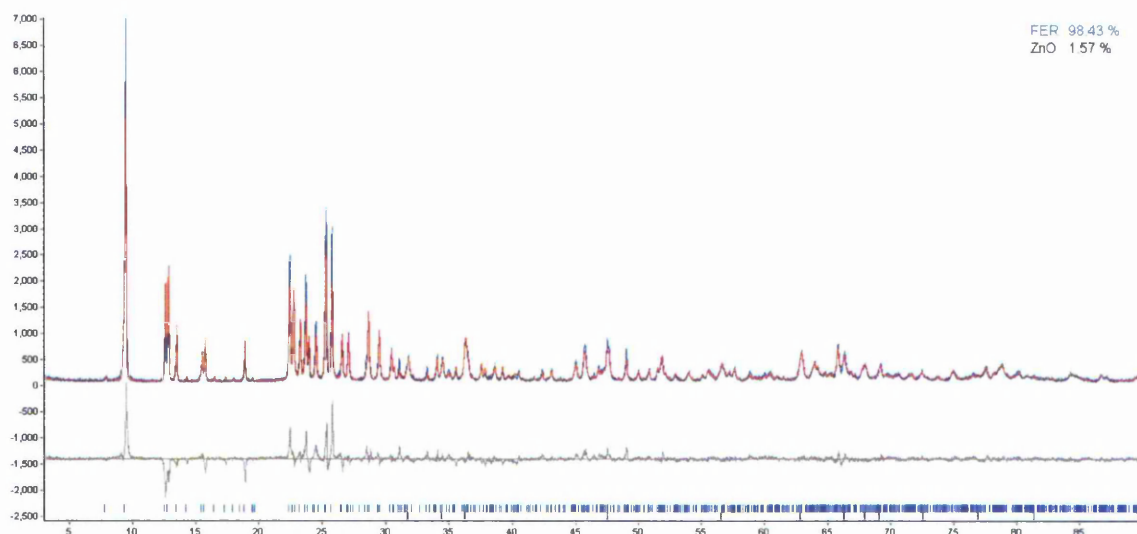


Figure 184: Rietveld fit for molten salt-treated FER with ZnO.

It is clear from Figure 184 that the zeolite structure is still intact upon molten salt impregnation and subsequent calcination. The diffraction from ZnO is relatively small so could be an indication that the ZnO present is within the FER pore structure.

The lattice parameters from FER samples with ZnO using both the solution and molten salt impregnation methods derived from Rietveld analysis of the XRD data are shown graphically in Figure 185 to Figure 187.

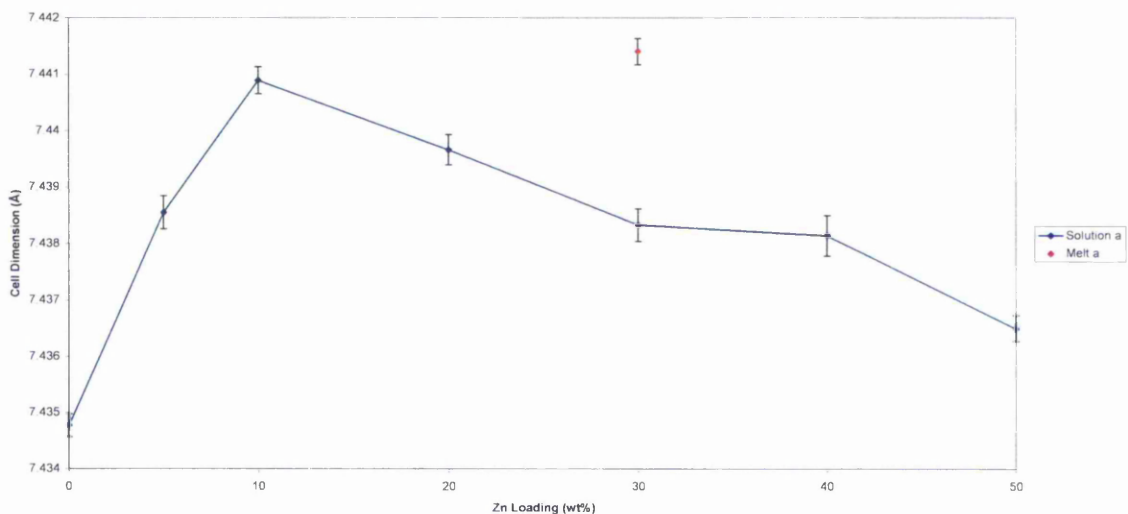


Figure 185: Unit cell parameter a for FER with ZnO.

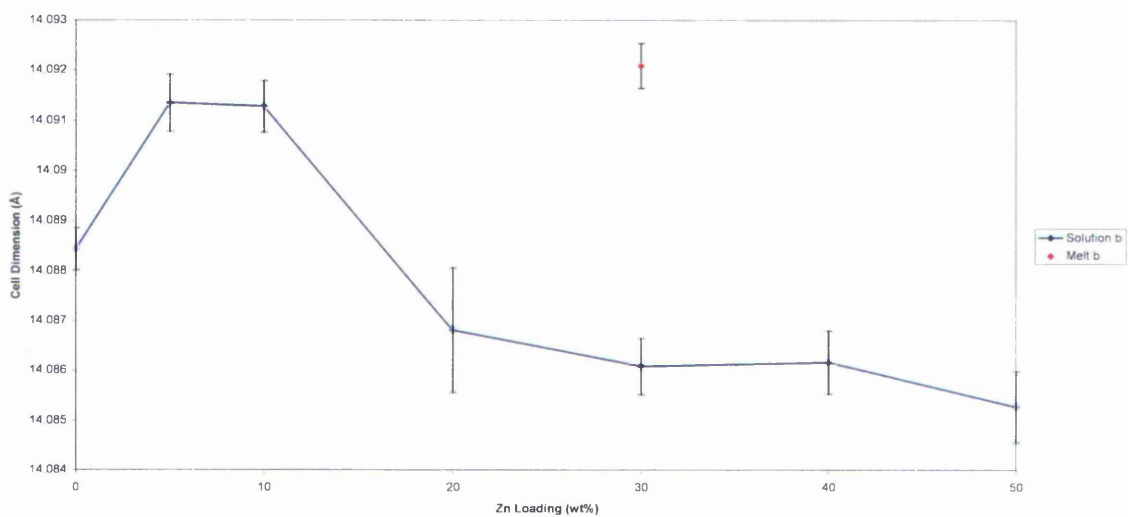


Figure 186: Unit cell parameter b for FER with ZnO.

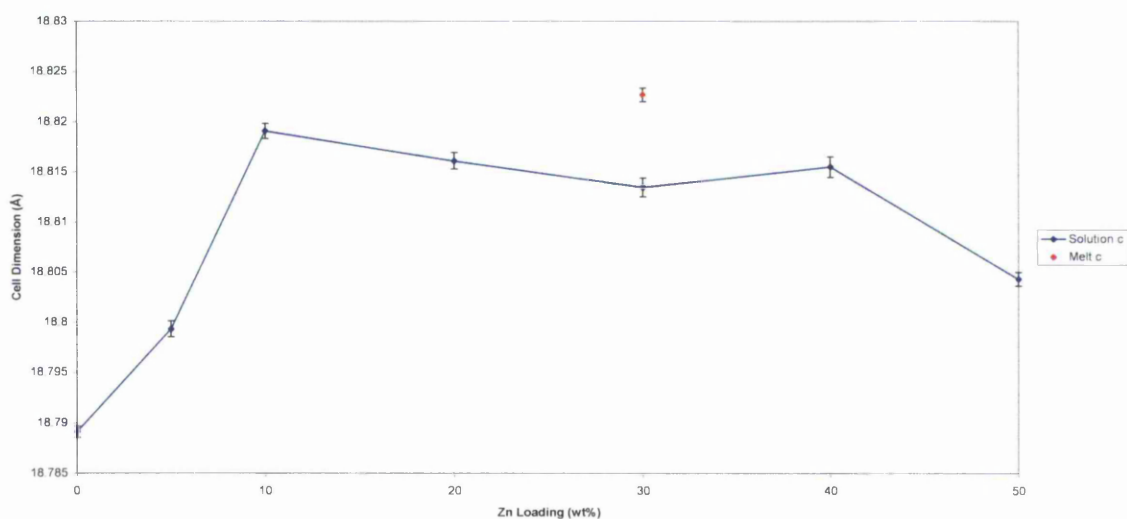


Figure 187: Unit cell parameter c for FER with ZnO.

These unit cell values show that the unit cell of the parent zeolite is generally increased upon impregnation and decreases gradually upon increased loading. They also show that the unit cell values for the molten salt-treated sample is greater than those recorded for the solution treated samples across the loading range of 0 – 50 wt% Zn. Experimental errors are insignificant with respect to these trends.

Figure 188 shows the UV-visible diffuse reflectance curves obtained for all FER samples impregnated with ZnO.

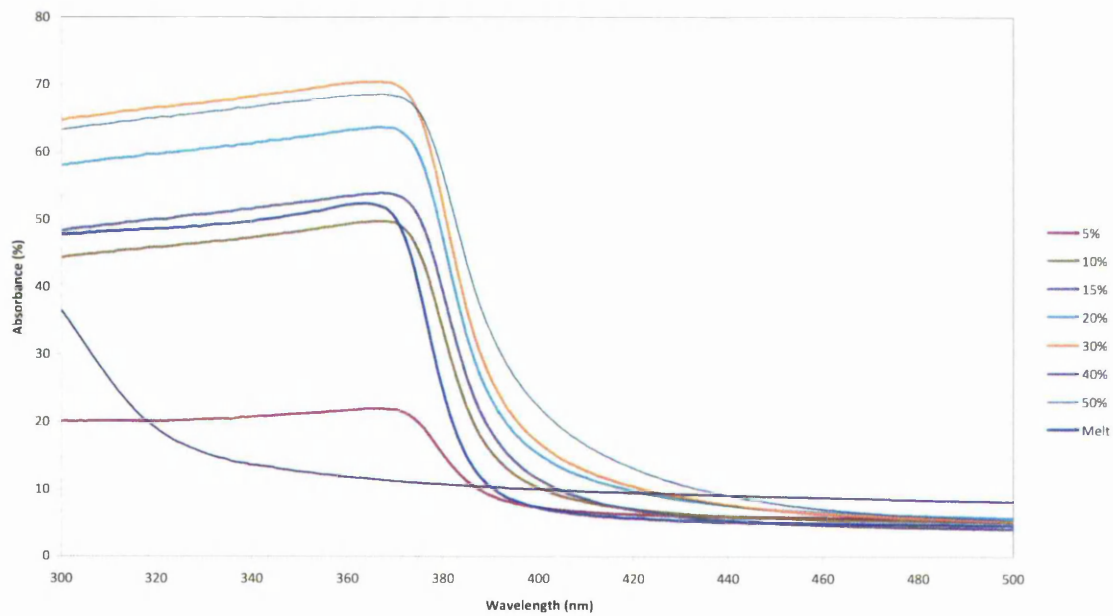


Figure 188: UV Vis Spectra for FER samples with ZnO.

The estimated band gaps in Table 11 and Figure 189 show that the band gap of ZnO upon solution impregnation into FER is comparable within error to bulk ZnO. By adopting the molten salt approach the band gap is increased with respect to the bulk phase.

Table 11: Band gaps for FER with ZnO.

Impregnation Method	Band Gap (eV)
Melt	3.283
5% Solution	3.26
10% Solution	3.262
15% Solution	3.256
20% Solution	3.246
30% Solution	3.252
50% Solution	3.23
Bulk	3.265

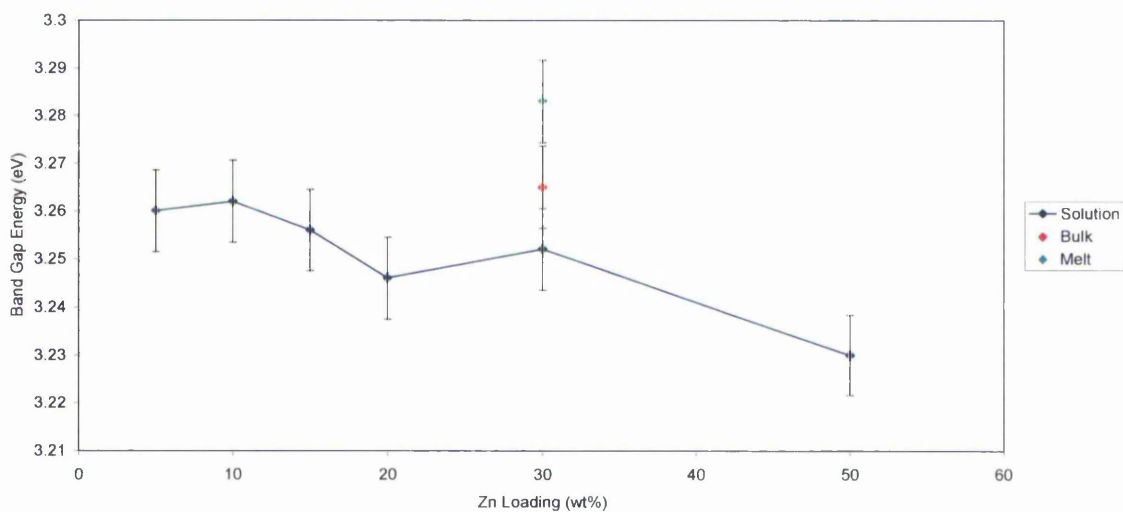


Figure 189: Band gap values for FER samples with ZnO.

The photoluminescence spectra comparing FER/ZnO prepared with a 15% solution and the melt process with bulk ZnO is shown in Figure 190.

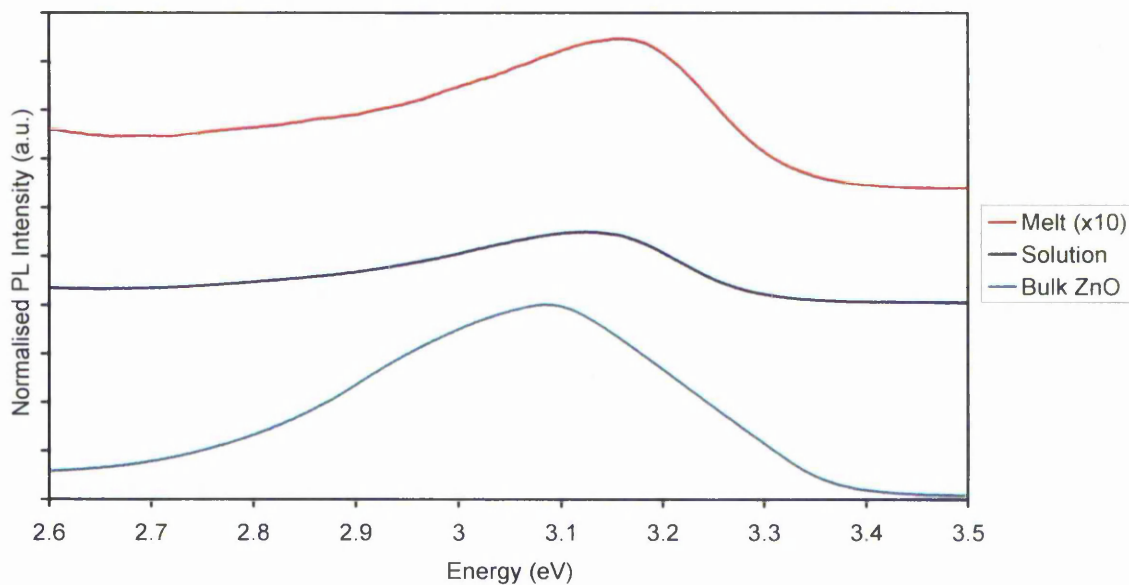


Figure 190: PL spectra for FER with ZnO.

As Figure 190 shows, the PL emission peak (E_{PL}) of ZnO is slightly blue-shifted upon zeolite inclusion using a 15 % solution with respect to the bulk ZnO spectrum, and is further shifted by using the melt process. The values of E_{PL} are shown in Table 12.

Table 12: E_{PL} for FER/ZnO.

Material	E_{PL} (eV)
FER/ZnO Melt	3.158
FER/ZnO 15% Solution	3.125
Bulk ZnO	3.084

8.2. Discussion and Conclusions

The unit cell parameters display a pattern similar to those found for the zeolite-GaN samples. In all cases the unit cell parameters for the molten salt-treated samples are larger than or are among the largest values of those seen in the solution-treated samples. As with the zeolite-GaN samples, this suggests the pores have been 'stretched' to accommodate the ZnO phase when $\text{Zn}(\text{NO}_3)_2$ is impregnated as a molten salt. Unlike the GaN sample, however, there is no evidence to show that the ZnO is present outside the pore network, as shown by HRTEM images. The reason for this has not been investigated, yet theories could include a difference in crystallisation mechanisms, a 'weakening' of the zeolite structure during nitridation (the reasons for which may be alluded to in Section 0) or a simple difference in energetics between the crystallisation of ZnO and GaN relative to ammoniation of the zeolite.

The absorption spectra for all three zeolites containing ZnO are consistent, with the molten salt-treated samples having the largest band gap, followed by bulk ZnO, then the solution-treated samples. The solution-treated samples show decreasing E_g values upon increasing Zn loading. This implies that the smaller particles exhibit larger E_g values and that by adopting the molten-salt impregnation method either larger particle sizes are achieved or that some other effect increases the band gap with respect to the bulk phase. What can't be ruled out in all of these cases is the effect of ion exchange in the samples. Due to the relatively low temperatures involved and the lack of solvent, it is possible that a greatly reduced degree of ion exchange occurs during the molten salt impregnation when compared to the solution-based method. Although low silica zeolites have been used throughout this work, thus significantly reducing the amount of ion exchange capability of the

zeolites, it may still affect the band structure of the guest phases, possibly reducing E_g for the solution-impregnated samples with respect to the bulk value. Also, as a dense phase is impregnated during the molten-salt impregnation, strain may also play a part. This may not have presented itself as a significant contributor in the GaN work, which may be attributed to the fact that the GaN broke free of the zeolite pore system, but as the ZnO is still confined within the pores there may be a considerable amount of strain within the ZnO clusters.

The emission spectra for all the samples show a slightly different pattern. In these spectra the molten salt value is largest, followed by those for the solution impregnation and the bulk value, which is the lowest. This is an example of Stokes Shift, in which the emission energy is lower than that of the absorption. This effect can be more pronounced in strained materials and those with reduced dimensionality.

9. Indium Gallium Nitride

9.1. Introduction

$\text{In}_x\text{Ga}_{1-x}\text{N}$ is a semiconducting material with a band gap similar to GaN, but which can change depending on x , which is typically ≤ 0.3 .^[120] In this series of experiments $\text{In}_x\text{Ga}_{1-x}\text{N}$ was introduced into the zeolites ZSM-5 and FAU by way of the molten salt process using a mixture of $\text{In}(\text{NO}_3)_3$ and $\text{Ga}(\text{NO}_3)_3$ to obtain the following materials in both zeolites:



9.2. Results

9.2.1. ZSM-5

Diffraction profiles were refined using Topas Academic V4.1 against the ZSM-5 structure reported by Li, et al. [89] and GaN structure reported by Kaminski, et al. [90]. The GaN structure was modified by the addition of In sites occupying locations also occupied by Ga. The crystallographic ratio of occupation was determined by the experimental ratio of Ga:In and consequently refined. The Rietveld profiles are shown in Figure 191 to Figure 195.

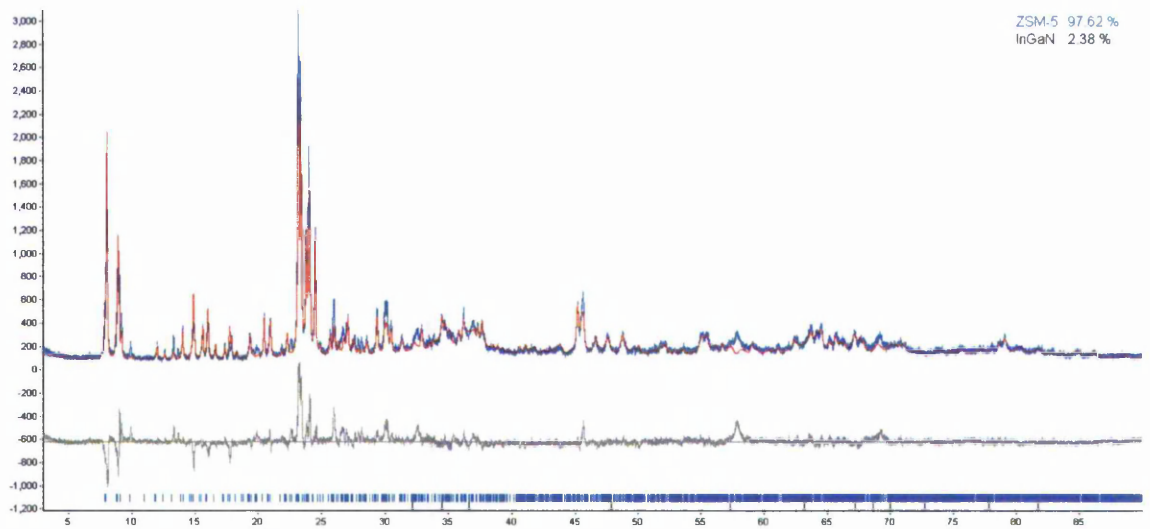


Figure 191: Rietveld fit for ZSM-5 with In_xGa_{1-x}N (x=0.3).

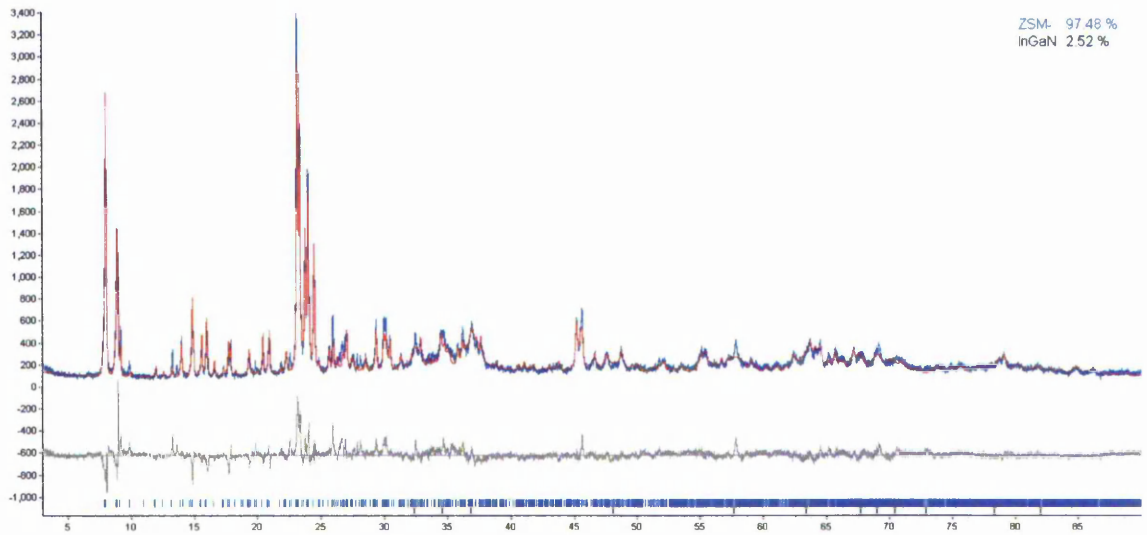


Figure 192: Rietveld fit for ZSM-5 with $\text{In}_x\text{Ga}_{1-x}\text{N}$ ($x=0.2$).

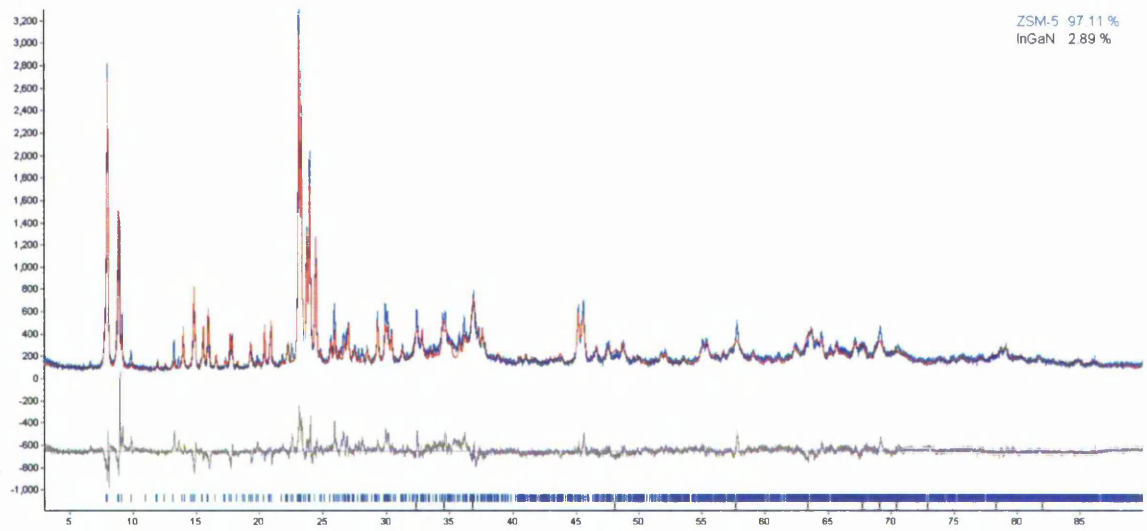


Figure 193: Rietveld fit for ZSM-5 with $\text{In}_x\text{Ga}_{1-x}\text{N}$ ($x=0.1$).

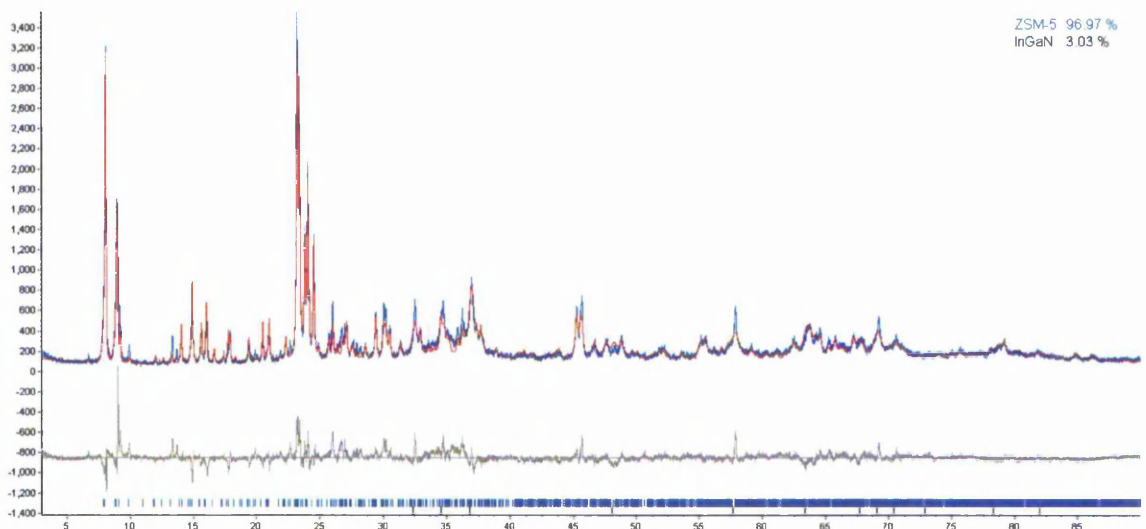


Figure 194: Rietveld fit for ZSM-5 with $\text{In}_x\text{Ga}_{1-x}\text{N}$ ($x=0.05$).

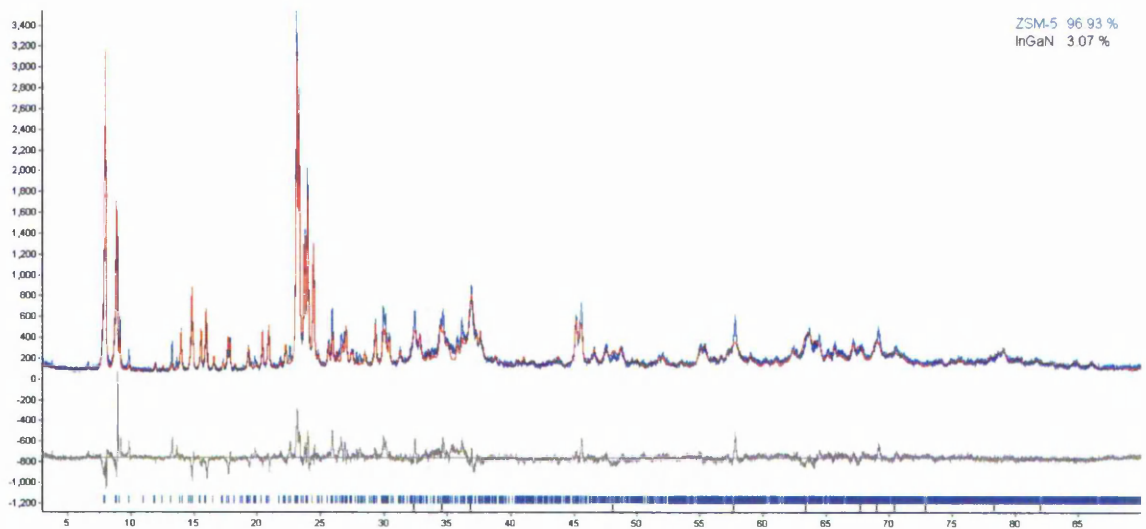


Figure 195: Rietveld fit for ZSM-5 with $\text{In}_x\text{Ga}_{1-x}\text{N}$ ($x=0.025$).

The Rietveld profiles shown in Figure 191 to Figure 195 show that the zeolite host structure is retained in all samples and that the calculated $\text{In}_x\text{Ga}_{1-x}\text{N}$ content in each case is between 2.5 and 3.1%. There is no significant pattern in crystallinity and a very slight increase in $\text{In}_x\text{Ga}_{1-x}\text{N}$ content with decreasing x , i.e. decreasing In content. This may suggest that $\text{In}_x\text{Ga}_{1-x}\text{N}$ is not actually formed and that by decreasing the In content, and thus increasing the Ga content that the overall

nitride content is increased as In is not incorporated into the GaN lattice. This, unfortunately is not possible to probe using laboratory powder diffraction data.

The lattice parameters from ZSM-5 samples with $\text{In}_x\text{Ga}_{1-x}\text{N}$ derived from Rietveld analyses of the XRD data are shown graphically in Figure 196 to Figure 198.

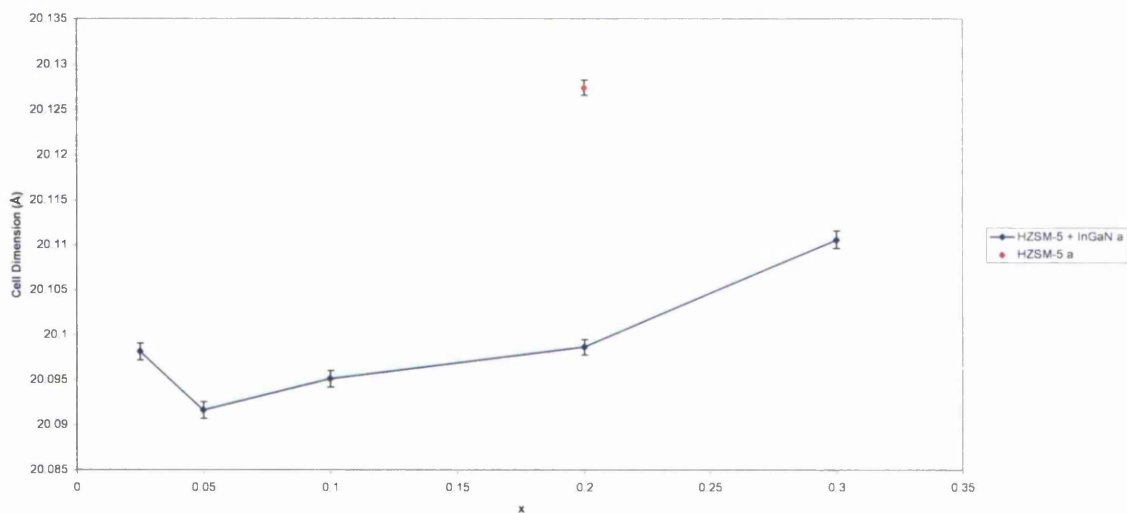


Figure 196: Unit cell parameter a for ZSM-5 with $\text{In}_x\text{Ga}_{1-x}\text{N}$.

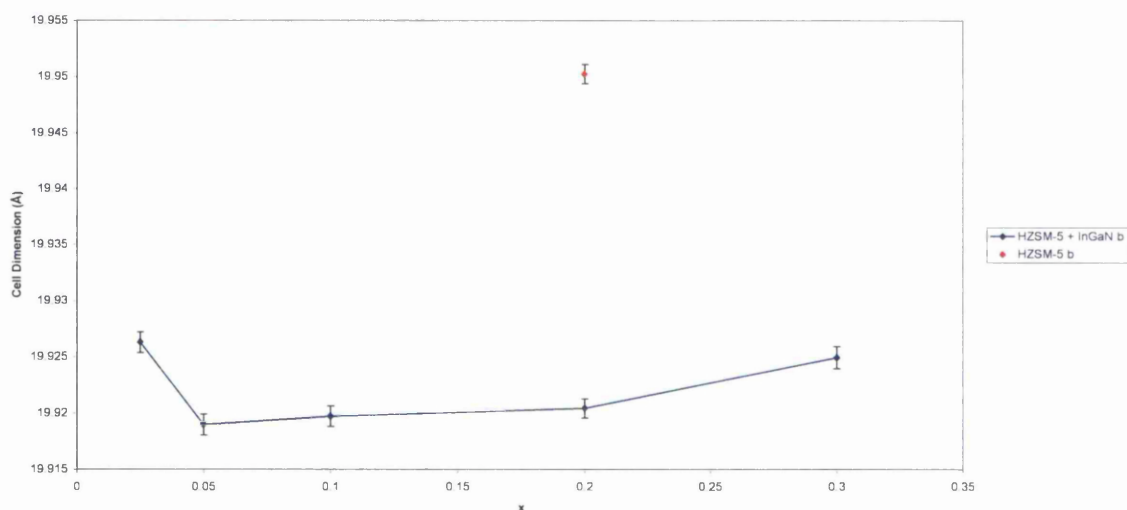


Figure 197: Unit cell parameter b for ZSM-5 with $\text{In}_x\text{Ga}_{1-x}\text{N}$.

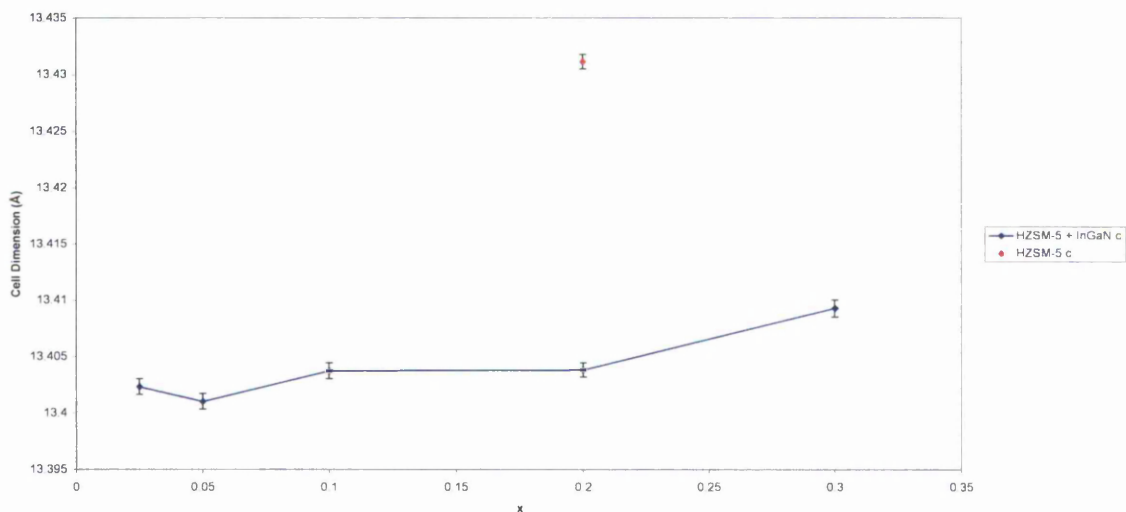


Figure 198: Unit cell parameter c for ZSM-5 with $\text{In}_x\text{Ga}_{1-x}\text{N}$.

It can be seen that all 3 of the unit cell parameters of ZSM-5 with $\text{In}_x\text{Ga}_{1-x}\text{N}$ are smaller than that of the parent zeolite by 0.04 – 0.06 Å across the entire range of x , beyond experimental error, which is consistent with ZSM-5 with GaN.

Figure 199 shows the UV Vis diffuse reflectance curves obtained for ZSM-5 samples with $\text{In}_x\text{Ga}_{1-x}\text{N}$.

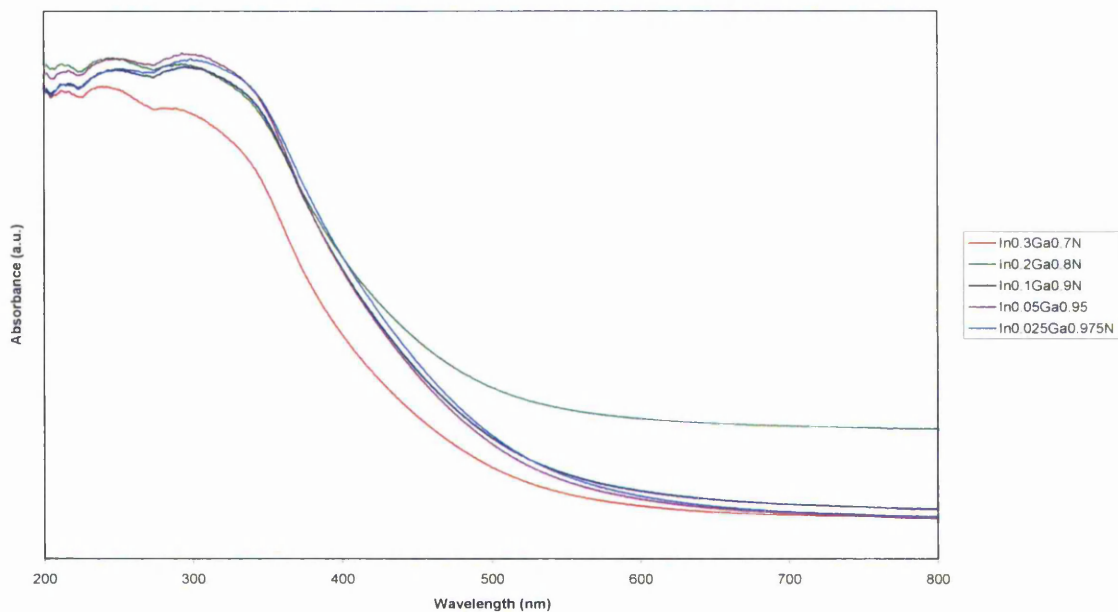


Figure 199: UV Vis data for ZSM-5 samples with $\text{In}_x\text{Ga}_{1-x}\text{N}$.

By taking the 1st derivative of the absorption data and reading the position of the maxima, the band gaps for all samples were estimated at 3.42 eV (± 0.009433) with exception of when $x = 0.3$, which has a band gap of 3.48 eV (± 0.009766).

9.2.2. Faujasite

Diffraction profiles were refined using Topas Academic V4.1 against the faujasite structure reported by Parise, et al. ^[91] and GaN structure reported by Kaminski, et al. ^[90] The GaN structure was modified by the addition of In sites occupying locations also occupied by Ga. The crystallographic ratio of occupation was determined by the experimental ratio of Ga:In and consequently refined. The Rietveld profiles are shown in Figure 200 to Figure 204.

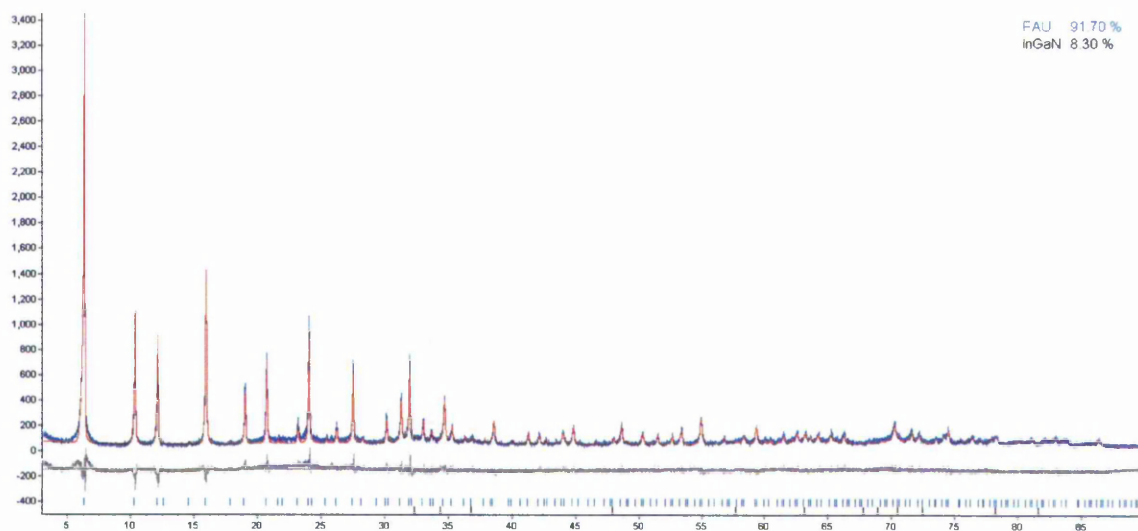


Figure 200: Rietveld fit for FAU with $\text{In}_x\text{Ga}_{1-x}\text{N}$ ($x=0.3$).

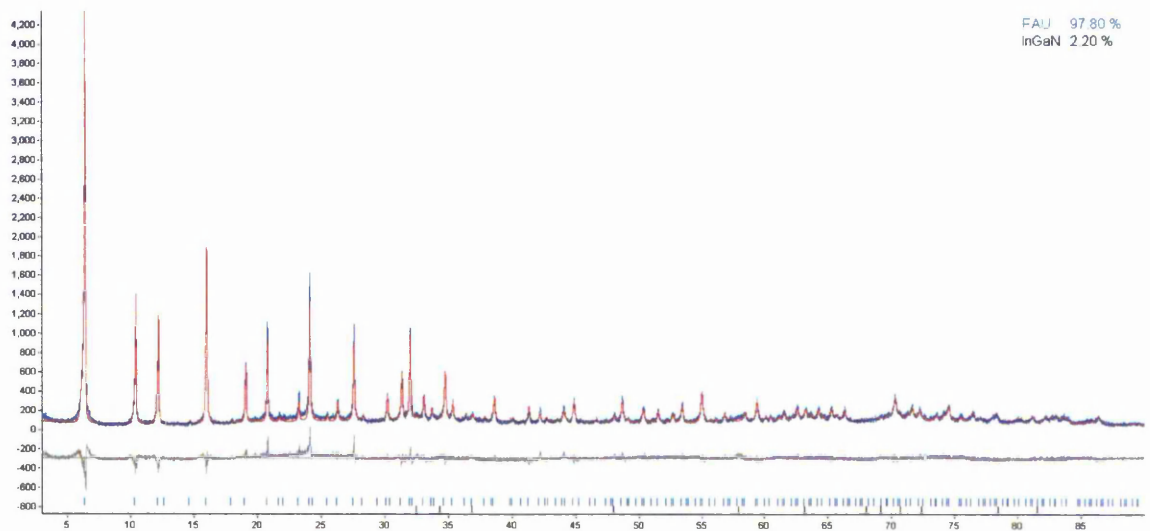


Figure 201: Rietveld fit for FAU with $\text{In}_x\text{Ga}_{1-x}\text{N}$ ($x=0.2$).

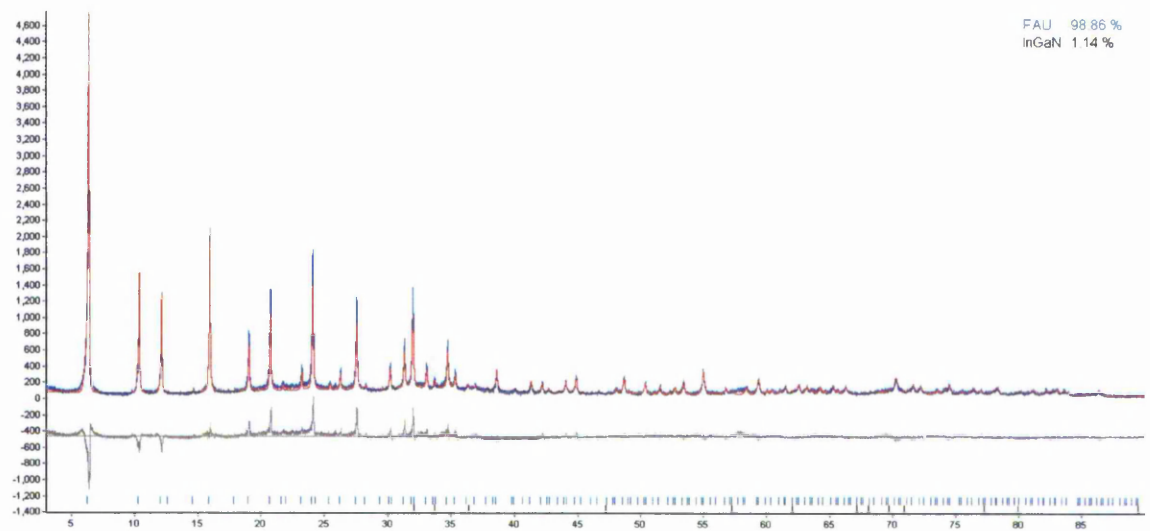


Figure 202: Rietveld fit for FAU with $\text{In}_x\text{Ga}_{1-x}\text{N}$ ($x=0.1$).

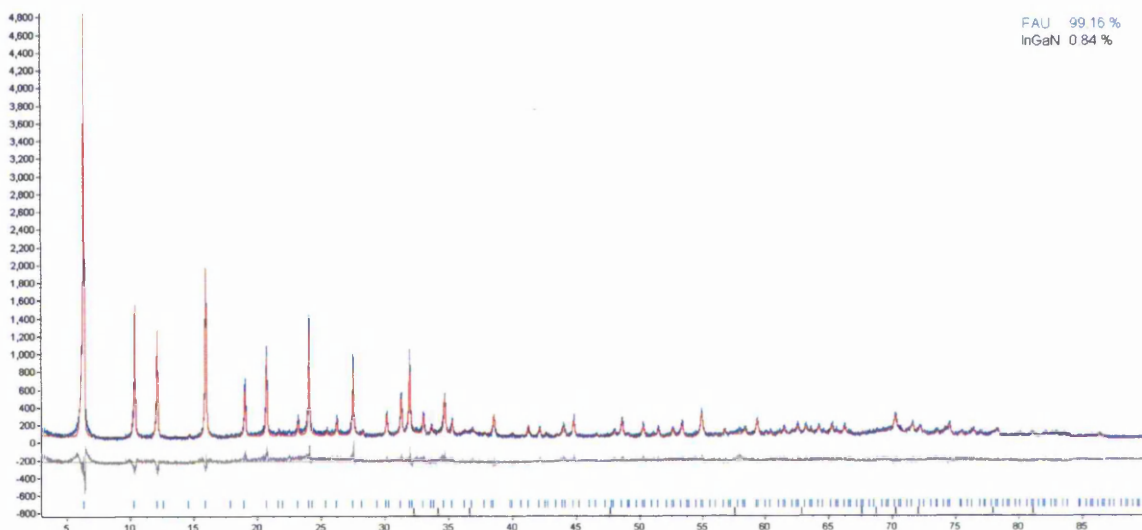


Figure 203: Rietveld fit for FAU with $\text{In}_x\text{Ga}_{1-x}\text{N}$ ($x=0.05$).

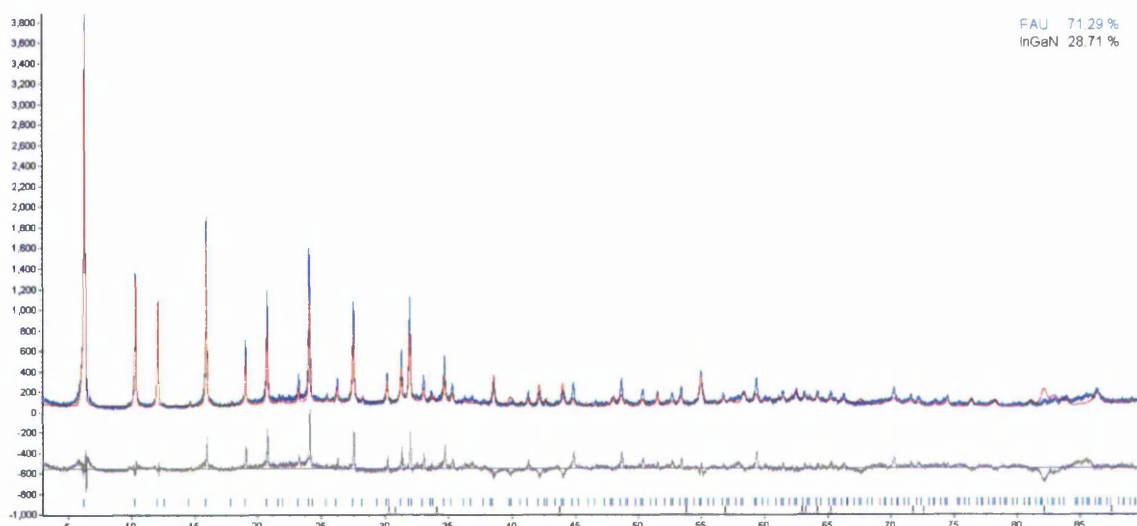


Figure 204: Rietveld fit for FAU with $\text{In}_x\text{Ga}_{1-x}\text{N}$ ($x=0.025$).

The Rietveld profiles shown in Figure 200 to Figure 204 show that the zeolite host structure is retained in all samples and that the calculated $\text{In}_x\text{Ga}_{1-x}\text{N}$ content in each case is between 2.5 and 3.1%. There is no significant pattern in crystallinity and a very slight decrease in $\text{In}_x\text{Ga}_{1-x}\text{N}$ content with decreasing x , i.e. decreasing In content, until $x=0.025$, in which the calculated $\text{In}_x\text{Ga}_{1-x}\text{N}$ content rises sharply to 28.71%. This is in contrast to the data obtained from the ZSM-5 samples, in which the calculated $\text{In}_x\text{Ga}_{1-x}\text{N}$ content increased with decreasing In content. Given the

difficulties associated with synthesising pure InN, it is unlikely the inverse of the suggested situation in ZSM-5 has occurred in this experiment. Again, an investigation of this result is beyond the capabilities of laboratory powder XRD measurements and beyond the scope of this project.

The lattice parameters from FAU samples with $\text{In}_x\text{Ga}_{1-x}\text{N}$ derived from Rietveld analysis of the XRD data are shown graphically in Figure 205.

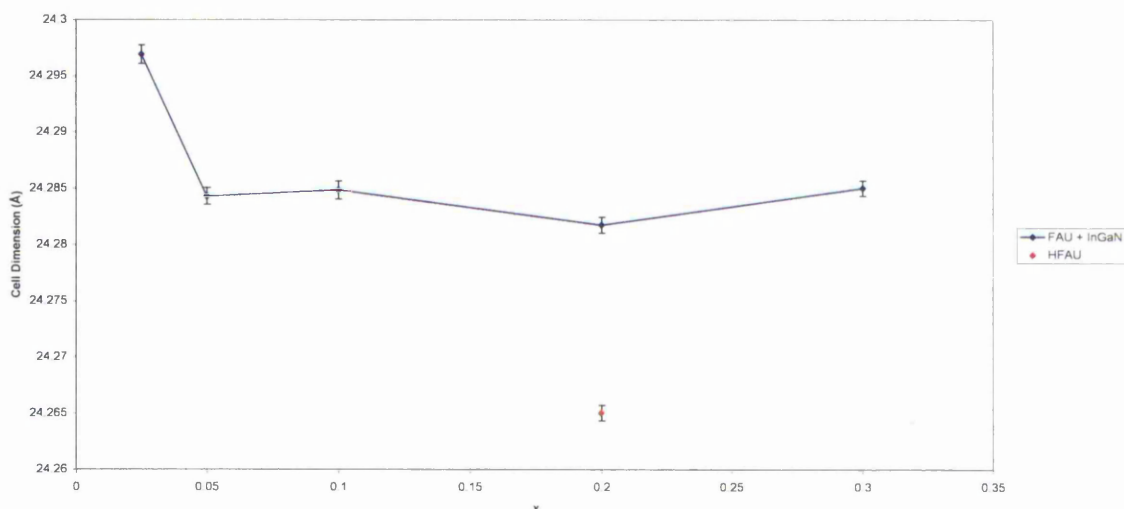


Figure 205: Unit cell parameter for FAU with $\text{In}_x\text{Ga}_{1-x}\text{N}$.

As Figure 205 shows, the unit cell parameter for FAU with $\text{In}_x\text{Ga}_{1-x}\text{N}$ is consistently greater than that of the parent zeolite across the entire range of x, beyond experimental error, which is inconsistent with what was found for ZSM-5 with $\text{In}_x\text{Ga}_{1-x}\text{N}$, yet consistent with FAU with GaN.

Figure 206 shows the UV Vis diffuse reflectance curves obtained for FAU samples with $\text{In}_x\text{Ga}_{1-x}\text{N}$. $\text{In}_{0.2}\text{Ga}_{0.8}\text{N}$ and $\text{In}_{0.3}\text{Ga}_{0.7}\text{N}$ have very different absorption profiles when compared to the samples of lesser In doping, suggesting the band structure is lost upon higher In doping levels, a phenomenon not seen in the ZSM-5 samples. By taking the 1st derivative of the UV Vis data and reading the peak maxima E_g is estimated as 3.4 eV (± 0.009323) for samples where $x \leq 0.1$.

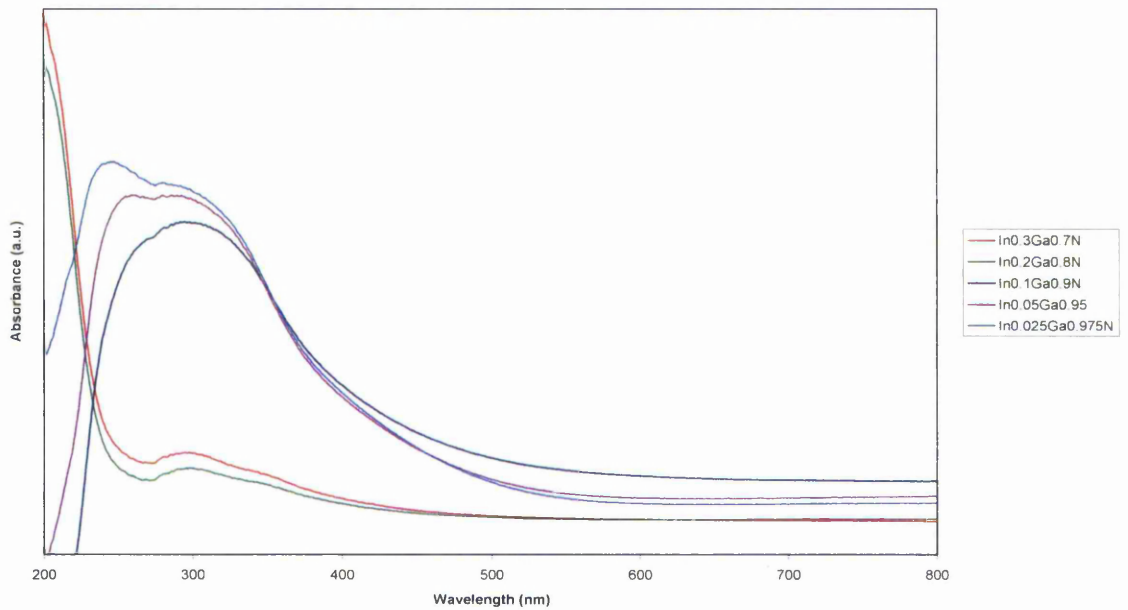


Figure 206: UV Vis data for FAU samples with $\text{In}_x\text{Ga}_{1-x}\text{N}$.

9.3. Discussion and Conclusions

Structurally the two zeolite materials tested behave similarly when impregnated with $\text{In}_x\text{Ga}_{1-x}\text{N}$ as they do with GaN, which comes as no surprise. Electronically, however, there is no change in band gap with increased In loading; as would be expected with an increasing number of random In sites located throughout a bulk GaN sample. This may be an indication of selective ion exchange by the zeolite host; possibly favouring In over Ga; therefore producing GaN clusters within an In-exchanged-zeolite. It may also suggest that under the conditions involved In is simply not incorporated into the GaN structure, either due to the relatively low synthesis temperature or possibly an immiscibility of the two molten nitrate phases, which could lead to GaN and InN clusters, although In will probably be present as metallic clusters due to the relative difficulty of synthesising pure and highly crystalline InN due to the narrow processing temperature window.^[121] Even if pure InN were made, the band gap of the material may be so low (possibly as low as 0.7 eV) as to be invisible to the UV Vis absorption equipment used. Also, the lattice mismatch experienced when In is introduced into a GaN lattice may be more profound on such a small scale, i.e. within the zeolite pores. Therefore a higher In loading may prevent the formation of the nitride altogether; which may go some way to explaining the lack of an observed band gap at higher loadings in FAU and possibly the increased band gap energy for $\text{In}_{0.3}\text{Ga}_{0.7}\text{N}$ in ZSM-5 when compared to lower loadings.

This work highlights the limitations of incorporating mixed-metal electronic materials into anionic zeolite host frameworks. Problems with preferential ion-exchange, framework-guest phase interactions, precursor miscibility and

exaggerated lattice mismatch effects on reducing the particle size to such an extent may all play a part in disrupting the band structure of the guest material beyond intentions.

10. Lanthanides

10.1. Introduction

Of particular interest in this context are the nitrides of Eu and Yb, which have been shown to exhibit higher than expected activity in catalysing the hydrogenation of benzene, ^[71, 73] which is an important method used for the production of cyclohexene, which is itself important in the nylon industry. Binary lanthanide nitrides crystallise with a cubic rock salt structure with cell parameters of 4.775 Å and 5.017 Å for YbN and EuN respectively. As the main channel diameter of ZSM-5 is about 6 Å, the largest YbN crystallite encapsulated in the pore structure of ZSM-5 would be ~ 1.26 unit cells in diameter and for EuN ~1.20 unit cells.

It has been demonstrated that metallic Eu and Yb can be dissolved in liquid ammonia, and leads to the formation of bulk and nanocrystalline lanthanide amide, imide and nitrides. ^[122, 123] Impregnation of silica matrices with solutions of these species results in the formation of surface amide species by reaction with surface hydroxyl groups. The materials formed in this way demonstrate significant variations in the catalytic selectivity of the lanthanide species. ^[124-126] Another route by which the synthesis of nanocrystalline lanthanide nitrides has been achieved is the reaction of lanthanide cyclopentadienyl complexes with liquid ammonia at -78 °C^[76]; this route has been demonstrated in the synthesis of nanocrystalline ErN with crystallite sizes of 100-400 Å. This method is, however, impractical for zeolite impregnation due to the relatively small zeolite pore windows in comparison to the cross-sectional area of the lanthanide complex.

In this work the nitrides of Eu, Yb and Tb were synthesised within the pores of HZSM-5 after impregnation of the zeolite with the respective chloride by the solution-based impregnation method.

10.2. Results

10.2.1. Europium Nitride

Diffraction profiles were refined using Topas Academic V4.1 against the ZSM-5 structure reported by Li, et al. [89] and EuN structure reported by Jacobs, et al [127].

The Rietveld profiles are shown in Figure 207 to Figure 209.

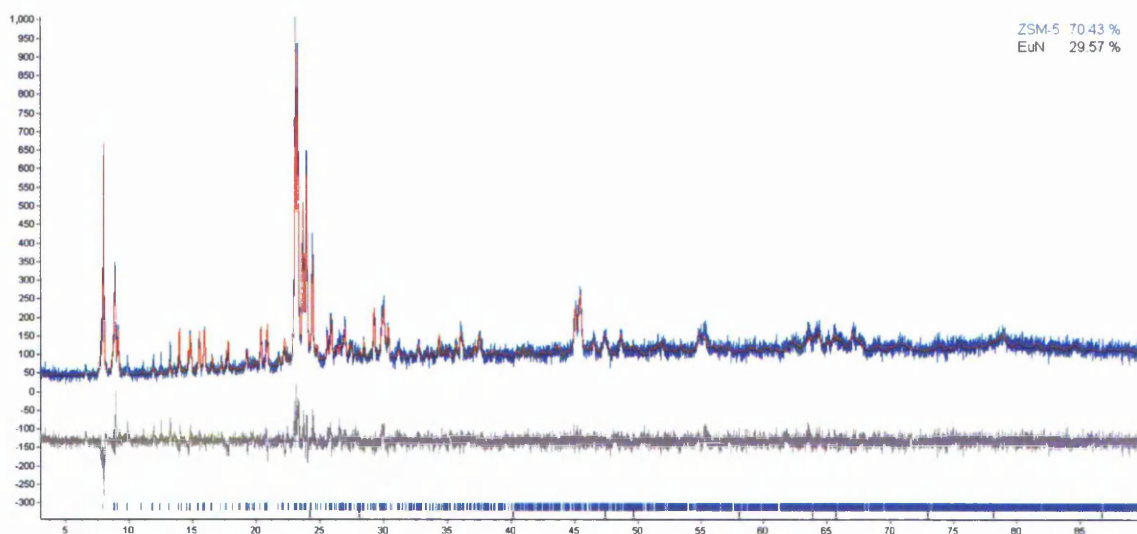


Figure 207: Rietveld profile for ZSM-5 with 5wt% Eu as EuN.

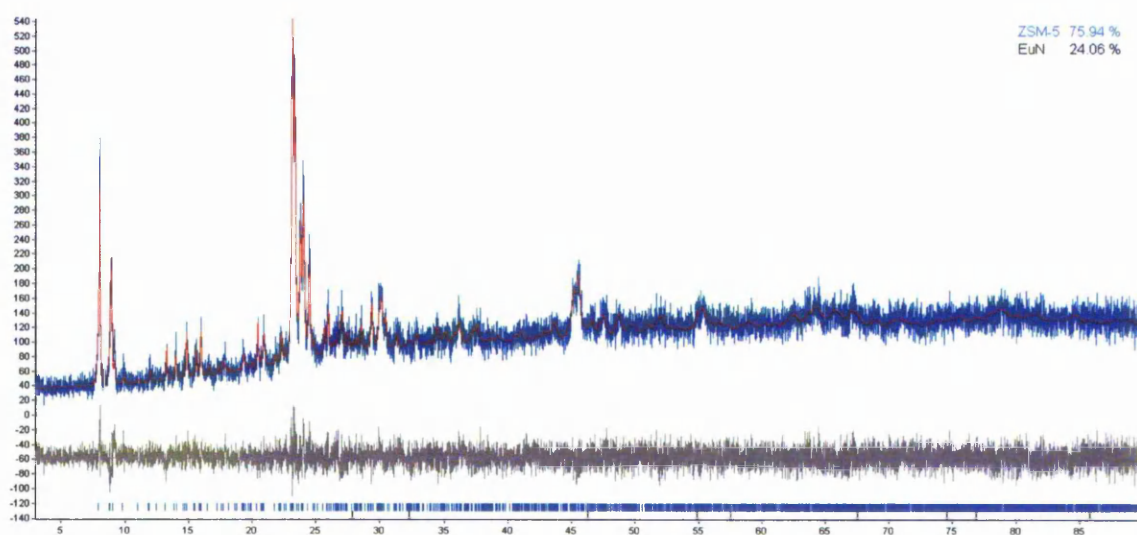


Figure 208: Rietveld profile for ZSM-5 with 10wt% Eu as EuN.

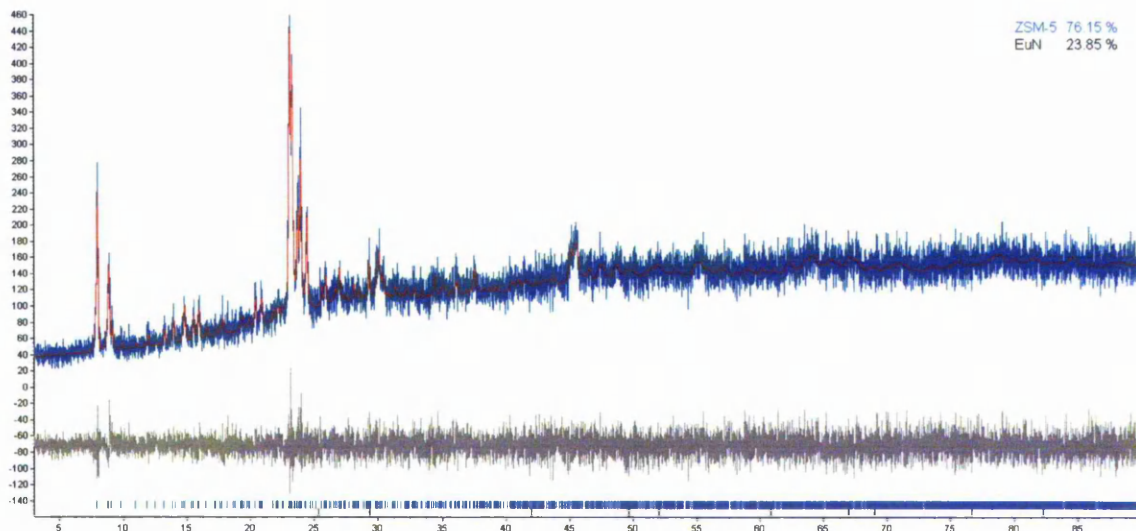


Figure 209: Rietveld profile for ZSM-5 with 15wt% Eu as EuN.

The Rietveld profiles show that there is a significant degree of x-ray fluorescence from the Eu, characterised by profile noise that increases with increasing 2θ and Eu loading. This makes accurate determination of the host phase content and identity difficult, yet proves the presence of Eu in these samples that seems to increase with Eu loading.

The lattice parameters from ZSM-5 samples with EuN using the solution impregnation method derived from Rietveld analysis of the XRD data are shown graphically in Figure 210.

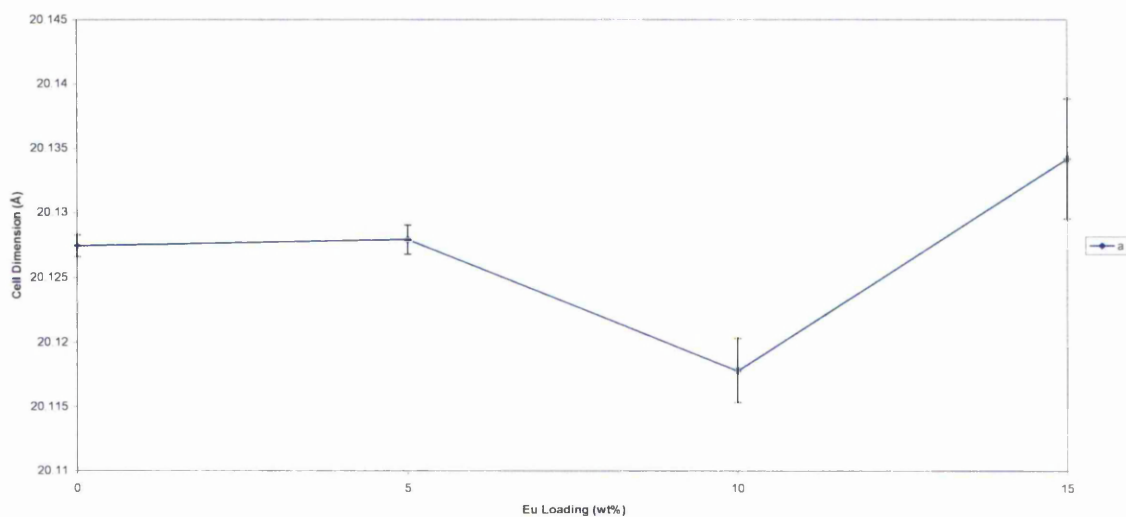


Figure 210: Unit cell parameter *a* for ZSM-5 with EuN.

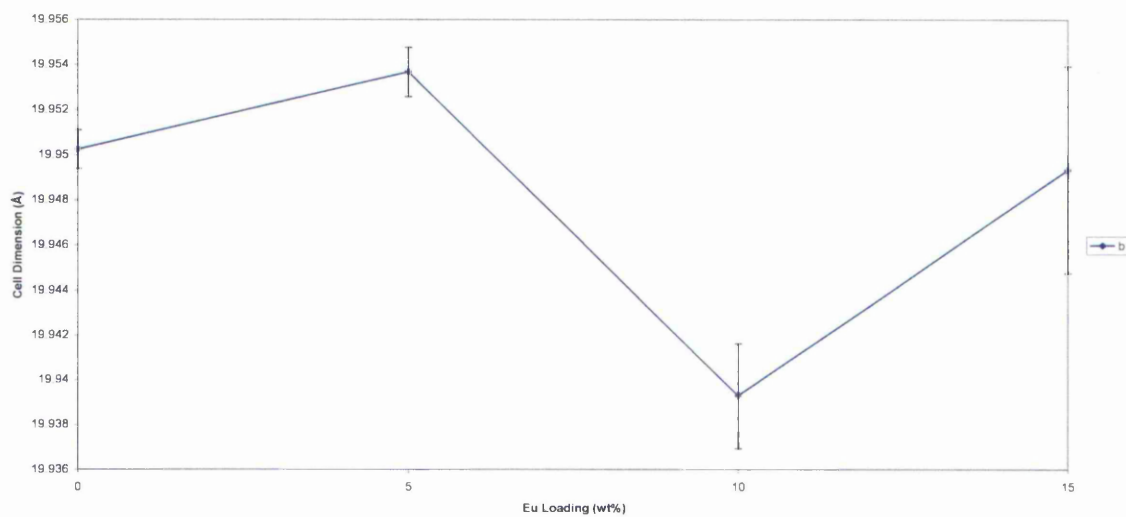


Figure 211: Unit cell parameter *b* for ZSM-5 with EuN.

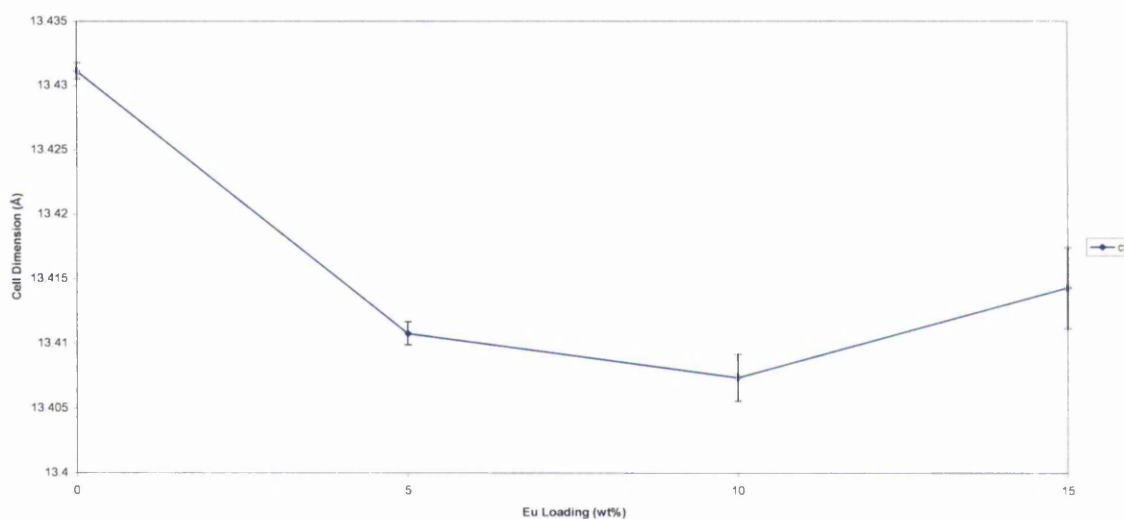


Figure 212: Unit cell parameter c for ZSM-5 with EuN.

The XRD data shows that the crystallographic parameters of the zeolite remain relatively unchanged within experimental error during EuN inclusion, but the parameters for EuN can vary significantly. This can be attributed to the relatively low EuN content and particle size, and therefore reduced accuracy of the refinement.

Figure 213 displays the N(1s) region of the XPS spectra for ZSM-5 with 5 wt% Eu as both the chloride and nitride forms. What is evident is that the peak at 398.2 eV is attributable to the nitride, which is consistent with the value reported for bulk γ - Mo_2N (397.8 eV) ^[128] and online databases for metal nitrides. ^[129] The higher binding energy peak is attributed to NH_x species; present from either the parent zeolite's ammonium-based SDAs or the ammonia-based nitride preparation method.

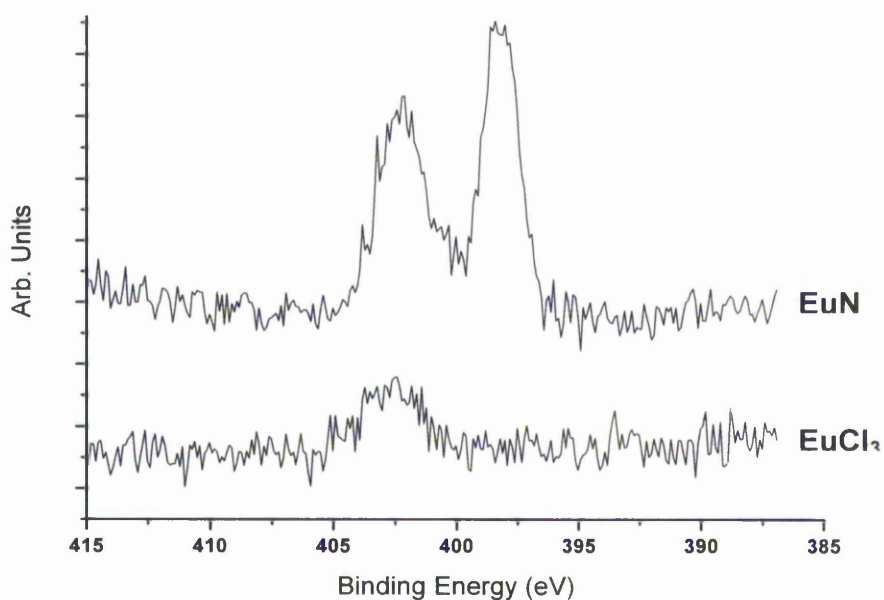


Figure 213: N(1s) Spectra for 5 wt% EuCl_3 and 5 wt% EuN containing zeolites.

Sputtering the sample (Figure 214) reveals that the NH_x species are confined to the surface of the material as the peak is lost after the first sputter, yet the nitride component remains, suggesting the nitride is present throughout the sample.

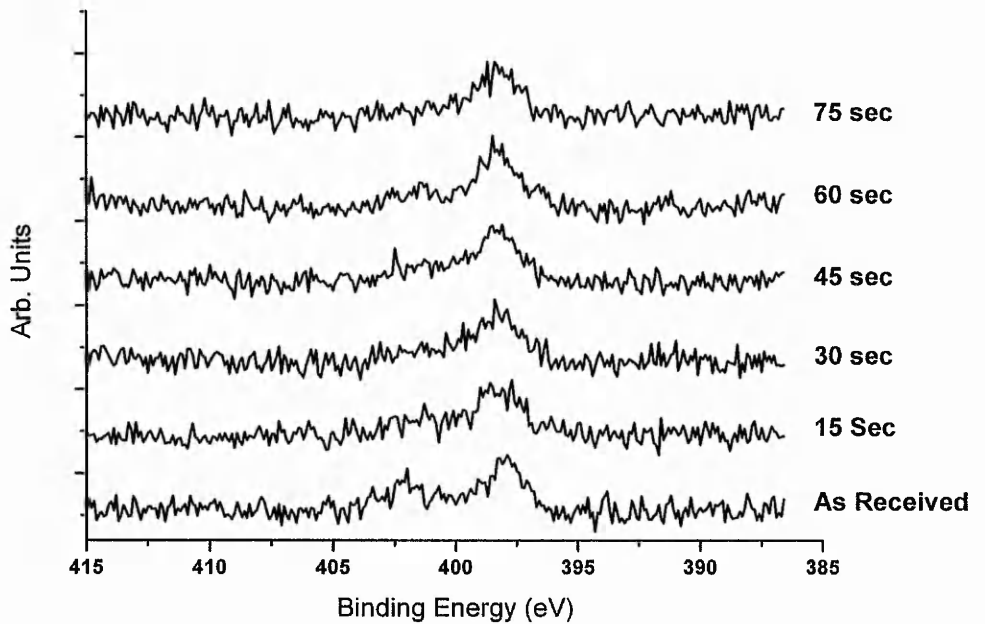


Figure 214: N(1s) spectra for increasing sputter time for 5 wt% EuN containing zeolite. Estimated sputter rate is 0.3 nm/s.

The HRTEM image shown in Figure 215(a) clearly shows the zeolite pore structure with channel spacings of 1.051 nm, Figure 215(b) shows a high level of dispersion of the EuN clusters (dark spots in the image) throughout the ZSM-5 pore structure and the EDX spectrum in Figure 215(c) confirms the presence of Eu.

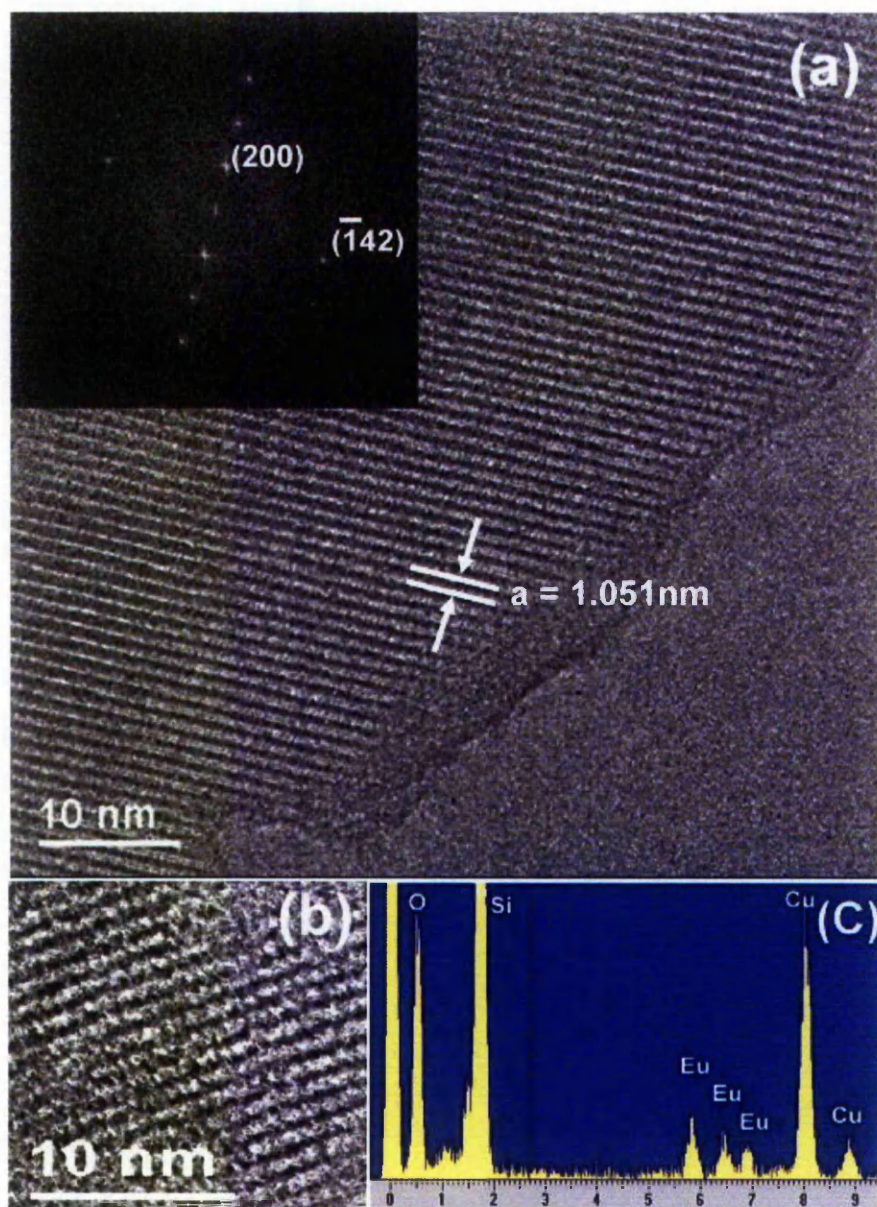


Figure 215: (a) HRTEM image of ZSM-5 with 15% Eu. The inset is a FFT pattern created from the image. The pattern is indexed to the ZSM-5 crystal structure and the d-spacing marked in the image matches (200) atomic planes. (b) An enlarged HRTEM image showing a rosary pattern of black spots along the principal channels. (c) EDX spectrum showing Eu.

The UV-Vis spectra for HZSM-5 supported Eu compounds shown in Figure 216 clearly show peaks relating to EuCl_3 at 1400 and 1900 nm, which decrease upon nitridation of the 5 and 15 wt% loaded sample and almost completely disappear upon nitridation of the 10 wt% loaded sample. The nitridation products show additional absorbance at 1520 and 2000 nm. The inset in Figure 216 highlights very weak absorption peaks around 530, 465 and 395 nm (denoted '+' in Figure 216) that can be assigned to electronic transitions of the lanthanide ion (${}^7\text{F}_0 \rightarrow {}^5\text{D}_1$, ${}^7\text{F}_1 \rightarrow {}^5\text{D}_2$ and ${}^7\text{F}_0 \rightarrow {}^5\text{L}_7$ respectively). These peaks are not apparent in the spectra after the nitridation process, due to the presence of an absorption edge which has its onset at around 500 nm. The appearance of this edge may indicate the EuN is semiconducting; analysis of the spectrum suggests a band gap of 3.4 eV (± 0.009323) if this is the case.

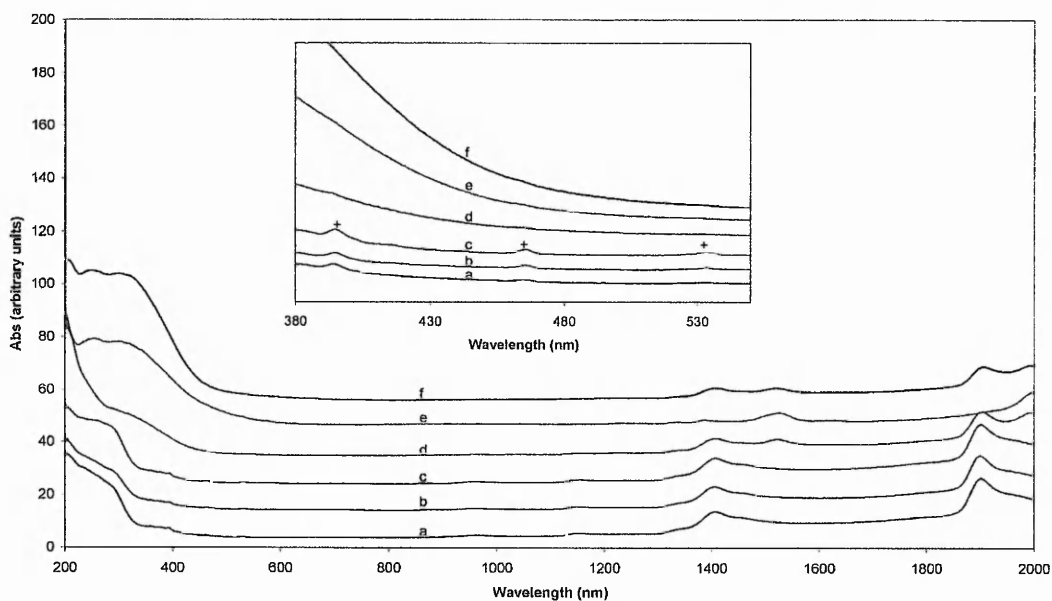


Figure 216: UV-Vis Spectra for HZSM-5 with (a) 5 wt% loading of Eu as EuCl_3 (b) 10 wt% loading of Eu as EuCl_3 (c) 15 wt% loading of Eu as EuCl_3 (d) 5 wt% loading of Eu as EuN (e) 10 wt% loading of Eu as EuN (f) 15 wt% loading of Eu as EuN. (+ marks electronic transitions from Eu^{3+}).

10.2.2. Ytterbium Nitride

Diffraction profiles were refined using Topas Academic V4.1 against the ZSM-5 structure reported by Li, et al. [89] and YbN structure reported. by [130] The Rietveld profiles are shown in Figure 217 to Figure 219.

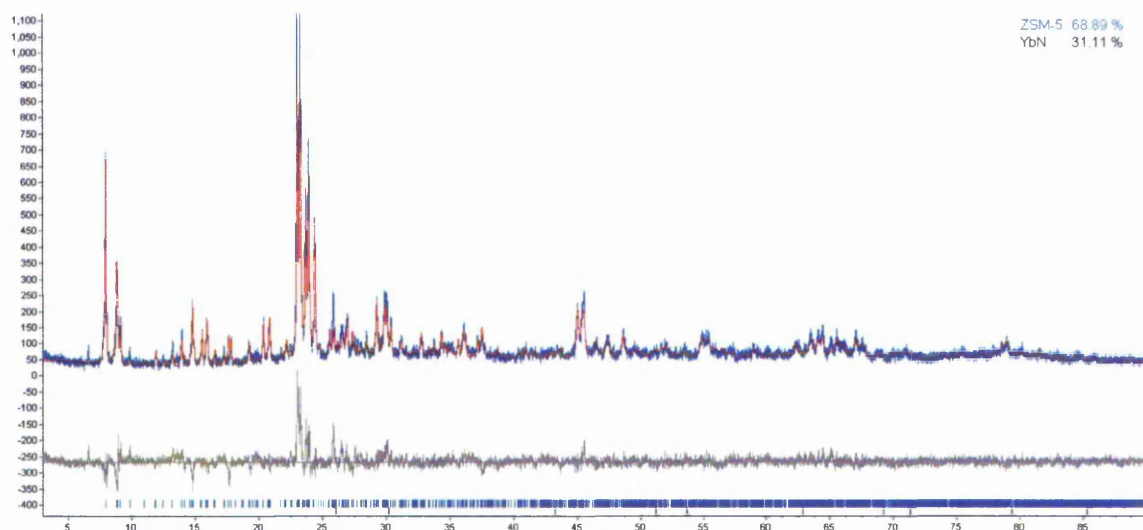


Figure 217: Rietveld profile for ZSM-5 with 5wt% Yb as YbN.

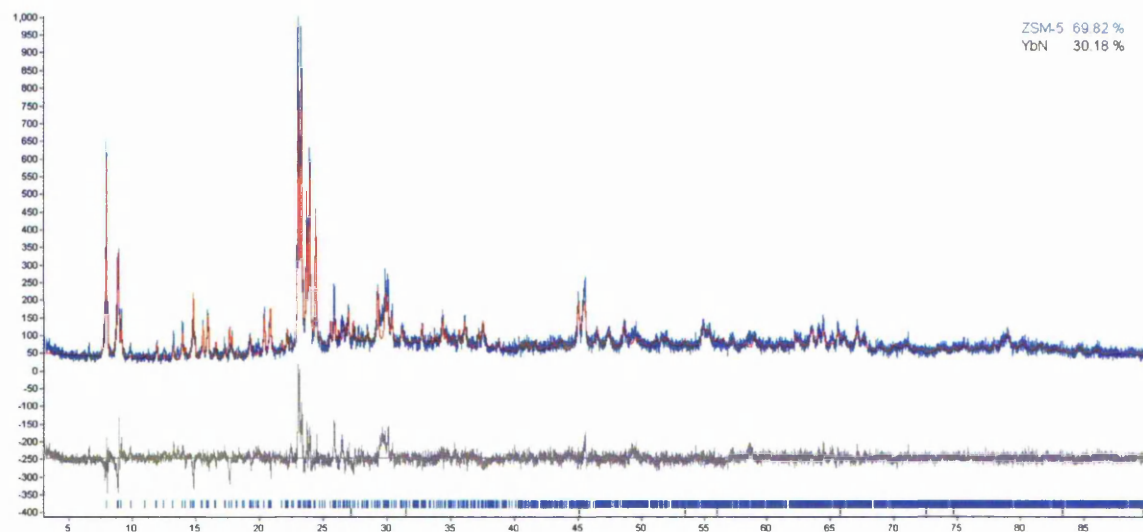


Figure 218: Rietveld profile for ZSM-5 with 10wt% Yb as YbN.

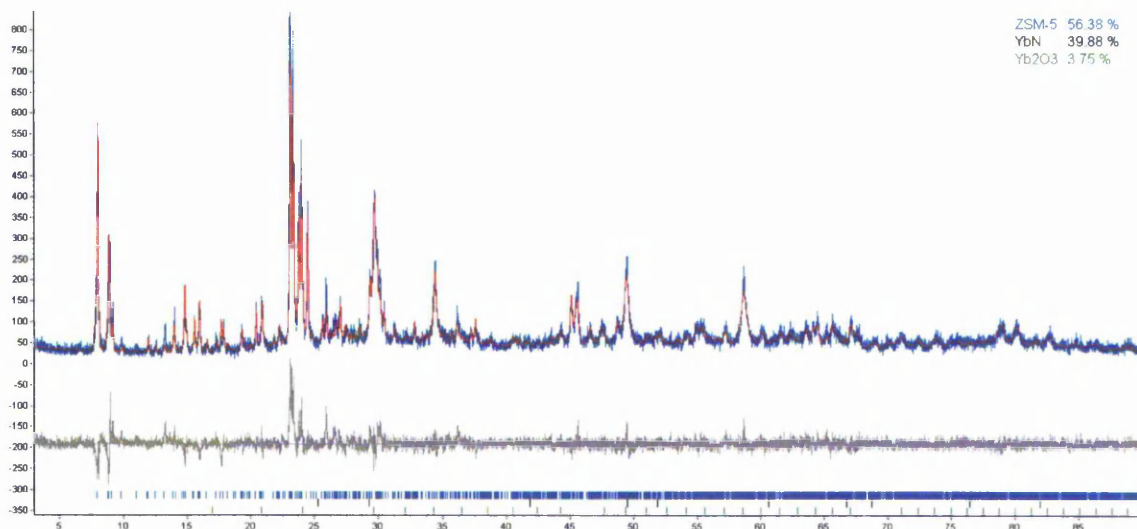


Figure 219: Rietveld profile for ZSM-5 with 15wt% Yb as YbN and Yb₂O₃.

The Rietveld profiles show the zeolite is left unaffected by the YbN occlusion process and no YbN diffraction peaks are visible at all loadings. However, at 15wt% Yb there is significant diffraction by a Yb₂O₃ phase at a calculated 3.75% content. This has also been seen in Zn₃N₂ at 50wt% loading in FER, in which it was suggested that the oxygen-rich environment may not allow the formation of nitride phases.

The lattice parameters from ZSM-5 samples with YbN using the solution impregnation method derived from Rietveld analysis of the XRD data are shown graphically in Figure 220 to Figure 222.

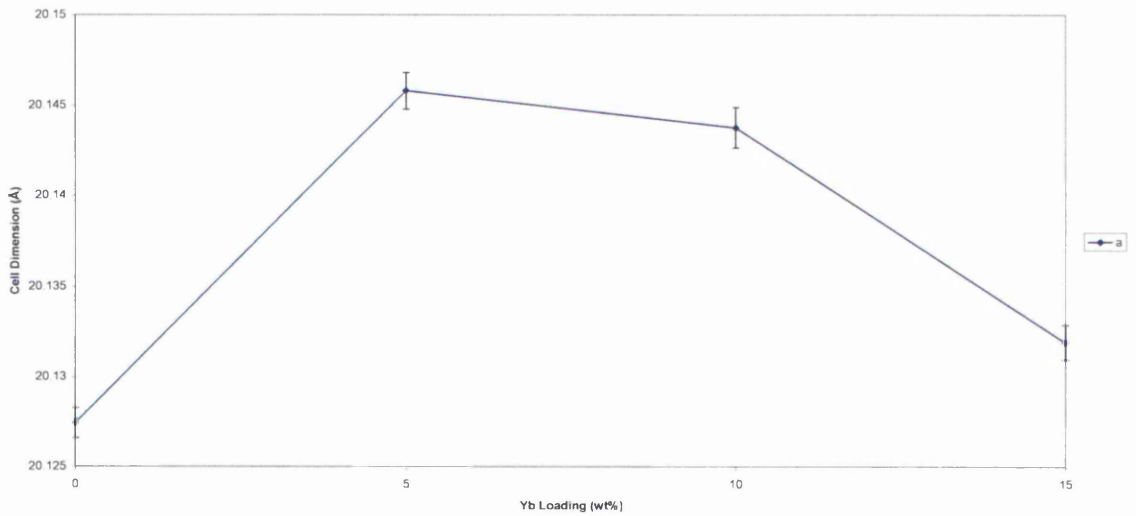


Figure 220: Unit cell parameter *a* for ZSM-5 with YbN.

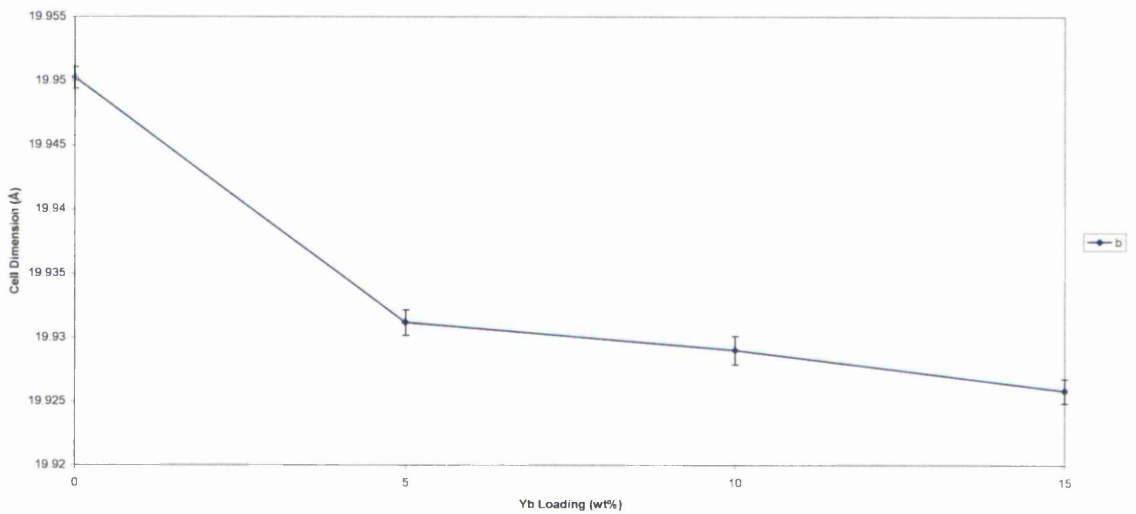


Figure 221: Unit cell parameter *b* for ZSM-5 with YbN.

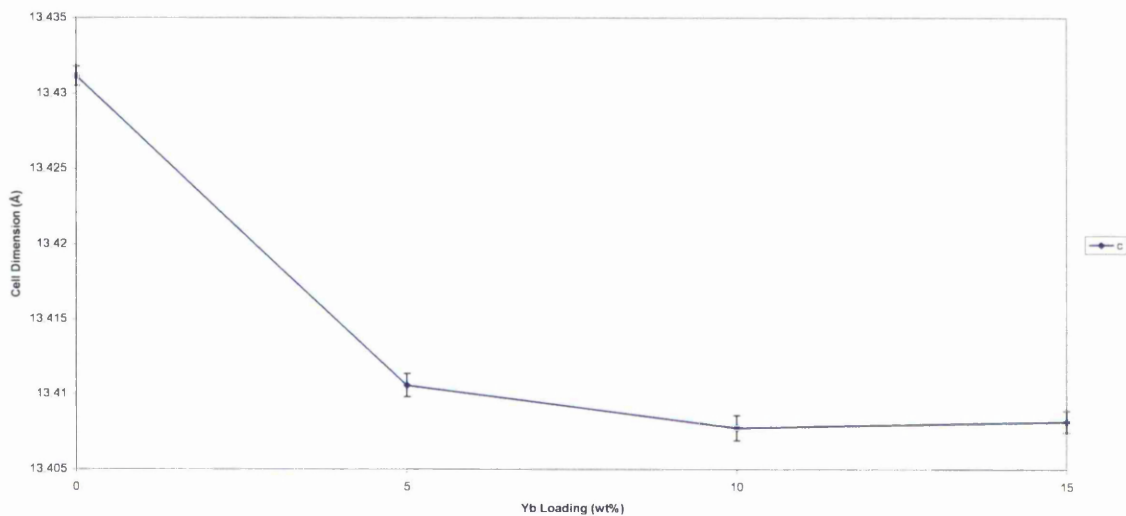


Figure 222: Unit cell parameter *c* for ZSM-5 with YbN.

The unit cell values generally decrease with increasing Yb loading, within experimental error.

Curve fitting analysis of the overlapping N(1s) and Yb(4p_{1/2}) regions in the XPS spectrum for the 10 wt% loaded YbN sample indicated 3 components, the energies of which were 397.1, 398.1 and 401.7 eV respectively (Figure 223). Due to the absence of much data for Ytterbium compounds in the literature it is difficult to ascertain the true binding energy of the Yb(4p_{1/2}) photoelectron peak, however, the spin-orbit splitting of metallic Yb is approximately 49 eV, which would suggest that, from the Yb(4p_{3/2}) peak, which is present at 346.9 eV, the peak at 397.1 eV is the Yb(4p_{1/2}) peak. Therefore it may be concluded that the other peaks are due to nitrogen in the form of nitride and NH_x groups respectively; whether this is due to YbNH_x or NH_x groups on the zeolite from residual ammonia cannot be ascertained readily from the current data.

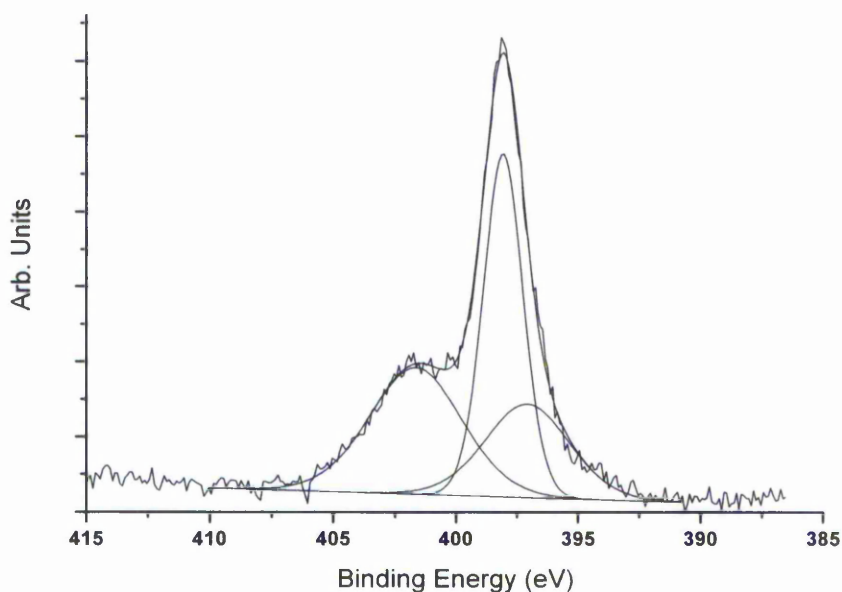


Figure 223: N(1s) and Yb(4p_{1/2}) Core level spectra for 10 wt% YbN containing zeolite. Peak designations are discussed within the main text.

The UV-Vis-NIR spectra for HZSM-5 supported Yb compounds shown in Figure 224 contain distinct peaks at 345, 968 ($^3F_{1/2} \rightarrow ^2F_{8/2}$), 1400 and 1900 nm for samples containing YbCl₃. The peak at 345 nm is no longer observed after the samples were nitrided. The other peaks are still present in the spectra for the nitrided samples. After the nitridation process, however, extra peaks at 920, 1515 and 1990 nm are observed.

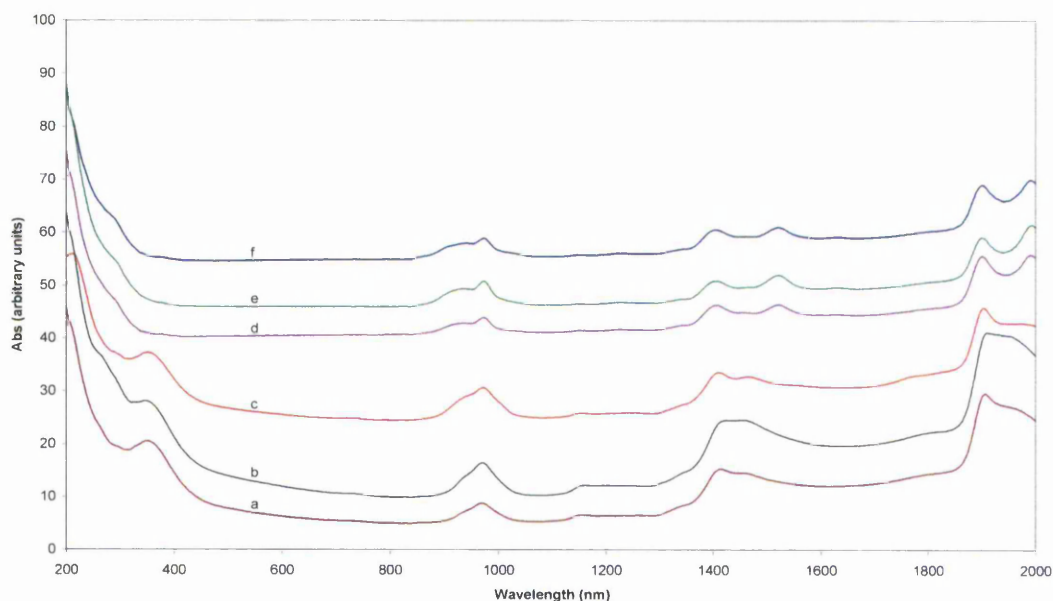


Figure 224: UV-Vis Spectra for HZSM-5 with (a) 5 wt% loading of Yb as YbCl₃ (b) 10 wt% loading of Yb as YbCl₃ (c) 15 wt% loading of Yb as YbCl₃ (d) 5 wt% loading of Yb as YbN (e) 10 wt% loading of Yb as YbN (f) 15 wt% loading of Yb as YbN.

10.2.3. Terbium Nitride

Diffraction profiles were refined using Topas Academic V4.1 against the ZSM-5 structure reported by Li, et al. [89] and TbN structure reported by Klesnar, et al. [131]

Rietveld profiles are shown in Figure 225 to Figure 227.

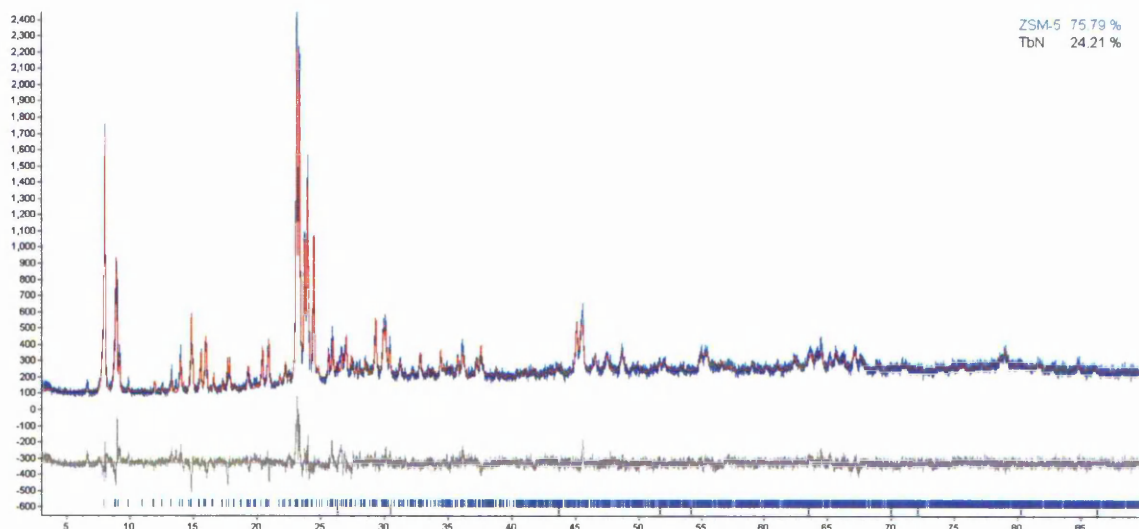


Figure 225: Rietveld profile for ZSM-5 with 5wt% Tb as TbN.

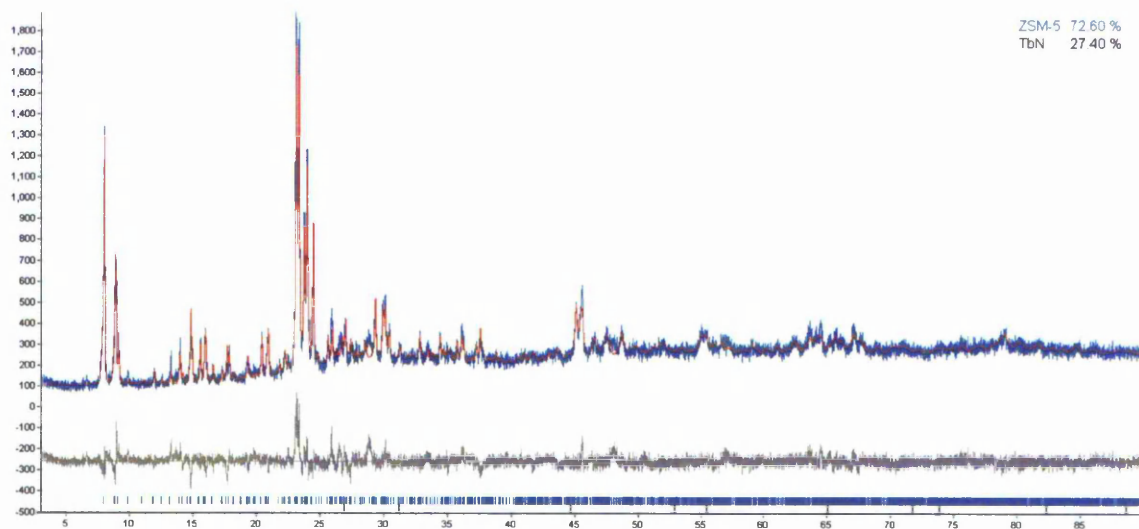


Figure 226: Rietveld profile for ZSM-5 with 10wt% Tb as TbN.

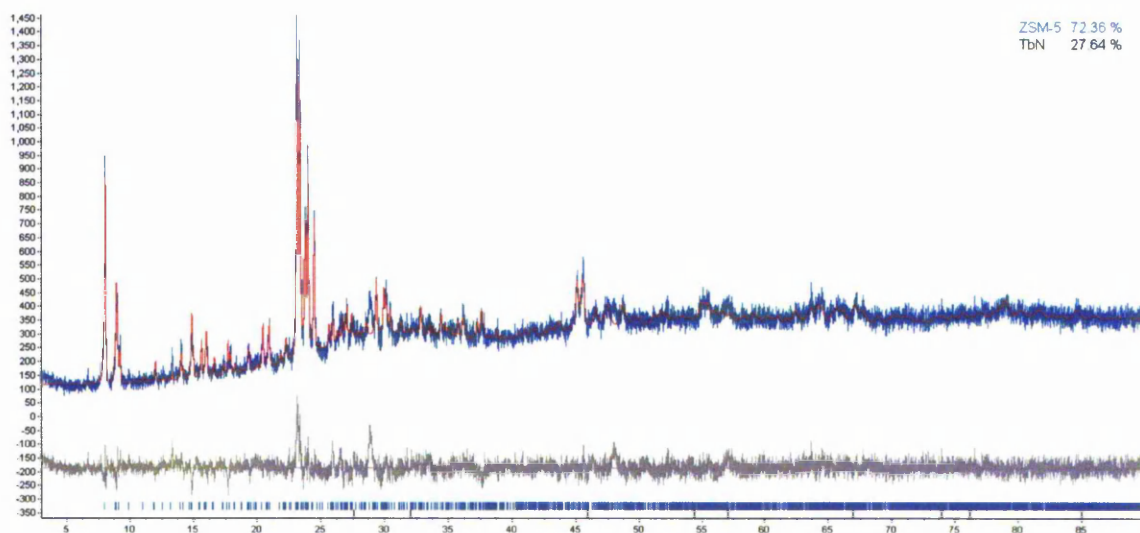


Figure 227: Rietveld profile for ZSM-5 with 15wt% Tb as TbN.

The Rietveld profiles show that the zeolite structure is unaffected by TbN occlusion and the increase in x-ray fluorescence, indicated by an increase in profile noise at increasing 2θ , confirms the presence of Tb. The calculated TbN content is similar for all three samples, yet given the degree of fluorescence this is not a reliable value. Also, the lack of any visible diffraction from TbN is unreliable due to the fluorescence.

Figure 228 shows the unit cell values for ZSM-5 samples loaded with TbN. As is clear, the values remain relatively constant in all three samples.

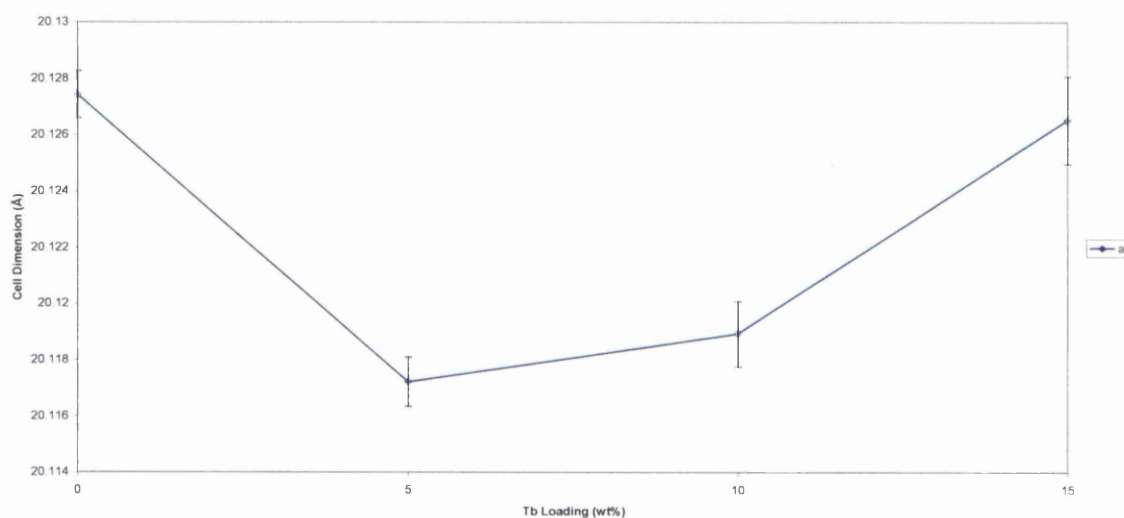


Figure 228: Unit cell parameter a for ZSM-5 with TbN.

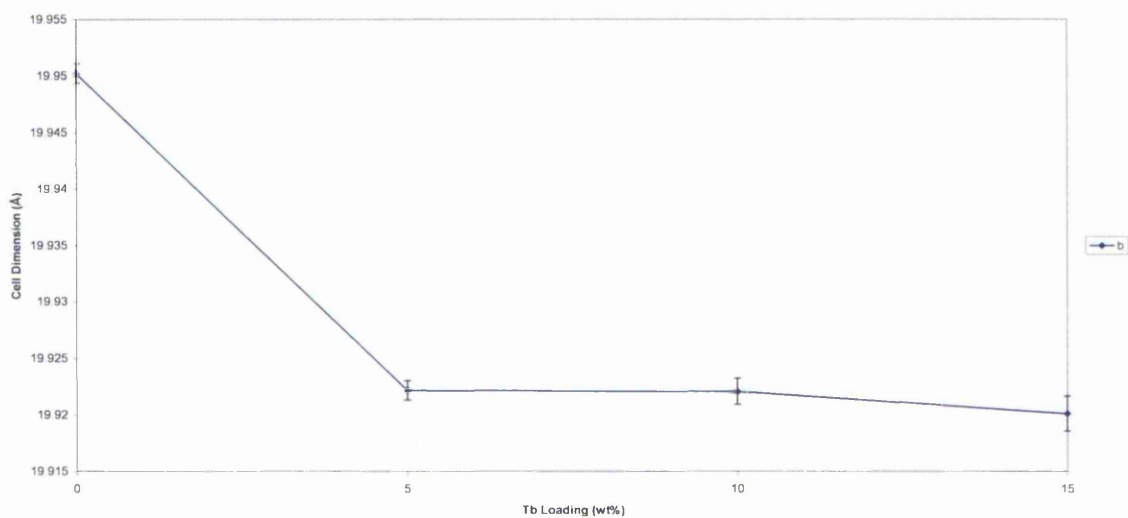


Figure 229: Unit cell parameter *b* for ZSM-5 with TbN.

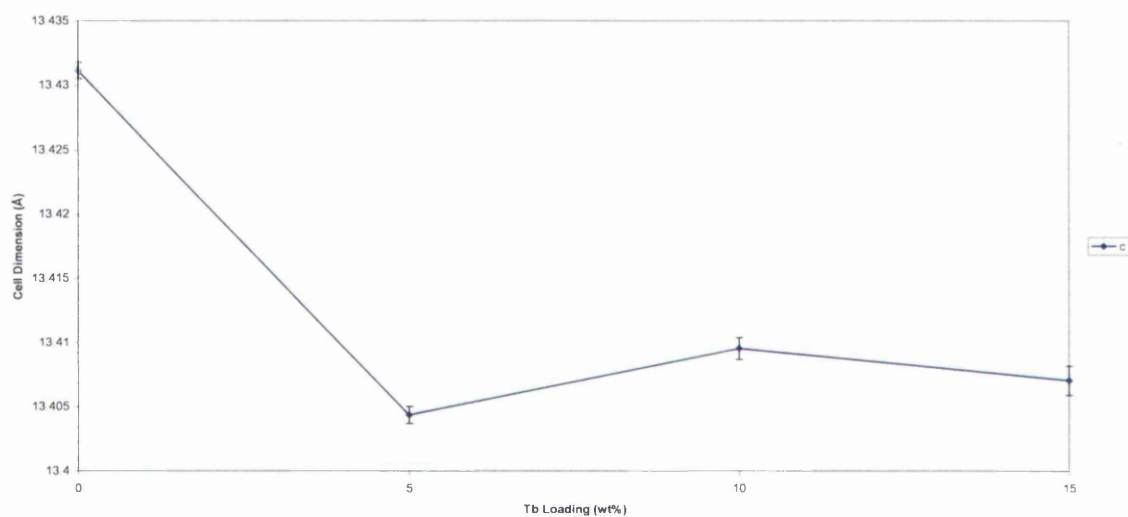


Figure 230: Unit cell parameter *c* for ZSM-5 with TbN.

The unit cell values in the *a* direction increase with increasing Tb loading. The other directions remain similar within experimental error.

The UV-Vis-NIR spectra for HZSM-5 supported Tb compounds shown in Figure 231 contain peaks at 235, 282, 356, 966, 1150, 1410, 1458 and 1903 nm for samples containing $TbCl_3$. Upon nitridation the peak at 235 nm is broadened, while the peak at 282 nm is increased and broadened. The peak at 1458 nm is removed upon nitridation and another peak at 1520 nm emerges. The other peaks are still present in the spectra for the nitrided samples.

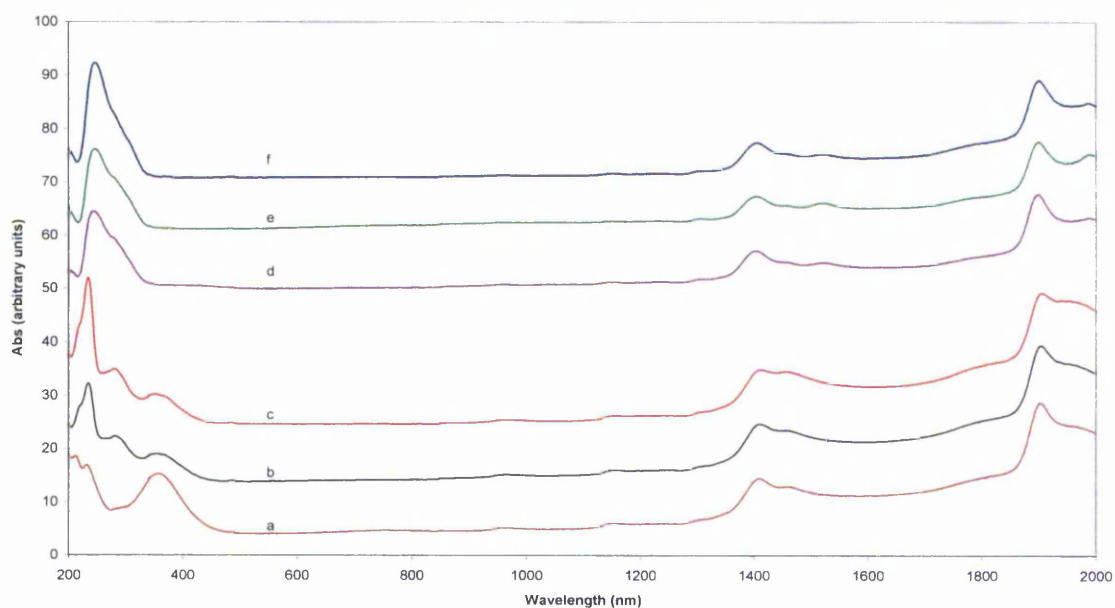


Figure 231: UV-Vis Spectra for HZSM-5 with (a) 5 wt% loading of Tb as $TbCl_3$ (b) 10 wt% loading of Tb as $TbCl_3$ (c) 15 wt% loading of Tb as $TbCl_3$ (d) 5 wt% loading of Tb as TbN (e) 10 wt% loading of Tb as TbN (f) 15 wt% loading of Tb as TbN.

10.3. Discussion and Conclusions

The data presented in this work demonstrates that the methods used in the preparation of zeolite-supported molybdenum nitride catalysts are more widely applicable to other metal nitride systems. [30] The XRD profiles confirm the integrity of the host zeolite structure throughout the procedures involved, and the absence of an extra-framework nitride phase in all EuN samples and in the 5 and 10 wt% YbN samples. At 15 wt% loading of Yb, it is clear however, that an agglomeration process takes place, resulting in the formation of a small amount of extra-framework Yb_2O_3 crystals. The reason for oxidation taking place in an ammonia atmosphere is not immediately clear, but it is worth noting that the host zeolite provides a rich source of oxygen and that slight degradation of the framework under such harsh conditions as those of the nitridation process is entirely possible. Whilst this is not the desired outcome, the presence of these Yb_2O_3 nanoparticles in this material may be of interest with regards to catalysing reactions such as dehydration of 1,5-pentanediol and 1,4-butanediol or the isomerisation of α -pinene. [132-135] The XPS spectra of the 10 wt% Yb-containing sample show no clear indication of Yb_2O_3 and suggest that the majority of Yb is present as nitrogen-containing species after nitridation. The presence of YbN and YbNH_x within the pores of the samples with lower loadings and the presence of EuN inside the Eu-containing samples are confirmed by XPS data. XPS measurements for the two samples examined confirm that in both cases the lanthanide ions are dispersed throughout the pore structure of the LnCl_3 -zeolite precursor. The apparent lack of Cl, when considering the relative amounts of Ln^{3+} and Cl^- ions is accounted for by considering that some metal ions replace protons in an ion exchange process. The XPS data for the EuN-containing samples and the 5 and 10 wt% YbN-containing

samples confirm the lanthanide is well dispersed throughout the ZSM-5 pore structure and not localized on the surface of the zeolite crystallites. This conclusion has been supported by HRTEM images and EDX results. UV-Vis spectroscopy compliments the XPS data and confirms the presence of the lanthanides and a change in spectroscopic (and hence electronic) properties upon nitridation of the chloride precursors.

The data also suggest the possibility of the existence of LnNH_x species, which have proven to be active catalysts in a number of processes. YbNH , for example, has been shown to catalyse the isomerisation of but-1-ene and the Michael reaction of cyclopent-2-enone with dimethylmalonate.^[123] The catalytic behaviour of zeolite-supported LnNH_x nanoparticles will be of interest in terms of these processes with respect to their bulk counterparts.

11. Other Nitrides in ZSM-5

The work presented so far in this thesis has proven that the band-gaps of a small selection of semiconducting materials can be altered by impregnation into microporous zeolites and that the degree of band-gap alteration depends on the zeolite framework and the impregnation method. In order to investigate further a number of other nitrides were explored as an initial venture into expanding the work.

As the molten salt impregnation method is limited in regards to the metal salts that can be used in the process (i.e. the salt has to have a low melting point), this method was not used in the preparation of the following reported materials. A modified solution-based impregnation method was used, with a washing step between the impregnation and nitridation processes, thus removing any surface material prior to nitridation.

11.1. Cerium Nitride

The diffraction profile was refined using Topas Academic V4.1 against the ZSM-5 structure reported by Li, et al.^[89] and CeN structure reported by Rossat-Mignod, et al.^[136] The Rietveld profile is shown in Figure 232.

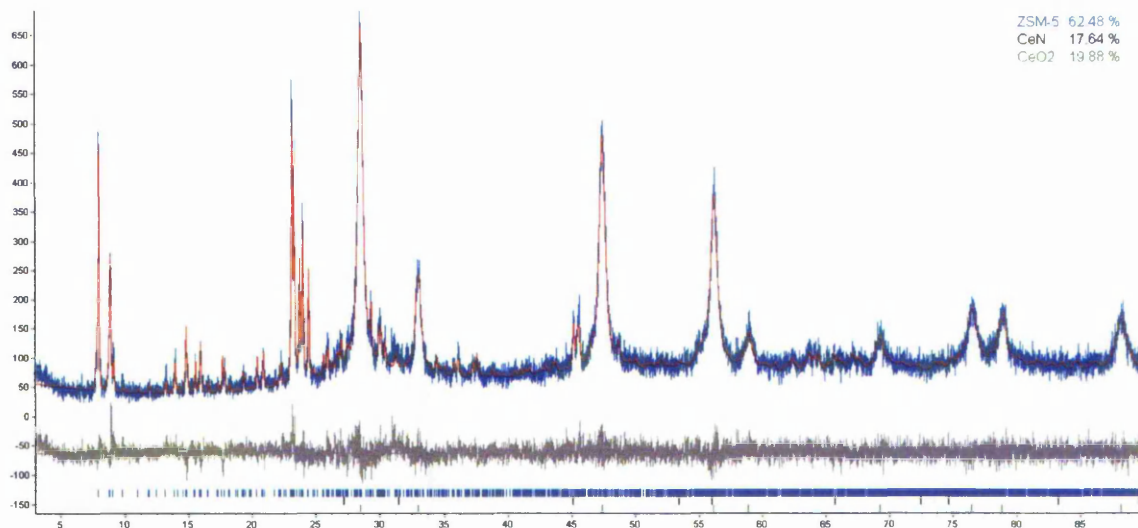


Figure 232: Rietveld plot of ZSM-5 with CeN and CeO₂.

As the Rietveld plot clearly shows, there is a significant amount of CeO₂, calculated at 19.88%, in the sample. There is a small degree of diffraction from the nitride, which is calculated at 17.64% of the content. This is another example of significant oxidation, likely to be due to the oxygen-rich zeolite environment.

The unit cell parameters, derived from Rietveld refinement, of both the parent zeolite and the zeolite with CeN are shown in Table 13.

Table 13: ZSM-5-CeN Unit Cell Parameters.

Material	Unit Cell Parameters, Å		
	<i>a</i>	<i>b</i>	<i>c</i>
HZSM-5	20.14424 ±0.00091	19.96171 ±0.00093	13.45895 ±0.00069
ZSM-5 – CeN	20.08953 ±0.00141	19.92092 ±0.00140	13.40121 ±0.00105
Difference	0.05471	0.04079	0.05774

As shown in Table 13, the unit cell of ZSM-5 shrinks by approximately 0.05 nm.

Figure 233 shows the UV Vis diffuse reflectance curve obtained for ZSM-5 with 15 wt% Ce as CeN. A significant absorbance at ~450 nm is present, which equates to a band gap of approximately 3.35 eV (± 0.00905) (cf. 1.76 eV for a stoichiometric thin film or 3.15 eV for CeO₂ [137]).

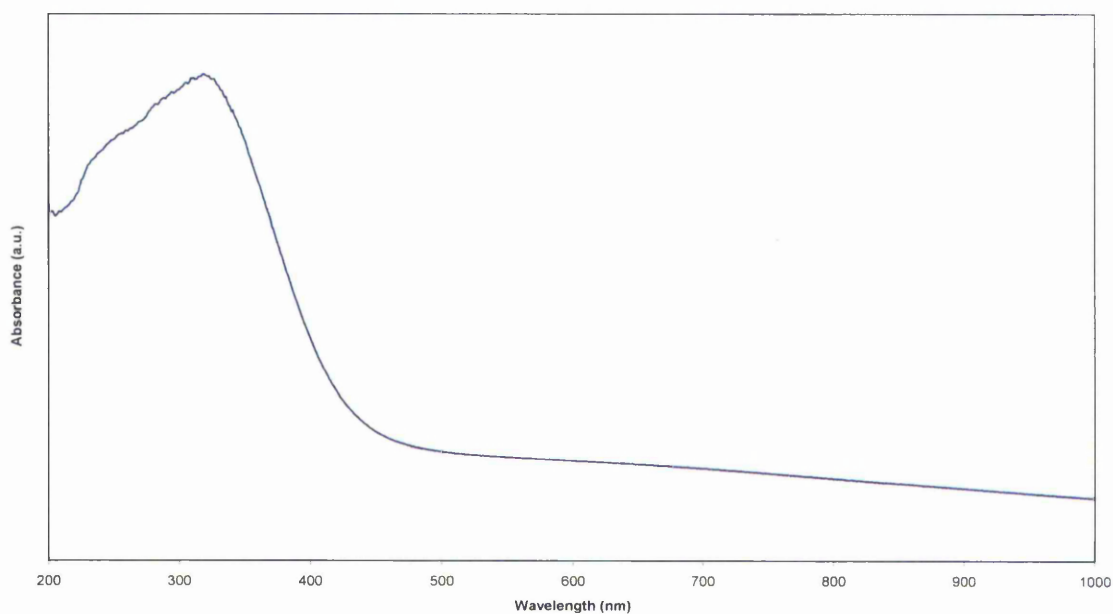


Figure 233: UV Vis data for ZSM-5 with CeN.

11.2. Chromium Nitride

The diffraction profile was refined using Topas Academic V4.1 against the ZSM-5 structure reported by Li, et al.^[89] and CrN structure reported by Etmayer, et a.^[138]

The Rietveld profile is shown in Figure 234.

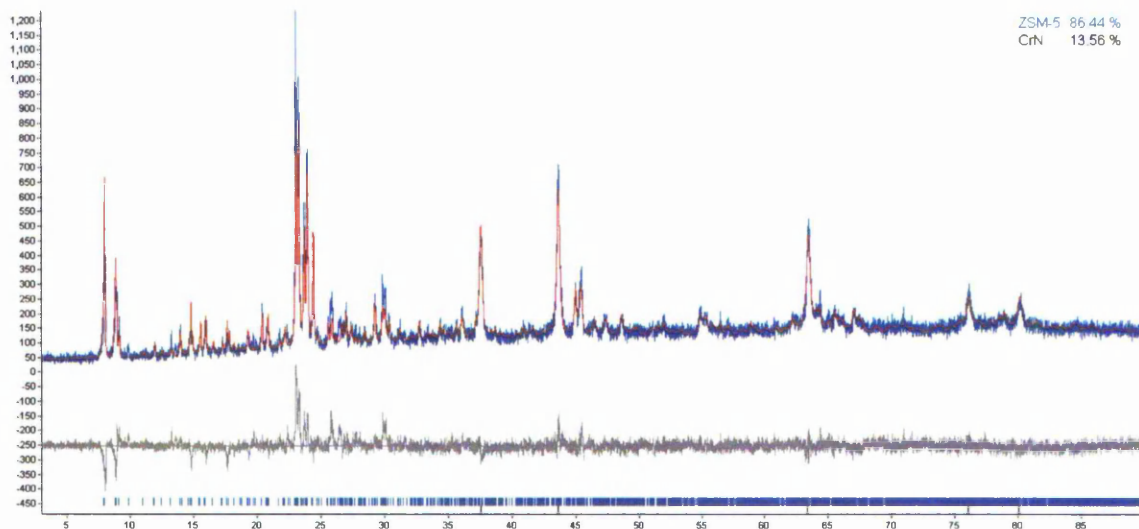


Figure 234: Rietveld profile of ZSM-5 with CrN.

The Rietveld plot shows the zeolite is unaffected by occlusion of CrN, but also that the CrN is not entirely confined to the zeolite pores, indicated by significant diffraction lines from the CrN phase with a calculated content contribution of 13.56%. There is no detectable diffraction from an oxide phase.

The unit cell parameters, derived from Rietveld refinement, of both the parent zeolite and the zeolite with CrN are shown in Table 14.

Table 14: ZSM-5-CrN Unit Cell Parameters.

Material	Unit Cell Parameters, Å		
	<i>a</i>	<i>b</i>	<i>c</i>
HZSM-5	20.14424 ±0.00091	19.96171 ±0.00093	13.45895 ±0.00069
ZSM-5 – CrN	20.16475 ±0.00115	19.96037 ±0.00110	13.41395 ±0.00083
Difference	-0.02051	0.00134	0.045

As shown in Table 14, the change in unit cell of ZSM-5 varies between the three directions and is more profound in the *c* direction.

Figure 235 shows the UV Vis diffuse reflectance curve obtained for ZSM-5 with 15 wt% Cr as CrN. There is a considerable absorption step at 565 nm, which equates to a band gap of 2.2 eV (± 0.003903) (cf. 0.19 eV ^[139], which would be beyond the analytical capabilities of the UV-Vis spectrometer used in this work).

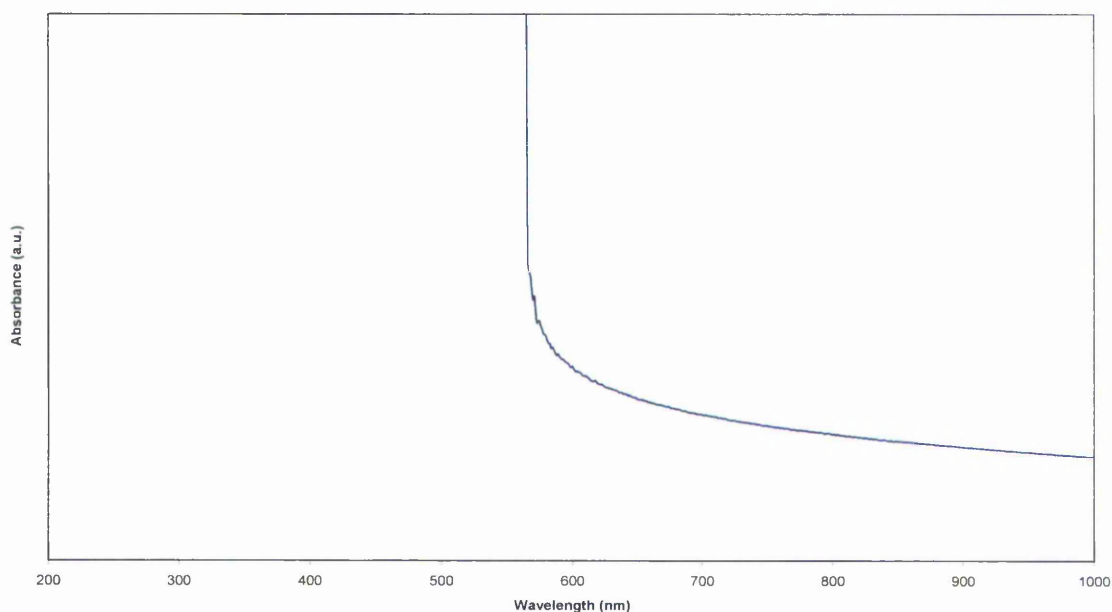


Figure 235: UV Vis data for ZSM-5 with CrN.

11.3. Copper Nitride

The diffraction profile was refined using Topas Academic V4.1 against the ZSM-5 structure reported by Li, et al.^[89] and Cu_3N structure reported by Paniconi, et al.^[140] the Rietveld profile is shown in Figure 236.

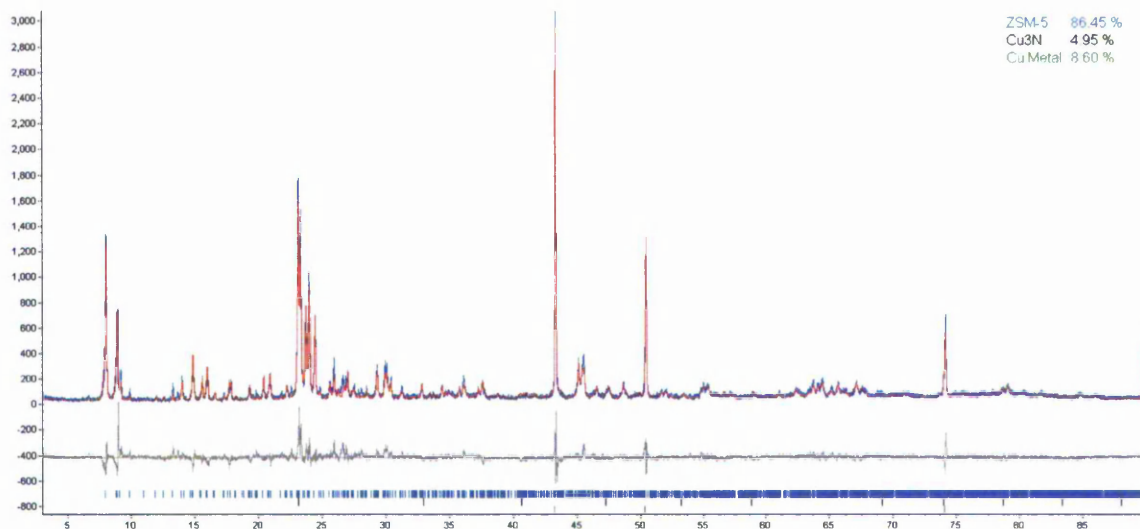


Figure 236: Rietveld profile of ZSM-5 with Cu_3N and Cu metal.

The Rietveld profile shows that the zeolite host framework remains intact and that a small amount (4.95%) of Cu_3N is present. It also shows, however, that there is a significant amount of metallic Cu (8.60%). Cu_3N is difficult to synthesise, therefore the NH_3 may in this case act more as a reducing atmosphere than an ammonolysis one, thus reducing $\text{Cu}(\text{NO}_3)_2$ to Cu^0 . It could also be the case that the metal is an intermediate product of Cu ammonolysis, therefore if the reaction were allowed to continue the emergence of one phase over the other may have occurred. In this case the oxygen-rich zeolite framework may have played no part in the synthesis of the non-nitride product.

The unit cell parameters, derived from Rietveld refinement, of both the parent zeolite and the zeolite with Cu₃N are shown in Table 15.

Table 15: ZSM-5-Cu₃N Unit Cell Parameters.

Material	Unit Cell Parameters, Å		
	<i>a</i>	<i>b</i>	<i>c</i>
HZSM-5	20.14424 ±0.00091	19.96171 ±0.00093	13.45895 ±0.00069
ZSM-5 – Cu₃N	20.09717 ±0.00077	19.92969 ±0.00077	13.40266 ±0.00054
Difference	0.04707	0.03202	0.05629

As shown in Table 15, the change in unit cell of ZSM-5 varies slightly between the three directions but lies between a 0.03 and 0.06 Å reduction in size.

Figure 237 shows the UV Vis diffuse reflectance curve obtained for ZSM-5 with 15 wt% Cu as Cu_3N . There is a very slight absorption step at 565 nm, which equates to a band gap of 2.15 eV (± 0.003728) (cf. 1.2-1.9 eV ^[141-145]).

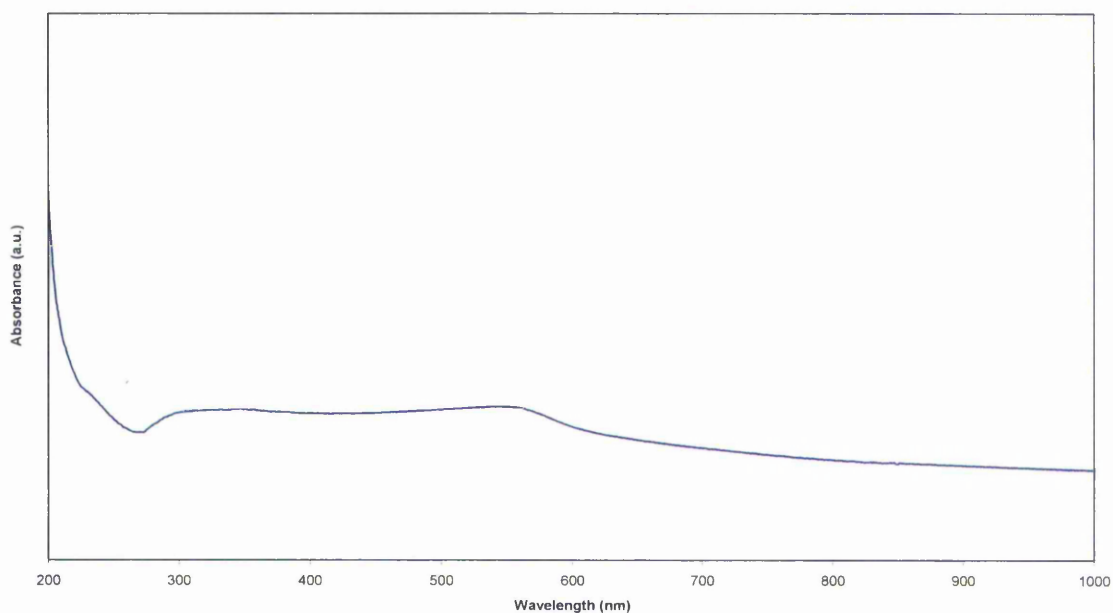


Figure 237: UV Vis data for ZSM-5 with Cu_3N .

11.4. Tin Nitride

The diffraction profile was refined using Topas Academic V4.1 against the ZSM-5 structure reported by Li, et al.^[89] and Sn_3N_4 structure reported by Scotti, et al.^[146]

The Rietveld profile is shown in Figure 238.

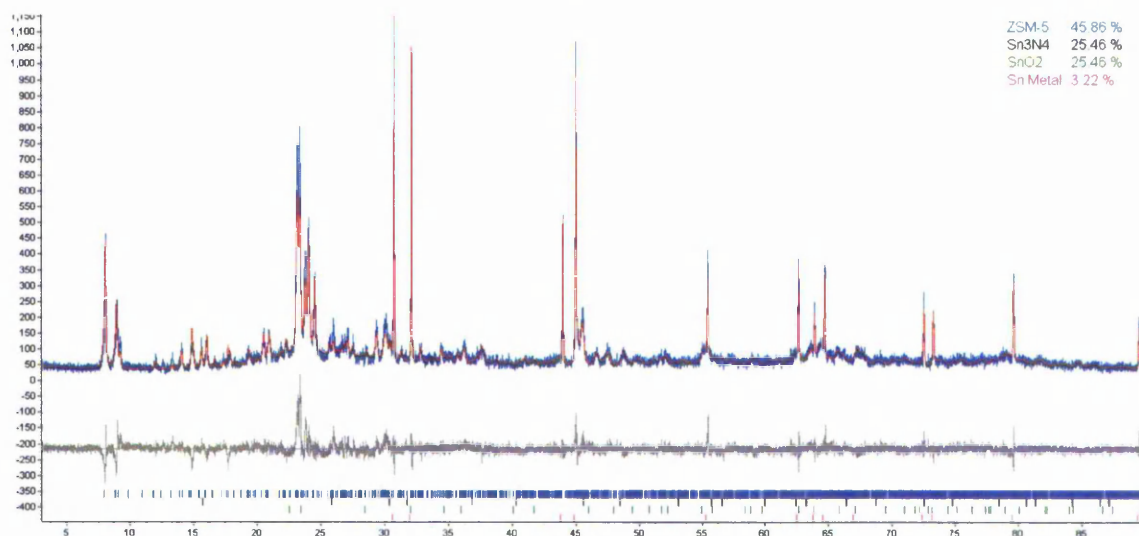


Figure 238: Rietveld profile of ZSM-5 with Sn_3N_4 , SnO_2 and Sn Metal.

The Rietveld profile shows that the zeolite structure has undergone slight amorphisation, indicated by an increased degree of profile noise. Also, as well as Sn_3N_4 (25.46%), SnO_2 (25.46%) and metallic Sn (3.22%) are present. It can be assumed that the oxygen made available by the amorphisation of the zeolite framework has led to oxidation of the Sn and that in this experiment the NH_3 has acted as both an ammonolysis and a reducing atmosphere. This could also be a case where the metal is an intermediate of the ammonolysis, thus continuing the experiment may have shown the nitride phase content increase. However, given the oxygen-rich zeolite environment, the presence of SnO_2 would remain.

The unit cell parameters, derived from Rietveld refinement, of both the parent zeolite and the zeolite with Sn_3N_4 are shown in Table 16.

Table 16: ZSM-5- Sn_3N_4 Unit Cell Parameters.

Material	Unit Cell Parameters, Å		
	<i>a</i>	<i>b</i>	<i>c</i>
HZSM-5	20.14424	19.96171	13.45895
	±0.00091	±0.00093	±0.00069
ZSM-5 – Sn_3N_4	20.14288	19.94851	13.38446
	±0.00142	±0.00125	±0.00102
Difference	0.00136	0.0132	0.07449

As shown in Table 16, the change in unit cell of ZSM-5 varies considerably between the three directions with the most significant reduction in size along the *c* direction. As well as Sn_3N_4 , which was present as 25.46% of the sample, SnO_2 and Sn metal were detected by Rietveld refinement as 25.46% and 3.22% of the sample respectively.

Figure 239 shows the UV Vis diffuse reflectance curve obtained for ZSM-5 with 15 wt% Sn as Sn_3N_4 . There is an absorption peak at 241 nm, which equates to an energy of 5.145 eV (± 0.021348) (cf. 1.5 eV for a tin nitride thin film, ^[147] which would have resulted in an absorption step at ~ 826 nm and 3.6–4 eV for SnO_2 thin films ^[148, 149]).

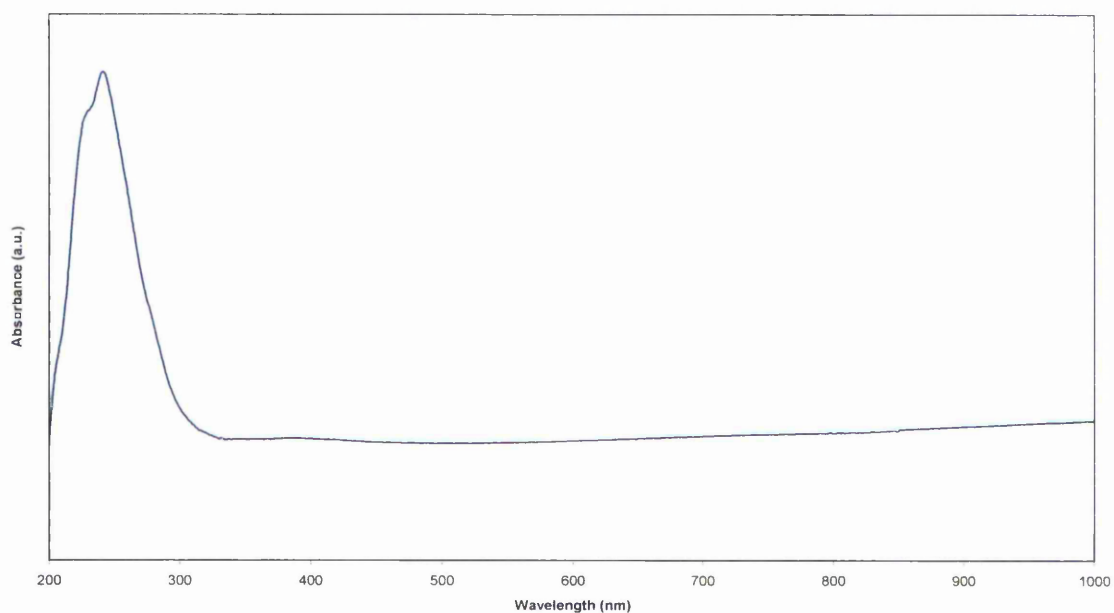


Figure 239: UV Vis data for ZSM-5 with Sn_3N_4 .

11.5. Discussion and Conclusions

The work presented in this chapter highlights the versatility of the solution impregnation method and subsequent nitridation processes, yet also draws attention to the difficulties that can be encountered when choosing the guest phase. These results show that while there are some materials that will readily form the nitride phase under the synthesis conditions, others may also be reduced to the metal in the NH_3 atmosphere and/or become oxidised; an unfortunate side-effect of hosting the nitridation reaction within an oxygen rich framework.

In terms of the effect of zeolite confinement on the optical properties of the materials; there is some evidence to support previous data that show the band gap of a material is generally increased upon zeolite inclusion via the solution impregnation method. This data is, however, far from conclusive due to the mixtures of nitride/oxide/metal phases and the position of some band gaps lying beyond analytical capabilities.

12. Conclusions and Further Work

12.1. Summary and Conclusions

This work shows that zeolites have the potential to be used in optoelectronic applications as crystal engineering templates. The results show not only that semiconducting nitrides and oxides can be occluded within the pore structure of a zeolite, but also that in doing so the band structure of the guest semiconducting phase will change. This work also shows that the route by which the occlusion of optoelectronic materials is achieved can influence the physical structure of the clusters and the electronic properties of the end products.

Traditionally, the occlusion of guest phases within zeolite frameworks has been carried out by a number of methods, such as solution and gaseous impregnation. These methods, however, have largely been investigated with improvements in catalysis as the driving force. With that in mind, research groups have endeavoured to create isolated atoms/clusters of atoms of catalytic materials about the internal and external surfaces of various zeolites. This approach has allowed the area of zeolite catalysis to bloom, yet has not contributed much to the discovery of novel applications for zeolites. In this work, where the zeolites were used as templating materials, the main objective was to produce occluded materials that had adopted the shape of the internal cavities of the zeolite and had not been deposited on the outer surface. With only a small amount of research dedicated to this area of zeolite science, in comparison to zeolite catalysis, this work had to be focussed more on synthetic method development than application.

The motivation behind the work, however, remains unchanged. It is now well known that the area of nano-science is more than simply making things fit in smaller packages. In many areas of science it has been seen that the reduced dimensionality of materials and processes can yield very interesting results. This work fixes upon the properties of semiconducting materials and the effect of reduced dimensionality, or quantum confinement, on their intrinsic optical properties. There is a wealth of evidence and even commercially available devices that prove that semiconducting quantum structures are not only interesting materials, but also useful and in demand. Therefore we sought to build upon current knowledge in semiconductor technology and improve on the fabrication of quantum devices by using zeolites as template materials.

This was no easy task. As mentioned previously, the bulk of the research into zeolite science has been in the field of catalysis, in which most synthetic and analytical methods and techniques simply don't apply when looking into electronic materials. This, compounded with the plethora of zeolites and semiconductors to study and the complexity of both subject areas, made finding a place to start extremely difficult. Therefore, a logical and concise approach was taken. The three zeolites in the study were not only commercially available, but were also different enough in their framework geometries to enable the beginnings of a comprehensive study to ensue. The choice of semiconductors was more commercially informed. GaN is a relatively newly discovered semiconductor, given its wide band gap and is therefore in high demand, yet it is quite expensive to make. ZnO has been extensively studied and is widely used and relatively cheap to synthesise. These two materials form the basis of the work and other guest materials were investigated out of pure scientific curiosity.

The results presented in this work demonstrate the feasibility of the methods investigated and the complexity of issues that may arise if this were to be taken further into device fabrication. What is evident is that the choice of zeolite/semiconductor/impregnation method combination is vital in determining the success in material synthesis. In most of the experiments it was seen that there was a distinct difference in the band gap values of solution impregnated and melt impregnated materials, where the molten salt treated samples had larger band gap energies than the solution-treated samples. This highlights the differences in deposition between the two methods, resulting in dense or disperse phases, thus different sizes of clusters. Of course, in the case of GaN in ZSM-5 it was noted that GaN nanowires were formed, protruding from the zeolite crystals. It is obvious that in this case the zeolite acted as a crystal engineering template, yet was unable to contain the crystallisation process, again highlighting the importance of the choice of zeolite to match the guest phase.

Another example of the possible importance of the choice of host/guest combination was seen in the Ga_2O_3 and Zn_3N_2 experiments, in which no band gap was observed in most samples. This may be an indication that the pore sizes of these zeolites are too small to enable a band structure to be detected in the guest materials, i.e. the response in UV-Vis spectrometry may be too weak, or that the guest phases are not formed at all. These theories, of course, would need further confirmation, possibly with synchrotron radiation experiments complemented with HRTEM and the investigation of larger pore materials, such as MCM-41 and SBA-15.

Although the impregnation of materials was indirectly alluded to by powder XRD data, in the way the unit cell dimensions of the host zeolite increased upon impregnation, the conclusive evidence of impregnation came in the form of HRTEM. Unfortunately due to the limited availability of the technique a correlation between the unit cell values and actual degree of impregnation was not possible. However, if there were a correlation, the use of unit cell dimensions from powder XRD data may be used in the future as a quick test to determine whether impregnation was successful.

With regards to the initial aims of this work, this work has shown that it is possible to produce metal nitrides within zeolites and that there is an effect on the optoelectronic properties upon zeolite occlusion. Unfortunately, the oxygen rich environment that zeolites provide doesn't lend them to oxygen-sensitive material storage, yet oxygen deficient zeotypes may offer a solution. There are distinct changes in the optical band gap energies, which could allow known semiconducting materials to be tailored to specific applications by slightly altering the band structure. The extent to which a band gap can be altered depends on the zeolite geometry and pore sizes, the guest material and the impregnation method. This is obviously not trivial given the number of zeolite geometries available, the ability to change the Si:Al ratio and the existence of zeotypes containing atoms other than Si, Al and O. Given the complexity of zeolite science the integration of these types of composite materials within electronic devices is still distant, however with a significant amount of work from the zeolite community it may still become a reality.

12.2. Further Work

The work presented in this thesis presents a number of interesting topics that could be investigated further in order to fully assess the feasibility of producing zeolite-occluded optoelectronic materials, the effect of zeolite-templating on the properties of said materials and the suitability of zeolite-occluded materials for integration into devices.

A number of routes can be explored when taking this work further. The most obvious direction would be to expand on the number of zeolites studied, which, considering that there are nearly 200 unique structures reported to date and only 3 of them have been studied in this work, is not an insignificant amount of work. This could be more focussed by either categorising the frameworks by pore geometry and comparing zeolites with similar geometries yet different pore sizes, or by comparing frameworks of like pore size yet different geometry type. Another clear direction to take would be to investigate a wider range of semiconductor materials with the aim of recording patterns of behaviour that may relate to chemical composition, crystal structure, band structure or physical properties of the material and its precursors.

The analytical aspects of this work could be elaborated on. For example, a more in depth crystallographic study could be undertaken using a synchrotron radiation source to identify interactions between the host framework and the guest phases and the structural nature of the occluded materials (such as that conducted by Anderson, et al. ^[17]). Also, a very limited portion of the materials made in this work were studied using HRTEM. By expanding these studies a more in depth

understanding of the mechanism of diffusion of the nitride/oxide precursors through the zeolite frameworks could be achieved. Regarding the electronic characteristics of the materials; a study of the properties other than the band gap energy that may be affected by quantum confinement (such as conductivity, current thresholds, current threshold temperatures and spectral linewidths) would be instrumental in characterising the effect of zeolite confinement on optoelectronic materials and the feasibility of device integration.

This work has also called into question the feasibility of using zeolites, which are oxygen-rich framework materials, to host air-unstable nitride materials. This could also be a factor to consider when contemplating the occlusion of other, non-oxide materials. Therefore, an investigation into the use of non-oxidic zeotype materials (i.e. framework oxygen is replaced by, for example, nitrogen) as possible nitride hosts could quell some of the uncertainty surrounding the chemical composition and purity of zeolite-occluded materials.

In summation, this work provides an initial suggestion that zeolites could be used to engineer the optoelectronic properties of metal nitride and oxide materials. However, the work has also presented a number of questions, which need to be addressed before any zeolite-based materials are to be tested on devices.

13. References

- [1] D. W. Breck, *Zeolite molecular sieves: structure, chemistry, and use*, Wiley, New York, **1973**.
- [2] C. Colella, A. F. Gualtieri, *Microporous and Mesoporous Materials*, **2007**, *105*, 213.
- [3] FJ Dzierzanowski, WL Haden Jr., **1960**.
- [4] E. Michalko, **1965**.
- [5] H. Eichhorn, *Pogg. Ann. Phys. Chem*, **1858**, *105*, 126.
- [6] O. Weigel, E. Steinhoff, *Z. Kristallogr.*, **1925**, *61*, 125.
- [7] W. Loewenstein, M. Loewenstein, *Am Miner*, **1954**, *39*, 92.
- [8] K. Jung Chao, S. Ping Sheu, L. Lin, M. J. Genet, M. Hsiang Feng, *Zeolites*, **1997**, *18*, 18.
- [9] G. Coudurier, A. Auroux, J. C. Vedrine, R. D. Farlee, L. Abrams, R. D. Shannon, *Journal of Catalysis*, **1987**, *108*, 1.
- [10] C. Baerlocher, L. B. McCusker, *Database of Zeolite Structures*.
- [11] G. W. Morey, F. E. Ingerson, *Economic Geology*, **1937**, *32*, 607.
- [12] E. M. Flanigen, **1991**, Volume 58, 13.
- [13] L. A. Bray, H. T. Fullam, *Advances in Chemistry Series*, **1971**, 450.
- [14] G. T. Kerr, G. F. Shipman, *J. Phys. Chem.*, **1968**, *72*, 3071.
- [15] J. E. Readman, I. Gameson, J. A. Hriljac, P. A. Anderson, *Microporous and Mesoporous Materials*, **2007**, *104*, 83.
- [16] A. Goldbach, P. D. Barker, P. A. Anderson, P. P. Edwards, *Chemical Physics Letters*, **1998**, *292*, 137.
- [17] J. E. Readman, I. Gameson, J. A. Hriljac, P. P. Edwards, P. A. Anderson, **2000**, 595.
- [18] A. Mayoral, P. A. Anderson, *Nanotechnology*, **2007**, *18*, 6.
- [19] P. A. Anderson, M. J. Edmondson, P. P. Edwards, I. Gameson, P. J. Meadows, S. R. Johnson, W. Z. Zhou, *Z. Anorg. Allg. Chem.*, **2005**, *631*, 443.
- [20] C. Tiseanu, V. A. Lorenz-Fonfria, V. I. Parvulescu, A. Gessner, M. U. Kumke, *J. Appl. Phys.*, **2008**, *104*, 033530.
- [21] C. Tiseanu, V. A. Lorenz-Fonfria, A. Gessner, M. U. Kumke, B. Gagea, **2009**, *20*, 312.
- [22] C. Tiseanu, M. U. Kumke, V. I. Parvulescu, A. Gessner, B. C. Gagea, J. A. Martens, *J Phys Chem B*, **2006**, *110*, 25707.
- [23] C. Tiseanu, A. Gessner, M. U. Kumke, *J. Non Cryst. Solids*, **2008**, *354*, 1969.
- [24] C. Tiseanu, A. Gessner, M. Kumke, B. Gagea, V. I. Parvulescu, J. Martens, **2008**, *128*, 751.
- [25] C. Tiseanu, L. Frunza, M. Kumke, *Physica B-Condensed Matter*, **2004**, *352*, 358.
- [26] Y. V. Meteleva, F. Roessner, G. F. Novikov, **2008**, *196*, 154.
- [27] Y. V. Meteleva, F. Roessner, G. F. Novikov, *Russian Journal of General Chemistry*, **2007**, *77*, 532.
- [28] S. Yuan, M. Tomonari, D. Matsuo, K. Mori, T. Uruga, H. Yamashita, **2008**, *34*, 519.
- [29] S. Yuan, M. Tomonari, D. Matsuo, K. Mori, T. Ohmichi, I. Katayama, H. Yamashita, **2007**, *882*, 774.
- [30] D. McKay, J. Hargreaves, R. Howe, *Catal. Lett.*, **2006**, *112*, 109.
- [31] T. Kadono, T. Kubota, Y. Okamoto, *Catalysis Today*, **2003**, *87*, 107.
- [32] P. P. Edwards, P. A. Anderson, L. J. Woodall, A. Porch, A. Robert Armstrong, *Materials Science and Engineering A*, **1996**, *217-218*, 198.

- [33] C. Bouvy, W. Marine, R. Sporcken, B. L. Su ,*Chemical Physics Letters*,**2006**,428,312.
- [34] L. Li, J. L. Shi ,*Nanotechnology*,**2006**,17,344.
- [35] C. S. Lim, S. J. Lee, W. Oh, I. J. Kim ,*Journal of Ceramic Processing Research*,**2009**,10,382.
- [36] J. Shi, J. Chen, Z. Feng, T. Chen, X. Wang, P. Ying, C. Li ,*J. Phys. Chem. B*,**2006**,110,25612.
- [37] H. Uchida, T. Ogata, H. Yoneyama ,*Chemical Physics Letters*,**1990**,173,103.
- [38] F. Wang, H. Song, G. Pan, L. Fan, Q. Dai, B. Dong, H. Liu, J. Yu, X. Wang, L. Li ,*Mater. Res. Bull.*,**2009**,44,600.
- [39] I. I. Abu, K. J. Smith ,*JOURNAL OF CATALYSIS*,**2006**,241,356.
- [40] A. Andreyev, M. Akaishi, D. Golberg ,*Chemical Physics Letters*,**2003**,372,635.
- [41] H. Yamane, M. Shimada, S. J. Clarke, F. J. DiSalvo ,*Chemistry of Materials*,**1997**,9,413.
- [42] S. J. Henderson, A. L. Hector ,*Journal of Solid State Chemistry*,**2006**,179,3518.
- [43] Y. J. Park, C. S. Oh, T. H. Yeom, Y. M. Yu ,*J. Cryst. Growth*,**2004**,264,1.
- [44] P. Vongpayabal, S. Kimura ,*Powder Technol*,**2005**,156,73.
- [45] Z. Zhang, R. Liu, Y. Qian ,*Mater. Res. Bull.*,**2002**,37,1005.
- [46] G. Ziegenbalg, U. Breuel, E. Ebrecht, H. Holldorf, R. Brink ,*Journal of the European Ceramic Society*,**2001**,21,947.
- [47] G. Paniconi, Z. Stoeva, R. I. Smith, P. C. Dippo, B. L. Gallagher, D. H. Gregory ,*Journal of Solid State Chemistry*,**2008**,181,158.
- [48] J. L. Coffey, M. A. Johnson, L. Zhang, R. L. Wells, J. F. Janik ,*Chemistry of Materials*,**1997**,9,2671.
- [49] B. Mazumder, A. L. Hector ,*J. Mater. Chem.*,**2009**,19,4673.
- [50] V. Ryzhii ,*Semicond. Sci. Technol.*,**1996**,11,759.
- [51] M. Asada, Y. Miyamoto, Y. Suematsu ,*IEEE J. Quantum Electron.*,**1986**,22,1915.
- [52] M. Henini, M. Bugajski ,*Microelectron. J.*,**2005**,36,950.
- [53] D. Wasserman, C. Gmachl, S. A. Lyon, E. A. Shaner ,**2006**,88,191118.
- [54] H. Chia-Fu, O. Jeong-Seok, P. Zory, D. Botez ,*Selected Topics in Quantum Electronics, IEEE Journal of*,**2000**,6,491.
- [55] N. N. Ledentsov, V. M. Ustinov, V. A. Shchukin, P. S. Kop'ev, Z. I. Alferov, D. Bimberg ,*Semiconductors*,**1998**,32,343.
- [56] L. E. Brus ,*J. Chem. Phys.*,**1984**,80,4403.
- [57] M. J. Kelly ,*Journal of Physics: Condensed Matter*,**1995**,7,5507.
- [58] M. Thomas ,*Chemical Vapor Deposition*,**1997**,3,288.
- [59] A. Mang, K. Reimann, S. Rübenacke ,*Solid State Commun.*,**1995**,94,251.
- [60] D. H. Gregory ,*Coordination Chemistry Reviews*,**2001**,215,301.
- [61] D. H. Gregory, P. M. O'Meara, A. G. Gordon, D. J. Siddons, A. J. Blake, M. G. Barker, T. A. Hamor, P. P. Edwards ,*Journal of Alloys and Compounds*,**2001**,317-318,237.
- [62] A. G. Gordon, D. H. Gregory, A. J. Blake, D. P. Weston, M. O. Jones ,*International Journal of Inorganic Materials*,**2001**,3,973.
- [63] G. Y. Li, X. D. Li, H. Wang, Z. Q. Li ,*Appl. Phys. A-Mater. Sci. Process.*,**2008**,93,471.
- [64] W. W. Lei, D. Liu, P. W. Zhu, Q. S. Wang, G. Liang, J. Hao, X. H. Chen, Q. L. Cui, G. T. Zou ,*J. Phys. Chem. C*,**2008**,112,13353.
- [65] Y. F. Shi, Y. Wan, R. Y. Zhang, D. Y. Zhao ,*Adv. Funct. Mater.*,**2008**,18,2436.
- [66] J. H. Ma, Y. H. Du ,*J. Alloy. Compd.*,**2008**,463,196.

- [67] K. Y. Bao, S. Z. Liu, L. Shi, S. L. Xiong, J. Li, X. B. Hu, J. Cao, Y. T. Qian, *J. Solid State Chem.*, **2008**, *181*, 1634.
- [68] S. B. Xue, X. Zhang, R. Huang, D. H. Tian, H. Z. Zhuang, C. S. Xue, *Cryst. Growth Des.*, **2008**, *8*, 2177.
- [69] S. V. Nand, K. Ankur, K. Brijesh, M. B. Raj, *Solid State Sci.*, **2008**, *10*, 569.
- [70] R. Niewa, D. A. Zherebtsov, M. Kirchner, M. Schmidt, W. Schnelle, *Chem. Mat.*, **2004**, *16*, 5445.
- [71] H. Imamura, Y. Sakata, T. Nuruyu, T. Imahashi, *J. Alloy. Compd.*, **2006**, *418*, 251.
- [72] T. Suehiro, N. Hirosaki, T. Wada, Y. Yajima, M. Mitomo, *Powder Diffr.*, **2005**, *20*, 40.
- [73] H. Imamura, T. Nuruyu, T. Kawasaki, T. Teranishi, Y. Sakata, *Catal. Lett.*, **2004**, *96*, 185.
- [74] J. Karpinski, E. Kaldis, E. Jilek, *Inorg. Chim. Acta*, **1987**, *140*, 87.
- [75] H. Imamura, T. Kuhara, M. Furutachi, T. Sakamoto, Y. Sakata, *Chem. Lett.*, **2002**, 744.
- [76] U. Baisch, S. Pagano, M. Zeuner, N. Barros, L. Maron, W. Schnick, *Chem. -- Eur. J.*, **2006**, *12*, 4785.
- [77] K. J. Laidler, J. H. Meiser, B. C. Sanctuary, *Physical Chemistry*, **2002**.
- [78] W. L. Bragg, *The Development of X-ray Analysis*, **1975**.
- [79] W. Clegg, *Crystal Structure Determination*, Oxford University Press, **1998**.
- [80] C. Hammond, *The Basics of Crystallography and Diffraction*, Oxford University Press, **1997**.
- [81] H. M. Rietveld, *J. Appl. Cryst.*, **1969**, *2*, 65.
- [82] Alan Coelho, Topas Academic, *4.1*, 2007.
- [83] C. R. Brundle, A. D. Baker, *Electron Spectroscopy: Theory, Techniques and Applications*, **1977**.
- [84] G. D. Gilliland, *Materials Science and Engineering: R: Reports*, **1997**, *18*, 99.
- [85] C. Yeh, Z. W. Lu, S. Froyen, A. Zunger, *Phys. Rev. B*, **1992**, *46*, 10086.
- [86] C. T. Yang, M. H. Huang, *J Phys Chem B*, **2005**, *109*, 17842.
- [87] C. Y. Zhi, D. Y. Zhong, E. G. Wang, *Chemical Physics Letters*, **2003**, *381*, 715.
- [88] C. - Chen, C. - Yeh, C. - Liang, C. - Lee, C. - Chen, M. - Yu, H. - Liu, L. C. Chen, Y. - Lin, K. - Ma, K. H. Chen, *Journal of Physics and Chemistry of Solids*, **2001**, *62*, 1577.
- [89] X. Li, C. Gu, B. Zhong, *Fenzi Cuihua*, **1992**, *6*, 104.
- [90] M. Kaminski, S. Podsiadlo, K. Wozniak, L. Dobrzycki, R. Jakiela, A. Barcz, M. Psoda, J. Mizera, *J. Cryst. Growth*, **2007**, *303*, 395.
- [91] J. B. Parise, D. R. Corbin, L. Abrams, D. E. Cox, *Acta Crystallographica Section C*, **1984**, *40*, 1493.
- [92] I. Bull, P. Lightfoot, L. A. Villaescusa, L. M. Bull, R. K. B. Gover, J. S. O. Evans, R. E. Morris, *J. Am. Chem. Soc.*, **2003**, *125*, 4342.
- [93] H. G. Kim, W. T. Kim, *J. Appl. Phys.*, **1987**, *62*, 2000.
- [94] J. Hao, M. Cocivera, *J. Phys. D*, **2002**, *35*, 433.
- [95] J. Ahman, G. Svensson, J. Albertsson, **1996**, *52*, 1338.
- [96] L. Dai, L. P. You, X. F. Duan, W. C. Lian, G. G. Qin, *J. Cryst. Growth*, **2004**, *267*, 538.
- [97] H. Xiao, H. Ma, C. Xue, H. Zhuang, J. Ma, F. Zong, X. Zhang, *Mater. Chem. Phys.*, **2007**, *101*, 99.
- [98] Y. Luo, Z. Hou, J. Gao, D. Jin, X. Zheng, *Materials Science and Engineering: B*, **2007**, *140*, 123.
- [99] N. M. Al-Otaibi, G. Hutchings, *Catalysis Letters*, **2010**, *134*, 191.

- [100] S. V. Awate, P. N. Joshi, T. H. Kim, K. I. Kim, V. P. Shiralkar, *Adsorption Science & Technology*, **1999**, *17*, 651.
- [101] V. R. Choudhary, S. K. Jana, B. P. Kiran, *Journal of Catalysis*, **2000**, *192*, 257.
- [102] A. C. Faro Junior, J. G. Eon, L. Nogueira, R. F. da Silva, V. d. O. Rodrigues, *Catalysis Today*, **2008**, *133*, 913.
- [103] M. Haneda, Y. Kintaichi, H. Shimada, H. Hamada, *Journal of Catalysis*, **2000**, *192*, 137.
- [104] B. Xu, T. Li, B. Zheng, W. Hua, Y. Yue, Z. Gao, *Catalysis Letters*, **2007**, *119*, 283.
- [105] K. Toyoura, H. Tsujimura, T. Goto, K. Hachiya, R. Hagiwara, Y. Ito, *Thin Solid Films*, **2005**, *492*, 88.
- [106] K. Kuriyama, Y. Takahashi, F. Sunohara, *Phys. Rev. B*, **1993**, *48*, 2781.
- [107] D. E. Partin, D. J. Williams, M. O'Keeffe, *Journal of Solid State Chemistry*, **1997**, *132*, 56.
- [108] F. Zong, H. Ma, C. Xue, H. Zhuang, X. Zhang, H. Xiao, J. Ma, F. Ji, *Solid State Commun.*, **2004**, *132*, 521.
- [109] F. J. Zong, H. L. Ma, C. S. Xue, W. Du, X. J. Zhang, J. Ma, F. Ji, H. D. Xiao, *Rare Metal Materials and Engineering*, **2006**, *35*, 55.
- [110] F. J. Zong, H. L. Ma, W. Liang, W. Du, X. J. Zhang, H. D. Xiao, J. Ma, F. Ji, C. S. Xue, H. Z. Zhuang, *Chinese Physics Letters*, **2005**, *22*, 907.
- [111] F. J. Zong, H. L. Ma, J. Ma, W. Du, X. J. Zhang, H. D. Xiao, F. Ji, C. S. Xue, *Appl. Phys. Lett.*, **2005**, *87*, 233104.
- [112] F. J. Zong, H. L. Ma, J. Ma, C. S. Xue, X. J. Zhang, H. D. Xiao, F. Ji, H. Z. Zhuang, *Mater Lett*, **2005**, *59*, 2643.
- [113] F. J. Zong, H. L. Ma, C. S. Xue, H. Zhuang, X. J. Zhang, M. Jin, J. Feng, H. D. Xiao, *Science in China Series G-Physics Mechanics & Astronomy*, **2005**, *48*, 201.
- [114] F. J. Zong, H. L. Ma, C. S. Xue, H. Z. Zhuang, X. J. Zhang, H. D. Xiao, J. Ma, F. Ji, *Prism 5: the Fifth Pacific Rim International Conference on Advanced Materials and Processing, Pts 1-5*, **2005**, 475-479, 3787.
- [115] F. J. Zong, H. L. Ma, C. S. Xue, H. Z. Zhuang, X. J. Zhang, H. D. Xiao, J. Ma, F. Ji, *Solid State Commun.*, **2004**, *132*, 521.
- [116] S. Cui, W. Feng, H. Hu, Z. Feng, Y. Wang, *J. Alloys Compounds*, **2009**, *476*, 306.
- [117] G. Kenanakis, D. Vernardou, E. Koudoumas, N. Katsarakis, *J. Cryst. Growth*, **2009**, *311*, 4799.
- [118] X. Yan, Z. Li, C. Zou, S. Li, J. Yang, R. Chen, J. Han, W. Gao, *The Journal of Physical Chemistry C*, **2010**, *114*, 1436.
- [119] H. Rozale, L. Beldi, B. Bouhafs, P. Ruterana, *physica status solidi (b)*, **2007**, *244*, 1560.
- [120] F. K. Yam, Z. Hassan, *Superlattices and Microstructures*, **2008**, *43*, 1.
- [121] Y. Chang, F. C. Hong, *Mater Lett*, **2009**, *63*, 1855.
- [122] T. Baba, S. Hikita, Y. Ono, T. Yoshida, T. Tanaka, S. Yoshida, *J. Mol. Catal. A: Chem.*, **1995**, *98*, 49.
- [123] T. Baba, S. Hikita, R. Koide, Y. Ono, T. Hanada, T. Tanaka, S. Yoshida, *J. Chem. Soc., Faraday Trans.*, **1993**, 3177.
- [124] H. Imamura, S. Hiranaka, Y. Sakata, S. Tsuchiya, *J. Chem. Soc., Faraday Trans.*, **1992**, *88*, 1577.
- [125] H. Imamura, T. Konishi, Y. Sakata, S. Tsuchiya, *J. Chem. Soc., Chem. Commun.*, **1993**, 1852.
- [126] H. Imamura, H. Yoshimochi, Y. Harada, *J. Mol. Catal.*, **1991**, *66*, L33.

- [127] H. Jacobs, U. Fink, *Zeitschrift für anorganische und allgemeine Chemie*, **1978**, *438*, 151.
- [128] T. Becue, J. Manoli, C. Potvin, G. Djega-Mariadassou, M. Delamar, *J. Phys. Chem. B*, **1997**, *101*, 6429.
- [129] NIST X-Ray Photoelectron Spectroscopy Database, Version 3.5, (National Institute of Standards and Technology, Gaithersburg); <http://srdata.nist.gov/xps/>.
- [130] A. Dönni, P. Fischer, A. Furrer, W. Bacsa, P. Wachter, *Zeitschrift für Physik B Condensed Matter*, **1990**, *80*, 269.
- [131] H. P. Klesnar, P. Rogl, *HT-HP*, **1990**, *22*, 453.
- [132] S. Sato, R. Takahashi, N. Yamamoto, E. Kaneko, H. Inoue, *Appl. Catal. A*, **2008**, *334*, 84.
- [133] A. Igarashi, S. Sato, R. Takahashi, T. Sodesawa, M. Kobune, *Catal. Commun.*, **2007**, *8*, 807.
- [134] T. Yamamoto, T. Matsuyama, T. Tanaka, T. Funabiki, S. Yoshida, *J. Mol. Catal. A: Chem.*, **2000**, *155*, 43.
- [135] T. Yamamoto, T. Matsuyama, T. Tanaka, T. Funabiki, S. Yoshida, *Phys. Chem. Chem. Phys.*, **1999**, 2841.
- [136] J. Rossat-Mignod, P. Burlet, S. Quezel, J. M. Effantin, D. Delacôte, H. Bartholin, O. Vogt, D. Ravot, *J Magn Magn Mater*, **1983**, *31-34*, 398.
- [137] I. Porqueras, C. Person, C. Corbella, M. Vives, A. Pinyol, E. Bertran, *Solid State Ionics*, **2003**, *165*, 131.
- [138] P. Etmayer, W. Schebesta, A. Vendl, R. Kieffer, *Monatshefte fuer Chemie und verwandte Teile anderer Wissenschaften*, **1978**, *109*, 929.
- [139] X. Y. Zhang, D. Gall, *PHYSICAL REVIEW B*, **2010**, *82*, .
- [140] G. Paniconi, Z. Stoeva, H. Doberstein, R. I. Smith, B. L. Gallagher, D. H. Gregory, *Solid State Sciences*, **2007**, *9*, 907.
- [141] S. Ghosh, F. Singh, D. Choudhary, D. K. Avasthi, V. Ganesan, P. Shah, A. Gupta, *Surface and Coatings Technology*, **2001**, *142-144*, 1034.
- [142] F. Fendrych, L. Soukup, L. Jastrabik, M. Sícha, Z. Hubicka, D. Chvostová, A. Tarasenko, V. Studnicka, T. Wagner, *Diamond and Related Materials*, **1999**, *8*, 1715.
- [143] K. Joo Kim, J. Hyuk Kim, J. Hoon Kang, *J. Cryst. Growth*, **2001**, *222*, 767.
- [144] D. Wang, N. Nakamine, Y. Hayashi, *J. Vac. Sci. Technol. A*, **1998**, *16*, 2084.
- [145] T. Maruyama, T. Morishita, *J. Appl. Phys.*, **1995**, *78*, 4104.
- [146] N. Scotti, W. Kockelmann, J. Senker, S. Trassel, H. Jacobs, *Zeitschrift fuer Anorganische und Allgemeine Chemie*, **1999**, *625*, 1435.
- [147] T. Maruyama, T. Morishita, *Appl. Phys. Lett.*, **1996**, *69*, 890.
- [148] D. P. Joseph, P. Renugambal, M. Saravanan, S. P. Raja, C. Venkateswaran, *Thin Solid Films*, **2009**, *517*, 6129.
- [149] Q. Wu, J. Song, J. Kang, Q. Dong, S. Wu, S. Sun, *Mater Lett*, **2007**, *61*, 3679.